A Stark Decelerator on a Chip

Am Fritz-Haber-Institut
der Max-Planck-Gesellschaft
entstandene und

im Fachbereich Physik
der Freien Universität Berlin
eingereichte Dissertation
von

Samuel A. Meek

Berlin, 2010

Erstgutachter:	Prof. Dr. Gerard Meijer Fritz-Haber-Institut der Max-Planck-Gesellschaft Freie Universität Berlin
Zweitgutachter:	Prof. Dr. Martin Wolf Freie Universität Berlin Fritz-Haber-Institut der Max-Planck-Gesellschaft
Disputation:	12. Juli, 2010

Kurzfassung

Ein lithographisch gefertigter Chip, der 1254 mikroskopische Elektroden mit einem Mitten-Abstand von 40 µm besitzt, wird genutzt, um eine lineare Anordnung von Minima des elektrischen Feldes zu generieren in einem Abstand von 120 µm und eine Höhe von 25 µm über der Oberfläche. Hierzu werden sechs Spannungen benötigt, die extern angelegt werden. Für polare Moleküle in einem tieffeld-suchenden Zustand sind diese Feldminima auch mechanische Minima und fungieren als Fallen. Werden die angelegten Spannungen in definierter Weise variiert, bewegen sich die Feldminima längs der Struktur mit konstantem Abstand zur Oberfläche.

Experimente wurden mit CO im metastabilen $a^3\Pi_1$, $v = 0$, $J = 1$ Zustand durchgeführt, der eine starke lineare Stark-Verschiebung für tieffeld-suchende Komponenten aufweist. Er hat eine Anregungsenergie von 6 eV, die einfachen Nachweis über einen Augerprozess erlaubt, und eine natürliche Lebensdauer von 2,6 ms, die für die hier beschriebenen Experimente ausreicht. Metastabiles CO wird in einem gepulsten Molekularstrahl durch direkte Anregung mit einem 5 ns Laserpuls produziert. Die Moleküle durchlaufen einen Skimmer und erreichen den Chip in einer Flugbahn parallel zur Oberfläche und senkrecht zur Elektrodenrichtung. Über dem Chip selbst werden sie durch die elektrischen Felder geführt und verlassen ihn in Richtung des Detektors.

Metastabile ^{12}CO Moleküle wurden bei konstante Geschwindigkeiten zwischen 276 and 360 $\frac{\mathrm{m}}{\mathrm{s}}$ geführt und auch von 360 $\frac{\mathrm{m}}{\mathrm{s}}$ zu Endgeschwindigkeiten zwischen 336 und 240 $\frac{\mathrm{m}}{\mathrm{s}}$ abgebremst. Wenn die Endgeschwindigkeit abnimmt, reduziert sich die Zahl der detektierten Moleküle. Während dieser Effekt erwartet wird, ist die im Experiment beobachtete Anzahl allerdings weitaus geringer als vorausgesehen. In den Experimenten beträgt diese Reduktion für eine Abbremsung von 360 auf 240 $\frac{\mathrm{m}}{\mathrm{s}}$ 1:25 (relativ zu den bei 360 $\frac{\mathrm{m}}{\mathrm{s}}$ geführten Molekülen), während parallele Simulationsrechnungen der Trajektorien eine Reduktion von 1:6 erwarten ließen.

Als wesentlicher Verlustmechanismus, der bei stärkerer Abbremsung deutlich wird, konnte der nichtadiabatische Übergang in Zustände identifiziert werden, die nicht eingefangen sind. Bei elektrischem Nullfeld ist das tieffeld-suchende Niveau des $a^3\Pi_1$, $v = 0$, $J = 1$ Zustands von ^{12}C^{16}O streng mit einem Niveau entartet, das nur schwach mit dem elektrischen Feld wechselwirkt. Durchlaufen die Moleküle in den Mikrofallen nun einen Bereich nahe der Nullfeld-Region, kann ein Übergang in diesen Zustand erfolgen, so dass das Molekül die Falle verläßt. Eine Möglichkeit, diesen Verlustkanal zu unterdrücken, bietet das ^{13}C^{16}O Isotopolog. Da der ^{13}C Kern einen Spin besitzt, weist ^{13}C^{16}O Hyperfeinstruktur auf, und im $a^3\Pi_1$, $v = 0$, $J = 1$ Zustand resultiert eine minimale Aufspaltung von 50 MHz zwischen dem tieffeld-suchenden und dem schwach beeinflussten Zustand, womit nichtadiabatische Übergänge weitgehend unterdrückt sind. Während bei einer Abbremsung von ^{12}C^{16}O von 312 $\frac{\mathrm{m}}{\mathrm{s}}$ auf unter 240 $\frac{\mathrm{m}}{\mathrm{s}}$ kein Signal nachweisbar war, war für ^{13}C^{16}O eine Abbremsung auf 96 $\frac{\mathrm{m}}{\mathrm{s}}$ problemlos beobachtbar, eine Reduktion der kinetischen Energie von über 90%.

Ensembles von metastabilem ^{13}C^{16}O wurden auch bis zum Stillstand über dem Chip abgebremst und für einen Zeitraum zwischen 0 und 2,5 ms gehalten. Die Zahl der nachgewiesenen Moleküle nahm zwar für längere Haltezeiten ab, aber die Verlustrate ist vereinbar mit der natürlichen Lebensdauer des metastabilen CO von 2,6 ms.

Weitere Experimente zeigen, daß nichtadiabatische Verluste in ^{12}CO ebenfalls unterdrückt werden, wenn zusätzlich ein magnetisches senkrecht zum elektrischen Feld angelegt wird.

Abstract

A lithographically-etched chip containing 1254 microscopic electrodes at a center-to-center spacing of 40 μm is used to produce an array of electric field strength minima 25 μm above the surface with a spacing between neighboring minima of 120 μm. These minima are produced by applying a series of six potentials to the electrodes. For polar molecules in low field seeking states, the electric field minima are potential energy minima and thus act as traps. By varying the potentials in a controlled manner, the field minima can be translated with respect to the electrodes at a constant distance from the surface.

Experiments were performed with CO in the metastable $a^3\Pi_1$, $v = 0$, $J = 1$ state, which has a strong, linear Stark shift with low field seeking components, a 6 eV internal energy that enables easy detection through an Auger process, and a radiative lifetime of 2.6 ms, which is long enough for the experiments here. CO molecules in a pulsed molecular beam are directly excited to the metastable state with a 5 ns laser pulse. The metastable CO molecules pass through a skimmer and arrive to the chip traveling parallel to the surface and perpendicular to the electrodes. While above the chip, the molecules are manipulated by the electric fields and subsequently ejected from the other side toward the detector.

Metastable ^{12}CO molecules have been guided over the chip at constant velocities ranging from 276 $\frac{\text{m}}{\text{s}}$ to 360 $\frac{\text{m}}{\text{s}}$ and decelerated from 360 $\frac{\text{m}}{\text{s}}$ to final velocities ranging from 336 $\frac{\text{m}}{\text{s}}$ to 240 $\frac{\text{m}}{\text{s}}$. As the final velocity decreases (i.e. the deceleration increases), the decelerated molecules arrive at the detector successively later, and the number of decelerated molecules reaching the detector also decreases. While this effect is expected, the fraction of molecules lost is much greater than expected: in the experiment, the number of molecules decelerated from 360 $\frac{\text{m}}{\text{s}}$ to 240 $\frac{\text{m}}{\text{s}}$ is $\frac{1}{25}$ of the number guided at 360 $\frac{\text{m}}{\text{s}}$, whereas trajectory simulations predict that this ratio should be $\frac{1}{6}$.

Most of this excess loss at higher decelerations results from non-adiabatic transitions to untrapped states. At zero electric field, the low field seeking level of the $a^3\Pi_1$, $v = 0$, $J = 1$ state of ^{12}C^{16}O is exactly degenerate with a level that is only weakly affected by the fields. As the molecules pass near the zero field region at the center of a microtrap, they can transition to this level, after which they are lost from the trap. One way to avoid this loss channel is to use ^{13}C^{16}O instead of ^{12}C^{16}O: because the ^{13}C nucleus has a non-zero spin, ^{13}C^{16}O has hyperfine structure, and in the $a^3\Pi_1$, $v = 0$, $J = 1$ state, this hyperfine structure results in a 50 MHz minimum splitting between the low field seeking levels and the levels unaffected by electric fields. While deceleration of ^{12}C^{16}O from 312 $\frac{\text{m}}{\text{s}}$ to velocities below 240 $\frac{\text{m}}{\text{s}}$ could not be observed, ^{13}C^{16}O is easily decelerated to 96 $\frac{\text{m}}{\text{s}}$, corresponding to a removal of over 90% of the molecules' kinetic energy.

Ensembles of metastable ^{13}C^{16}O molecules have been decelerated to zero velocity above the chip and held for variable durations ranging from 0 ms to 2.5 ms. It is observed that fewer molecules are detected after longer trapping times on the chip, but the rate of this loss is consistent with the 2.6 ms radiative lifetime of the metastable CO molecules.

Further experiments demonstrate that the Zeeman splitting due to an external magnetic field perpendicular to the electric field is a valid and more general way to prevent non-adiabatic losses in ^{12}CO.

Contents

Chapter 1

Cold molecules and microchips

Producing cold molecules and gaining complete control over both their internal state and translational motion has become a hot field of research with applications ranging from high resolution spectroscopy to studying low energy collisions. Among the many devices that have been constructed to produce cold molecules, one that has been particularly successful in producing sub-Kelvin samples of polar molecules is the Stark decelerator [1]. These decelerators operate on the principle that polar molecules in certain states have a higher potential energy in an electric field than in a field free region. If molecules in these so-called *low field seeking* states move from a region of low electric field strength to a region of higher electric field strength, they will lose kinetic energy. A molecular beam produced in a pulsed supersonic expansion provides the molecules to be decelerated: such a beam contains a packet of molecules that starts at the same position at the same time. Although the molecules are traveling fairly fast (several hundred meters per second), they are simultaneously cold, in the sense that all molecules are traveling at roughly the same velocity. The kinetic energy that the molecules lose when traveling from the low field to the high field region is not sufficient to stop molecules in even the slowest molecular beam. If the electric field configuration is switched, however, when the molecules reach the high field region such that they are in a low field region again, the molecules can once more climb from a low field region to a high field region, and more kinetic energy can be removed. If this process is repeated about a hundred times, the entire kinetic energy of the molecules can be removed, and the molecules can be loaded into an electrostatic trap that confines the molecules in three dimensions around an electric field strength minimum [2].

The Stark decelerators used thus far to trap cold molecules have been relatively large: the largest of these are over one meter long [3], and the smallest devices constructed that are capable of trapping molecules are still over 40 cm long [2]. The smaller of these two decelerators utilizes pairs of 3 mm diameter rods separated by 1.6 mm, and the molecular packets it decelerates have a volume of a few cubic millimeters [1]. These dimensions are partly a consequence of the techniques used to build and assemble the decelerator: since the electrodes are fashioned using lathes and assembled with human hands, there are practical lower limits to the size at which they can be built. For producing small samples of cold trapped molecules, though, such large device dimensions are not strictly necessary. A decelerator constructed to capture molecules in a cylindrical volume 20 μm in diameter and 4 mm long and in a 4 $\frac{\mathrm{m}}{\mathrm{s}}$-wide velocity distribution along each axis would

have a position-velocity phase space volume of 10^{-10} $\frac{\mathrm{m}^6}{\mathrm{s}^3}$. If this decelerator is loaded using a standard pulsed supersonic molecular beam, typically containing 10^{11} trappable molecules per cubic centimeter and having a full-width-half-maximum velocity spread of 50 $\frac{\mathrm{m}}{\mathrm{s}}$, corresponding to a peak phase space density of 10^{12} $\frac{\mathrm{s}^3}{\mathrm{m}^6}$), a hundred molecules could be simultaneously decelerated.

A 10 μm-scale Stark decelerator has certain advantages over the larger models. For one, the electric potentials necessary to produce the same electric field strength are much lower: instead of applying 10 kV to the electrodes, only 100 V is necessary. Also, because the electric field strength transitions from low field strength to high field strength over a very short distance, the electric field gradients and thus the forces on the molecules are much higher than in the traditional decelerators. With these stronger forces, such a miniature decelerator can bring molecules to a standstill in a few centimeters instead of a few meters. A number of other benefits offered by such a decelerator will be described later. While constructing a Stark decelerator this small is impractical using the construction techniques used to build larger models, modern lithographic techniques enable fabrication of planar structures at this length scale [4].

This thesis describes a miniature Stark decelerator based on an planar array of 1254 10 μm-wide and 4 mm long electrodes arranged with a center-to-center spacing of 40 μm. Every sixth electrode in the array is connected together, and by applying a specific set of potentials to the six sets of electrodes, an array of 418 two-dimensional local electric field minima (one for every third electrode) can be produced about 25 μm above the chip's surface. By changing the six potentials applied to the electrodes, the electric field minima can be shifted parallel to the surface of the chip while retaining the same shape. Since low field seeking molecules are attracted to regions of low electric fields, the minima serve as movable molecular traps. These traps are initially translated at a velocity that matches that of the molecules in the beam. After the molecules are captured in the moving traps, the traps are decelerated, and if this deceleration is gradual enough, the molecules will remain in the traps and will themselves be decelerated. If the traps are brought to a standstill, the molecules will be trapped above the chip.

The following sections will motivate this research and summarize the work that has been done so far. Section 1.1 will list some of the applications for cold molecules, both those that have been experimentally demonstrated and those that have so far only been proposed. The various methods for producing cold molecules that have been shown in experiments will be described in section 1.2. Finally, in section 1.3, the subject of miniaturization will be addressed, particularly why making devices smaller has advantages beyond just making them more compact.

1.1 Applications of Cold Molecules

Once the external motions of the molecules are completely under control, many experiments can be performed with these molecules that were impractical or impossible before. Particularly, experiments that benefit from long interaction times are improved when the molecules being examined are either slow enough that they require much more time to pass through the interaction region or are trapped and thus prevented from leaving. One such class of experiments are those involving high resolution spectroscopy: since time

and energy are related by an uncertainty relation given by

$$\Delta E \, \Delta t \geq \frac{\hbar}{2} \tag{1.1}$$

measuring an energy with a very high resolution requires allowing a system to evolve unperturbed for a long period of time.

High resolution spectroscopy using trapped fundamental particles and atoms has already enabled the measurement of fundamental constants with unprecedented precision. Trapped electrons, for example, have been used to measure the electron spin g-factor to better than one part in 10^{12} [5], and ultracold cesium atoms that are trapped and subsequently ejected upward have become the basis for official time standards [6]. With cold molecules, several new measurements will become possible. It is expected that the parity-violating weak nuclear force will induce a small difference in the energy level spacings between the two enantiomers of a chiral molecule, and experiments are already underway to measure such differences [7]. Cold molecules also have the potential to determine whether electrons have a non-zero electric dipole moment (EDM), which would be a violation of time reversal symmetry and an indicator for physics beyond the Standard Model [8]. The most sensitive tests so far, carried out using a beam of thallium atoms, constrain the magnitude of this dipole moment to be less than $1.6 \cdot 10^{-27}$ e·cm [9], and it is expected that heavy diatomic molecules, such as YbF, are a thousand times more sensitive to an electron EDM, since they can be much more strongly polarized in an electric field [8]. Cold molecules also hold promise for measuring possible time variation of fundamental constants such as the fine structure constant α and the proton to electron mass ratio $\frac{m_p}{m_e}$. Since energy splittings due to nuclear degrees of freedom (such as vibration and rotation) have different dependencies on α and $\frac{m_p}{m_e}$ than energy splittings due to electronic degrees of freedom (such as fine and hyperfine splittings), splittings between nearly-degenerate states with very different quantum numbers (e.g. nearly-degenerate states that have different rotational quantum numbers in different spin-orbit manifolds) are very sensitive to small changes in these constants [10, 11]. By measuring these splittings with high precision over a period of several years, upper limits can be placed on the time variation of α and $\frac{m_p}{m_e}$. The experiments using molecules in the works cited above were carried out using fast molecular beams, and in each of these experiments, the sensitivity could potentially be improved if the molecules were slowed or even trapped (although it is not clear whether high resolution spectroscopy in traps is feasible [12]). In a proof-of-principle experiment, high resolution spectroscopy was carried out on Stark-decelerated ND_3 molecules, and it was shown that the resolution could be significantly enhanced over that obtained using a fast molecular beam [13].

Confining molecules in a trap also enables the measurement of the lifetimes of long-lived excited states. Once Paul traps for ions became available, for example, lifetimes of long-lived ionic states on the order of tens of seconds could be measured [14]. While excited states of molecules with short lifetimes can be measured in a fast beam, longer lived states are somewhat more difficult to measure, since the fraction of the molecules that decay during the interaction time is small and also because the measurements must be carried out at two different positions in the molecular beam, posing normalization issues. By trapping the molecules, the interaction times can be much longer, and the measurements are always done at the same position. Several such experiments have

already been carried out using trapped molecules. Using Stark decelerated molecules confined in an electrostatic quadrupole trap, the lifetime of the $X^2\Pi_{3/2}$, $v = 1$, $J = 3/2$ state of OH was measured to be 58.0 ± 1.0 ms [15], the lifetime of the $a^3\Pi_1$, $v = 0$, $J = 1$ state of CO was found to be 2.63 ± 0.03 ms [16], and the lifetime of the $a^1\Delta$, $v = 0$, $J = 2$ state of NH was constrained to be longer than 2.7 s [17]. More recently, the lifetime of the $X^3\Sigma^+$, $v = 1$, $N = 0$ state of NH was measured to be 37 ms using a magnetic trap loaded by buffer gas cooling [18]. It should be noted that the lifetime of the $a^3\Pi_1$, $v = 0$, $J = 1$ state of CO was previously measured in a fast molecular beam, using detectors 1.0 m and 1.8 m away from the source, to have a lifetime of 3.8 ± 0.5 ms [19]. While this measurement is almost consistent with the newer result, the large uncertainty demonstrates the difficulty of measuring a lifetime of even a few milliseconds in a beam.

Some proposals suggest that single trapped polar molecules could be used as qubits in a quantum computer. A single molecule could be trapped at each antinode of an optical standing wave and an inhomogeneous electric field could be applied such that each molecule sees a slightly different electric field strength and can thereby be individually addressed [20]. In addition to the externally-applied electric field, a molecule would also see the electric field produced by the electric dipole moment of neighboring molecules, so the parallel/antiparallel energy splitting for each molecule would be shifted slightly, depending on the state of its neighbors. This arrangement can be used as a conditional-NOT (CNOT) gate, since radio frequency radiation applied at the shifted frequency would only change the orientation of the molecule if its neighbors are in one particular orientation. This scheme would work well on polar molecules due to the large dipole-dipole interaction: the energy levels of two molecules with an effective electric dipole moment of one Debye separated by 532 nm (the spacing between antinodes in a standing wave produced by a 1064 nm laser) will be shifted by 1 kHz as a result of the neighboring molecule. In contrast, the energy levels of two atoms with a magnetic dipole moment of one Bohr magneton separated by the same distance will be shifted less than 0.1 Hz. Single polar molecules could also be trapped in microscopic electrostatic traps coupled to superconducting microwave stripline resonators [21]. Pairs of trapped molecules would be selectively coupled to each other by changing the electric field strength in the two traps containing these molecules and by applying a resonant microwave pulse [21].

Slowing molecules also enables the study of collisions in an energy regime where only a few partial waves contribute. In other words, since angular momenta must be quantized in units of $\hbar$, the angular momentum of the two collision partners in the center-of-mass frame at low collision energies is small enough that only a few discrete values are possible. Reducing the number of partial waves, limiting the initial molecular state to a single quantum state, and state-selectively detecting the molecules after the collision enables detailed studies of collision mechanisms. Collisions between ground state CO and helium at energies below 4 cm^{-1}, for example, are expected to show sharp resonances in the elastic cross section due to contributions of individual partial waves [22]. At very low energies, only the zero angular momentum partial wave contributes, and the collision cross section for neutral particles becomes inversely proportional to relative velocity [23]. First experiments have been carried out in which low energy collisions between OH and xenon [24], helium, deuterium molecules [25], or argon [26] have been studied.

1.2 Methods for Producing Cold Molecules

Several methods have been developed starting in the mid 1990s for producing samples of translationally cold molecules. The first method developed to successfully trap neutral molecules was buffer gas cooling [27]. This method operates on the principle of thermalizing molecules with a cold environment. Although directly cooling gas-phase molecules to temperatures near 1 K is somewhat difficult since the molecules will stick to most solid surfaces at this temperature, the molecules can transfer their heat to the walls through a helium buffer gas. Since helium has a significant vapor pressure, even below 1 K, sufficient quantities of the gas can be available to facilitate this heat exchange. The molecules can be cooled in the presence of a magnetic quadrupole field so that the molecules in diamagnetic states will be trapped near the magnetic field minimum as the collisions cool them.

Another class of techniques for producing cold molecules makes use of supersonic molecular beams: although the molecules in such beams have a high velocity in the laboratory frame, their velocity distribution is relatively narrow. Using non-dissipative forces, a significant fraction of the molecules can be decelerated to a low velocity in the laboratory frame. The earliest experiments in this class used the force experience by neutral polar molecules in an inhomogeneous electric field as a result of the Stark effect. Stark deceleration was first demonstrated for decelerating metastable CO [1] and decelerating and trapping ND_3 [2] but has since been used to decelerate or trap many other molecules [28]. Following the example set by Stark decelerators, other devices were constructed to make use of other forces to decelerate molecules: optical Stark decelerators have been used to slow molecules using the force in an optical standing wave due to the AC Stark effect [29], Zeeman decelerators have slowed diamagnetic atoms and molecules in an inhomogeneous magnetic field with forces due to the Zeeman effect [30, 31], and anion decelerators have shown, in a proof of principle experiment using I^-, that molecular anions could be slowed in an electrostatic potential and that the extra electron could subsequently be photodetached, resulting in slow neutral molecules [32]. Direct deceleration is not the only way that the narrow velocity distribution of a supersonic molecular beam can be used to produce cold molecules, though. One type of device uses rotating arms to simply move the nozzle backwards at a velocity comparable to that of the molecular beam, eliminating the need for a deceleration force [33, 34]. Slow molecules could also be produced by scattering the molecules in supersonic beam from a paddle that recedes from the beam source: already, a helium beam was slowed by 250 $\frac{\mathrm{m}}{\mathrm{s}}$ using this approach [35].

The narrow velocity distribution in a molecular beam can also be used in conjunction with collisions, chemical reactions, or photodissociation to produce cold molecules. This is done by arranging the system such that one of the collision partners, reaction products, or dissociation fragments carries most of the momentum of the system away, leaving the other particle nearly at rest. Slowing of molecules with collisions has been shown with a pair of crossed molecular beams [36]. Since the kinetic energy must be conserved in an elastic collision, the particle carrying away the momentum of the system must also carry away the initial kinetic energy of both particles, but this condition can often be satisfied by choosing the proper angle between the two beams. Production of slow NO molecules has also been demonstrated by photodissociating NO_2 with a laser slightly above the

dissociation threshold [37, 38]. If the oxygen fragment dissociates in the direction of the molecular beam, the NO fragment will recoil in the opposite direction, and its final velocity in the laboratory frame can be much lower than the velocity of the parent NO_2, or it can even be at rest. The direction of the dissociation can be preferentially aligned along the molecular beam axis by choosing the polarization of the dissociation laser. Slow KBr molecules have been produced in the reaction of HBr and potassium atoms from two counterpropagating beams [39]. After the reaction, the hydrogen atom can carry away the initial momentum and absorbs both the initial kinetic energy and the reaction energy into its final kinetic energy. All of these techniques in principle rely on the narrow velocity distribution of molecular beam, since they only produce slow molecules if the collision partners or parent molecules have the correct velocities before the collision, reaction, or dissociation.

It is also possible to produce cold molecules by simply extracting the low energy molecules already present in any thermal distribution. Even in a monoatomic gas with a temperature of 300 K, one in 10^4 particles has an energy less than $k_B \cdot 1$ K, and if the temperature of the gas is reduced to 77 K, this fraction increases to one in 10^3. The main challenge for producing cold molecules in this manner is separating the cold fraction from the rest before they undergo collisions, since after the molecules have collided, a different subset of molecules is cold. One solution is to inject the molecules into vacuum in an effusive molecular beam (i.e. a beam with a low enough density such that the molecules do not experience collisions) and into a curved electrostatic [40] or magnetostatic [41] guide. The guide serves two purposes: first, it selects the cold fraction of molecules by guiding the slow fraction around the bend while allowing the faster molecules to escape over the barrier, and second, it spatially separates the cold fraction from the hot fraction before the molecules in the two groups can collide. This method can produce a continuous stream of slow molecules, but the molecules are only translationally slow: since many different rotational and vibrational states can be guided if they are slow enough, the temperature of the internal rotational and vibrational degrees of freedom is often much higher than the translational temperature [42].

One final approach to producing cold molecules is to first cool the constituent atoms using standard atom cooling techniques and associate the cold atoms in a controlled manner. So far, the most successful technique for converting a pair of free atoms into a strongly bound diatomic molecule requires two steps. First, the atoms are associated using a magnetic Feshbach resonance to form a molecule in a highly-excited vibrational state. After being associated, the molecule is transferred into a more deeply bound state using stimulated Raman adiabatic passage (STIRAP). This technique has been used to produce KRb molecules in the rovibronic ground state [43], deeply-bound Cs_2 molecules [44], and Rb_2 molecules in the triplet rovibrational ground state [45]. It is also possible to radiatively transfer a pair of atoms from an unbound state to a deeply-bound molecular state. In one instance, LiCs molecules were produced by exciting them from an unbound state to an electronically-excited bound state, after which the molecule decayed with 23% probability to the vibronic ground state [46]. Unfortunately, only diatomic molecules consisting of atoms that can be laser cooled can be produced in this way.

1.3 Miniaturization

While cold molecules have only been an experimental reality for a little over a decade, cold atoms have now been available for nearly 25 years already [47]. Many of the achievements of the cold atom community, such as measuring atomic transitions with high precision [48], studying low energy collisions [49], and Bose-Einstein condensation [50], have more recently been pursued in cold molecule research. One field that developed out of cold atom research is the production of ultracold atoms in miniaturized magnetic traps. Creating such traps is not merely an effort to make ultracold atom production more compact: in fact, their development was initially motivated by the desire to create strong confinement, which brings quantum degeneracy to higher temperatures [51]. The short distances possible due to the microscopic trap size also permits coupling through short range forces, which can be used to detect atoms in strongly coupled optical cavities [52, 53] and which makes the atoms sensitive to small variations in the current carrying wires that provide the trapping potential [51]. Since neighboring microtraps can be very closely spaced, quantum interference between atoms stored in these traps can be more readily observed [54]. Perhaps most importantly, the microtraps can be built on a planar substrate using lithographic techniques, making it possible to integrate many different devices onto the same chip.

Extending this research to polar molecules, trapping them above the chip using electric instead of magnetic fields, offers new advantages. Due to the additional vibrational and rotational degrees of freedom present in molecules, it is possible to couple them to photons over a wide range of frequencies. In particular, many molecular transitions, such as those between Λ-doublet or rotational levels, can be driven by microwave radiation. Polar molecules also couple to each other with a long range dipole-dipole interaction. A pair of molecules separated by a distance on the order of 1 μm can have a measurable energetic splitting between an aligned and an antialigned state that can be driven by radio frequency radiation, and such a transition can form the basis for a gate in a quantum computer, as discussed earlier [20, 21]. Molecules confined in microscopic traps would, like atoms, reach quantum degeneracy at much higher temperatures than in macroscopic traps, but as a result of the dipole-dipole interaction, the stability of a molecular Bose-Einstein condensate should depend on the geometry of the trap [55]. The effect of a magnetic dipole-dipole interaction has recently been observed in a BEC of ^{52}Cr atoms [56].

The manipulation of polar molecules above a chip with electric fields holds great promise but also faces major challenges. Likely the biggest challenge is the production of cold, dense samples of gas-phase molecules: laser cooling, which has been an essential process for loading atom chips, remains unrealized for molecules, despite several proposals of possible implementations [57, 58, 59], although first promising results have been obtained [60]. Detecting molecules is also much more difficult than detecting atoms: while atoms trapped above a chip can be efficiently detected either through absorption or laser induced fluorescence, since a single atom can scatter as many as 10^7 photons per second [61], molecules generally can only scatter one photon before decaying to another vibrational or rotational state, and as a result, such detection methods are much less sensitive for molecules.

The molecule chip presented in this thesis offers a solution to both of these difficulties.

Molecules are loaded onto the chip from a pulsed supersonic molecular beam that, while fast in the lab frame, is cold in a frame that moves with the packet of molecules. Since the microtraps can be continuously translated over the chip, they can initially move at the same velocity as the incoming packet of molecules and gradually bring the molecules to a standstill. At the end of the experiment, the trapped molecules are reaccelerated and ejected from the chip. Doing so enables sensitive detection techniques developed for molecules in a free beam, such as resonance-enhanced multiphoton ionization (REMPI) or detection using Auger processes for molecules in energetic metastable states, to be exploited. The ability to trap molecules on a chip and subsequently detect them is an important first step toward the production of a molecular laboratory on a chip.

Chapter 2

Manipulation of Polar Molecules Using Electric Fields

In 1913, Johannes Stark observed that emission lines of hydrogen and helium atoms split into multiple components with slightly different wavelengths when the atoms are in an electric field [62]. This observation that the energy levels in a quantum system shift when an external electric field is applied is thus referred to as the Stark effect. Based on Stark's observations, one can devise a thought experiment: first, a particle that experiences a Stark shift in an electric field is excited in a field free region, and then flies into a region with a strong electric field. We assume that it decays to the original state while in this region, emitting a photon that, due to the Stark shift, is shifted in energy relative to the photon that it absorbed. For the purpose of this thought experiment, it is assumed that the emitted photon is more energetic than the photon initially absorbed. The particle then continues flying and returns to a field free region. Since the photon emitted was more energetic than the photon absorbed, and the particle both starts and ends the experiment in a field free region, it might naively seem that energy was created in this process, but in fact, this "extra" energy must have been extracted from the particle's kinetic energy. Either in the process of traveling from the low field region to the high field region in the excited state or in traveling from the high field region to the low field region in the ground state (or possibly in both processes), the molecule was decelerated. It becomes clear from this that the Stark effect can be used to create a mechanical potential.

When Stark first observed the splitting of spectral lines in an electric field, he was ill-equipped to explain the effect quantitatively. For one thing, the Schrödinger equation would not be written for another 13 years [63], and even the Bohr model of the hydrogen atom had only just been published a few months earlier [64]. Based on the information available at the time, it could not be determined how much each of the two levels connected by an emission line was shifted by the electric field, as only the difference of the shifts was observed. Later, using the solution of the hydrogenic wavefunction that came with the development of quantum mechanics, the observations of the Stark shift in hydrogen could be readily explained.

For polar molecules, i.e. molecules that have an electric dipole moment along a fixed axis relative to the nuclei of the molecule, the Stark shift can be understood largely in terms of an electric dipole of a well defined magnitude in an electric field. Classically, the

potential energy given by a dipole in a field is

$$U = -\vec{\mu} \cdot \vec{E} = -|\vec{\mu}||\vec{E}| \cos\theta \tag{2.1}$$

where $\vec{\mu}$ is the electric dipole vector and $\vec{E}$ is the electric field vector. Classically, U can vary from $-|\vec{\mu}||\vec{E}|$ to $|\vec{\mu}||\vec{E}|$, but quantum mechanically, $\cos\theta$ can only take discrete values. Since $|\vec{\mu}|$ is constant, it follows that the potential energy is proportional to $|\vec{E}|$.

This is only a rough approximation: in reality, many details of the rotational, fine, and hyperfine structure of the molecule come into play. Such details, particularly those applicable to the $a^3\Pi$ state of CO used in the experiments, will be discussed at length in chapter 4, and in later sections of this chapter, a somewhat better model will be described. It is generally assumed, however, that U is only a function of $|\vec{E}|$ and is not affected by the direction of the vector. If this is the case, it is possible to create electric field distributions that confine the molecules to a small region in free space. A framework for describing these field distributions is outlined in section 2.1. This ability to confine the molecules in free space forms the basis of the deceleration and trapping presented in subsequent chapters. Using the Stark shift as a mechanical potential requires that, as $\vec{E}$ changes in time (either as a result of the motion of the molecule or as a result of a time dependence of the applied potential), the molecules do not transition to another quantum state where $\cos\theta$ takes a different value. The conditions under which this assumption is valid will be examined in section 2.2.

2.1 Fields for Manipulating Molecules

In most cases, the states of molecules that have a Stark shift in an electric field can be divided into two classes: those that increase in energy as a function of electric field strength and those that decrease in energy. While there are states where the slope of the Stark shift changes sign, these are generally not considered except if the electric fields are limited to a region where the energy is monotonic. These two classes of states are described as low field seeking and high field seeking, respectively: since the force on a molecule always points toward regions of lower energy, molecules in states with increasing energy in a field will be attracted to regions of lower field and molecules in states with decreasing energy in a field will be attracted to regions of higher field. To confine the molecules to a specific region, it is necessary to create a local electric field strength minimum for low field seeking levels or a local maximum for high field seeking levels. A static electric field strength maximum, however, is not compatible with Maxwell's equations, so it is not possible to build a static trap for molecules in high field seeking states [65]. This is rather unfortunate: because the absolute ground state is always high field seeking, transitions from this state are energetically impossible if the surroundings have a low enough temperature. While a minimum of the electric field strength is possible, allowing the trapping of molecules in a low field seeking state, molecules in this state can always undergo transitions to a high field seeking state and become lost from the trap.

The electric fields that can be created to manipulate molecules cannot be arbitrarily chosen; their form must obey Maxwell's equations. In particular, they must obey

Faraday's Law and Gauss's Law:

$$\vec{\nabla} \times \vec{E} = -\frac{\partial \vec{B}}{\partial t} \tag{2.2}$$

$$\vec{\nabla} \cdot \vec{E} = \frac{\rho}{\epsilon_0} \tag{2.3}$$

For the case of a quasi-static field (i.e. the timescale of changes is much longer than the typical length scale divided by the speed of light) in a region free of electric charges, both of these equations must be zero. The first equation being zero implies that the electric field $\vec{E}$ can be written as a gradient of a potential, i.e.

$$\vec{E} = -\vec{\nabla} V \tag{2.4}$$

Combining equations (2.3) and (2.4) results in Laplace's equation

$$\vec{\nabla}^2 V = \frac{\partial^2 V}{\partial x^2} + \frac{\partial^2 V}{\partial y^2} + \frac{\partial^2 V}{\partial z^2} = 0 \tag{2.5}$$

Any electric potential distribution $V(x, y, z)$ satisfying equation (2.5) can be produced in free space using a static distribution of charge.

2.1.1 Two Dimensional Multipole Fields

This work deals with electric field distributions and potentials that are two dimensional. While the physical system used in the experiments is, of course, three dimensional, the electrodes used to produce the electric fields change little along one direction, so the electric potential is mostly independent of this coordinate. Laplace's equation (equation (2.5)) can be written in two-dimensional polar coordinates as

$$\vec{\nabla}^2 V = \frac{1}{r}\frac{\partial}{\partial r}\Big(r\frac{\partial V}{\partial r}\Big) + \frac{1}{r^2}\frac{\partial^2 V}{\partial \phi^2} = 0. \tag{2.6}$$

This partial differential equation can be solved using a separation of variables ansatz: by choosing R and Φ such that

$$V(r, \phi) = R(r)\Phi(\phi) \tag{2.7}$$

the left side of the equation can be rewritten as the sum of a term depending only on r and a term depending only on ϕ.

$$\frac{r}{R}\frac{d}{dr}\Big(r\frac{dR}{dr}\Big) + \frac{1}{\Phi}\frac{d^2\Phi}{d\phi^2} = 0 \tag{2.8}$$

As a result, both terms must be independent of both r and ϕ. The first term is assigned the value n^2 and the second term $-n^2$, resulting in the solutions

$$R(r) = \begin{cases} A_n r^n + B_n r^{-n} & n \neq 0 \\ A_0 + B_0 \ln r & n = 0 \end{cases} \tag{2.9}$$

$$\Phi(\phi) = C_n \cos(n\phi + \delta_n) \tag{2.10}$$

Solutions where $B_n \neq 0$ diverge at $r = 0$ and represent the potential produced by a charge distribution near the origin at points farther away from the origin. It is more relevant to consider only A_n terms, which represent potentials produced by charges far away at a charge-free region near the origin. Because equation (2.6) is linear, linear combinations of solutions to the differential equation are also solutions. A complete solution for V can then be written as

$$V = A_0 + \sum_{n=1}^{\infty} A_n n^{-1} \Big(\frac{r}{r_0}\Big)^n \cos(n\phi + \delta_n) \tag{2.11}$$

Here, each A_n has been redefined so as to absorb the C_n coefficient and incorporate the typical length scale parameter r_0. A factor of n has also been included in A_n to simplify subsequent equations, hence the factor of n^{-1} in equation (2.11). Because each term can be negated by adding π to δ_n, A_n is assumed, without loss of generality, to always be positive.

The terms of equation (2.11) are named based on the minimum number of distinct charges needed to produce them as a leading order term. For example, because the term where $n = 1$ oscillates once as a function of ϕ, creating it as a leading order term requires at least two charges: a positive charge where $\phi + \delta_1 = 0$ and a negative charge where $\phi + \delta_1 = \pi$. As a result, the $n = 1$ term is referred to as the "dipole" term. Producing the $n = 2$ term requires two positive and two negative charges, and thus is called the "quadrupole" term, and $n = 3$ and $n = 4$ are referred to as "hexapole" and "octopole" terms, respectively. In a charge-free region around the origin, the potential can always be expanded in terms of these multipole components.

The electric field resulting from this potential in equation (2.11) is given by

$$\vec{E} = -\vec{\nabla} V = \sum_{n=1}^{\infty} \frac{A_n}{r_0} \Big(\frac{r}{r_0}\Big)^{n-1} (-\cos(n\phi + \delta_n)\hat{r} + \sin(n\phi + \delta_n)\hat{\phi}) \tag{2.12}$$

If only a single A_n is non-zero, the strength of the electric field is given by

$$|\vec{E}| = \sqrt{\vec{E} \cdot \vec{E}} = \frac{A_n}{r_0} \Big(\frac{r}{r_0}\Big)^{n-1} \tag{2.13}$$

For molecules in low field seeking states, this creates a restoring force toward $r = 0$, since the potential energy is a monotonically-increasing function of electric field strength. If $n = 2$, the two level system molecule sees a mechanical potential proportional to r^2 near $r = 0$ and proportional to r farther away. For small displacements from the origin, this potential is harmonic, which implies, for the molecules moving in this potential, a well-defined oscillation frequency independent of amplitude and separability of motions in two orthogonal Cartesian directions (e.g. in the x and y coordinates). Farther away from $r = 0$ where the mechanical potential is linear, the frequency is no longer independent of oscillation amplitude, and the x and y motions become coupled. To achieve a harmonic potential farther away from the origin, a potential with $n = 3$ is needed, but this results in a potential that is proportional to r^4 at small r.

Two dimensional multipole potentials have been frequently applied to transverse focusing of beams of molecules, but this only works optimally when the mechanical potential produced is harmonic, since only then is the time required for half an oscillation independent of the amplitude of the oscillation. If the splitting Λ is very large, the mechanical

potential remains quadratic in r even for large fields, so it is possible for such molecular states to create an accurate harmonic potential using a quadrupole ($n = 2$) electric potential. Such a quadrupole potential was used to focus a low field seeking state of ammonia for which Λ is 23.87 GHz (a rather large value) into a microwave cavity, producing the population inversion needed to power a maser [66]. For states in which Λ is very small, the anharmonicity of the mechanical potential produced by a hexapole ($n = 3$) electric potential near $r = 0$ can be neglected, so for low field seeking states with a highly linear Stark shift, a hexapole is an efficient focuser [67].

In certain cases, a combination of multiple multipole components creates a useful field configuration not possible with a single component. One case of particular interest is the combination of a dipole ($n = 1$) and a hexapole ($n = 3$) field. If only these two terms are non-zero, the electric field strength is given by

$$\begin{aligned} |\vec{E}| &= \frac{A_1}{r_0}\sqrt{1 + 2\frac{A_3}{A_1}\left(\frac{r}{r_0}\right)^2 \cos(2\phi + \delta_3 - \delta_1) + \left(\frac{A_3}{A_1}\left(\frac{r}{r_0}\right)^2\right)^2} \\ &\approx \frac{A_1}{r_0} + \frac{A_3}{r_0}\left(\frac{r}{r_0}\right)^2 \cos(2\phi + \delta_3 - \delta_1) \;\text{ if }\; r \ll r_0\sqrt{\frac{A_1}{A_3}} \end{aligned} \tag{2.14}$$

At $r = 0$, the field strength is $\frac{A_1}{r_0}$, in the directions where $\phi = \frac{1}{2}(\delta_1 - \delta_3)$ or $\phi = \frac{1}{2}(\delta_1 - \delta_3) + \pi$, the field strength *increases* quadratically in r, and in the directions where $\phi = \frac{1}{2}(\delta_1 - \delta_3) + \frac{\pi}{2}$ or $\phi = \frac{1}{2}(\delta_1 - \delta_3) + \frac{3\pi}{2}$, the field *decreases* quadratically in r. If the field strength $\frac{A_1}{r_0}$ is large enough that the Stark shift is linear, then this electric field distribution results in a saddle-shaped mechanical potential, focusing molecules in one direction and defocusing them in the perpendicular direction. This is true regardless whether the molecule is in a low field seeking state or a high field seeking state. While the molecules would eventually be lost along the direction where they are defocused, if the field is switched such that the defocusing direction becomes the focusing direction (and vice versa), the molecules that are in the process of being defocused will be refocused. The potential in a given direction is quadratic, so the focusing or defocusing force increases proportionally to r. Because of this, the molecules that were defocused in the first part of the switching cycle and have moved to a position with larger r are focused more strongly in the second part of the switching cycle. Similarly, the molecules that were focused in the first part of the switching cycle have moved to a position with smaller r and are defocused less strongly in the second part of the switching cycle. For the correct switching frequency, the result is a net restoring force toward $r = 0$ for all molecules in the trap. This principle has been used in the Paul trap for ions [68] and for molecules with a linear Stark shift in an inhomogeneous electric field [69].

2.2 The Adiabatic Theorem

The adiabatic theorem states that, if the states of a system are enumerated in order of increasing (or decreasing) energy, as long as the Hamiltonian changes sufficiently slowly, a system initially in the nth eigenstate will remain in the nth instantaneous eigenstate.

The task of understanding how a quantum mechanical system evolves under a chang-

ing Hamiltonian begins with the time-dependent Schrödinger equation

$$i\hbar\Big|\frac{\partial\psi}{\partial t}\Big\rangle = \hat{H}(t)|\psi\rangle. \tag{2.15}$$

Assume $|\psi\rangle$ has the form

$$|\psi\rangle(t) = \sum_n c_n(t)|\phi_n\rangle(t)e^{\frac{1}{i\hbar}\int_0^t E_n(t')\,dt'}, \tag{2.16}$$

where c_n is a complex coefficient and E_n and $|\phi_n\rangle$ are the nth instantaneous eigenvalue and eigenvector of $\hat{H}(t)$, respectively, i.e.

$$\hat{H}(t)|\phi_n\rangle(t) = E_n(t)|\phi_n\rangle(t). \tag{2.17}$$

Since the eigenvectors $|\phi_n\rangle$ form a complete basis set, any $|\psi\rangle$ can be written in this form. Substituting $|\psi\rangle$ from equation (2.16) into (2.15) results in the equation

$$\sum_n\Big(\frac{dc_n}{dt}|\phi_n\rangle + c_n\Big|\frac{\partial\phi_n}{\partial t}\Big\rangle\Big)e^{\frac{1}{i\hbar}\int_0^t E_n(t')\,dt'} = 0 \tag{2.18}$$

By multiplying on the left by $e^{-\frac{1}{i\hbar}\int_0^t E_m(t')\,dt'}\langle\phi_m|$, the first-order differential equation for c_n can be reduced to

$$\frac{dc_m}{dt} + \sum_n c_n\Big\langle\phi_m\Big|\frac{\partial\phi_n}{\partial t}\Big\rangle e^{i\theta_{mn}(t)} = 0 \tag{2.19}$$

where

$$\theta_{mn}(t) = \frac{1}{\hbar}\int_0^t \big[E_m(t') - E_n(t')\big]\,dt' \tag{2.20}$$

The factor $\Big\langle\phi_m\Big|\frac{\partial\phi_n}{\partial t}\Big\rangle$ can be calculated by taking a time derivative of equation (2.17) and multiply on the left by $\langle\phi_m|$.

$$\Big\langle\phi_m\Big|\frac{\partial\hat{H}}{\partial t}\Big|\phi_n\Big\rangle + E_m\Big\langle\phi_m\Big|\frac{\partial\phi_n}{\partial t}\Big\rangle = \frac{dE_n}{dt}\delta_{nm} + E_n\Big\langle\phi_m\Big|\frac{\partial\phi_n}{\partial t}\Big\rangle \tag{2.21}$$

If the eigensystem is non-degenerate (i.e. $E_n = E_m \rightarrow n = m$), $\Big\langle\phi_m\Big|\frac{\partial\phi_n}{\partial t}\Big\rangle$ can be computed as

$$\Big\langle\phi_m\Big|\frac{\partial\phi_n}{\partial t}\Big\rangle = \frac{\big\langle\phi_m\big|\frac{\partial\hat{H}}{\partial t}\big|\phi_n\big\rangle - \frac{dE_n}{dt}\delta_{nm}}{E_n - E_m} \tag{2.22}$$

and equation (2.19) can be reformulated in terms of $\frac{\partial\hat{H}}{\partial t}$

$$\frac{dc_m}{dt} + c_m\Big\langle\phi_m\Big|\frac{\partial\phi_m}{\partial t}\Big\rangle + \sum_{n\neq m} c_n\frac{\big\langle\phi_m\big|\frac{\partial\hat{H}}{\partial t}\big|\phi_n\big\rangle}{E_n - E_m}e^{i\theta_{mn}(t)} = 0 \tag{2.23}$$

It can be quickly shown that $\Big\langle\phi_m\Big|\frac{\partial\phi_m}{\partial t}\Big\rangle$ must be pure imaginary

$$\begin{aligned}\frac{\partial}{\partial t}\langle\phi_m|\phi_m\rangle &= \Big\langle\phi_m\Big|\frac{\partial\phi_m}{\partial t}\Big\rangle + \Big\langle\frac{\partial\phi_m}{\partial t}\Big|\phi_m\Big\rangle \\ &= \Big\langle\phi_m\Big|\frac{\partial\phi_m}{\partial t}\Big\rangle + \Big\langle\phi_m\Big|\frac{\partial\phi_m}{\partial t}\Big\rangle^* \\ &= 2\Re\Big\langle\phi_m\Big|\frac{\partial\phi_m}{\partial t}\Big\rangle = 0\end{aligned} \tag{2.24}$$

As a result, the second term of equation (2.23) only represents a time-dependent change of the complex phase of c_m. By instead attributing any possible phase shift to the individual $|\phi_m\rangle$ (such a shift would not affect the orthonormality of the basis set, nor does it change equation (2.17)), this term can be ignored.

If the Hamiltonian evolves from an initial to a final form over a time T, the final wavefunction can be found by rewriting equation (2.23) as an integral equation

$$c_m(T) = c_m(0) - \sum_{n \neq m} \int_0^T c_n \frac{\left\langle \phi_m \middle| \frac{\partial \hat{H}}{\partial t} \middle| \phi_n \right\rangle}{E_n - E_m} e^{\frac{i}{\hbar} \int_0^t \left[E_m(t') - E_n(t') \right] dt'} \, dt \tag{2.25}$$

By substituting $t = sT$, this becomes

$$c_m(T) = c_m(0) - \sum_{n \neq m} \int_0^1 c_n \frac{\left\langle \phi_m \middle| \frac{\partial \hat{H}}{\partial s} \middle| \phi_n \right\rangle}{E_n - E_m} e^{\frac{iT}{\hbar} \int_0^s \left[E_m(s') - E_n(s') \right] ds'} \, ds \tag{2.26}$$

If T is changed such that the passage from the initial to final Hamiltonian, while following the same path, takes a different amount of time, only the phase factor in equation (2.26) will change. For small T, the phase will change slowly as a function of s, and significant amplitude can be accumulated during the integration. If T is large, however, the phase will change very rapidly, and the integral will accumulate little amplitude. A more mathematically-rigorous treatment of the integral in equation (2.26) is given by Born and Fock [70]. If there is no degeneracy between the E_n at any point in the path, and the real and imaginary parts of $(E_m - E_n)^{-2} \left\langle \phi_m \middle| \frac{\partial \hat{H}}{\partial s} \middle| \phi_n \right\rangle$ have a bounded number N of piecewise monotone segments, then as long as T satisfies the condition

$$T \gg N\hbar \frac{\left| \left\langle \phi_m \middle| \frac{\partial \hat{H}}{\partial s} \middle| \phi_n \right\rangle \right|}{(E_m - E_n)^2} = N\hbar \frac{\left| \left\langle \phi_m \middle| \frac{\partial \phi_n}{\partial s} \right\rangle \right|}{|E_m - E_n|} \tag{2.27}$$

non-adiabatic transitions between the mth and nth states will be minimal.

The second form of the adiabatic criterion given in equation (2.27) indicates a simpler approximation of this rule. If the system would progress from its initial to its final state in such a way that $\frac{\partial \phi_n}{\partial s}$ is constant, $\left| \left\langle \phi_m \middle| \frac{\partial \phi_n}{\partial s} \right\rangle \right|$ will always be less than or equal to one, and so if $\frac{\partial \phi_n}{\partial s}$ is never significantly larger than its average value, $\left| \left\langle \phi_m \middle| \frac{\partial \phi_n}{\partial s} \right\rangle \right|$ will be at most of order one. As a result, non-adiabatic transitions between the mth and nth state are small as long as the timescale of changes is long compared to the inverse of the splitting between those levels, i.e.

$$T \gg \frac{h}{|E_m - E_n|} \tag{2.28}$$

To examine the adiabatic theorem in more detail, two specific Hamiltonians are now considered.

2.2.1 Two Level System

Consider a system consisting of two levels that, unperturbed, are separated by an energy Λ and are subsequently mixed with a parameter with a strength given by ϵ.

$$\hat{H} = \begin{pmatrix} \frac{\Lambda}{2} & \epsilon \\ \epsilon & -\frac{\Lambda}{2} \end{pmatrix} \tag{2.29}$$

Choosing β such that $\tan(2\beta) = \frac{2\epsilon}{\Lambda}$, the eigenvalues E and eigenvectors $\hat{U}$ of $\hat{H}$ can be written as

$$E_\pm = \pm\sqrt{\left(\frac{\Lambda}{2}\right)^2 + \epsilon^2} = \pm\frac{\Lambda}{2}\sec(2\beta) \tag{2.30}$$

$$\hat{U} = \begin{pmatrix} \cos\beta & \sin\beta \\ \sin\beta & -\cos\beta \end{pmatrix} \tag{2.31}$$

If the ratio of ϵ to Λ changes in time, i.e. β changes in time, transitions can occur between the upper and lower states. The value of $\left\langle \phi_m \middle| \frac{\partial \phi_n}{\partial s} \right\rangle$ is given in this case by

$$\left\langle \phi_\pm \middle| \frac{\partial \phi_\mp}{\partial s} \right\rangle = \pm\frac{d\beta}{ds} = \pm\left[\frac{d}{ds}\left(\frac{\epsilon}{\Lambda}\right)\right]\cos^2(2\beta) \tag{2.32}$$

If $\frac{\epsilon}{\Lambda}$ is changing at a constant rate, the most critical region will be near where $\frac{\epsilon}{\Lambda} = 0 \equiv \beta = 0$. From the criterion given in equation (2.27), non-adiabatic transitions will be avoided as long as the system passes uniformly through the region between $\frac{\epsilon}{\Lambda} = -1$ and $\frac{\epsilon}{\Lambda} = 1$ on a timescale much longer than $h\Lambda^{-1}$. In all other regions, losses are suppressed by the factor $\cos^2(2\beta) = \left(1 + \left(\frac{2\epsilon}{\Lambda}\right)^2\right)^{-1}$, so passage through such regions can be correspondingly faster without the occurrence of non-adiabatic losses.

The two level system can be used as a model for a polar molecule with two closely-spaced parity levels in an electric field. Since the zero-field eigenstates have definite parity and electric fields only mix states of opposite parity (more on this in chapter 4), Λ describes the splitting between the two zero-field states, and ϵ describes the coupling of the states due to an external electric field. In the case of ^{12}CO in the $a^3\Pi_1$, $v = 0$, $J = 1$, $M_J = 1$ state, the zero-field splitting Λ is 394 MHz and $\epsilon = 0.4967\mu_E E_z$, where $\mu_E = 1.37\,\text{Debye}$ is the body-fixed dipole moment of the molecule and E_z is the electric field strength (it is assumed here that the electric field is always along the $\hat{z}$-axis). If the electric field strength is changing rapidly but at a constant rate, as long as it passes through the region where $|E_z| < 1\frac{\text{kV}}{\text{cm}}$ over a period much longer than 3 ns, the non-adiabatic losses will be minimal.

2.2.2 Symmetric Top State

Unfortunately, the two level model assumes that the electric field always stays along the same axis. Because rotations around the electric field axis leave the Hamiltonian invariant, the projection of the total angular momentum along that axis, M_J, is a good quantum number, and as a result, only states with the same M_J can be mixed by the electric field. As soon as the field is free to rotate, however, states with different M_J can mix. At zero field, states whose quantum numbers differ only in M_J become degenerate, leading to a divergence in equation (2.27). In regions where the electric field is very small, non-adiabatic transitions become very likely. Chapter 4 will address the subject of quantum mechanical symmetric tops in detail, but for now, the basis set and matrix elements described in that chapter are applied here without further explanation.

To examine the effects of rotating fields more quantitatively, we consider the case of a molecular symmetric top with a total angular momentum of $J = 1$ and an angular momentum along its body-fixed axis of magnitude $|\Omega| = 1$. This molecule is assumed to

have a splitting between its positive and negative parity components of Λ and is placed in an external electric and magnetic field: the magnetic field is along the space-fixed $\hat{z}$-axis, and the electric field is in the xy-plane with and angle with respect to the $\hat{x}$-axis α. Six basis states can contribute to this wavefunction and are enumerated as follows:

1. $\Omega = 1,\ M = 1$
2. $\Omega = 1,\ M = 0$
3. $\Omega = 1,\ M = -1$
4. $\Omega = -1,\ M = 1$
5. $\Omega = -1,\ M = 0$
6. $\Omega = -1,\ M = -1$

Using these six states, the Hamiltonian can be written as follows

$$\hat{H} = \begin{pmatrix} Z & -\frac{1}{\sqrt{2}}e^{-i\alpha}S & 0 & \frac{\Lambda}{2} & 0 & 0 \\ -\frac{1}{\sqrt{2}}e^{i\alpha}S & 0 & -\frac{1}{\sqrt{2}}e^{-i\alpha}S & 0 & \frac{\Lambda}{2} & 0 \\ 0 & -\frac{1}{\sqrt{2}}e^{i\alpha}S & -Z & 0 & 0 & \frac{\Lambda}{2} \\ \frac{\Lambda}{2} & 0 & 0 & Z & \frac{1}{\sqrt{2}}e^{-i\alpha}S & 0 \\ 0 & \frac{\Lambda}{2} & 0 & \frac{1}{\sqrt{2}}e^{i\alpha}S & 0 & \frac{1}{\sqrt{2}}e^{-i\alpha}S \\ 0 & 0 & \frac{\Lambda}{2} & 0 & \frac{1}{\sqrt{2}}e^{i\alpha}S & -Z \end{pmatrix} \tag{2.33}$$

Here, S and Z are proportional to electric and magnetic field strengths, respectively. For the case of ^{12}CO in the $a^3\Pi_1$, $v = 0$, $J = 1$, $M_J = 1$ state, Λ is 394 MHz and S and Z are given by

$$S = 0.4967\,\mu_E|\vec{E}| = 343\,\mathrm{MHz}\left(\frac{\mathrm{kV}}{\mathrm{cm}}\right)^{-1}|\vec{E}| \tag{2.34}$$

$$Z = 0.3332\,\mu_B B_z = 0.466\,\mathrm{MHz\,Gauss}^{-1}B_z \tag{2.35}$$

In these equations, the body-fixed electric dipole moment μ_E is 1.37 Debye and μ_B is the Bohr magneton. The prefactors are derived by fitting Stark and Zeeman curves calculated using the more rigorous treatment given later in chapter 4. If there were no mixing between states of different Ω, both of these prefactors should be exactly $\frac{1}{2}$.

A parameter β is chosen, as in the two level system, such that $\tan(2\beta) = \frac{2S}{\Lambda}$. Using the unitary transformation given by

$$\hat{U} = \begin{pmatrix} \frac{1}{2}e^{-i\alpha}\cos\beta & -\frac{1}{2}e^{-i\alpha} & \frac{1}{2}e^{-i\alpha}\sin\beta & \frac{1}{2}e^{-i\alpha}\cos\beta & -\frac{1}{2}e^{-i\alpha} & \frac{1}{2}e^{-i\alpha}\sin\beta \\ \frac{1}{\sqrt{2}}\sin\beta & 0 & -\frac{1}{\sqrt{2}}\cos\beta & -\frac{1}{\sqrt{2}}\sin\beta & 0 & \frac{1}{\sqrt{2}}\cos\beta \\ \frac{1}{2}e^{i\alpha}\cos\beta & \frac{1}{2}e^{i\alpha} & \frac{1}{2}e^{i\alpha}\sin\beta & \frac{1}{2}e^{i\alpha}\cos\beta & \frac{1}{2}e^{i\alpha} & \frac{1}{2}e^{i\alpha}\sin\beta \\ -\frac{1}{2}e^{-i\alpha}\cos\beta & \frac{1}{2}e^{-i\alpha} & -\frac{1}{2}e^{-i\alpha}\sin\beta & \frac{1}{2}e^{-i\alpha}\cos\beta & -\frac{1}{2}e^{-i\alpha} & \frac{1}{2}e^{-i\alpha}\sin\beta \\ \frac{1}{\sqrt{2}}\sin\beta & 0 & -\frac{1}{\sqrt{2}}\cos\beta & \frac{1}{\sqrt{2}}\sin\beta & 0 & -\frac{1}{\sqrt{2}}\cos\beta \\ -\frac{1}{2}e^{i\alpha}\cos\beta & -\frac{1}{2}e^{i\alpha} & -\frac{1}{2}e^{i\alpha}\sin\beta & \frac{1}{2}e^{i\alpha}\cos\beta & \frac{1}{2}e^{i\alpha} & \frac{1}{2}e^{i\alpha}\sin\beta \end{pmatrix} \tag{2.36}$$

the Hamiltonian $\hat{H}$ can be reduced to

$$\hat{U}^\dagger \hat{H} \hat{U} = \begin{pmatrix} -\frac{\Lambda}{2}\sec(2\beta) & -Z\cos\beta & 0 & 0 & 0 & 0 \\ -Z\cos\beta & -\frac{\Lambda}{2} & -Z\sin\beta & 0 & 0 & 0 \\ 0 & -Z\sin\beta & \frac{\Lambda}{2}\sec(2\beta) & 0 & 0 & 0 \\ 0 & 0 & 0 & \frac{\Lambda}{2}\sec(2\beta) & -Z\cos\beta & 0 \\ 0 & 0 & 0 & -Z\cos\beta & \frac{\Lambda}{2} & -Z\sin\beta \\ 0 & 0 & 0 & 0 & -Z\sin\beta & -\frac{\Lambda}{2}\sec(2\beta) \end{pmatrix} \tag{2.37}$$

In the absence of a magnetic field, the matrix is already diagonal, and $\hat{U}$ contains the eigenvectors. If it is assumed that β is constant, the various $\left\langle \phi_m \middle| \frac{\partial \phi_n}{\partial s} \right\rangle$ are given by

$$\left\langle \phi_1 \middle| \frac{\partial \phi_2}{\partial s} \right\rangle = \left\langle \phi_2 \middle| \frac{\partial \phi_1}{\partial s} \right\rangle = \left\langle \phi_4 \middle| \frac{\partial \phi_5}{\partial s} \right\rangle = \left\langle \phi_5 \middle| \frac{\partial \phi_4}{\partial s} \right\rangle = i\cos\beta \frac{d\alpha}{ds} \tag{2.38}$$

$$\left\langle \phi_2 \middle| \frac{\partial \phi_3}{\partial s} \right\rangle = \left\langle \phi_3 \middle| \frac{\partial \phi_2}{\partial s} \right\rangle = \left\langle \phi_5 \middle| \frac{\partial \phi_6}{\partial s} \right\rangle = \left\langle \phi_6 \middle| \frac{\partial \phi_5}{\partial s} \right\rangle = i\sin\beta \frac{d\alpha}{ds} \tag{2.39}$$

and all others are zero. Since states 1 and 2 and states 4 and 5 become degenerate as β or $\frac{S}{\Lambda}$ go to zero, the timescale of passage between states must become very long to avoid non-adiabatic losses.

$$T \gg \frac{2\hbar}{\Lambda} \frac{\cos\beta}{\sec(2\beta) - 1} \frac{d\alpha}{ds} \tag{2.40}$$

Equivalently, $\nu = (2\pi)^{-1} \frac{d\alpha}{dt} = (2\pi T)^{-1} \frac{d\alpha}{ds}$ represents the frequency with which the electric field vector rotates in the xy-plane, and using this, the criterion for the suppression of non-adiabatic losses can be rewritten as

$$\nu \ll h^{-1} \frac{\Lambda}{2} (\sec(2\beta) - 1) \sec\beta \tag{2.41}$$

For $S \ll \Lambda$, this condition is $\nu \ll \frac{S^2}{h\Lambda}$, so at low fields, the maximum frequency decreases quadratically with the field strength. At 100 $\frac{\mathrm{V}}{\mathrm{cm}}$ in the state of CO mentioned above, for example, the frequency of rotation should be much lower than 12 MHz to prevent transitions, but at 50 $\frac{\mathrm{V}}{\mathrm{cm}}$, the frequency must be much lower than 3 MHz.

These arguments apply for a system initially in a non-rotating field, and describes the transitions that result when the field suddenly starts to rotate. If the field always rotates, however, it is possible that there is a stationary state in the rotating frame. In fact, the field distributions used in the experiments have exactly this property: as they are translated in space, the electric field vector at every point in the distribution rotates at a constant rate. A stationary state in a rotating frame can potentially be found by applying a unitary transformation to the wavefunction such that $|\psi(t)\rangle = \hat{U}(t)|\psi'(t)\rangle$. Substituting this into equation (2.15) and operating on the left with $\hat{U}^\dagger$ results in

$$i\hbar \left| \frac{\partial \psi'}{\partial t} \right\rangle = \left(\hat{U}^\dagger \hat{H}(t) \hat{U} - i\hbar \hat{U}^\dagger \frac{d\hat{U}}{dt} \right) |\psi'\rangle \tag{2.42}$$

Though its individual components are time dependent, the coefficient of $|\psi'\rangle$ on the right side can be time independent for certain $\hat{U}(t)$. The result is an equation that has the same form as the time-dependent Schrödinger equation for a time independent Hamiltonian,

and can be similarly solved as an eigenvalue problem. The eigenvalues that result are called "quasienergies" [71, 72].

In fact, the $\hat{U}(\alpha(t))$ given in equation (2.36), in conjunction with the real Hamiltonian $H(\alpha(t))$ (2.33) results in a time-independent quasienergy Hamiltonian if the field rotates at a constant rate, i.e. $\frac{d\alpha}{dt}$ is constant.

$$\begin{aligned}
&\hat{U}^\dagger \hat{H}(t)\hat{U} - i\hbar\hat{U}^\dagger \frac{d\hat{U}}{dt} \\
&= \begin{pmatrix}
-\frac{\Lambda}{2}\sec(2\beta) & R\cos\beta & 0 & 0 & 0 & 0 \\
R\cos\beta & -\frac{\Lambda}{2} & R\sin\beta & 0 & 0 & 0 \\
0 & R\sin\beta & \frac{\Lambda}{2}\sec(2\beta) & 0 & 0 & 0 \\
0 & 0 & 0 & \frac{\Lambda}{2}\sec(2\beta) & R\cos\beta & 0 \\
0 & 0 & 0 & R\cos\beta & \frac{\Lambda}{2} & R\sin\beta \\
0 & 0 & 0 & 0 & R\sin\beta & -\frac{\Lambda}{2}\sec(2\beta)
\end{pmatrix}
\end{aligned} \tag{2.43}$$

Here, $R = \hbar\frac{d\alpha}{dt} - Z$ is the frequency of the rotation of the electric field in units of energy minus the magnetic field coupling strength. Interestingly, the effect of a continuously rotating field and a magnetic field on the quasienergy Hamiltonian is exactly the same in this particular Hamiltonian: a magnetic field that would induce a 1 MHz splitting between neighboring M states within a single parity level is equivalent to the electric field rotating with a frequency of 1 MHz.

Until now, it has been assumed that β is constant in time and that the entire time dependence of $\hat{H}$ and $\hat{U}$ comes from the phase factor α. If α is now assumed to increase at a linear rate (i.e. $\frac{d\alpha}{dt}$ is constant), the effect of a time-dependent β can be considered. At low electric field strength ($\beta \ll 1$), the couplings of the form $\sin\beta$ can be neglected, especially since they always couple states separated in energy by $\frac{\Lambda}{2}(\sec(2\beta)+1)$, in contrast to the couplings of the form $\cos\beta$, which couple states separated in energy by only $\frac{\Lambda}{2}(\sec(2\beta)-1)$. Using this approximation, the third and sixth quasistates become decoupled, but in fact, transitions involving these quasistates would still be possible for changes of magnitude $\Delta\beta = 1$ on the timescale $h\Lambda^{-1}$, according to the criterion developed in section 2.2.1. The remaining two pairs of quasistates have the same form, so only the pair consisting of the fourth and fifth state is considered. This pair of states is strongly coupled by R, even when $\beta \to 0$, so it is useful to apply a unitary transform such that the matrix is diagonal when $\beta = 0$. The relevant section of the quasienergy Hamiltonian and the unitary matrix are

$$\hat{H}' = \begin{pmatrix} \frac{\Lambda}{2}\sec(2\beta) & R\cos\beta \\ R\cos\beta & \frac{\Lambda}{2} \end{pmatrix} \tag{2.44}$$

$$\hat{U}' = \begin{pmatrix} \frac{1}{\sqrt{2}} & \frac{1}{\sqrt{2}} \\ \frac{1}{\sqrt{2}} & -\frac{1}{\sqrt{2}} \end{pmatrix} \tag{2.45}$$

and transformed, the matrix takes the form

$$\begin{aligned}
\hat{U}'^\dagger \hat{H}' \hat{U}' = &\frac{\Lambda}{2}\sec(2\beta)\cos^2\beta \begin{pmatrix} 1 & 0 \\ 0 & 1 \end{pmatrix} \\
&+ R\cos\beta \begin{pmatrix} 1 & \frac{\Lambda}{2R}\sec(2\beta)\sin\beta\tan\beta \\ \frac{\Lambda}{2R}\sec(2\beta)\sin\beta\tan\beta & -1 \end{pmatrix}
\end{aligned} \tag{2.46}$$

The first term of equation (2.46) is an energy offset that shifts all levels by the same amount. The second term, however, has the same form as a two level system that can be described with a parameter β' that is defined such that $\tan(2\beta') = \frac{\Lambda}{2R}\sec(2\beta)\sin\beta\tan\beta$, and to lowest order in β, $\beta' = \frac{\Lambda}{4R}\beta^2 + O(\beta^4)$. From the form of equation (2.46), it can be concluded that changes to β' of magnitude order 1 (equivalently, changes to β of magnitude order $\sqrt{\frac{4R}{\Lambda}}$) will not result in transitions between quasienergy states as long as the timescale of these transitions is much longer than $\frac{h}{2R}$. Additionally, because β' is quadratic in β, at very low fields, losses will be further suppressed.

2.3 Summary

It has been shown that, as long as the time variation of the electric field seen by a molecule is sufficiently slow, the molecules can be manipulated and confined by these electric fields. This means that the time variation of the externally applied fields and the motion of the molecules in these fields must be slow enough that the molecules do not "lose their orientation" and end up in an untrappable state. The exact timescale at which the non-adiabatic transitions become important is often difficult to calculate, since it depends on many details of the motion, but a number of experimental results presented in later chapters show that the assumptions of slow time variation are being pushed to their limits, and non-adiabatic transitions do, in fact, play a major role in the loss of molecules from their confining potentials. This is not surprising, since the rate at which fields change on a microchip is much higher than in the macroscopic molecular manipulation devices that have been constructed previously, both in terms of high frequency of the applied fields and of the high oscillation frequency of the molecules within the traps. The experimental effort toward preventing of these losses will be described in more detail in chapter 7.

Chapter 3

The Electric Field of a Periodic Electrode Array

It has long been known that it is possible to make an electric field minimum above a surface using overlapping dipoles. A short dipole produces an electric field that dominates close to a surface and a longer dipole produces a field that dominates farther from the surface. If these dipoles are oriented in opposite directions, then they will cancel out at some position, forming a zero-field minimum along the central axis of the dipoles. If these dipoles are realized with physical electrodes, the minimum is centered between two electrodes.

It is said that a little knowledge is a dangerous thing. Sometimes, though, new discoveries come from not knowing all the details. During the work on a molecular mirror for ND_3 [73], plans were being made to load a trap above a chip from a Stark decelerated beam, much in the same way that atom chips are generally loaded from a MOT. Stephan Schulz, the student on this project at the time, knew that it was possible to make a trap above the chip, but not knowing how exactly it should be constructed, set out to find the correct electrode configuration for himself. It was only through later comparison that everyone involved realized that this configuration produced a field minimum at a different position relative to the electrodes: while the previous configuration produced a minimum between two electrodes, this one produced a minimum directly above an electrode. Nevertheless, both configurations produced minima with about the same shape and depth. If these two positions are possible, it was reasoned, then shouldn't other, intermediate positions also be possible? With a bit of interpolation it was found that minima at other positions are indeed possible, and in the end, the minima can be moved to an arbitrary position above the electrodes by choosing the right potentials. Surprisingly, the shape of the minima always remained relatively unchanged.

This method of creating movable quadrupole minima was discovered mostly by accident. To understand how these minima are formed and why their shape changes so little as they are moved, it is necessary to approach the problem from first principles. By doing so, it is possible to discover other potentials that may not have become evident from a more haphazard approach. The first section will discuss the mathematical form that the electric fields must have. In the next section, it will be shown how these potentials can be created with discrete electrodes, and in the third section, how any potential created can be translated over the surface. The fourth section will describe how to create multipole

potentials using these building block, and finally, the fifth section will describe the details of the chip that was constructed for experiments described in this thesis.

3.1 A Periodic Solution to Laplace's Equation

An electric potential in free space $V(x, y, z)$ must be a solution to Laplace's equation (equation (2.5)). If the electrodes used to produce the electric fields extend over a sufficiently long distance in x without changing, then V is effectively independent of x, and the first term in equation (2.5) vanishes. The equation can then be solved in y and z using a separation of variables ansatz:

$$V(y, z) = Y(y)Z(z) \tag{3.1}$$

This results in two ordinary differential equations

$$\frac{d^2Y}{dy^2} - k^2 Y = 0 \tag{3.2}$$

$$\frac{d^2Z}{dz^2} + k^2 Z = 0 \tag{3.3}$$

$$\tag{3.4}$$

The general solution of these equation is given by[1]

$$Y(y) = C_1 \exp(-ky) + C_2 \exp(ky) \tag{3.5}$$

$$Z(z) = \Re\left\{\tilde{C}_3 \exp(ikz)\right\} \tag{3.6}$$

If the condition is imposed that V vanish as $y \to \infty$, then C_2 must be zero. Additionally, if $Z(z)$ is constrained to be periodic such that $Z(z) = Z(z + \ell)$, this forces k to obey the equation $k\ell = 2\pi n$, where n is an integer. Combining equations (3.5) and (3.6) with these constraints yield a solution to V

$$\begin{aligned} V_n(y, z) =& \Re\left\{\tilde{A}_n \exp\left(\frac{2\pi i n z}{\ell}\right)\right\} \exp\left(-\frac{2\pi n y}{\ell}\right) \\ =& |\tilde{A}_n| \cos\left(\frac{2\pi n z}{\ell} + \arg \tilde{A}_n\right) \exp\left(-\frac{2\pi n y}{\ell}\right) \end{aligned} \tag{3.7}$$

Finally, because Laplace's equation is linear, linear combinations of V_n are also solutions to Laplace's equation

$$V(y, z) = \sum_{n=0}^{\infty} V_n(y, z) = \sum_{n=0}^{\infty} \Re\left\{\tilde{A}_n \exp\left(\frac{2\pi i n z}{\ell}\right)\right\} \exp\left(-\frac{2\pi n y}{\ell}\right) \tag{3.8}$$

3.2 Building Fields with Discrete Electrodes

The building blocks of the fields described in following sections will be the V_n terms described above. In order to produce the fields, however, one must generally rely on the

[1] $\Re$ denotes the real component of a complex number, while $\Im$ (used later) denotes the imaginary part. Variables with a tilde, such as $\tilde{C}_3$ denote complex quantities.

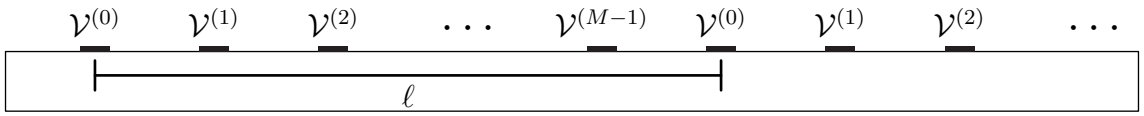

Figure 3.1: Periodic electrodes on a surface, spaced at an interval of $\frac{\ell}{M}$. Every Mth electrode has the same potential, and the electrodes repeat for many periods in either direction.

use of discrete electrodes. The simplest approach is to use an array of identical electrodes in a single plane, spaced at an interval of $\frac{\ell}{M}$, where M is a natural number. To generate the desired periodicity, the electrodes should be grouped together such that an electrode at position (y_0, z_0) has the same potential as the electrode at $(y_0, z_0 + \ell)$, i.e. every Mth electrode has the same potential. Arranging the electrodes in this manner provides M degrees of freedom which can be used to control the $\tilde{A}_n$ in equation (3.8).

The solution of the electric potential distribution for M arbitrary electrode voltages can be solved by first solving the case in which 1 volt is applied to one set of electrodes and 0 to all other electrodes. This solution for which the 1 volt is applied to the mth set of electrodes must have the same form as equation (3.8)

$$V^{(m)}(y,z) = \sum_{n=0}^{\infty} V_n^{(m)}(y,z) = \sum_{n=0}^{\infty} \Re\left\{\tilde{A}_n^{(m)} \exp\left(\frac{2\pi i n z}{\ell}\right)\right\} \exp\left(-\frac{2\pi n y}{\ell}\right) \tag{3.9}$$

If this is repeated for each of the electrode sets, then the general solution can be computed as a linear combination of these individual solutions.

In general, once the problem is reduced to this form, the electric potential for the simplified case must be calculated numerically to determine the coefficients $\tilde{A}_n^{(m)}$. If the numerically calculated potential satisfies the conditions that it be periodic with a period length ℓ and that it vanish as y goes to infinity, then it must be possible to describe the electric potential in the region above the electrodes (toward increasing y) using equation (3.9). At a constant y value, equation (3.9) represents a Fourier series in z. Thus, the coefficients $\tilde{A}_n^{(m)}$ can be found by computing a discrete Fourier transform in z on the numerical solution along the line $y = y_0$. The choice of y_0 is in principle arbitrary; the only requirement is that no part of the electrodes should be above this value. In practice, however, the best results will be obtained by choosing a y_0 to be as close to the electrodes as possible: since the voltages applied to the electrodes constrain the electric potential in the free space around the electrodes, the potentials are most accurate at the surface of the electrodes.

If all sets of electrodes are identical, it is only necessary to compute $V^{(0)}$: the other single electrode solutions $V^{(m)}$ are obtained by shifting the solution by an integral number of electrode spacings in the z direction.

$$V^{(m)}(y,z) = V^{(0)}\left(y, z - \frac{m\ell}{M}\right) \tag{3.10}$$

Incidentally, if each individual electrode has a mirror symmetry across a plane of constant z, then the position of $z = 0$ can be chosen, without loss of generality, to correspond to the center of an electrode from the $m = 0$th set. By choosing z in this way, $V^{(0)}$ will be

symmetric in z, and thus all $\tilde{A}_n^{(0)}$ will be real. Subsequent equations do not rely on this assumption, however.

If the shape of all electrodes is the same, the overall solution can be obtained by superimposing the $V^{(m)}$ obtained by shifting $V^{(0)}$. The electric potential $V(y,z)$ obtained when applying voltages $\mathcal{V}^{(m)}$ to the M electrodes is then given by

$$\begin{aligned} V(y,z) &= \sum_{m=0}^{M-1} \mathcal{V}^{(m)} V^{(m)}(y,z) \\ &= \sum_{n=0}^{\infty} \Re\left\{ \tilde{A}_n \exp\left(\frac{2\pi i n z}{\ell}\right)\right\} \exp\left(-\frac{2\pi n y}{\ell}\right) \end{aligned} \tag{3.11}$$

where

$$\tilde{A}_n = \tilde{A}_n^{(0)} \sum_{m=0}^{M-1} \mathcal{V}^{(m)} \exp\left(-\frac{2\pi i m n}{M}\right) \tag{3.12}$$

Equation (3.12) gives the $\tilde{A}_n$ coefficients in equation (3.8) in terms of the set of potentials applied to discrete electrodes $\mathcal{V}^{(m)}$ and the $\tilde{A}_n^{(0)}$ that define the geometry of the electrodes. It would also be useful to be able to express $\mathcal{V}^{(m)}$ in terms of $\tilde{A}_n$ and $\tilde{A}_n^{(0)}$ in order to find the potentials that need to be applied to the chip to produce a specific field distribution. To do this, we first recognize that the summation in equation (3.12) is essentially a Fourier series and express the set of applied voltages $\mathcal{V}^{(m)}$ in terms of their Fourier components $\tilde{\mathcal{V}}_p$.

$$\mathcal{V}^{(m)} = \sum_{p=0}^{\lfloor M/2 \rfloor} \Re\left\{ \tilde{\mathcal{V}}_p \exp\left(\frac{2\pi i p m}{M}\right)\right\}. \tag{3.13}$$

The range of this summation is chosen without loss of generality to extend from 0 to $\lfloor M/2 \rfloor$ based on two fundamental symmetries. The first is that increasing or decreasing p by a multiple of M does not change the value of $\exp\left(\frac{2\pi i p m}{M}\right)$ for any integer value of m. As a result, $\tilde{\mathcal{V}}_{p+Mk}$, where k is an integer, has the same effect on the $\mathcal{V}^{(m)}$ as $\tilde{\mathcal{V}}_p$, so p can be limited to the range $0 \leq p < M$ without losing the ability to express any arbitrary set of $\mathcal{V}^{(m)}$. The second symmetry is that replacing p with $M-p$ while simultaneously replacing $\tilde{\mathcal{V}}_p$ with its complex conjugate also does not not change the values of $\mathcal{V}^{(m)}$. This makes values of p larger than $\lfloor M/2 \rfloor$ also unnecessary.

Physically, the limitation on possible values of p is a result of the harmonic waveforms being described by discrete electrodes. Particularly, the Shannon sampling theorem [74] states that it is impossible, using M sampling points, to represent a waveform that oscillates more than $M/2$ times. Waves that oscillate more than $M/2$ times over the set of electrodes are mapped back to the range between 0 and $M/2$, so the only meaningful values of p are in the range $0 \leq p \leq M/2$.

To obtain the inverse of equation (3.13) ($\tilde{\mathcal{V}}_p$ in terms of $\mathcal{V}^{(m)}$) both sides of equation

(3.13) are multiplied by $\exp\left(-\frac{2\pi i p' m}{M}\right)$ and summed over all m from 0 to $M-1$.

$$\begin{aligned}&\sum_{m=0}^{M-1} \exp\left(-\frac{2\pi i p' m}{M}\right) \mathcal{V}^{(m)} \\ &= \sum_{p=0}^{\lfloor M/2 \rfloor} \sum_{m=0}^{M-1} \left\{ \frac{1}{2}\tilde{\mathcal{V}}_p \exp\left(\frac{2\pi i (p-p')m}{M}\right) + \frac{1}{2}\tilde{\mathcal{V}}_p^* \exp\left(-\frac{2\pi i (p+p')m}{M}\right)\right\}\end{aligned} \tag{3.14}$$

The first term will vanish when summed over m unless $(p-p')/M$ is an integer.[2] Similarly, the second term can only sum to a non-zero value when $(p+p')/M$ is an integer. Since p and p' are limited to the range from 0 to $M/2$, $(p-p')/M$ is only an integer when $p = p'$, and $(p+p')/M$ is only an integer when $p = p' = 0$ or $p = p' = M/2$. Equation (3.14) then reduces to

$$\sum_{m=0}^{M-1} \exp\left(-\frac{2\pi i p' m}{M}\right) \mathcal{V}^{(m)} = \frac{M}{2}\tilde{\mathcal{V}}_{p'} + \frac{M}{2}\tilde{\mathcal{V}}_{p'}^* (\delta_{p',0} + \delta_{p',M/2}) \tag{3.15}$$

and the inverse transform is given by

$$\tilde{\mathcal{V}}_p = \begin{cases} \frac{1}{M}\sum_{m=0}^{M-1} \mathcal{V}^{(m)} \exp\left(-\frac{2\pi i p m}{M}\right) & p = 0 \text{ or } M/2 \\ \frac{2}{M}\sum_{m=0}^{M-1} \mathcal{V}^{(m)} \exp\left(-\frac{2\pi i p m}{M}\right) & \text{otherwise} \end{cases} \tag{3.16}$$

In addition to having a different leading factor than the other coefficients, $\tilde{\mathcal{V}}_0$ and $\tilde{\mathcal{V}}_{M/2}$ are also always real. The coefficient $\tilde{\mathcal{V}}_0$ is real because it is the mean of the voltages applied to the electrodes, and $\tilde{\mathcal{V}}_{M/2}$ is real because $\exp(-\pi i p)$ can only be ± 1. That $\tilde{\mathcal{V}}_{M/2}$ is real also reflects the physical reality that only one possible phase exists for a waveform that completes an oscillation over two electrodes: one of the two electrodes will contribute the maximum of the wave while the other contributes the minimum.

Substituting equation (3.13) into equation (3.12) results in $\tilde{A}_n$ in terms of $\tilde{\mathcal{V}}_p$.

$$\tilde{A}_n = \tilde{A}_n^{(0)} \sum_{p=0}^{\lfloor M/2 \rfloor} \sum_{m=0}^{M-1} \left\{ \frac{1}{2}\tilde{\mathcal{V}}_p \exp\left(\frac{2\pi i (p-n)m}{M}\right) + \frac{1}{2}\tilde{\mathcal{V}}_p^* \exp\left(-\frac{2\pi i (p+n)m}{M}\right)\right\} \tag{3.17}$$

When the sum over m is carried out, the first term sums to zero unless $p = n \bmod M$, and the second term sums to zero unless $p = (M-n) \bmod M$. The explicit conversion from the $\tilde{\mathcal{V}}_p$, the Fourier transform of the potentials applied to the electrodes, to the $\tilde{A}_n$ in equation (3.8) that describe the phase and amplitude of the periodic potentials in z can be simplified to

$$\tilde{A}_n = \begin{cases} M\tilde{A}_n^{(0)}\tilde{\mathcal{V}}_{(n \bmod M)} & n \bmod M = 0 \text{ or } M/2 \\ \frac{M}{2}\tilde{A}_n^{(0)}\tilde{\mathcal{V}}_{(n \bmod M)} & 0 < n \bmod M < M/2 \\ \frac{M}{2}\tilde{A}_n^{(0)}\tilde{\mathcal{V}}^*_{((M-n) \bmod M)} & M/2 < n \bmod M < M \end{cases} \tag{3.18}$$

[2] This is the orthogonality condition used for discrete Fourier transforms. If n and M are integers, the series

$$\sum_{m=0}^{M-1} \exp\left(\frac{2\pi i m n}{M}\right)$$

can only be non-zero if n is a multiple of M. A simple explanation of this can be given in terms of evenly spaced vectors around a unit circle: due to symmetry, the vectors will sum to zero, unless all the vectors are spaced by a multiple of 2π, in which case the vectors add constructively.

Using M discrete electrodes per period, it is possible to "write" $\tilde{A}_n$ with an arbitrary phase and amplitude, as long as $n < M/2$. As a side effect of writing $\tilde{A}_n$, however, other coefficients, such as $\tilde{A}_{M-n}$ and $\tilde{A}_{n+M}$ must appear as well, unless the corresponding $\tilde{A}_n^{(0)}$ (such as $\tilde{A}_{M-n}^{(0)}$ or $\tilde{A}_{n+M}^{(0)}$) are zero. It is also possible to determine a coefficient $\tilde{A}_{M/2}$, but since this coefficient is always real, its phase is fixed. If these limitations are accepted, equation (3.18) can be used to find the individual $\tilde{\mathcal{V}}_n$ in terms of $\tilde{A}_n$, and these $\tilde{\mathcal{V}}_n$ can be converted to $\mathcal{V}^{(m)}$, the real potentials applied to the electrodes, using equation (3.16).

3.3 Moving the Electric Potentials

For a given electric potential, $V(y, z)$, it is useful to be able to translate it by a certain amount, i.e. to create a new potential such that $V'(y, z) = V(y - y_0, z - z_0)$. Such a shift is equivalent to scaling $\tilde{A}_n$ in equation (3.8).

$$\tilde{A}_n \to \tilde{A}_n \exp\left(\frac{2\pi n y_0}{\ell}\right) \exp\left(-\frac{2\pi i n z_0}{\ell}\right) \tag{3.19}$$

When the fields are produced with discrete electrodes, however, exerting the necessary control over $\tilde{A}_n$ can require a large number of electrodes per period. Specifying the first s terms in equation (3.8) with full phase control requires the use of at least $2s+1$ electrodes per period. Terms after V_s cannot be constrained, and cannot be forced to follow this transform.

It is possible to reduce the relative effect of terms after V_s by shifting the potential in the $+y$ direction. When the amplitude of $\tilde{A}_n$ is scaled using transformation (3.19), coefficients with larger n must be scaled more. When using real electrodes, however, $\tilde{A}_{M-n}$ will be scaled the same amount as $\tilde{A}_n$, and so the relative influence of $\tilde{A}_{M-n}$ will be reduced by $\exp\left(-\frac{2\pi(M-2n)\Delta y}{\ell}\right)$. To guarantee that all undesired terms are suppressed by at least a factor of two, the potential should be shifted upward by $\frac{\ln 2}{2\pi}\ell \approx \frac{\ell}{9}$.

For polar molecules, where only the strength and not the direction of the electric field is important, it is not absolutely necessary to shift V perfectly; it would suffice to simply shift the field strength. The electric field produced by a single V_n is

$$\begin{aligned}\vec{E}_n =& -\vec{\nabla} V_n \\ =& \frac{2\pi n}{\ell} \exp\left(-\frac{2\pi n y}{\ell}\right) \left(\Re\left\{\tilde{A}_n \exp\left(\frac{2\pi i n z}{\ell}\right)\right\} \hat{y} + \Im\left\{\tilde{A}_n \exp\left(\frac{2\pi i n z}{\ell}\right)\right\} \hat{z}\right)\end{aligned} \tag{3.20}$$

The field strength produced by a single V_n is independent of z and the argument of $\tilde{A}_n$; it is only a function of y and the magnitude of $\tilde{A}_n$. The direction of the field rotates in the yz plane. If ϕ is defined as the angle of the field vector with respect to the $+\hat{y}$ axis toward the $+\hat{z}$ axis, then

$$\phi_n = \frac{2\pi n z}{\ell} + \arg \tilde{A}_n \tag{3.21}$$

For the general case, in which there are multiple V_n terms in V, multiplying each $\tilde{A}_n$ by a constant phase factor $\exp(i\delta)$ would rotate the field at every position but would leave

the electric field magnitude unchanged. The transformation in (3.19) can be expanded to include this phase shift

$$\tilde{A}_n \rightarrow \tilde{A}_n \exp\left(\frac{2\pi n y_0}{\ell}\right) \exp\left(\frac{2\pi i s z_0}{\ell} - \frac{2\pi i n z_0}{\ell}\right) \tag{3.22}$$

The result is that V_s no longer needs to be phase shifted to shift the potential, and only $2s$ electrodes are needed to define s terms in equation (3.8). Yet, there is a much more profound effect in this transformation than simply eliminating one electrode per period. If $n > s$, the change in phase to $\tilde{A}_n$ has the opposite sign as for $n < s$. More specifically

$$\exp\left(\frac{2\pi i s z_0}{\ell} - \frac{2\pi i (2s-n) z_0}{\ell}\right) = \exp\left(-\left(\frac{2\pi i s z_0}{\ell} - \frac{2\pi i n z_0}{\ell}\right)\right) \tag{3.23}$$

The phase shift in equation (3.22) follows the same relation as the $\tilde{\mathcal{V}}$ in equation (3.18) for $0 \leq n < M$ if $M = 2s$. Thus, by using the transformation (3.22) instead of (3.19) to shift the potential in z, the transformation is guaranteed to be accurate for V_n up to $n = M$.

3.4 Expanding Field Geometries as Multipoles

The electric potential described in equation (3.8) can be used to produce a cylindrical multipole potential, i.e. a potential of the form $V \propto r^n \cos(n\phi + \delta_n)$ in two-dimensional polar coordinates. A single multipole field produces an electric field strength proportional to r^{n-1}, so for $n \geq 2$, a multipole field forms a trap for low field seekers. Combinations of multipole fields can also produce useful field arrangements. A combination of a dipole ($n = 1$) field and a hexapole ($n = 3$) field, for example, produces a saddle point of electric field strength at $r = 0$. This is discussed in more detail in chapter 2.

A single V_n component in equation (3.8) can be expanded in a multipole series. If r and ϕ are defined such that $y = r\cos\phi + y_0$ and $z = r\sin\phi + z_0$, then $y - iz = r\exp(-i\phi) + (y_0 - iz_0)$. This can be substituted into equation (3.7) and the result expanded as a series.

$$\begin{aligned} V_n(y,z) &= \Re\left\{\tilde{A}_n \exp\left(-\frac{2\pi n(y-iz)}{\ell}\right)\right\} \\ &= \Re\left\{\tilde{A}_n \exp\left(-\frac{2\pi n(y_0-iz_0)}{\ell}\right) \exp\left(-\frac{2\pi n r \exp(-i\phi)}{\ell}\right)\right\} \\ &= \sum_{q=0}^{\infty} \frac{(-1)^q}{q!}\left(\frac{2\pi n}{\ell}\right)^q r^q \Re\left\{\tilde{A}_n \exp\left(-\frac{2\pi n(y_0-iz_0)}{\ell}\right)\exp(-iq\phi)\right\} \end{aligned} \tag{3.24}$$

By summing over all V_n, as in equation(3.8), V is found to be

$$\begin{aligned} V(y,z) = &\sum_{n=0}^{\infty} \Re\left\{\tilde{A}_n \exp\left(-\frac{2\pi n(y_0-iz_0)}{\ell}\right)\right\} + \\ &\sum_{q=1}^{\infty}\left(\frac{2\pi}{\ell}\right)^q q^{-1} r^q \Re\left\{\tilde{A}'_q \exp(-iq\phi)\right\} \end{aligned} \tag{3.25}$$

where

$$\tilde{A}'_q = \frac{(-1)^q}{(q-1)!} \sum_{n=0}^{\infty} \tilde{A}_n \exp\left(-\frac{2\pi n(y_0 - iz_0)}{\ell}\right) n^q \tag{3.26}$$

A potential consisting of a single multipole term can be created by solving the system of equations given by (3.26) such that only one $\tilde{A}'_q$ is non-zero.[3] An exact solution would require an infinite number of diverging $\tilde{A}_n$, so is only possible in practice to exclude unwanted $\tilde{A}'_q$ up to $q = q_0$. This requires q_0 $\tilde{A}_n$ components to be constrained. To produce a potential that is locally a multipole of order q_0, all $\tilde{A}'_q$ with $q < q_0$ must be suppressed, requiring control over q_0 $\tilde{A}_n$ coefficients.

3.4.1 Quadrupole Potentials

The simplest local quadrupole field can be created by eliminating the dipole field. If $(y_0, z_0) = (0, 0)$, $\tilde{A}'_1$ is given by

$$\tilde{A}'_1 = -(\tilde{A}_1 + 2\tilde{A}_2 + 3\tilde{A}_3 + \dots) = 0 \tag{3.27}$$

This can be solved non-trivially using two $\tilde{A}_n$ by choosing $\tilde{A}_{n_1} = -\tilde{A}'_2(n_2 - n_1)^{-1}n_1^{-1}$ and $\tilde{A}_{n_2} = \tilde{A}'_2(n_2 - n_1)^{-1}n_2^{-1}$ if all other $\tilde{A}_n$ are zero. The electric potential is then

$$\begin{aligned} V = -\Re\Bigg\{ \tilde{A}'_2(n_2 - n_1)^{-1}\Bigg(& n_1^{-1} \exp\left(\frac{2\pi i n_1 z}{\ell}\right) \exp\left(-\frac{2\pi n_1 y}{\ell}\right) - \\ & n_2^{-1} \exp\left(\frac{2\pi i n_2 z}{\ell}\right) \exp\left(-\frac{2\pi n_2 y}{\ell}\right)\Bigg)\Bigg\} \end{aligned} \tag{3.28}$$

While the resulting quadrupole electric field minimum is centered at $(y_0, z_0) = (0, 0)$, additional minima are formed when the condition

$$\frac{2\pi n_2 z}{\ell} - \frac{2\pi n_1 z}{\ell} = 2\pi m \tag{3.29}$$

is satisfied, where m is an integer. There are therefore a total of $|n_2 - n_1|$ evenly spaced minima in each period of the potential.

By choosing n_1 and n_2 to be widely separated, it is possible to improve the packing of minima, that is, to decrease the number of electrodes needed per minimum. If $n_1 = 1$ and $n_2 = 2$, one minimum is created per period, and four electrodes are needed to form the V_2 potential. If n_2 is increased to 3, two minima are formed per period, but only two additional electrodes are needed to produce the V_3 potential, yielding one minimum for every three electrodes. In general, if $n_1 = 1$, a minimum can be formed for every $2(1 - n_2^{-1})^{-1}$ electrodes. The limiting case as $n_2 \to \infty$, there is a minimum every two electrodes: this corresponds to a dipole field with a period of two electrodes combined with a rotating external field.

[3] Using this definition of $\tilde{A}'_q$, any pure multipole components $\tilde{A}'_q$ will produce an electric field at a characteristic length scale $r = r_0 = \ell/(2\pi)$ of $|\vec{E}| = |\tilde{A}'_q| r_0^{-1}$. If r_0 is a reasonable estimate of the size of the trap, then the maximum field produced with two different pure multipole terms $\tilde{A}'_{q_1}$ and $\tilde{A}'_{q_2}$ will be comparable if $|\tilde{A}'_{q_1}| = |\tilde{A}'_{q_2}|$.

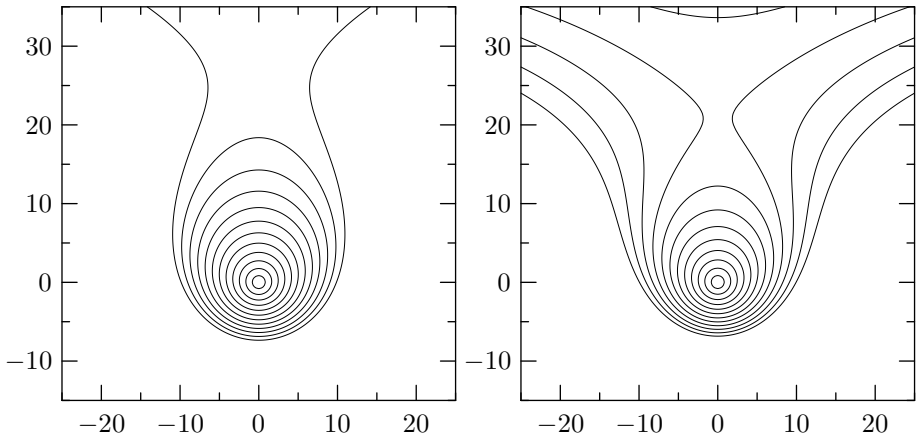

Figure 3.2: Two quadrupole potentials each formed with two A_n. On the left, $\tilde{A}_1 = 1$ and $\tilde{A}_2 = \frac{1}{2}$, while all other terms are zero. On the right, $\tilde{A}_1 = \frac{1}{2}$ and $\tilde{A}_3 = \frac{1}{6}$. Near the minima, both potentials have the same strength. While the configuration on the right results in one minimum for every three electrodes, in contrast to the case on the left for which there is one minimum for every four electrodes, the height of barrier is lower.

If exactly two $\tilde{A}_n$ are non-zero, an array of quadrupole minima will always be produced. A quadrupole minimum occurs when

$$\tilde{A}_{n_1} \exp\left(-\frac{2\pi n_1(y_0 - iz_0)}{\ell}\right) n_1 = \tilde{A}_{n_2} \exp\left(-\frac{2\pi n_2(y_0 - iz_0)}{\ell}\right) n_2 \tag{3.30}$$

By solving this equation for $y_0 - iz_0$, the position of this minimum can be found.

$$y_0 - iz_0 \;=\; \frac{\ell}{2\pi(n_2 - n_1)} \ln\left(\frac{\tilde{A}_{n_2} n_2}{\tilde{A}_{n_1} n_1}\right) \tag{3.31}$$

For any $\tilde{A}_{n_1}$ and $\tilde{A}_{n_2}$, the quadrupole minima will be found at a position (y_0, z_0), given in equation (3.31), assuming that all other A_n are zero.

A more exact quadrupole field can be created by excluding higher order terms. This requires more $\tilde{A}_n$ to be constrained and also requires the individual $\tilde{A}_n$ to have higher amplitudes. To eliminate the hexapole term, at least three $\tilde{A}_n$ must be constrained. Using $\tilde{A}_1$, $\tilde{A}_2$, and $\tilde{A}_3$ to form a quadrupole minimum at $(y_0, z_0) = (0, 0)$ results in the system of equations

$$\begin{pmatrix} 1 & 2 & 3 \\ 1 & 4 & 9 \\ 1 & 8 & 27 \end{pmatrix} \begin{pmatrix} \tilde{A}_1 \\ \tilde{A}_2 \\ \tilde{A}_3 \end{pmatrix} = \begin{pmatrix} -\tilde{A}'_1 \\ \tilde{A}'_2 \\ -2\tilde{A}'_3 \end{pmatrix} = \begin{pmatrix} 0 \\ \tilde{A} \\ 0 \end{pmatrix} \tag{3.32}$$

which has the solution $\tilde{A}_1 = -\frac{5}{2}\tilde{A}$, $\tilde{A}_2 = 2\tilde{A}$, and $\tilde{A}_3 = -\frac{1}{2}\tilde{A}$. In contrast, for the quadrupole potential described before using $n_1 = 1$ and $n_2 = 2$, the solution $\tilde{A}_1 = -\tilde{A}$ and $\tilde{A}_2 = \frac{1}{2}\tilde{A}$ will produce a quadrupole potential of the same strength, even with smaller $\tilde{A}_n$.

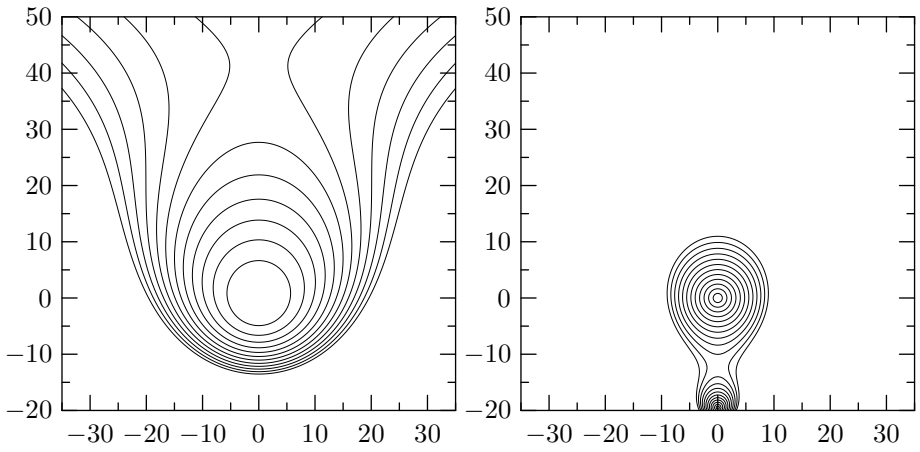

Figure 3.3: By controlling three $\tilde{A}_n$, it is possible to control three $\tilde{A}'_q$. On the left, a hexapole potential is made by eliminating the dipole and quadrupole terms. On the right, a more accurate quadrupole potential is produced by eliminating both the dipole and the hexapole terms.

3.4.2 Hexapole and Saddle-Point Potentials

By eliminating both the dipole and the quadrupole terms, it is possible to produce a hexapole potential. This requires constraining at least three $\tilde{A}_n$. Using $\tilde{A}_1$, $\tilde{A}_2$, and $\tilde{A}_3$ to form a hexapole minimum at $(y_0, z_0) = (0, 0)$, the system of equations is

$$\begin{pmatrix} 1 & 2 & 3 \\ 1 & 4 & 9 \\ 1 & 8 & 27 \end{pmatrix} \begin{pmatrix} A_1 \\ A_2 \\ A_3 \end{pmatrix} = \begin{pmatrix} -\tilde{A}'_1 \\ \tilde{A}'_2 \\ -2\tilde{A}'_3 \end{pmatrix} = \begin{pmatrix} 0 \\ 0 \\ -2\tilde{A} \end{pmatrix} \tag{3.33}$$

for which the solution is $\tilde{A}_1 = -\tilde{A}$, $\tilde{A}_2 = \tilde{A}$, and $\tilde{A}_3 = -\frac{1}{3}\tilde{A}$. The hexapole potential has the advantage that, for molecules with a linear Stark shift, the potential is harmonic, so the motion in the y direction is decoupled from the motion in the z direction.

Combining a hexapole potential with a dipole potential can create a saddle point in the electric field strength. This can be used to manipulate molecules in high field seeking states. A saddle point will focus molecules in one direction (along which the saddle point is a maximum) and defocus them in the perpendicular direction (where the field is a minimum). If the saddle point is reversed, such that the molecules are focused where they were previously defocused and vice versa, the net effect will be to focus the molecules in both directions. This reversal can be achieved by changing the sign of the hexapole while keeping the dipole the same.

The system of equations for this potential is

$$\begin{pmatrix} 1 & 2 & 3 \\ 1 & 4 & 9 \\ 1 & 8 & 27 \end{pmatrix} \begin{pmatrix} \tilde{A}_1 \\ \tilde{A}_2 \\ \tilde{A}_3 \end{pmatrix} = \begin{pmatrix} -\tilde{A}'_1 \\ \tilde{A}'_2 \\ -2\tilde{A}'_3 \end{pmatrix} = \begin{pmatrix} -\tilde{A} \\ 0 \\ \mp 2\tilde{A} \end{pmatrix} \tag{3.34}$$

For the case where $\tilde{A}'_3 = \tilde{A}'_1$, $\tilde{A}_1 = -4\tilde{A}$, $\tilde{A}_2 = \frac{5}{2}\tilde{A}$, and $\tilde{A}_3 = -\frac{2}{3}\tilde{A}$. When $\tilde{A}'_3 = -\tilde{A}'_1$, $\tilde{A}_1 = -2\tilde{A}$, $\tilde{A}_2 = \frac{1}{2}\tilde{A}$, and $\tilde{A}_3 = 0$.

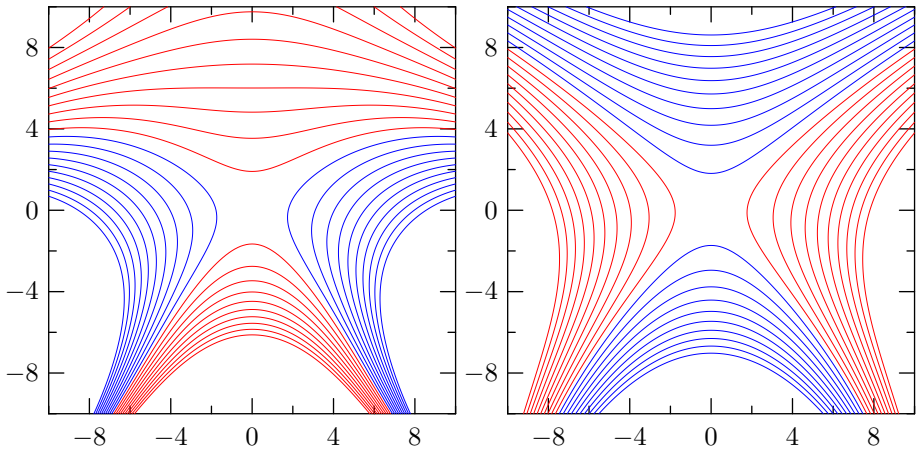

Figure 3.4: Two different configurations of a saddle point potential. Red contours describe fields higher than those at the saddle point and blue contours describe fields lower than those at the saddle point. By alternating rapidly between these two configurations, molecules in both high and low field seeking states could be confined.

3.4.3 Forming Multipole Fields with Real Electrodes

Until now, the multipole fields have been described using the assumption that all $\tilde{A}_n$ above a certain n are zero. With a set of M periodic electrodes, creating a non-zero $\tilde{A}_n$ will generally lead to a non-zero $\tilde{A}_{M-n}$, so this assumption may not be valid. However, it is possible to formulate the multipole components in terms of $\tilde{\mathcal{V}}_n$ instead of $\tilde{A}_n$ by combining equations (3.18) and (3.26).

$$\tilde{A}'_q = \frac{(-1)^q}{(q-1)!}\frac{M}{2}\sum_{n=0}^{\lfloor \frac{M}{2} \rfloor}\sum_{k=0}^{\infty}\left(\tilde{R}_q(kM+n)+\tilde{R}_q(kM+M-n)\right)\tilde{\mathcal{V}}_n \tag{3.35}$$

$$\tilde{R}_q(n) = \tilde{A}_n^{(0)} n^q \exp\left(-\frac{2\pi n(y_0 - iz_0)}{\ell}\right) \tag{3.36}$$

Using these equations, it is possible to write a linear relation between $\tilde{\mathcal{V}}_n$ and $\tilde{A}'_q$ for a given y_0 and z_0 if the $\tilde{A}_n^{(0)}$ are known. This relation will be given explicitly in the next section.

3.5 The Chip as Constructed

The design used to produce the potentials used in the experiments in this thesis consists of six independent electrodes per period. The electrodes are 10 micrometers wide, with a center-to-center spacing of 40 micrometers, giving a period length $\ell = 240$ μm. These electrodes are deposited on a glass substrate and are covered with layer of SU-8 photoresist. For calculation purposes, the glass and SU-8 are assumed to have a relative permittivity of $\epsilon_r = 4$, and the dielectric layer is assumed to extend 5 μm above the center of the electrodes. The electrodes themselves are assumed to have a thickness of 2 μm, and the height of their centers defines $y = 0$.

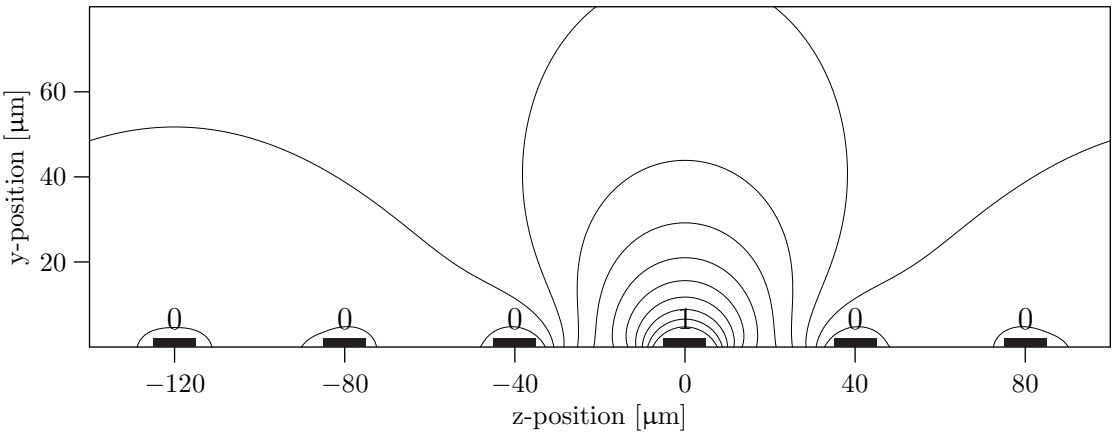

Figure 3.5: The electric potential produced by setting one set of electrodes to 1 volt and the rest to 0. By computing a Fourier transform along a line of constant y, it is possible to obtain the $\tilde{A}_n^{(0)}$ coefficients.

The fields are calculated numerically and then read out along the line $y_0 = 5\,\mu\text{m}$. This corresponds the top of the dielectric layer and is the bottom edge of the vacuum region above the electrodes. By calculating the Fourier transform along this line in z and scaling each Fourier component by $\exp\left(\frac{2\pi n y_0}{\ell}\right)$, the $\tilde{A}_n^{(0)}$ can be calculated. The Fourier transform is carried out with $z = 0$ defined by the center of an electrode from the 0th set, so the $\tilde{A}_n^{(0)}$ components are real.

$\tilde{A}_0^{(0)}$	$\tilde{A}_1^{(0)}$	$\tilde{A}_2^{(0)}$	$\tilde{A}_3^{(0)}$	$\tilde{A}_4^{(0)}$	$\tilde{A}_5^{(0)}$	$\tilde{A}_6^{(0)}$	$\tilde{A}_7^{(0)}$
0.16544	0.30334	0.25737	0.19929	0.13365	0.06544	0.00168	0.02273

Although there are many more $\tilde{A}_n^{(0)}$ components, their effect at positions greater than 20 μm from the surface is minimal. Eliminating these components reduces both the computation time and the noise found at short length scales in the numerical field calculations.

Using this electrode arrangement, it is possible to constrain the coefficients $\tilde{A}_0$, $\tilde{A}_1$, $\tilde{A}_2$, and $\tilde{A}_3$ in equation (3.8). As stated before, however, this will have side effects on higher-order coefficients, starting with $\tilde{A}_4$, which will gain intensity from a non-zero $\tilde{\mathcal{V}}_2$. On the other hand, by eliminating $\tilde{A}_2$, the first undesired coefficient will be $\tilde{A}_5$.

If $\tilde{\mathcal{V}}_1$ and $\tilde{\mathcal{V}}_3$ are the only non-zero $\tilde{\mathcal{V}}_n$, then a quadrupole minimum will be formed for every third electrode. If $\tilde{\mathcal{V}}_1$ and $\tilde{\mathcal{V}}_3$ are chosen such that $\tilde{\mathcal{V}}_3 = -\tilde{\mathcal{V}}_1 = \tilde{\mathcal{V}}$,[4] then $\tilde{A}_1 = -3\tilde{A}_1^{(0)}\tilde{\mathcal{V}}$ and $\tilde{A}_3 = 6\tilde{A}_3^{(0)}\tilde{\mathcal{V}}$. According to equation (3.31), this should produce a minima at a height $y_0 = \frac{60\,\mu\text{m}}{\pi} \ln\left|\frac{6\tilde{A}_3^{(0)}}{\tilde{A}_1^{(0)}}\right| \approx 26.2\ \mu\text{m}$ above the surface. In reality, due to the $\tilde{A}_5$ component, the minimum will be slightly lower, at 24.75 μm above the surface. If equation (3.35) is expanded around $(y_0, z_0) = (24.75\ \mu\text{m}, 0)$, the relationship between

[4]It should be noted that all experiments described in later chapters use this choice of $\tilde{\mathcal{V}}_n$. Other configurations described merely show what could be possible for future experiments.

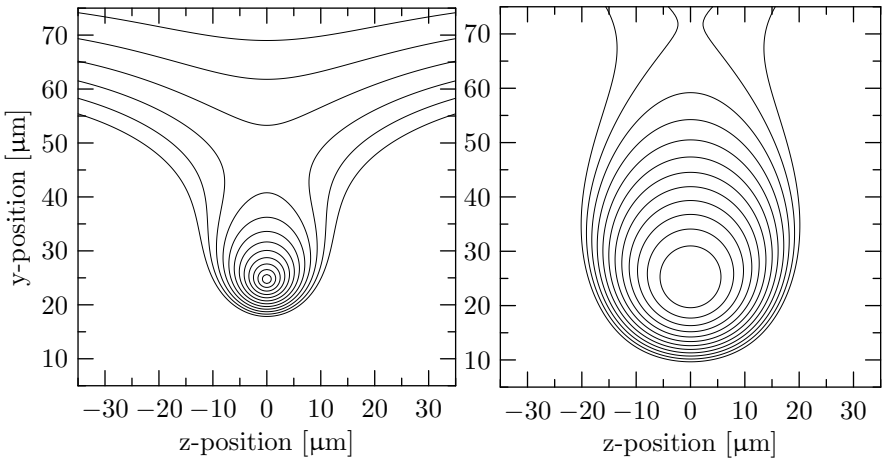

Figure 3.6: Electric field strength of potentials produced by real electrodes. Left: the quadrupole potential produced by setting $\tilde{\mathcal{V}}_3 = -\tilde{\mathcal{V}}_1$. Right: By solving equation (3.37) for $\tilde{A}'_1 = 0$, $\tilde{A}'_2 = 0$ and $\tilde{A}'_3 = \tilde{A}$, a hexapole potential can be produced, although it is much weaker than a quadrupole produced with similar applied potentials.

$\tilde{A}'_q$ and $\tilde{\mathcal{V}}_n$ can be found.

$$\begin{pmatrix} \tilde{A}'_1 \\ \tilde{A}'_2 \\ \tilde{A}'_3 \\ \tilde{A}'_4 \\ \tilde{A}'_5 \end{pmatrix} = \begin{pmatrix} -0.520 & -0.549 & -0.520 \\ 0.710 & 1.382 & 1.600 \\ -0.877 & -2.048 & -2.577 \\ 1.291 & 2.543 & 3.110 \\ -1.853 & -3.095 & -3.534 \end{pmatrix} \begin{pmatrix} \tilde{\mathcal{V}}_1 \\ \tilde{\mathcal{V}}_2 \\ \tilde{\mathcal{V}}_3 \end{pmatrix} \tag{3.37}$$

Note that, for $\tilde{\mathcal{V}}_3 = -\tilde{\mathcal{V}}_1$, $\tilde{A}'_1$ will be zero, leaving a quadrupole as the lowest order term.

In addition to a quadrupole field, it is also possible to make a hexapole potential by solving equation (3.37) for $\tilde{A}'_1 = 0$, $\tilde{A}'_2 = 0$, and $\tilde{A}'_3 = \tilde{A}$. The resulting electric fields are roughly a factor of ten weaker than those in a quadrupole potential for the same applied potentials.

3.6 Calculating Forces and Particle Trajectories in an Inhomogeneous Field

If the mechanical potential experienced by the molecules is only dependent on the magnitude - and not the direction - of an external electric field, the force experienced by the molecules in such a field can be calculated using the first and second partial derivatives of V with respect to y and z. Given a mechanical potential, $U(y, z)$, the force is defined by

$$\vec{F} = -\vec{\nabla} U \tag{3.38}$$

If U is only a function of electric field strength, i.e. $U(y, z) = U(|\vec{E}|(y, z))$, then equation (3.38) can be split into two factors by the chain rule

$$\vec{F} = -\frac{dU}{d|\vec{E}|}\vec{\nabla}|\vec{E}| = -\left(\frac{1}{|\vec{E}|}\frac{dU}{d|\vec{E}|}\right)\left(\frac{1}{2}\vec{\nabla}|\vec{E}|^2\right) \tag{3.39}$$

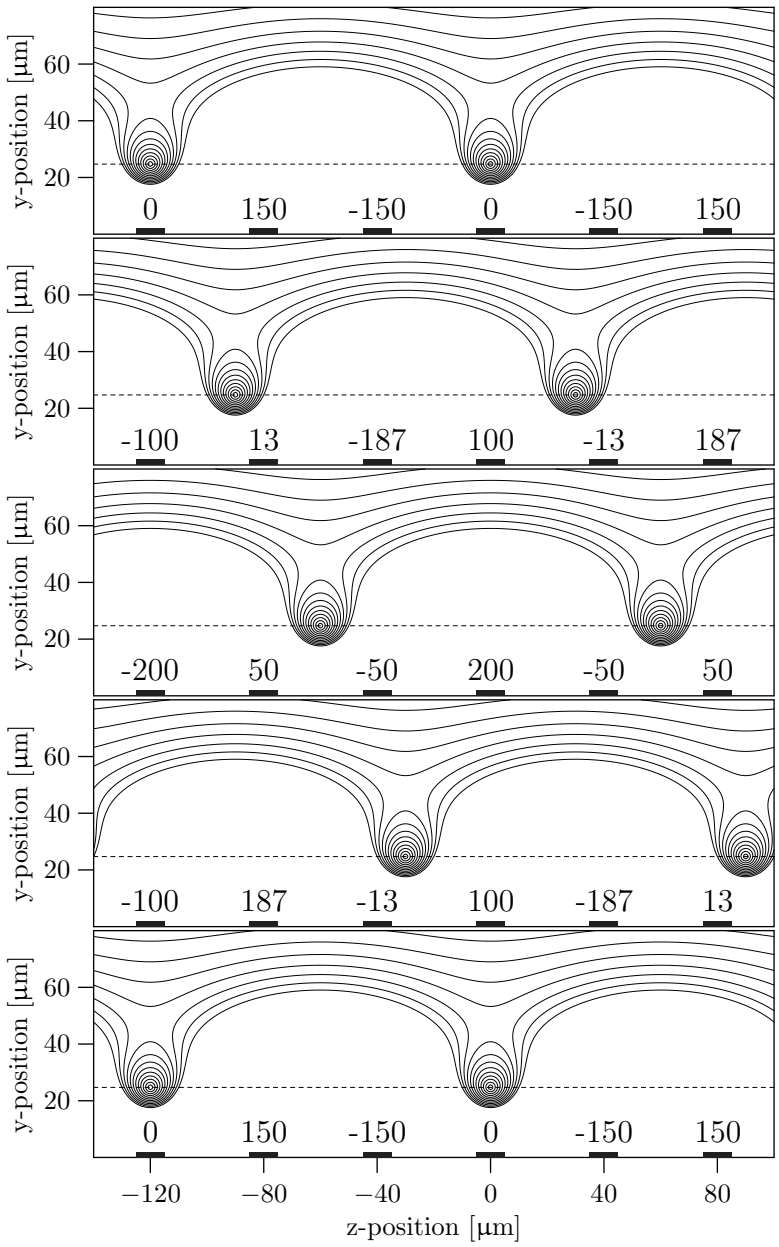

Figure 3.7: By applying the transformation in (3.22), the quadrupole potential shown in the left half of figure 3.6 can be translated over the chip in a continuous manner. The electrodes are shown schematically at the bottom of each frame along with the potential applied to each one to produce the electric field strength contours. Contour lines are separated by 500 $\frac{V}{cm}$.

Because $|\vec{E}|^2 = \left(\frac{\partial V}{\partial y}\right)^2 + \left(\frac{\partial V}{\partial z}\right)^2$, $\frac{1}{2}\vec{\nabla}|\vec{E}|^2$ can be expanded as

$$\left(\frac{1}{2}\vec{\nabla}|\vec{E}|^2\right) = \left(\frac{\partial^2 V}{\partial y^2}\frac{\partial V}{\partial y} + \frac{\partial^2 V}{\partial y\,\partial z}\frac{\partial V}{\partial z}\right)\hat{y} + \left(\frac{\partial^2 V}{\partial y\,\partial z}\frac{\partial V}{\partial y} + \frac{\partial^2 V}{\partial z^2}\frac{\partial V}{\partial z}\right)\hat{z} \tag{3.40}$$

Thus, the force $\vec{F}$ can be written (in matrix form) as

$$\begin{pmatrix} F_y \\ F_z \end{pmatrix} = -\left(\frac{1}{|\vec{E}|}\frac{dU}{d|\vec{E}|}\right)\begin{pmatrix} \frac{\partial^2 V}{\partial y^2} & \frac{\partial^2 V}{\partial y\,\partial z} \\ \frac{\partial^2 V}{\partial y\,\partial z} & -\frac{\partial^2 V}{\partial y^2} \end{pmatrix}\begin{pmatrix} \frac{\partial V}{\partial y} \\ \frac{\partial V}{\partial z} \end{pmatrix} \tag{3.41}$$

Using Laplace's equation (equation (2.5)), $\frac{\partial^2 V}{\partial z^2}$ has been replaced with $-\frac{\partial^2 V}{\partial y^2}$, reducing the number of partial derivatives that need to be computed to four. These four partial derivatives can easily be computed using the analytic form of the electric potential presented earlier in this chapter. Even in cases where an analytic form is not available, equation (3.41) can still be used by storing numerically computed partial derivatives in a table. The advantage of storing partial derivatives of the electric potential instead of force vectors is that the partial derivatives can be superimposed, so that contributions from multiple electrodes can be varied in a continuous manner.

The computation of the Stark potential, $U(|\vec{E}|)$, will be described in detail in the next chapter. However, there is a simple analytic form that is valid in many cases, given by

$$U(|\vec{E}|) = \pm\sqrt{\left(\frac{E_\Lambda}{2}\right)^2 + \left(\mu_{\text{eff}}|\vec{E}|\right)^2} \tag{3.42}$$

where E_Λ is the Λ-doublet splitting, μ_{eff} is the effective dipole moment (see equation (4.125)), and the plus-minus sign distinguishes between low field seeking states (positive) and high field seeking states (negative). The first factor in equation (3.41) can then be computed as

$$\frac{1}{|\vec{E}|}\frac{dU}{d|\vec{E}|} = \pm\frac{{\mu_{\text{eff}}}^2}{\sqrt{\left(\frac{E_\Lambda}{2}\right)^2 + \left(\mu_{\text{eff}}|\vec{E}|\right)^2}} \tag{3.43}$$

The computed force directly gives the acceleration on a molecule, and the acceleration can be incorporated into a system of four first-order ordinary differential equations for the position and velocity of the molecule as a function of time.

$$\frac{dv_y}{dt} = \frac{1}{m}F_y(y,z,t) \tag{3.44}$$

$$\frac{dv_z}{dt} = \frac{1}{m}F_z(y,z,t) \tag{3.45}$$

$$\frac{dy}{dt} = v_y \tag{3.46}$$

$$\frac{dz}{dt} = v_z \tag{3.47}$$

Here, v_y and v_z are the y- and z-components of the velocity and m is the mass of the molecule. Given an initial position and velocity, i.e. v_y, v_z, y, and z at any time $t = t_0$,

these equations can be solved unambiguously. In later chapters, this system of equations will be solved to find the trajectory of low field seeking molecules near moving quadrupole minima above the chip.

In general, this system of differential equations cannot be solved algebraically and must be solved instead numerically. This is carried out using algorithms that, given the system of differential equations and the values $v_y(t_0)$, $v_z(t_0)$, $y(t_0)$, and $z(t_0)$, approximate the values of $v_y(t_0 + \Delta t)$, $v_z(t_0 + \Delta t)$, $y(t_0 + \Delta t)$, and $z(t_0 + \Delta t)$ for a small value of Δt. The position and velocity of a particle at any time $t > t_0$ can be calculated by repeating the algorithm many times, each time advancing t by Δt. As long as the magnitude of the error at each step is of order Δt^2 or higher, the accuracy of the calculation can be improved by decreasing the size of Δt and increasing the number of steps.

The simplest stepping algorithm, the Euler method [75], assumes that the time derivatives are constant between t_0 and $t_0 + \Delta t$, so $v_y(t_0 + \Delta t)$, for example could be calculated as

$$v_y(t_0 + \Delta t) = v_y(t_0) + \left.\frac{dv_y}{dt}\right|_{t=t_0} \Delta t = v_y(t_0) + \frac{1}{m} F_y(y(t_0), z(t_0), t_0)\, \Delta t \tag{3.48}$$

The Euler method is not very efficient, though: since it has an error of order Δt^2, Δt must be very small and the number of steps very large to achieve a solution with reasonable accuracy. Another somewhat better class of stepping algorithms, the Runge-Kutta algorithms, evaluate the right sides of the differential equations in the system for several values of t, v_y, v_z, y, and z and combine the results of these evaluations to produce estimates of the state of the system at time $t_0 + \Delta t$ that have errors of order Δt^4 or higher. Due to the frequency with which Runge-Kutta algorithms are used, there are many software libraries available that implement the stepping algorithms and handle many of the subtle details, such as choosing the step size. The trajectory simulations shown in later chapters make use of an implementation from the GNU Scientific Library [76].

3.7 Conclusions

Using the equations presented here, a multipole field can be produced at $z = 0$ with M electrodes with control up to the $\frac{M}{2}$th order. For the chip that has been used in experiments thus far, multipole components up to the hexapole can be controlled. Regardless of what potential is created, its position can be shifted with high accuracy in z; the lowest order error caused by shifting the potential will occur in the term V_{M+1}. For most purposes, this is good enough. If higher accuracy is required, however, the multipole expansions can also be constructed at positions where $z \neq 0$. By calculating the $\tilde{\mathcal{V}}_n$ required to produce the desired multipole at each position, more accurate movement can be achieved.

The equations here assume that the electrodes are evenly spaced, symmetric, and identical, but this is also not strictly necessary. Due to perceived technical limitations, early designs of the chip required the electrodes to be placed in three separate levels, though this was fortunately not necessary. The consequence of breaking this symmetry is merely that the various $\tilde{\mathcal{V}}^{(m)}$, which are here computable by a shift in the z direction, must be individually calculated. For a given position, the multipole expansion produced by each electrode set individually can be calculated, using a slight modification of equation

(3.24), and the system of equations solved for the individual $\tilde{\mathcal{V}}^{(m)}$. While this is probably necessary for complicated, asymmetric electrode arrangements, much of the insight shown above would be lost.

In the end, even the most fundamental assumptions, such as two-dimensional structure and strict periodicity, may be mutable. Breaking either of these assumptions would likely lead to an explosion of complexity. If the electrodes can no longer be assumed to be periodic, the sum in equation (3.8) becomes an integral, and it is no longer possible to enumerate the coefficients. Similarly, by adding a third dimension x to the potentials, equation (3.8) becomes at the very least a two-dimensional sum, and at worst, includes an integral as well. Currently, these effects are neglected: while the electrodes are neither infinitely long (V does in fact vary in x), nor do the electrode sets repeat infinitely (the electrode sets are not strictly periodic), these effects only play a role near the edges of the electrode array. Nevertheless, in future designs where strong three-dimensional confinement becomes more important, it may be necessary to handle these effects quantitatively.

Chapter 4

Properties of $a^3\Pi$ Metastable CO

In its $X^1\Sigma^+$ ground state, carbon monoxide is relatively uninteresting for Stark manipulation. It has a closed-shell electronic structure given by

$$X^1\Sigma: \ (1s\,O)^2(1s\,C)^2(2s\,\sigma)^2(2s\,\sigma^*)^2(2p\,\pi)^4(2p\,\sigma)^2 \tag{4.1}$$

The dipole moments produced by these orbitals nearly cancel out, so the experimentally observed dipole moment is small (about 0.112 Debye) [77]. Furthermore, the first two states that can be mixed by an electric field are 3.8 cm^{-1} apart at zero field, and thus the Stark shift that results at any reasonable field is quadratic in its electric field strength dependence.

The $a^3\Pi$ state, in contrast, has many advantages over the ground state. Its electronic configuration is given by:

$$a^3\Pi: \ (1s\,O)^2(1s\,C)^2(2s\,\sigma)^2(2s\,\sigma^*)^2(2p\,\pi)^4(2p\,\sigma)(2p\,\pi^*) \tag{4.2}$$

The $2p\,\pi^*$ orbital has a significantly lower electron density around the carbon atom than the $2p\,\sigma$ orbital from which the electron was excited [78]. Because of this, the a state has a much larger body-fixed dipole moment, determined experimentally to be 1.37 Debye [79]. For reasons that will become clear shortly, each rotational level of a Π electronic state is split into two closely spaced sublevels which have opposite parity and can therefore mix in an electric field. For the state of ^{12}CO where $J = 1$, $M = 1$, and $\Omega = 1$, this splitting is $E_\Lambda = 394$MHz, and as a result, this state has a strong, linear Stark shift already at 1 $\frac{\text{kV}}{\text{cm}}$.

The $a^3\Pi$ state has the additional advantage that molecules in this state carry with them 6.0 eV of internal energy. When a molecule collides with the surface of a metal such as gold, this internal energy can be used to drive an electron from the metal, which can be directed toward an electron detector such as a microchannel plate (MCP), which amplifies the electron.

To understand the motions of this molecule in an electric field, it is necessary to understand its fine and, in the case of the ^{13}CO isotopologue, hyperfine structure. The process of calculating a quantum mechanical eigenenergy is conceptually fairly simple. First, an orthonormal basis set, i.e. a set of ϕ_n where $\langle\phi_i|\phi_j\rangle = \delta_{ij}$, is chosen that can describe the wavefunction of the system. Next, the Hamiltonian matrix elements H_{ij} based on this basis are calculated. These describe how basis vectors are coupled through

the Hamiltonian operator.

$$H_{ij} = \langle \phi_i | \hat{H} | \phi_j \rangle \tag{4.3}$$

Finally, this matrix is diagonalized. The resulting eigenvalues give the energies of the various energy eigenstates.

The basis set used to calculate the rotational energy level structure of $a^3\Pi$ CO, the Hund's case (a) basis set, will be described in section 4.1. In order to enable the calculation of the matrix elements, certain mathematical tools will be introduced, particularly the formalism of spherical tensor operators in section 4.3. The fine structure and hyperfine structure Hamiltonian contributions will be described and their resulting matrix elements calculated in section 4.4. Finally, the resulting level structure will be shown, including the effect of electric and magnetic fields, in section 4.5.

4.1 Hund's Case (a) Basis Set

In 1926, Friedrich Hund published an article describing four different possible hierarchies which describe the coupling of electronic motion and nuclear motion in various molecules [80]. The first of these, now known as Hund's coupling case (a), provides a good description of $^3\Pi$ molecules such as metastable CO at reasonable low J values.

Hund's case (a) assumes that the interaction between the nuclear rotation and the total electronic motion is small compared to the interaction between the electron orbital and spin angular momenta, and that both of these interactions are much smaller than the interaction of the electronic orbital angular momentum with the internuclear axis. Thus, it is possible to describe a case (a) molecule through a hierarchy of angular momentum contributions. The first of these is the projection of the electronic orbital angular momentum along the internuclear axis, which is labeled with the quantum number Λ. Because the orbital and spin angular momenta are also strongly coupled, the projection of the electronic spin along the internuclear axis is also well defined and is given the quantum number Σ. Unlike the electron orbital angular momentum, however, the electron spin angular momentum is not so strongly coupled to the internuclear axis that the total spin is mixed, so the total electron spin can be assigned a quantum number S. These two projection quantum numbers form a total electronic angular momentum projection given by $\Omega = \Lambda + \Sigma$. The electronic angular momentum finally couples to the nuclear rotation to form a total angular momentum given by J. Because J obeys the normal angular momentum commutation relations, it is also possible to quantize its projection along a space-fixed axis (generally assumed to be the $\hat{Z}$ axis). This quantum number is labeled M.

Of the six quantum numbers listed above (Λ, S, Σ, J, Ω, and M), only J and M are rigorously good, though even these quantum numbers can mix in an external electric or magnetic field. The total spin S is also treated as being a rigorously good quantum number, even though it is ever so slightly mixed. This small amount of mixing leads to the $a^3\Pi$ state of CO to have a finite lifetime, despite the fact that the transition to the ground state is spin forbidden. For all other purposes, however, this mixing can be ignored.

Basically, there is no molecule that fits Hund's case (a) exactly. Nevertheless, for many molecules, it is good enough that it can be used as a basis set to describe the

molecule's rotational and fine structure. The true energy eigenstates then contain a mixture of states with different quantum numbers Λ, Σ, and Ω. By calculating the couplings between the different basis states, expressing these couplings as a matrix, and diagonalizing the matrix, the energy eigenvalues can be calculated

If one or more of the nuclei in the molecule have a spin, Hund's case (a) must be extended. In nearly all case (a) molecules, the nuclear spin I is included by coupling it directly to all other components of the angular momentum J to form a total angular momentum F. This coupling scheme is usually referred to as a_β, and consists of the quantum numbers Λ, S, Σ, J, Ω, I, F, and M_F for a given vibronic state [81]. The quantum number J from case (a) is no longer rigorously good, and M ceases to be included in the basis. Instead, the total angular momentum F and its projection along the space-fixed $\hat{Z}$ axis, M_F, become the rigorously defined quantum numbers in the absence of a field. While I is not strictly a good quantum number, mixing between different I states is almost non-existent.

To summarize, in the absence of a nuclear spin, the wavefunction within a vibronic state effectively has three parts: an electron orbital angular momentum wavefunction, given by the quantum number Λ, an electron spin angular momentum wavefunction, given by the quantum numbers S and Σ, and a total angular momentum wavefunction, given by the quantum numbers J, Ω, and M. If a nuclear spin is included, M ceases to be used as a quantum number, and two new wavefunction parts appear: a total nuclear spin wavefunction, given by the quantum number I and a total angular momentum wavefunction including nuclear spin, given by the quantum numbers F and M_F.

4.2 Orientation of a CO Molecule

For certain energetic properties of a molecule, it is useful to know the orientation of the molecule with respect to an external coordinate system. The dipole moment of a polar molecule will be fixed with respect to the nuclei for diatomic molecules, so the orientation describes the angle between the dipole and the external electric field, and hence the energy due to this field. Certain symmetry properties, such as parity, are also connected to the orientation of the molecule, and so a state of a given parity will have a wavefunction of a particular form as a result. Even the end-over-end rotation of the molecule has a wavefunction that is a function of the orientation. Describing the orientation wavefunction can provide insight into some aspects of a molecule's spectroscopy without any specific knowledge of its internal structure.

4.2.1 Euler Angles

It is possible to uniquely describe an arbitrary rotation of two coordinate systems with respect to each other using three angles. This is useful for describing a rigid molecule, since it allows the characterization of some aspects of the system with respect to a set of fixed nuclei and other aspects with respect to the outside world. In this spirit, we define two coordinate systems: a space-fixed, given by (X, Y, Z), and a molecule-fixed, given by (x, y, z). Following the convention of Brown and Carrington [82], we define a transformation between these two systems. Assume that the two systems are initially

aligned, i.e. $X = x$, $Y = y$, and $Z = z$. The molecule-fixed coordinates are then transformed with three sequential rotations:

1. Rotation through an angle χ about the $\hat{Z}$ axis.
2. Rotation through an angle θ about the $\hat{Y}$ axis.
3. Rotation through an angle ϕ about the $\hat{Z}$ axis.

In matrix form, this can be written as

$$\begin{pmatrix} X \\ Y \\ Z \end{pmatrix} = \begin{pmatrix} \cos\phi & -\sin\phi & 0 \\ \sin\phi & \cos\phi & 0 \\ 0 & 0 & 1 \end{pmatrix} \begin{pmatrix} \cos\theta & 0 & \sin\theta \\ 0 & 1 & 0 \\ -\sin\theta & 0 & \cos\theta \end{pmatrix} \begin{pmatrix} \cos\chi & -\sin\chi & 0 \\ \sin\chi & \cos\chi & 0 \\ 0 & 0 & 1 \end{pmatrix} \begin{pmatrix} x \\ y \\ z \end{pmatrix} \tag{4.4}$$

From this equation, it becomes obvious that the inverse Euler angles to (ϕ, θ, χ) are $(-\chi, -\theta, -\phi)$. The full transformation matrix from space-fixed coordinates to molecule-fixed coordinates is then given by

$$\begin{pmatrix} x \\ y \\ z \end{pmatrix} = R \begin{pmatrix} X \\ Y \\ Z \end{pmatrix} \tag{4.5}$$

where

$$R = \begin{pmatrix} \cos\chi\cos\theta\cos\phi - \sin\chi\sin\phi & \cos\chi\cos\theta\sin\phi + \sin\chi\cos\phi & -\cos\chi\sin\theta \\ -\cos\chi\sin\phi - \sin\chi\cos\theta\cos\phi & \cos\chi\cos\phi - \sin\chi\cos\theta\sin\phi & \sin\chi\sin\theta \\ \sin\theta\cos\phi & \sin\theta\sin\phi & \cos\theta \end{pmatrix} \tag{4.6}$$

Generally, the angle θ is limited to the domain $[0, \pi]$. This restriction is made without loss of generality, since Euler angles (ϕ, θ, χ) with θ larger than π can be reduced to $(\phi + \pi, 2\pi - \theta, \chi + \pi)$.

4.2.2 The Quantum Mechanical Effect of Rotations

To extend the Euler angle description to quantum mechanical systems, it is useful to describe the effect of a rotation on an angular momentum wavevector $|JM\rangle$. A rotation cannot alter the total angular momentum, but it can alter the projection of the angular momentum on a space-fixed axis. Thus, after a rotation through the Euler angles $\omega = (\phi, \theta, \chi)$, the state $|J, M\rangle$ is projected onto a linear combination of several states $|JM'\rangle$ whose intensities are described by a matrix.

$$R(\omega)|JM\rangle = \sum_{M'} \mathfrak{D}^J_{M'M}(\omega)|JM'\rangle \tag{4.7}$$

The symbol $\mathfrak{D}^J_{M'M}$ is the rotation matrix or the Wigner $\mathfrak{D}$ matrix. Their exact form is described elsewhere [83]. For the purposes of this chapter, a couple of their symmetry properties are listed here.

$${\mathfrak{D}^J_{M'M}}^*(\omega) = (-1)^{M'-M}\mathfrak{D}^J_{-M'-M}(\omega) = \mathfrak{D}^J_{MM'}(-\omega) \tag{4.8}$$

Additionally, if a Wigner $\mathfrak{D}$ matrix is integrated over all Euler angles, the result is zero unless $J = M' = M = 0$.

$$\int \mathfrak{D}^J_{M'M}(\omega)\, d\omega = \int_0^{2\pi}\int_0^{\pi}\int_0^{2\pi} \mathfrak{D}^J_{M'M}(\phi,\theta,\chi)\, d\phi\, \sin\theta d\theta\, d\chi = 8\pi^2 \delta_{J0}\delta_{M'0}\delta_{M0} \tag{4.9}$$

In a system with two coupled angular momenta, rotating each angular momentum vector separately and rotating the total angular momentum vector are equivalent. The first takes the form

$$R(\omega)|J_1M_1J_2M_2\rangle = \sum_{M_1'M_2'} \mathfrak{D}^{J_1}_{M_1'M_1}(\omega)\mathfrak{D}^{J_2}_{M_2'M_2}(\omega)|J_1M_1'J_2M_2'\rangle \tag{4.10}$$

and the latter has the form

$$\begin{aligned} R(\omega)|J_1M_1J_2M_2\rangle =& \sum_{JM}\langle J_1M_1J_2M_2|JM\rangle R(\omega)|JM\rangle \\ =& \sum_{JMM'} \langle J_1M_1J_2M_2|JM\rangle \mathfrak{D}^J_{M'M}(\omega)|JM'\rangle \\ =& \sum_{JMM'M_1'M_2'} \langle J_1M_1J_2M_2|JM\rangle\langle J_1M_1'J_2M_2'|JM'\rangle \mathfrak{D}^J_{M'M}(\omega)|J_1M_1'J_2M_2'\rangle \end{aligned} \tag{4.11}$$

Because the angular momentum vectors in the last expression of each equation are the same, the coefficients must also be the same.

$$\mathfrak{D}^{J_1}_{M_1'M_1}(\omega)\mathfrak{D}^{J_2}_{M_2'M_2}(\omega) = \sum_{JMM'} \langle J_1M_1J_2M_2|JM\rangle\langle J_1M_1'J_2M_2'|JM'\rangle \mathfrak{D}^J_{M'M}(\omega) \tag{4.12}$$

This is commonly referred to as the Clebsch-Gordan series. Since the Clebsch-Gordan coefficients are directly related to 3-j symbols

$$\langle J_1M_1J_2M_2|JM\rangle = (-1)^{J_1-J_2+M}\sqrt{2J+1}\begin{pmatrix} J_1 & J_2 & J \\ M_1 & M_2 & -M \end{pmatrix} \tag{4.13}$$

the Clebsch-Gordan series can be rewritten in terms of 3-j symbols.

$$\begin{aligned} &\mathfrak{D}^{J_1}_{M_1'M_1}(\omega)\mathfrak{D}^{J_2}_{M_2'M_2}(\omega) \\ &= \sum_{JMM'} (-1)^{M-M'}(2J+1)\begin{pmatrix} J_1 & J_2 & J \\ M_1 & M_2 & -M \end{pmatrix}\begin{pmatrix} J_1 & J_2 & J \\ M_1' & M_2' & -M' \end{pmatrix}\mathfrak{D}^J_{M'M}(\omega) \end{aligned} \tag{4.14}$$

The Clebsch-Gordan series allows the computation of integrals over multiple $\mathfrak{D}$ matrices. For example, the integral over two $\mathfrak{D}$ matrices can be computed by combining equations (4.9) and (4.14).

$$\begin{aligned} \int \mathfrak{D}^{J_1}_{M_1'M_1}(\omega)\mathfrak{D}^{J_2}_{M_2'M_2}(\omega)\, d\omega =& 8\pi^2 \begin{pmatrix} J_1 & J_2 & 0 \\ M_1 & M_2 & 0 \end{pmatrix}\begin{pmatrix} J_1 & J_2 & 0 \\ M_1' & M_2' & 0 \end{pmatrix} \\ =& 8\pi^2 \delta_{J_1J_2}\delta_{M_1-M_2}\delta_{M_1'-M_2'}(2J_1+1)^{-1}(-1)^{M_1-M_1'} \end{aligned} \tag{4.15}$$

The integral over three $\mathfrak{D}$ matrices can be computed by combining this with another instance of the Clebsch-Gordan series.

$$\begin{aligned}
&\int \mathfrak{D}^{J_1}_{M_1' M_1}(\omega)\mathfrak{D}^{J_2}_{M_2' M_2}(\omega)\mathfrak{D}^{J_3}_{M_3' M_3}(\omega)\, d\omega \\
=&\sum_{J_{12}M_{12}M_{12}'} (-1)^{M_{12}-M_{12}'}(2J_{12}+1)\int \mathfrak{D}^{J_{12}}_{M_{12}' M_{12}}(\omega)\mathfrak{D}^{J_3}_{M_3' M_3}(\omega)\, d\omega \\
&\begin{pmatrix} J_1 & J_2 & J_{12} \\ M_1 & M_2 & -M_{12} \end{pmatrix}\begin{pmatrix} J_1 & J_2 & J_{12} \\ M_1' & M_2' & -M_{12}' \end{pmatrix} \\
=&8\pi^2 \begin{pmatrix} J_1 & J_2 & J_3 \\ M_1 & M_2 & M_3 \end{pmatrix}\begin{pmatrix} J_1 & J_2 & J_3 \\ M_1' & M_2' & M_3' \end{pmatrix}
\end{aligned} \tag{4.16}$$

4.2.3 Symmetric Top Wavefunction

A Hund's case (a) molecule behaves approximately like a rigid rotor. Although the moment of inertia along the internuclear axis in a linear molecule is not well defined, the angular momentum along this axis due to the electrons must still be accounted for when computing the molecule's orientation. As a result, the molecule's wavefunction cannot be described as a free rotor, for which the wavefunctions are spherical harmonics. Instead, the wavefunctions must be calculated using a symmetric top model. This model can then be used as a description of the orientation of the molecule.

The Hamiltonian of a rigid body is given in the molecular frame by

$$\hat{H} = AJ_z^2 + BJ_y^2 + CJ_x^2 \tag{4.17}$$

where J_x, J_y, and J_z are the angular momenta along the principal axes in the body-fixed system. The coefficients B and C, which are perpendicular to the internuclear axis, are equal. Since the coefficients are inversely proportional to the moment of inertia, the coefficient A, which relates to the moment of inertia of the electrons, is much larger than B or C. Thus the Hamiltonian of the symmetric top is

$$\hat{H} = B\hat{J}^2 + (A-B){J_z}^2 \tag{4.18}$$

Since the molecule-fixed angular momentum operator J_z commutes with the space-fixed angular momentum operators, we define a wavefunction $|JM\rangle$ which is an eigenstate of $\hat{J}^2$ (with an eigenvalue $J(J+1)$) and J_Z (with an eigenvalue M). In principle, a rotation of a coordinate system around a particular set of Euler angles is equivalent to rotating the function itself in the opposite direction. Thus, one can evaluate a function at a position given by the Euler angles (ϕ, θ, χ) by rotating the entire function through the Euler angles $(-\chi, -\theta, -\phi)$ and then evaluating the transformed function at $\theta = 0$. Combining this fact with the definition of the Wigner $\mathfrak{D}$ matrix, the wavefunction can be expressed as

$$\begin{aligned}
|JM\rangle(\phi,\theta,\chi) &= R(-\chi,-\theta,-\phi)\,|JM\rangle(0,0,0) \\
&= \sum_{\Omega'} |J\Omega'\rangle(0,0,0)\,\mathfrak{D}^J_{\Omega' M}(-\chi,-\theta,-\phi) \\
&= \sum_{\Omega'} |J\Omega'\rangle(0,0,0)\,{\mathfrak{D}^J_{M\Omega'}}^*(\phi,\theta,\chi)
\end{aligned} \tag{4.19}$$

Because J_z commutes with the Hamiltonian, the molecule has a well defined angular momentum along its internuclear axis, and $|JM\rangle$ is an eigenfunction of J_z with an eigenvalue defined to be Ω. Since the Wigner matrix is already an eigenfunction of J_z,

$$J_z \mathfrak{D}^{J}_{M\Omega'}{}^{*}(\phi,\theta,\chi) = \Omega' \mathfrak{D}^{J}_{M\Omega'}{}^{*}(\phi,\theta,\chi) \tag{4.20}$$

$|J\Omega'\rangle(0,0,0)$ is only non-zero when $\Omega' = \Omega$. Including the normalization, the symmetric top wavefunction is then

$$|J\Omega M\rangle = \sqrt{\frac{2J+1}{8\pi^2}} \mathfrak{D}^{J}_{M\Omega}{}^{*}(\omega) \tag{4.21}$$

Because A is not well-defined, since it can represent both the energy of electron orbital angular momentum and electron spin angular momentum, which both contribute to the total Ω, the eigenenergies given by this wavefunction are not particularly meaningful. The wavefunction itself, however, is independent of A, and thus accurately describes the orientation of the molecule.

4.2.4 The Inversion Operator

It is often informative to consider the effect of the inversion operator on a wavefunction. The inversion operator simply reverses the sign of all coordinates in the space-fixed coordinate system.

$$\hat{p} f(X,Y,Z) = f(-X,-Y,-Z) \tag{4.22}$$

The main utility of this operator comes from the fact that electromagnetic forces are invariant under inversion: a physical system and its mirror image are both valid from the point of view of electrodynamics, and will both have the same energy. As a result, the inversion operator will commute with any purely electromagnetic Hamiltonian, i.e. $[\hat{H},\hat{p}] = 0$. This implies that any eigenvector of the Hamiltonian must also be an eigenvector of $\hat{p}$.[1]

Applying $\hat{p}$ to a wavefunction twice returns it to its initial form, so $\hat{p}^2$ is the identity operator.

$$\hat{p}^2 f(X,Y,Z) = \hat{p} f(-X,-Y,-Z) = f(X,Y,Z) \tag{4.23}$$

As a result, the only possible eigenvalues for $\hat{p}$ are +1 and -1. The corresponding eigenvectors are described as having positive parity or negative parity, respectively.

Since the wavefunction of a symmetric top is described in terms of Euler angles, we first seek to find the effect of this operator on the Euler angles. That is, we seek transformations to the Euler angles which produce an inversion in the space-fixed frame while leaving the molecule-fixed frame unchanged. Of course this is not strictly possible, since Euler angles can only describe a rotation group, of which an inversion is not a member. It is possible, however, to fix the x and z coordinates and allow y to invert to account for the reflection. The operation of $\hat{p}$ on the internal coordinates is then defined as

$$\hat{p} f(x,y,z) = f(x,-y,z) \tag{4.24}$$

[1] An exception to this can occur when two or more states are degenerate: while certain linear combinations of these states will also be eigenvectors of $\hat{p}$, if there is more than one possible $\hat{p}$ eigenvalue among the degenerate states, then other linear combinations of these states will not be eigenvectors of $\hat{p}$.

To preserve the z coordinate when X, Y, and Z invert requires that $\theta \to \pi - \theta$ and $\phi \to \pi + \phi$, since the bottom row of the transformation matrix in (4.6) must be negated to compensate. Preserving the x component similarly requires $\chi \to \pi - \chi$ in order to negate the top row. The second row is then unchanged by the transformations to the Euler angles, implying $y \to -y$.

To summarize, the effect of the inversion operator on the Euler angles is

$$\hat{p}(\phi, \theta, \chi) = (\pi + \phi, \pi - \theta, \pi - \chi) \tag{4.25}$$

with the caveat that the reflection in the xz plane must be accounted for separately. This is the approach used in Brown and Carrington [84].

Next, we examine the effect of $\hat{p}$ on the Hund's case (a) wavefunction. Using the symmetric top wavefunction (equation (4.21)) as description of the external degrees of freedom of the molecule, we find

$$\hat{p}{\mathfrak{D}^J_{M\Omega}}^*(\phi, \theta, \chi) = {\mathfrak{D}^J_{M\Omega}}^*(\pi + \phi, \pi - \theta, \pi - \chi) = (-1)^{J+\Omega}{\mathfrak{D}^J_{M-\Omega}}^*(\phi, \theta, \chi) \tag{4.26}$$

Accounting for the reflection through the xz plane of the internal wavefunctions shows that $\Sigma \to -\Sigma$ and $\Lambda \to -\Lambda$, as expected, and contributes an additional factor of $(-1)^{\Lambda+S+\Sigma}$ [84]. The inverted wavefunction is then

$$\hat{p}|\Lambda S \Sigma J \Omega M\rangle = (-1)^{J-S}|{-\Lambda} S {-\Sigma} J {-\Omega} M\rangle \tag{4.27}$$

Therefore, a single Λ, Σ, or Ω state is not an eigenfunction of the inversion operator and might not be a stationary state. To assure that the wavefunctions have a definite parity, i.e. that they are eigenvectors of $\hat{p}$, the wavefunction should instead take the form

$$|\Lambda S \Sigma J \Omega M \pm\rangle = \frac{1}{\sqrt{2}}(|\Lambda S \Sigma J \Omega M\rangle \pm (-1)^{J-S}|{-\Lambda} S {-\Sigma} J {-\Omega} M\rangle) \tag{4.28}$$

In the definite parity form of the basis vector, Λ is assumed, by convention, to always be positive: if Λ were negative, the same vector would be obtained up to a phase factor. The quantum number Σ can still vary from $-S$ to S, and Ω will vary from $\Lambda - S$ to $\Lambda + S$. If $S \leq \Lambda$, Ω will always be non-negative.

There is then a direct relation between matrix elements calculated between states of a single Λ, Σ, and Ω and matrix elements calculated between states of definite parity.

$$\begin{aligned}\langle \Lambda S \Sigma J \Omega M \pm |\hat{H}|\Lambda S \Sigma' J' \Omega' M' \pm\rangle =& \frac{1}{2}\langle \Lambda S \Sigma J \Omega M|\hat{H}|\Lambda S \Sigma' J' \Omega' M'\rangle \\ &+\frac{1}{2}(-1)^{J-J'}\langle {-\Lambda} S {-\Sigma} J {-\Omega} M|\hat{H}|{-\Lambda} S {-\Sigma'} J' {-\Omega'} M'\rangle \\ &\pm\frac{1}{2}(-1)^{J-S}\langle {-\Lambda} S {-\Sigma} J {-\Omega} M|\hat{H}|\Lambda S \Sigma' J' \Omega' M'\rangle \\ &\pm\frac{1}{2}(-1)^{J'-S}\langle \Lambda S \Sigma J \Omega M|\hat{H}|{-\Lambda} S {-\Sigma'} J' {-\Omega'} M'\rangle\end{aligned} \tag{4.29}$$

For most contributions to the effective Hamiltonian described later in this chapter, only the first two terms are non-zero, and in these cases, the first two terms turn out to be

equal. As a result, these contributions can be calculated using only the first term. For another set of components of the effective Hamiltonian, the Λ-doubling Hamiltonian, only the last two terms are non-zero, and thus these components introduce an explicit dependence on parity into the Hamiltonian.

An energy eigenstate is only required to have definite parity if all contributions to the Hamiltonian are affected by the inversion operator. If some components are exempted, then states of opposite parity can mix. Such a situation can occur with an externally applied field. A complete inversion operator would reverse the positions of the charged electrodes that generate the external electric field, thus reversing the direction of the electric field, but because a "reasonable"[2] inversion operator does not affect macroscopic objects, the external electric field will only mix states of opposite parity, and parity will no longer commute with the full Hamiltonian. Magnetic fields, on the other hand, do not change direction under inversion of spatial coordinates anyway, since both the position and the velocity of the charges generating them are reversed, so a magnetic field will not mix states of opposite parity.

The matrix elements between two states of opposite parity are given by

$$\begin{aligned}\langle \Lambda S\Sigma J\Omega M \pm |\hat{H}|\Lambda S\Sigma' J'\Omega' M' \mp\rangle =& \frac{1}{2}\langle \Lambda S\Sigma J\Omega M|\hat{H}|\Lambda S\Sigma' J'\Omega' M'\rangle \\ & -\frac{1}{2}(-1)^{J-J'}\langle -\Lambda S-\Sigma J-\Omega M|\hat{H}|-\Lambda S-\Sigma' J'-\Omega' M'\rangle \\ & \pm\frac{1}{2}(-1)^{J-S}\langle -\Lambda S-\Sigma J-\Omega M|\hat{H}|\Lambda S\Sigma' J'\Omega' M'\rangle \\ & \mp\frac{1}{2}(-1)^{J'-S}\langle \Lambda S\Sigma J\Omega M|\hat{H}|-\Lambda S-\Sigma' J'-\Omega' M'\rangle\end{aligned} \tag{4.30}$$

In the case of an external electric field, only the first two terms are non-zero, and they are equal, so it is only necessary to calculate the first term.

4.3 Spherical Tensor Operators

To evaluate the elements of the Hamiltonian in the case (a) basis set, it is useful to express the operators in terms of spherical tensors. A spherical tensor operator is an object that transforms like a spherical harmonic under rotations. The transformation for a spherical harmonic is given by equation (4.7): a single rotation of the physical system produces a linear combination of projection eigenstates whose coefficients are given by the Wigner $\mathfrak{D}$ matrices. In order to rotate a spherical tensor operator, however, two rotations of the physical system are required: one rotates the system over a set of Euler angles $-\omega = (-\chi, -\theta, -\phi)$, which effectively rotates the operator through the Euler angles

[2] In principle, one could work with an inversion operator that reverses the position of the plates generating the electric field. The result would be a coherent superposition of the electrodes with two different orientations, and parity would again be conserved. Of course, this is not exactly reasonable: first, coherent superpositions of macroscopic objects do not generally occur, and secondly, to make the superposition would require the plates, or at least the charges in them, to tunnel to the opposite side, a process which likely has an extremely high barrier. It is much simpler and much more instructive to exclude the plates from the inversion operator.

$\omega = (\phi, \theta, \chi)$. After the operator is applied, the system is rotated back to its original position through the set of angles ω. If T^k_q is a spherical tensor operator, it should satisfy the equation

$$R(\omega)T^k_q R(-\omega) = \sum_{q'} \mathfrak{D}^k_{q'q}(\omega) T^k_{q'} \tag{4.31}$$

If T^k_q is transformed by an infinitesimal rotation given by $R = 1 - i\epsilon J_\xi$, where ξ is an arbitrary space-fixed axis and ϵ is an infinitesimally small angle, then equation (4.31) becomes

$$T^k_q - i\epsilon[J_\xi, T^k_q] + O(\epsilon^2) = \sum_{q'} \mathfrak{D}^k_{q'q}(R) T^k_{q'} \tag{4.32}$$

Note that $R^{-1} = 1 + i\epsilon J_\xi$. The rotation matrix, instead of being defined using Euler angles, is defined here by the infinitesimal rotation itself. Using the definition given in equation (4.7), $\mathfrak{D}^k_{q'q}(R)$ can be calculated by

$$\mathfrak{D}^k_{q'q}(R) = \langle kq'|R|kq\rangle = \delta_{q'q} - i\epsilon\langle kq'|J_\xi|kq\rangle \tag{4.33}$$

By substitution, it can be seen that a spherical tensor operator must satisfy the equation

$$[J_\xi, T^k_q] = \sum_{q'} \langle kq'|J_\xi|kq\rangle T^k_{q'} \tag{4.34}$$

Three special cases of this equation are seen when $J_\xi = J_Z$ and when $J_\xi = J_\pm = J_X \pm iJ_Y$.

$$[J_Z, T^k_q] = qT^k_q \tag{4.35}$$

$$[J_\pm, T^k_q] = \sqrt{k(k+1) - q(q \pm 1)}\, T^k_{q\pm1} \tag{4.36}$$

The angular momentum vectors J_X, J_Y, and J_Z can be written as spherical tensor operators. Because they span a space of dimension three, k must be 1, so that the dimensionality is the same; q then has three possibilities: -1, 0, and 1. Because T^1_0 must commute with J_Z, it can be concluded that $T^1_0(\hat{J})$ may be set equal to J_Z. Since $[J_\pm, J_Z] = \mp J_\pm$, $T^1_{\pm1}(\hat{J})$ must then be $\mp\frac{1}{\sqrt{2}}J_\pm$. Using this result, it is possible to write a dot product in terms of spherical tensors.

$$\hat{A}\cdot\hat{B} = A_X B_X + A_Y B_Y + A_Z B_Z = \frac{1}{2}(A_+ B_- + A_- B_+) + A_Z B_Z = \sum_q (-1)^q T^1_q(\hat{A}) T^1_{-q}(\hat{B}) \tag{4.37}$$

Because spherical tensor operators rotate in the same way as spherical harmonics, they also couple the same way, namely through Clebsch-Gordan coefficients.

$$\begin{aligned} T^k_q(T^{k_1}(\hat{A}), T^{k_2}(\hat{B})) =& \sum_{q_1 q_2} \langle k_1 q_1 k_2 q_2|kq\rangle T^{k_1}_{q_1}(\hat{A}) T^{k_2}_{q_2}(\hat{B}) \\ =& \sum_{q_1 q_2} (-1)^{k_1 - k_2 + q} \sqrt{2k+1} \begin{pmatrix} k_1 & k_2 & k \\ q_1 & q_2 & -q \end{pmatrix} T^{k_1}_{q_1}(\hat{A}) T^{k_2}_{q_2}(\hat{B}) \end{aligned} \tag{4.38}$$

This makes the dot product simply a special case of coupling two tensors where $k = q = 0$.

$$\begin{aligned} T^0_0(T^{k_1}(\hat{A}), T^{k_1}(\hat{B})) =& \sum_{q_1} \frac{(-1)^{k_1 - q_1}}{\sqrt{2k_1+1}} T^{k_1}_{q_1} T^{k_1}_{-q_1} \\ =& \frac{(-1)^{k_1}}{\sqrt{2k_1+1}} \hat{A}\cdot\hat{B} \end{aligned} \tag{4.39}$$

4.3.1 Wigner-Eckart Theorem

When evaluating matrix elements, if the bra, the ket, and the operator are all rotated through the same Euler angles, the result should be independent of the rotation. Using a spherical harmonic basis and a spherical tensor operator, this rotation can be expressed using Wigner rotation matrices

$$\begin{aligned}\langle JM|T^k_q|J'M'\rangle =&\langle JM|R^{-1}(\omega)R(\omega)T^k_q R^{-1}(\omega)R(\omega)|J'M'\rangle \\ =&\sum_{\mu,\mu',q'} \mathfrak{D}^J_{\mu M}(\omega)^* \mathfrak{D}^k_{q'q}(\omega)\mathfrak{D}^{J'}_{\mu' M'}(\omega)\langle J\mu|T^k_{q'}|J'\mu'\rangle\end{aligned} \tag{4.40}$$

The integral of the product of the three Wigner matrices over all Euler angles is given by

$$\frac{1}{8\pi^2}\int \mathfrak{D}^J_{\mu M}(\omega)^* \mathfrak{D}^k_{q'q}(\omega)\mathfrak{D}^{J'}_{\mu' M'}(\omega)\, d\omega = (-1)^{\mu-M}\begin{pmatrix} J & k & J' \\ -\mu & q' & \mu'\end{pmatrix}\begin{pmatrix} J & k & J' \\ -M & q & M'\end{pmatrix} \tag{4.41}$$

By integrating the first and last part equation (4.40) over the Euler angles and dividing by $8\pi^2$, we find

$$\langle JM|T^k_q|J'M'\rangle = (-1)^{J-M}\begin{pmatrix} J & k & J' \\ -M & q & M'\end{pmatrix}\langle J||T^k||J'\rangle \tag{4.42}$$

where

$$\langle J||T^k||J'\rangle = \sum_{\mu,\mu',q'}(-1)^{J-\mu}\begin{pmatrix} J & k & J' \\ -\mu & q' & \mu'\end{pmatrix}\langle J\mu|T^k_{q'}|J'\mu'\rangle \tag{4.43}$$

Thus, any matrix element of a spherical tensor operator can be reduced to the product of a factor that is only dependent on J, J' and k, and a 3-j symbol that contains the entire dependence on M, M' and q.

Calculation of the Reduced Matrix Element

While it is in principle possible to calculate $\langle J||T^k||J'\rangle$ by directly evaluating equation (4.43), in practice, it is much easier to evaluate a specific case of $\langle JM|T^k_q|J'M'\rangle$ and then solve equation (4.42) for $\langle J||T^k||J'\rangle$.

To calculate the reduced matrix element $\langle J||T^1(\hat{J})||J'\rangle$, for example, we first calculate $\langle JM|T^1_0(\hat{J})|J'M'\rangle$

$$\begin{aligned}\langle JM|T^1_0(\hat{J})|J'M'\rangle =&\langle JM|J_Z|J'M'\rangle = \delta_{JJ'}\delta_{MM'}M \\ =&(-1)^{J-M}\begin{pmatrix} J & 1 & J' \\ -M & 0 & M'\end{pmatrix}\langle J||T^1(\hat{J})||J'\rangle\end{aligned} \tag{4.44}$$

By solving this equation for $\langle J||T^1(\hat{J})||J'\rangle$, we find that

$$\langle J||T^1(\hat{J})||J'\rangle = \sqrt{J(J+1)(2J+1)}\delta_{JJ'} \tag{4.45}$$

Equation (4.45) can be generalized to include reduced matrix elements for higher order tensors that consist of only one angular momentum coupled together multiple times. We start by noting that, for a spherical tensor $T^k_k(\hat{J},\ldots,\hat{J})$, $T^{k+1}_{k+1}(\hat{J},\ldots,\hat{J})$ is given by

$$T^{k+1}_{k+1}(\hat{J},\ldots,\hat{J}) = T^k_k(\hat{J},\ldots,\hat{J})T^1_1(\hat{J}) \tag{4.46}$$

The matrix elements for $T^{k+1}_{k+1}(\hat{J},\ldots,\hat{J})$ can be either computed directly or can be computed as a product of the matrix elements of the two factors on the right hand side of the equation.

$$\langle JM|T^{k+1}_{k+1}(\hat{J},\ldots,\hat{J})|J'M'\rangle = \sum_{J''M''}\langle JM|T^{k}_{k}(\hat{J},\ldots,\hat{J})|J''M''\rangle\langle J''M''|T^{1}_{1}(\hat{J})|J'M'\rangle \quad (4.47)$$

From the Wigner-Eckart theorem, this equation is only non-zero when $M' = M-(k+1)$ and $M'' = M-k$. From equation (4.45), $J'' = J'$. Equation (4.47) thus simplifies to

$$\begin{aligned}
&(-1)^{J-M}\begin{pmatrix} J & k+1 & J' \\ -M & k+1 & M-(k+1)\end{pmatrix}\langle J||T^{k+1}(\hat{J},\ldots,\hat{J})||J'\rangle \\
=&(-1)^{J-M}\begin{pmatrix} J & k & J' \\ -M & k & M-k\end{pmatrix}(-1)^{J'-(M-k)}\begin{pmatrix} J & 1 & J' \\ -(M-k) & 1 & M-(k+1)\end{pmatrix} \\
&\langle J||T^{k}(\hat{J},\ldots,\hat{J})||J'\rangle\langle J'||T^{1}(\hat{J})||J'\rangle
\end{aligned} \quad (4.48)$$

It has been assumed thus far that, although the reduced matrix element of $T^1(\hat{J})$ only connects states of the same J, $T^k(\hat{J},\ldots,\hat{J})$ could in principle connect different J values. However, an inductive argument shows that this is not the case: if $\langle J||T^k(\hat{J},\ldots,\hat{J})||J'\rangle$ is only non-zero when $J = J'$, it follows from equation (4.48) that $\langle J||T^{k+1}(\hat{J},\ldots,\hat{J})||J'\rangle$ is also only non-zero when $J = J'$. Since this condition has been shown previous to be true for $k = 1$, it must also be true for all $k \geq 1$.

Using equation (4.45), equation (4.48) can be further reduced to

$$\langle J||T^{k+1}(\hat{J},\ldots,\hat{J})||J\rangle = \frac{1}{2}\sqrt{\frac{(2J-k)(2J+k+2)(k+1)}{(2k+1)}}\langle J||T^{k}(\hat{J},\ldots,\hat{J})||J\rangle \quad (4.49)$$

Using this recursive formula and equation (4.45), it is possible to write a general formula for $\langle J||T^k(\hat{J},\ldots,\hat{J})||J'\rangle$.

$$\langle J||T^{k}(\hat{J},\ldots,\hat{J})||J'\rangle = k!\sqrt{\frac{(2J+k+1)!}{(2J-k)!(2k)!2^k}}\delta_{JJ'} \quad (4.50)$$

It should be noted that, although equation (4.50) was only proven for $k \geq 1$, it also produces the correct reduced matrix element for $T^0 = 1$. This trivial reduced matrix element is $\langle J||T^0||J'\rangle = \sqrt{2J+1}\delta_{JJ'}$.

One final commonly used spherical tensor is the complex conjugate of the Wigner matrix, $\mathfrak{D}^{k\ *}_{pq}(\omega)$, where p is used as the lower index. The matrix element of $\mathfrak{D}^{k\ *}_{pq}(\omega)$ evaluated in a symmetric top basis (equation (4.21)) is given by an integral over three $\mathfrak{D}$ matrices.

$$\begin{aligned}
&\langle J\Omega M|\mathfrak{D}^{k\ *}_{pq}(\omega)|J'\Omega'M'\rangle \\
=&\frac{\sqrt{(2J+1)(2J'+1)}}{8\pi^2}\int \mathfrak{D}^{J}_{M\Omega}(\omega)\mathfrak{D}^{k\ *}_{pq}(\omega)\mathfrak{D}^{J'\ *}_{M'\Omega'}(\omega)\,d\omega \\
=&(-1)^{M-\Omega}\frac{\sqrt{(2J+1)(2J'+1)}}{8\pi^2}\left(\int \mathfrak{D}^{J}_{-M-\Omega}(\omega)\mathfrak{D}^{k}_{pq}(\omega)\mathfrak{D}^{J'}_{M'\Omega'}(\omega)\,d\omega\right)^* \\
=&(-1)^{M-\Omega}\sqrt{(2J+1)(2J'+1)}\begin{pmatrix} J & k & J' \\ -M & p & M'\end{pmatrix}\begin{pmatrix} J & k & J' \\ -\Omega & q & \Omega'\end{pmatrix}
\end{aligned} \quad (4.51)$$

Thus it is possible to write a reduced matrix element for $\mathfrak{D}^{k\ *}_{pq}(\omega)$.

$$\langle J\Omega||\mathfrak{D}^{k\ *}_{.q}(\omega)||J'\Omega'\rangle = (-1)^{J-\Omega}\begin{pmatrix} J & k & J' \\ -\Omega & q & \Omega' \end{pmatrix}\sqrt{(2J+1)(2J'+1)} \tag{4.52}$$

The fact that it is possible to write a reduced matrix element for $\mathfrak{D}^{k\ *}_{pq}(\omega)$ shows that it is a spherical tensor operator with an index p and q fixed. In equation (4.52), the symbol $\mathfrak{D}^{k\ *}_{.q}(\omega)$ represents the general form of this tensor. This tensor can also be used in other contexts, such as being incorporated into a scalar product.

4.3.2 Evaluating Spherical Tensor Operators in Molecule-Fixed Coordinates

Normally, it is acceptable to evaluate a spherical tensor in any coordinate system, including molecule-fixed coordinates. The exception to this is when the coordinate system itself is a function of the integration variable, which occurs when integrating over the wavefunction that represents the orientation of the molecule. Several solutions have been devised to deal with this problem, but the safest is to simply transform the offending spherical tensor into a space-fixed coordinate system and evaluate it there [85]. In a Hund's case (a) basis set, the total angular momentum $\hat{J}$ depends on the orientation of the molecule. The spherical tensor operators in the molecule-fixed coordinates, $T^k_q(\hat{J},\ldots,\hat{J})$, must therefore be rewritten in terms of space fixed spherical tensor operators $T^k_p(\hat{J},\ldots,\hat{J})$ in order evaluate them in this basis. Note that in the remainder of this chapter, the index p refers to space-fixed coordinates, while the index q refers to molecule-fixed coordinates, following the notation used by Brown and Carrington [86].

The transformation from molecule-fixed coordinates to space-fixed coordinates is given by

$$T^k_q(\hat{J},\ldots,\hat{J}) = \sum_p \mathfrak{D}^k_{pq}(\omega)T^k_p(\hat{J},\ldots,\hat{J}) \tag{4.53}$$

To evaluate $\mathfrak{D}^k_{pq}(\omega)$ and $T^k_p(\hat{J},\ldots,\hat{J})$ separately, we insert a complete projection operator between the two factors

$$\begin{aligned} &\langle J\Omega M|T^k_q(\hat{J},\ldots,\hat{J})|J'\Omega'M'\rangle \\ =&\sum_p \langle J\Omega M|T^k_p(\hat{J},\ldots,\hat{J})\mathfrak{D}^k_{pq}(\omega)|J'\Omega'M'\rangle \\ =&\sum_{p,J'',\Omega'',M''} \langle J\Omega M|T^k_p(\hat{J},\ldots,\hat{J})|J''\Omega''M''\rangle\langle J''\Omega''M''|\mathfrak{D}^k_{pq}(\omega)|J'\Omega'M'\rangle \end{aligned} \tag{4.54}$$

The first factor can only be non-zero when $J'' = J$, $\Omega'' = \Omega$, and $M'' = M - p$.

$$\sum_p \langle J\Omega M|T_p^k(\hat{J},\ldots,\hat{J})\mathfrak{D}_{pq}^k(\omega)|J'\Omega'M'\rangle =$$
$$\sum_p \langle J\Omega M|T_p^k(\hat{J},\ldots,\hat{J})|J\Omega M-p\rangle\langle J\Omega M-p|(-1)^{p-q}\mathfrak{D}^k_{-p-q}{}^*(\omega)|J'\Omega'M'\rangle =$$
$$\sum_p (-1)^{J-M}\begin{pmatrix} J & k & J \\ -M & p & M-p\end{pmatrix}\langle J||T^k(\hat{J},\ldots,\hat{J})||J\rangle$$
$$(-1)^{J-M+q}\begin{pmatrix} J & k & J' \\ -(M-p) & -p & M'\end{pmatrix}(-1)^{J-\Omega}\begin{pmatrix} J & k & J' \\ -\Omega & -q & \Omega'\end{pmatrix}\sqrt{(2J+1)(2J'+1)} \tag{4.55}$$

Using the orthogonality relation

$$(2J+1)\sum_p \begin{pmatrix} J & k & J \\ -M & p & M-p\end{pmatrix}\begin{pmatrix} J & k & J' \\ -(M-p) & -p & M'\end{pmatrix} = \delta_{JJ'}\delta_{MM'} \tag{4.56}$$

this can be reduced to

$$\langle J\Omega M|T_q^k(\hat{J},\ldots,\hat{J})|J\Omega' M\rangle = (-1)^{J-\Omega+q}\begin{pmatrix} J & k & J \\ -\Omega & -q & \Omega'\end{pmatrix}\langle J||T^k(\hat{J},\ldots,\hat{J})||J\rangle \tag{4.57}$$

4.3.3 Tensors Acting on Individual Parts of a Coupled Angular Momentum

Often, matrix elements are calculated in a basis set that consists of coupled angular momentum vectors, but the Hamiltonian is defined in terms of each of the components separately. In other words, the matrix elements have the form $\langle J_1J_2JM|T_p^k(T^{k_1},T^{k_2})|J_1'J_2'J'M'\rangle$, where T^{k_1} only acts on the first part of the angular momentum (J_1 and J_1'), T^{k_2} only acts on the second part (J_2 and J_2'), and the two angular momenta couple to form a total angular momentum J with a projection M. To calculate this element, the coupled basis vectors and the coupled spherical tensor operators must first be decoupled as is shown in equations (4.13) and (4.38).

$$\langle J_1J_2JM|T_p^k(T^{k_1},T^{k_2})|J_1'J_2'J'M'\rangle =$$
$$\sum_{M_1M_2M_1'M_2'p_1p_2} (-1)^{J_1-J_2+M}(-1)^{J_1'-J_2'+M'}(-1)^{k_1-k_2+p}\sqrt{(2J+1)(2J'+1)(2k+1)}$$
$$\begin{pmatrix} J_1 & J_2 & J \\ M_1 & M_2 & -M\end{pmatrix}\begin{pmatrix} J_1' & J_2' & J' \\ M_1' & M_2' & -M'\end{pmatrix}\begin{pmatrix} k_1 & k_2 & k \\ p_1 & p_2 & -p\end{pmatrix} \tag{4.58}$$
$$(-1)^{J_1-M_1}\begin{pmatrix} J_1 & k_1 & J_1' \\ -M_1 & p_1 & M_1'\end{pmatrix}\langle J_1||T^{k_1}||J_1'\rangle$$
$$(-1)^{J_2-M_2}\begin{pmatrix} J_2 & k_2 & J_2' \\ -M_2 & p_2 & M_2'\end{pmatrix}\langle J_2||T^{k_2}||J_2'\rangle$$

By permuting and inverting the bottom row of various 3-j symbols, this can be rewritten as

$$\begin{aligned}&\langle J_1 J_2 JM|T^k_p(T^{k_1},T^{k_2})|J_1' J_2' J' M'\rangle = \\ &(-1)^{J'+J+k}(-1)^{J-M}\sqrt{(2J+1)(2J'+1)(2k+1)}\langle J_1||T^{k_1}||J_1'\rangle\langle J_2||T^{k_2}||J_2'\rangle \\ &\sum_{M_1 M_2 M_1' M_2' p_1 p_2}(-1)^{J_1+J_2+M}(-1)^{J'+M'}(-1)^{k_1+k_2-p}\begin{pmatrix}J_1 & J & J_2\\ -M_1 & M & -M_2\end{pmatrix}\begin{pmatrix}J_2 & k_2 & J_2'\\ M_2 & -p_2 & -M_2'\end{pmatrix} \\ &\qquad\begin{pmatrix}J_2' & J' & J_1'\\ M_2' & -M' & M_1'\end{pmatrix}\begin{pmatrix}J_1' & J_1 & k_1\\ -M_1' & M_1 & -p_1\end{pmatrix}\begin{pmatrix}k_1 & k & k_2\\ p_1 & -p & p_2\end{pmatrix}\end{aligned} \tag{4.59}$$

This sum over five 3-j symbols and phase factors on the last two lines can be reduced to the product of a 3-j symbol and a 9-j symbol [87].

$$\begin{aligned}&\langle J_1 J_2 JM|T^k_p(T^{k_1},T^{k_2})|J_1' J_2' J' M'\rangle \\ =&(-1)^{J'+J+k}(-1)^{J-M}\sqrt{(2J+1)(2J'+1)(2k+1)} \\ &\langle J_1||T^{k_1}||J_1'\rangle\langle J_2||T^{k_2}||J_2'\rangle\begin{pmatrix}J & J' & k\\ -M & M' & p\end{pmatrix}\begin{Bmatrix}J & J' & k\\ J_1 & J_1' & k_1\\ J_2 & J_2' & k_2\end{Bmatrix} \\ =&(-1)^{J-M}\sqrt{(2J+1)(2J'+1)(2k+1)} \\ &\langle J_1||T^{k_1}||J_1'\rangle\langle J_2||T^{k_2}||J_2'\rangle\begin{pmatrix}J & k & J'\\ -M & p & M'\end{pmatrix}\begin{Bmatrix}J & J' & k\\ J_1 & J_1' & k_1\\ J_2 & J_2' & k_2\end{Bmatrix}\end{aligned} \tag{4.60}$$

Interestingly, $\langle J_1 J_2 JM|T^k_p(T^{k_1},T^{k_2})|J_1' J_2' J' M'\rangle$ in terms of the reduced matrix element in the coupled basis set has a similar form.

$$\begin{aligned}&\langle J_1 J_2 JM|T^k_p(T^{k_1},T^{k_2})|J_1' J_2' J' M'\rangle \\ =&(-1)^{J-M}\begin{pmatrix}J & k & J'\\ -M & p & M'\end{pmatrix}\langle J_1 J_2 J||T^k(T^{k_1},T^{k_2})||J_1' J_2' J'\rangle\end{aligned} \tag{4.61}$$

Therefore, it is possible to write the reduced matrix element in the coupled basis set in terms of the reduced matrix element in the uncoupled basis set.

$$\begin{aligned}&\langle J_1 J_2 J||T^k(T^{k_1},T^{k_2})||J_1' J_2' J'\rangle = \\ &\qquad\sqrt{(2J+1)(2J'+1)(2k+1)}\langle J_1||T^{k_1}||J_1'\rangle\langle J_2||T^{k_2}||J_2'\rangle\begin{Bmatrix}J & J' & k\\ J_1 & J_1' & k_1\\ J_2 & J_2' & k_2\end{Bmatrix}\end{aligned} \tag{4.62}$$

There are a couple of recurring cases to which this equation can be applied in a simplified form. One is the case of a scalar product between two tensors acting on

different components of the coupled angular momentum.

$$\begin{aligned}\langle J_1 J_2 J M|T^k(\hat{A}_1)\cdot T^k(\hat{A}_2)|J_1' J_2' J' M'\rangle =&(-1)^k\frac{\sqrt{2k+1}}{\sqrt{2J+1}}\delta_{JJ'}\delta_{MM'}\\ &\langle J_1 J_2 J||T^0(T^k(\hat{A}_1),T^k(\hat{A}_2))||J_1' J_2' J\rangle\\ =&(-1)^k\sqrt{(2k+1)(2J+1)}\delta_{JJ'}\delta_{MM'}\\ &\langle J_1||T^k(\hat{A}_1)||J_1'\rangle\langle J_2||T^k(\hat{A}_2)||J_2'\rangle\begin{Bmatrix}J_1 & J_1' & k\\ J_2 & J_2' & k\\ J & J' & 0\end{Bmatrix}\\ =&(-1)^{J_1'+J_2+J}\delta_{JJ'}\delta_{MM'}\\ &\langle J_1||T^k(\hat{A}_1)||J_1'\rangle\langle J_2||T^k(\hat{A}_2)||J_2'\rangle\begin{Bmatrix}J_1 & J_1' & k\\ J_2' & J_2 & J\end{Bmatrix}\end{aligned} \tag{4.63}$$

Another frequent example is the case where the tensor only applies to one of the two angular momentum components.

$$\begin{aligned}\langle J_1 J_2 J||T^k(\hat{A}_1)||J_1' J_2' J'\rangle =&\sqrt{(2J+1)(2J'+1)(2k+1)}\\ &\langle J_1||T^k(\hat{A}_1)||J_1'\rangle\langle J_2||1||J_2'\rangle\begin{Bmatrix}J & J' & k\\ J_1 & J_1' & k\\ J_2 & J_2' & 0\end{Bmatrix}\\ =&(-1)^{J_1+J_2+J'+k}\delta_{J_2 J_2'}\sqrt{(2J+1)(2J'+1)}\\ &\langle J_1||T^k(\hat{A}_1)||J_1'\rangle\begin{Bmatrix}J & J' & k\\ J_1' & J_1 & J_2\end{Bmatrix}\end{aligned} \tag{4.64}$$

A similar relation exists for spherical tensors that only depend on the second component of the coupled angular momentum, and differs from this one only in a phase factor.

4.4 Fine Structure of $a^3\Pi$, $v = 0$ CO

It was stated previously that calculating a quantum mechanical eigenenergy consists of three steps: a basis set is chosen that can represent the wavefunction of the system, the Hamiltonian matrix elements H_{ij} are calculated, and the resulting matrix is diagonalized, yielding eigenenergies and energy eigenstates. In general, however, each energy eigenstate is a linear combination of an infinite number of basis vectors, and thus the matrix H is infinite. Choosing a reasonable basis set can minimize these couplings. After that, the remaining couplings can be handled in such a way that they remain within a single vibronic state. One way to do this is to follow the effective Hamiltonian framework described in Brown and Carrington [88]. Effective Hamiltonian theory is a method of eliminating the interactions which mix vibronic states by replacing them with effective interactions which operate within a single vibronic state. Formally, this is described through two projection operators: $\hat{P}$, which projects a wavefunction onto the vibronic state of interest, and $\hat{Q}$, which projects the wavefunction onto all other vibronic states. The results are reminiscent of standard perturbation theory used in quantum mechanics.

As in perturbation theory, the Hamiltonian, $\hat{H} = \hat{H}_0 + \hat{H}'$, is divided into two parts: a zeroth order term which has the basis functions as eigenfunctions, and a perturbing term, which can mix these states. The first order term of the effective Hamiltonian is

$$\hat{H}^{(1)}_{\text{eff}} = \hat{P}\hat{H}'\hat{P} \tag{4.65}$$

that is, the effect of the perturbing state within the vibronic state. The second order term has the form

$$\hat{H}^{(2)}_{\text{eff}} = \hat{P}\hat{H}'\frac{\hat{Q}}{\hat{H}_0 - E_0}\hat{H}'\hat{P} \tag{4.66}$$

This accounts for first order couplings to other vibronic states, but leaves the eigenvalues of the operator within the same state. While higher order terms are possible, these are not necessary to describe the energy levels of the $a^3\Pi$ state of CO.

Using the Hund's case (a) basis set and the effective Hamiltonian formalism to calculate the zero-field levels in $a^3\Pi$ ^{12}CO only requires considering three basis vectors at a time. To calculate the zero-field levels in the same state in ^{13}CO using the a_β basis set still requires only six states. Even when external fields are included, no more than a few hundred states are required to describe the energy level structure quite accurately. Such calculations can be easily performed on modern computers

Here, we consider seven components of the effective Hamiltonian in order to describe the fine structure energy levels within the $a^3\Pi, v = 0$ state of ^{12}CO, and one additional term to include the hyperfine structure seen in ^{13}CO. Four of these already appear in the zeroth-order Hamiltonian: the rotation of the nuclei around each other ($\hat{H}_{\text{rot}}$), the spin-orbit interaction of the electrons ($\hat{H}_{\text{so}}$), the spin-spin interaction ($\hat{H}_{\text{ss}}$), and the spin-rotation interaction ($\hat{H}_{\text{sr}}$). Additionally, the rotational Hamiltonian and the spin-rotation Hamiltonian include first-order coupling that mix states within the vibronic level. The centrifugal distortion terms, such as $\hat{H}_{\text{cd}}$, result from second-order mixings of other vibrational states through $\hat{H}_{\text{rot}}$. The Λ-doubling term, $\hat{H}_{\text{LD}}$ is another second-order term resulting from a combination $\hat{H}_{\text{rot}}$ and $\hat{H}_{\text{so}}$ mixing the wavefunction with other electronic states.

With the exception of the Λ-doubling terms, the Hamiltonian used here is taken from Brown and Carrington [89]. In the case of the Λ-doubling terms, the sign is reversed, as this results in positive coefficients, and also reflects the convention followed in other works [90, 91]. As is done elsewhere in this chapter, some notation is also adopted from Brown and Carrington. Particularly, the coefficients of the Hamiltonian terms all contain the subscript ηv (e.g. $B_{\eta v}$), indicating that the coefficient applies to a single vibronic state. In addition, this helps to distinguish the Λ-doubling parameters $p_{\eta v}$ and $q_{\eta v}$ from the space- and molecule-fixed spherical tensor indices p and q.

4.4.1 Nuclear Rotation Hamiltonian

The energy of two nuclei rotating around each other is given by

$$\hat{H}_{\text{rot}} = B'_{\eta v}\hat{R}^2 \tag{4.67}$$

where $\hat{R}$ is the rotational angular momentum of the nuclei. Generally, it is considered simpler to express this in terms of $\hat{N} = \hat{R} + \hat{L} = \hat{J} - \hat{S}$ because this mostly eliminates

the dependence of the function on the components of the orbital angular momentum L_x and L_y, which are ill defined in a diatomic molecule. The operator in this form is

$$\hat{H}_{\text{rot}} = B'_{\eta v}(\hat{N} - \hat{L})^2 = B'_{\eta v}\left(\hat{N}^2 + \sum_q (-1)^q T^1_q(\hat{L}) T^1_{-q}(\hat{L}) - 2\sum_q (-1)^q T^1_q(\hat{N}) T^1_{-q}(\hat{L})\right) \tag{4.68}$$

The terms involving $T^1_{q=\pm1}(\hat{L})T^1_{q=\mp1}(\hat{L})$ are not measurable and are generally included in the overall offset of the electronic state, since they are the same for all sublevels. The terms $T^1_{q=\pm1}(\hat{N})T^1_{q=\mp1}(\hat{L})$ mix with other electronic states, which can produce energy perturbations to second order. Cross terms in the second order Hamiltonian such as $P\,T^1_{q=1}(\hat{N})T^1_{q=-1}(\hat{L})\,\frac{Q}{\hat{H}_0 - E_0}\,T^1_{q=-1}(\hat{N})T^1_{q=1}(\hat{L})\,P$ have the same form as the first order operator, and therefore produce a small correction to $B'_{\eta v}$. Terms such as $P\,T^1_{q=-1}(\hat{N})T^1_{q=1}(\hat{L})\,\frac{Q}{\hat{H}_0 - E_0}\,T^1_{q=-1}(\hat{N})T^1_{q=1}(\hat{L})\,P$ can mix states with $\Delta\Lambda = 2$ and become important for the Λ-doubling component.

The only remaining terms are proportional to $\hat{N}^2$, $T^1_{q=0}(\hat{L})T^1_{q=0}(\hat{L})$, and $T^1_{q=0}(\hat{N})T^1_{q=0}(\hat{L})$. Thus, the $\hat{H}_{\text{rot}}$ operator can be simplified to

$$\hat{H}_{\text{rot}} = B'_{\eta v}(\hat{N}^2 - {N_z}^2) \tag{4.69}$$

where $B'_{\eta v}$ now includes the second order terms previously mentioned.

Because the coefficient $B'_{\eta v}$ is a function of the internuclear distance, it can mix different vibrational states, leading to a second-order perturbation, which is called the centrifugal distortion. This effect will be described in more detail later, but the rotational centrifugal distortion term is proportional to the square of the rotational Hamiltonian.

$$\hat{H}_{\text{rotcd}} = -D_{\eta v}(\hat{N}^2 - {N_z}^2)^2 \tag{4.70}$$

While many texts describe $\hat{H}_{\text{rot}}$ and $\hat{H}_{\text{rotcd}}$ in this form, it is not strictly necessary to include N_z, since it is the same for all levels of an electronic state. The sum of these two terms can then be written as

$$\hat{H}_{\text{rot}} + \hat{H}_{\text{rotcd}} = -({N_z}^2 B'_{\eta v} + {N_z}^4 D_{\eta v}) + (B'_{\eta v} + 2{N_z}^2 D_{\eta v})\hat{N}^2 - D_{\eta v}\hat{N}^4 \tag{4.71}$$

Thus, $\hat{H}_{\text{rot}}$ and $\hat{H}_{\text{rotcd}}$ can be simplified to

$$\hat{H}_{\text{rot}} = B_{\eta v}\hat{N}^2 \tag{4.72}$$

$$\hat{H}_{\text{rotcd}} = -D_{\eta v}\hat{N}^4 \tag{4.73}$$

where $B_{\eta v} = B'_{\eta v} + 2{N_z}^2 D_{\eta v}$. The remaining term, $-({N_z}^2 B'_{\eta v} + {N_z}^4 D_{\eta v})$, produces an overall offset to the Hamiltonian for a particular vibronic state.

To calculate the matrix elements, the rotational Hamiltonian, which is proportional to $\hat{N}^2$, must be rewritten in terms of the $\hat{J}$ and $\hat{S}$ used in the Hund's case (a) basis set.

$$\hat{H}_{\text{rot}} = B_{\eta v}\hat{N}^2 = B_{\eta v}(\hat{J} - \hat{S})^2 = B_{\eta v}(\hat{J}^2 + \hat{S}^2 - 2\hat{J}\cdot\hat{S}) \tag{4.74}$$

The terms $\hat{J}^2$ and $\hat{S}^2$ are diagonal in the case (a) basis, with eigenvalues $J(J+1)$ and $S(S+1)$ respectively. The dot product, however, can mix terms of differing Σ values. To calculate the dot product, we express it in terms of spherical tensors.

Because $\hat{S}$ is defined in the molecule fixed axes in the case (a) basis, while $\hat{J}$ must be defined in external coordinates, the spherical tensors based on $\hat{J}$ must be rotated into the external coordinate system.

$$\hat{J}\cdot\hat{S} = \sum_q (-1)^q T^1_{-q}(\hat{J}) T^1_q(\hat{S}) = \sum_{p,q} (-1)^q T^1_p(\hat{J}) \mathfrak{D}^1_{p-q}(\omega) T^1_q(\hat{S}) \tag{4.75}$$

The index p is defined in space-fixed axes, while the index q is effectively defined in molecule-fixed axes. The factor $T^1_q(\hat{S})$ acts on the electron spin component of the wavefunction, and can be computed using the Wigner-Eckart theorem.

$$\begin{aligned}\langle S\Sigma|T^1_q(\hat{S})|S\Sigma'\rangle &= (-1)^{S-\Sigma}\begin{pmatrix} S & 1 & S \\ -\Sigma & q & \Sigma'\end{pmatrix}\langle S||T^1(\hat{S})||S\rangle \\ &= (-1)^{S-\Sigma}\begin{pmatrix} S & 1 & S \\ -\Sigma & q & \Sigma'\end{pmatrix}\sqrt{S(S+1)(2S+1)}\end{aligned} \tag{4.76}$$

The remaining factors, $T^1_p(\hat{J})\mathfrak{D}^1_{p-q}(\omega)$, act on the total angular momentum component of the wavefunction. It was shown previously (equation (4.57)) that this part of the matrix element could be reduced to

$$\sum_p (-1)^q \langle J\Omega M|T^1_p(\hat{J})\mathfrak{D}^1_{p-q}(\omega)|J\Omega' M\rangle = \sqrt{J(J+1)(2J+1)}(-1)^{J-\Omega}\begin{pmatrix} J & 1 & J \\ -\Omega & q & \Omega'\end{pmatrix} \tag{4.77}$$

Thus, the rotational Hamiltonian can be written as

$$\begin{aligned}\frac{1}{B_{\eta v}}\langle \Lambda S\Sigma J\Omega M|\hat{H}_{\rm rot}|\Lambda S\Sigma' J\Omega' M\rangle =& \delta_{\Omega\Omega'}\delta_{\Sigma\Sigma'}(J(J+1)+S(S+1)) - \\ & 2\sqrt{J(J+1)(2J+1)}(-1)^{J-\Omega}\begin{pmatrix} J & 1 & J \\ -\Omega & \Omega-\Omega' & \Omega'\end{pmatrix} \\ & \sqrt{S(S+1)(2S+1)}(-1)^{S-\Sigma}\begin{pmatrix} S & 1 & S \\ -\Sigma & \Sigma-\Sigma' & \Sigma'\end{pmatrix}\end{aligned} \tag{4.78}$$

Since $\Omega = \Lambda + \Sigma$ and $\Omega' = \Lambda + \Sigma'$, then $\Omega - \Omega' = \Sigma - \Sigma'$, and replacing q by $\Omega - \Omega'$ in the first 3-j symbol and by $\Sigma - \Sigma'$ in the second is valid. Because the sum of the lower components in a 3-j symbol must be zero, $q = \Omega - \Omega' = \Sigma - \Sigma'$ is the only non-vanishing term in the series.

4.4.2 Spin-Orbit Hamiltonian

The coupling of the electronic spin to the electronic orbital angular momentum produces a term given by

$$\hat{H}_{\rm so} = A_{\eta v}\hat{L}\cdot\hat{S} = A_{\eta v}\sum_q (-1)^q T^1_q(\hat{L}) T^1_{-q}(\hat{S}) \tag{4.79}$$

As in the nuclear rotation Hamiltonian, the terms involving $T^1_{q=\pm1}(\hat{L})T^1_{q=\mp1}(\hat{S})$ mix the wavefunction with other electronic states. Cross terms such as

$P\,T^1_{q=1}(\hat{L})T^1_{q=-1}(\hat{S})\,\frac{Q}{\hat{H}_0-E_0}\,T^1_{q=-1}(\hat{L})T^1_{q=1}(\hat{S})\,P$ simultaneously produce second-order corrections to the spin-orbit Hamiltonian and spin-spin Hamiltonian. As with the rotational Hamiltonian, second order terms of the form $P\,T^1_{q=1}(\hat{L})T^1_{q=-1}(\hat{S})\,\frac{Q}{\hat{H}_0-E_0}\,T^1_{q=1}(\hat{L})T^1_{q=-1}(\hat{S})\,P$ contribute to the Λ-doubling.

The remaining term, $A_{\eta v}T^1_{q=0}(\hat{L})T^1_{q=0}(\hat{S})$, acts within the vibronic state. In the Hund's case (a) basis, the spin-orbit Hamiltonian is diagonal, and the matrix elements take the form

$$\frac{1}{A_{\eta v}}\langle \Lambda S\Sigma J\Omega M|\hat{H}_{\rm so}|\Lambda S\Sigma J\Omega M\rangle = \Lambda\Sigma \tag{4.80}$$

4.4.3 Spin-Spin and Spin-Rotation Hamiltonians

Two other contributions to the fine structure Hamiltonian which are important for fitting the energy levels of $a^3\Pi$ CO are the couplings of electron spins with each other and the coupling of electron spins to the rotation of the nuclei. These energies are given by

$$\hat{H}_{\rm ss} = \frac{2}{3}\lambda_{\eta v}(3(T^1_{q=0}(\hat{S}))^2 - \hat{S}^2) \tag{4.81}$$

$$\hat{H}_{\rm sr} = \gamma_{\eta v}\hat{N}\cdot\hat{S} \tag{4.82}$$

Both of these terms receive second-order contributions from the other couplings. The spin-spin term has a contribution from the spin-orbit terms mixing in other states, and the spin-rotation term through the rotation and spin-orbit terms simultaneously coupling other states. However, neither term couples to other electronic states.

The spin-spin Hamiltonian is diagonal in the case (a) basis set: $T^1_{q=0}(\hat{S})$ has the eigenvalue Σ and $\hat{S}^2$ has the eigenvalue $S(S+1)$. The matrix elements are then given by

$$\frac{1}{\lambda_{\eta v}}\langle \Lambda S\Sigma J\Omega M|\hat{H}_{\rm ss}|\Lambda S\Sigma J\Omega M\rangle = \frac{2}{3}(3\Sigma^2 - S(S+1)) \tag{4.83}$$

To calculate the matrix elements for the spin-rotation Hamiltonian, $\hat{N}$ must be rewritten as $\hat{J}-\hat{S}$, resulting in two terms. The first is proportional to $\hat{J}\cdot\hat{S}$, whose matrix elements have already been calculated in conjunction with the rotational Hamiltonian. The second term is proportional to $\hat{S}^2$, which is diagonal in the case (a) basis and has the eigenvalue $S(S+1)$. Thus, the matrix elements for the spin-rotation Hamiltonian are

$$\begin{aligned}\frac{1}{\gamma_{\eta v}}\langle \Lambda S\Sigma J\Omega M|\hat{H}_{\rm sr}|\Lambda S\Sigma' J\Omega' M\rangle =& \sqrt{J(J+1)(2J+1)}(-1)^{J-\Omega}\begin{pmatrix} J & 1 & J\\ -\Omega & \Omega-\Omega' & \Omega'\end{pmatrix}\\ & \sqrt{S(S+1)(2S+1)}(-1)^{S-\Sigma}\begin{pmatrix} S & 1 & S\\ -\Sigma & \Sigma-\Sigma' & \Sigma'\end{pmatrix}\\ & -\delta_{\Omega\Omega'}\delta_{\Sigma\Sigma'}S(S+1)\end{aligned} \tag{4.84}$$

4.4.4 Λ-Doubling Hamiltonian

If $\Lambda = 1$, terms of the Hamiltonian of the form $T^1_{q=1}(\hat{A})T^1_{q=-1}(\hat{L})$, where $\hat{A}$ is angular momentum other than $\hat{L}$, can mix in another electronic state with $\Lambda = 0$. This $\Lambda = 0$ state

can then be coupled to $\Lambda = -1$ through a Hamiltonian term of the form $T^1_{q=1}(\hat{A}')T^1_{q=-1}(\hat{L})$. Since $\Lambda = -1$ represents the same electronic state as $\Lambda = 1$, this pair of terms can lead to a second-order contribution to the effective Hamiltonian. In particular, two such terms exist that can result in such a coupling. The nuclear rotation Hamiltonian contains terms of the form $T^1_{q=\pm1}(\hat{N})T^1_{q=\mp1}(\hat{L})$, and the spin-orbit Hamiltonian contains terms of the form $T^1_{q=\pm1}(\hat{S})T^1_{q=\mp1}(\hat{L})$. These factors, along with their cross terms, form the Λ-doubling Hamiltonian

$$\hat{H}_{\mathrm{LD}} = o_{\eta v}\sum_{q=\pm1} e^{-2qi\phi}T^2_{2q}(\hat{S},\hat{S}) - p_{\eta v}\sum_{q=\pm1} e^{-2qi\phi}T^2_{2q}(\hat{N},\hat{S}) + q_{\eta v}\sum_{q=\pm1} e^{-2qi\phi}T^2_{2q}(\hat{N},\hat{N}) \quad (4.85)$$

The $e^{\pm2i\phi}$ factors are included to explicitly connect the $\Lambda = 1$ states to the $\Lambda = -1$ states. This assumes an effective form of the Λ component of the wavefunction

$$|\Lambda\rangle = \frac{1}{\sqrt{2\pi}}e^{i\Lambda\phi} \quad (4.86)$$

As in other cases, in order to evaluate the matrix elements in the case (a) basis set, the $\hat{N}$ operators must be replaced with $\hat{J} - \hat{S}$. The Hamiltonian can then be rewritten as

$$\begin{aligned}\hat{H}_{\mathrm{LD}} = (o_{\eta v} + p_{\eta v} + q_{\eta v})&\sum_{q=\pm1} e^{-2qi\phi}T^2_{2q}(\hat{S},\hat{S})\\ -(p_{\eta v} + 2q_{\eta v})&\sum_{q=\pm1} e^{-2qi\phi}T^2_{2q}(\hat{J},\hat{S})\\ +q_{\eta v}&\sum_{q=\pm1} e^{-2qi\phi}T^2_{2q}(\hat{J},\hat{J})\end{aligned} \quad (4.87)$$

The matrix elements of $e^{\mp2i\phi}T^2_{\pm2}(\hat{S},\hat{S})$ can be calculated using the Wigner-Eckart theorem and equation (4.50). Additionally, the matrix elements of $e^{\mp2i\phi}T^2_{\pm2}(\hat{J},\hat{S})$ can be computed by first decomposing $T^2_{\pm2}(\hat{J},\hat{S})$ to $T^2_{\pm2}(\hat{J},\hat{S}) = T^1_{\pm1}(\hat{J})T^1_{\pm1}(\hat{S})$. Since the tensors $T^1_{\pm1}(\hat{J})$ and $T^2_{\pm2}(\hat{J},\hat{J})$ are defined in a molecule-fixed coordinate system, the total angular momentum component of the matrix elements of $e^{\mp2i\phi}T^2_{\pm2}(\hat{J},\hat{S})$ and the matrix elements of $e^{\mp2i\phi}T^2_{\pm2}(\hat{J},\hat{J})$ must be evaluated using equation (4.57).

$$\begin{aligned}&\langle(\Lambda = \mp1)S(\mp\Sigma)J(\mp\Omega)M|e^{\mp2i\phi}T^2_{\pm2}(\hat{S},\hat{S})|(\Lambda = \pm1)S(\pm\Sigma')J(\pm\Omega')M\rangle\\ =&\delta_{\Omega+\Omega',0}(-1)^{S\pm\Sigma}\begin{pmatrix}S & 2 & S\\ \pm\Sigma & \pm2 & \pm\Sigma'\end{pmatrix}\sqrt{\frac{(2S+3)!}{24(2S-2)!}}\\ =&\delta_{\Omega+\Omega',0}(-1)^{S+\Sigma}\begin{pmatrix}S & 2 & S\\ \Sigma & 2 & \Sigma'\end{pmatrix}\sqrt{\frac{(2S+3)!}{24(2S-2)!}}\\ =&\frac{1}{2}\delta_{\Omega+\Omega',0}\delta_{\Sigma+\Sigma',-2}\sqrt{(S-\Sigma-1)(S-\Sigma)(S+\Sigma+1)(S+\Sigma+2)}\end{aligned} \quad (4.88)$$

$$\begin{aligned}
&\langle(\Lambda=\mp1)S(\mp\Sigma)J(\mp\Omega)M|e^{\mp2i\phi}T^2_{\pm2}(\hat{J},\hat{S})|(\Lambda=\pm1)S(\pm\Sigma')J(\pm\Omega')M\rangle\\
=&(-1)^{J\pm\Omega+S\pm\Sigma+1}\begin{pmatrix}J & 1 & J\\ \pm\Omega & \mp1 & \pm\Omega'\end{pmatrix}\begin{pmatrix}S & 1 & S\\ \pm\Sigma & \pm1 & \pm\Sigma'\end{pmatrix}\sqrt{J(J+1)(2J+1)S(S+1)(2S+1)}\\
=&(-1)^{J+\Omega+S+\Sigma+1}\begin{pmatrix}J & 1 & J\\ \Omega & -1 & \Omega'\end{pmatrix}\begin{pmatrix}S & 1 & S\\ \Sigma & 1 & \Sigma'\end{pmatrix}\sqrt{J(J+1)(2J+1)S(S+1)(2S+1)}\\
=&\frac{1}{2}\delta_{\Omega+\Omega',1}\delta_{\Sigma+\Sigma',-1}\sqrt{(J-\Omega+1)(J+\Omega)(S-\Sigma)(S+\Sigma+1)}
\end{aligned}\tag{4.89}$$

$$\begin{aligned}
&\langle(\Lambda=\mp1)S(\mp\Sigma)J(\mp\Omega)M|e^{\mp2i\phi}T^2_{\pm2}(\hat{J},\hat{J})|(\Lambda=\pm1)S(\pm\Sigma')J(\pm\Omega')M\rangle\\
=&(-1)^{J\pm\Omega}\begin{pmatrix}J & 2 & J\\ \pm\Omega & \mp2 & \pm\Omega'\end{pmatrix}\sqrt{\frac{(2J+3)!}{24(2J-2)!}}\\
=&(-1)^{J+\Omega}\begin{pmatrix}J & 2 & J\\ \Omega & -2 & \Omega'\end{pmatrix}\sqrt{\frac{(2J+3)!}{24(2J-2)!}}\\
=&\frac{1}{2}\delta_{\Omega+\Omega',2}\delta_{\Sigma+\Sigma',0}\sqrt{(J-\Omega+1)(J-\Omega+2)(J+\Omega-1)(J+\Omega)}
\end{aligned}\tag{4.90}$$

The factor $\delta_{\Omega+\Omega',0}$ in the first equation arises because the matrix element only depends on the spin portion of the wavefunction and thus vanishes unless $\mp\Omega=\pm\Omega'$. Similarly, the factor $\delta_{\Sigma+\Sigma',0}$ in the last equation arises because the matrix element only depends on the total angular momentum. The two Kronecker deltas in each equation are, however, redundant: because $\Omega=\Sigma+1$ and $\Omega'=\Sigma'+1$, then $\Omega+\Omega'=\Sigma+\Sigma'+2$. In subsequent equations, only Kronecker deltas involving $\Omega+\Omega'$ will be used.

It was stated earlier, in section 4.2.4, that wavefunctions that are eigenfunctions of the inversion operator are comprised of a linear combination of states where $\Lambda=|\Lambda|$ and $\Lambda=-|\Lambda|$. Equation (4.29) shows the matrix elements between two states of the same parity. Since the Λ-doubling Hamiltonian can only mix states of different Λ, the first two terms vanish. The last two terms can, however, mix states $\Lambda=-1$ and $\Lambda=1$. Equations (4.88), (4.89), and (4.90) demonstrate that these last two terms are the same for the $\hat{H}_{\mathrm{LD}}$, so the matrix elements for definite-parity wavefunctions can be written as

$$\begin{aligned}
&\langle(\Lambda=1)S\Sigma J\Omega M\pm|\hat{H}_{\mathrm{LD}}|(\Lambda=1)S\Sigma' J'\Omega' M'\pm\rangle\\
=&\pm(-1)^{J-S}\langle(\Lambda=-1)S(-\Sigma)J(-\Omega)M|\hat{H}_{\mathrm{LD}}|(\Lambda=1)S\Sigma' J'\Omega' M'\rangle
\end{aligned}\tag{4.91}$$

For matrix elements between two states of opposite parity, the first two terms of equation (4.30) are zero and the last two terms cancel, so the Λ-doubling Hamiltonian can only connect states of the same parity. This confirms that $\hat{H}_{\mathrm{LD}}$ commutes with the inversion operator.

The matrix elements of $\hat{H}_{\rm LD}$ in a definite-parity basis set are given by

$$\begin{aligned}
&\langle(\Lambda=1)S\Sigma J\Omega M \pm |\hat{H}_{\rm LD}|(\Lambda=1)S\Sigma' J\Omega' M\pm\rangle = \\
\pm\frac{1}{2}(-1)^{J-S}\Bigg(&(o_{\eta v}+p_{\eta v}+q_{\eta v})\delta_{\Omega+\Omega',0}\sqrt{(S-\Sigma-1)(S-\Sigma)(S+\Sigma+1)(S+\Sigma+2)} \\
&-(p_{\eta v}+2q_{\eta v})\delta_{\Omega+\Omega',1}\sqrt{(J-\Omega+1)(J+\Omega)(S-\Sigma)(S+\Sigma+1)} \\
&+q_{\eta v}\delta_{\Omega+\Omega',2}\sqrt{(J-\Omega+1)(J-\Omega+2)(J+\Omega-1)(J+\Omega)}\Bigg)
\end{aligned} \tag{4.92}$$

The matrix elements of the two parities are equal and opposite. In the case of $a^3\Pi$ CO, the eigenfunctions of the form $|\Lambda=1\rangle + |\Lambda=-1\rangle$ have positive matrix elements, and the eigenfunctions of the form $|\Lambda=1\rangle - |\Lambda=-1\rangle$ have negative matrix elements. If there are no other parity-dependent components of the Hamiltonian, the upper level of a Λ-doublet will always have a parity of $(-1)^{J-S}$.

4.4.5 Centrifugal Distortions

It has been stated previously that, because the rotational constant B is dependent on internuclear distance, a second-order correction term arises that is proportional to $\hat{N}^4$.

Because many terms depend at least slightly on internuclear distance, such terms can couple to other nearby vibrational states. The second-order coupling to other vibrational states is given by

$$\hat{H}^{(2)}_{\rm eff} = \sum_{v'\neq v}\frac{1}{E_{v'}-E_v}|v\rangle\langle v|(\hat{H}'+B(r)\hat{N}^2)|v'\rangle\langle v'|(\hat{H}'+B(r)\hat{N}^2)|v\rangle\langle v| \tag{4.93}$$

One of the product terms is the rotational centrifugal distortion term seen before, given by

$$\hat{H}_{\rm rotcd} = \sum_{v'\neq v}\frac{|\langle v|B(r)|v'\rangle|^2}{E_{v'}-E_v}\hat{N}^4 \tag{4.94}$$

In addition, two cross terms appear

$$\hat{H}_{\rm cd} = \sum_{v'\neq v}\frac{\langle v'|B(r)|v\rangle}{E_{v'}-E_v}\left\{\langle v|\hat{H}'|v'\rangle,\hat{N}^2\right\} = \sum_{v'\neq v}\frac{\langle v'|B(r)|v\rangle}{E_{v'}-E_v}\left(\langle v|\hat{H}'|v'\rangle\hat{N}^2+\hat{N}^2\langle v|\hat{H}'|v'\rangle\right) \tag{4.95}$$

However, other parameters are also dependent on internuclear distance, resulting in a centrifugal distortion terms of the form

$$\hat{H}_{\rm cd} = \frac{\text{constant}}{2}\left\{\hat{N}^2,\hat{H}_0\right\} = \frac{\text{constant}}{2}(\hat{N}^2\hat{H}_0+\hat{H}_0\hat{N}^2) \tag{4.96}$$

For example, in the spin-orbit Hamiltonian, $\hat{H}_{\rm so}$, the dependence of the coefficient $A_{\eta v}$ on the internuclear distance results in a centrifugal distortion term of the form

$$\hat{H}_{\rm socd} = \frac{\rm A_{D\eta v}}{2}\left\{\hat{N}^2, T^1_{q=0}(\hat{L})T^1_{q=0}(\hat{S})\right\} \tag{4.97}$$

The matrix elements in the Hund's case (a) basis can be calculated by inserting a complete projection operator between $\hat{N}^2$ and $T^1_{q=0}(\hat{L})T^1_{q=0}(\hat{S})$.

$$\begin{aligned}
&\frac{1}{A_{D\eta v}}\langle \Lambda S\Sigma J\Omega M|\hat{H}_{\rm socd}|\Lambda S\Sigma' J\Omega' M\rangle \\
=&\frac{1}{2}\sum_{\Sigma''\Omega''}\langle \Lambda S\Sigma J\Omega M|\hat{N}^2|\Lambda S\Sigma'' J\Omega'' M\rangle\langle \Lambda S\Sigma'' J\Omega'' M|T^1_{q=0}(\hat{L})T^1_{q=0}(\hat{S})|\Lambda S\Sigma' J\Omega' M\rangle \\
+&\frac{1}{2}\sum_{\Sigma''\Omega''}\langle \Lambda S\Sigma J\Omega M|T^1_{q=0}(\hat{L})T^1_{q=0}(\hat{S})|\Lambda S\Sigma'' J\Omega'' M\rangle\langle \Lambda S\Sigma'' J\Omega'' M|\hat{N}^2|\Lambda S\Sigma' J\Omega' M\rangle
\end{aligned} \tag{4.98}$$

Since $T^1_{q=0}(\hat{L})T^1_{q=0}(\hat{S})$ is diagonal in the Hund's case (a) basis set, the first term is only non-zero when $\Sigma'' = \Sigma'$ and $\Omega'' = \Omega'$ in the first term and when $\Sigma'' = \Sigma$ and $\Omega'' = \Omega$ in the second term. Using the matrix elements for $T^1_{q=0}(\hat{L})T^1_{q=0}(\hat{S})$ given in equation (4.80), equation (4.98) can be reduced to

$$\frac{1}{A_{D\eta v}}\langle \Lambda S\Sigma J\Omega M|\hat{H}_{\rm socd}|\Lambda S\Sigma' J\Omega' M\rangle = \frac{1}{2}(\Lambda\Sigma + \Lambda\Sigma')\langle \Lambda S\Sigma J\Omega M|\hat{N}^2|\Lambda S\Sigma' J\Omega' M\rangle \tag{4.99}$$

The matrix elements of $\hat{N}^2$ can be found in equation (4.78).

Other centrifugal distortion terms are given by

$$\hat{H}_{\rm sscd} = \frac{\lambda_{\rm D\eta v}}{3}\left\{\hat{N}^2, 3(T^1_{q=0}(\hat{S}))^2 - \hat{S}^2\right\} \tag{4.100}$$

$$\hat{H}_{\rm srcd} = \frac{\gamma_{\rm D\eta v}}{2}\left\{\hat{N}^2, \hat{N}\cdot\hat{S}\right\} \tag{4.101}$$

$$\begin{aligned}
\hat{H}_{\rm LDcd} = &\frac{\rm o_{D\eta v}}{2}\sum_{q=\pm1}\left\{\hat{N}^2, e^{-2qi\phi}T^2_{2q}(\hat{S},\hat{S})\right\} - \frac{\rm p_{D\eta v}}{2}\sum_{q=\pm1}\left\{\hat{N}^2, e^{-2qi\phi}T^2_{2q}(\hat{N},\hat{S})\right\} \\
&+ \frac{\rm q_{D\eta v}}{2}\sum_{q=\pm1}\left\{\hat{N}^2, e^{-2qi\phi}T^2_{2q}(\hat{N},\hat{N})\right\}
\end{aligned} \tag{4.102}$$

$$\tag{4.103}$$

As in equation (4.87), $\hat{H}_{\rm LDcd}$ can be rewritten in terms of $\hat{J}$ and $\hat{S}$.

$$\begin{aligned}
\hat{H}_{\rm LDcd} = &\frac{\rm o_{D\eta v} + p_{D\eta v} + q_{D\eta v}}{2}\sum_{q=\pm1}\left\{\hat{N}^2, e^{-2qi\phi}T^2_{2q}(\hat{S},\hat{S})\right\} \\
&-\frac{\rm p_{D\eta v} + 2q_{D\eta v}}{2}\sum_{q=\pm1}\left\{\hat{N}^2, e^{-2qi\phi}T^2_{2q}(\hat{J},\hat{S})\right\} \\
&+\frac{\rm q_{D\eta v}}{2}\sum_{q=\pm1}\left\{\hat{N}^2, e^{-2qi\phi}T^2_{2q}(\hat{J},\hat{J})\right\}
\end{aligned} \tag{4.104}$$

In $\hat{H}_{\rm sscd}$ and the first term of $\hat{H}_{\rm LDcd}$ in equation (4.104), the right side of the anticommutator is diagonal in the Hund's case (a) basis set, so the matrix elements of these terms can be calculated in the same manner as in equation (4.99). For all other Hamiltonian components, the matrix elements must be calculated using a complete projection operator, as in equation (4.98).

4.4.6 Magnetic Hyperfine Hamiltonian

If one or more nuclei in the molecule have a non-zero spin, this additional angular momentum can couple to the other angular momenta already present. In some molecules, coupling can occur through the electric quadrupole moment of a nucleus, but this is zero unless the nucleus has a spin of at least 1 [92]. For a molecule such as ^{13}CO, in which the oxygen nucleus has no spin, but the carbon nucleus has a spin $I = \frac{1}{2}$, coupling between the nuclear spin and other angular momenta is entirely through magnetic dipole interactions.

For the case that only one nucleus has an angular momentum, the magnetic hyperfine Hamiltonian has the form

$$\hat{H}_{\mathrm{mhf}} = a_{\eta v} T^1_{q=0}(\hat{I}) T^1_{q=0}(\hat{L}) + b_{F\eta v} T^1(\hat{I}) \cdot T^1(\hat{S}) + c_{\eta v} \frac{\sqrt{6}}{3} T^2_{q=0}(\hat{I}, \hat{S}) - d_{\eta v} \sum_{q=\pm 1} e^{-2iq\phi} T^2_{2q}(\hat{I}, \hat{S}) \tag{4.105}$$

The first term is the coupling between the nuclear spin and the electron orbital angular momentum, which is proportional to $T^1(\hat{I}) \cdot T^1(\hat{L})$. Because, to first order, terms containing $T^1_{q\neq 0}(\hat{L})$ only couple to other electronic states, the first term can be written as being proportional to $T^1_{q=0}(\hat{I}) T^1_{q=0}(\hat{L})$. Terms where $q \neq 0$ can couple to second order, however, and this results in a term resembling a Λ-doubling. The last term of the magnetic hyperfine Hamiltonian is effectively a cross term between the nuclear spin-electron orbital angular momentum coupling and the standard spin-orbit coupling.

The second and third terms are interactions between the nuclear spin and the electron spin. The third term is the normal dipole-dipole interaction. The second term, known as the Fermi contact term, results from the fact that the nucleus has a finite size, so if an electron is inside the nucleus, it sees a fairly constant field parallel to the nuclear spin. In the effective Hamiltonian framework, this term also receives a second-order contribution from the same terms that lead to the last term in the magnetic hyperfine Hamiltonian.

What each of these terms have in common is that they require knowledge of the nuclear spin in molecule-fixed coordinates, but in the a_β basis, I is only defined in space-fixed coordinates. Therefore, it is necessary to rotate spherical tensors defined in molecule-fixed coordinates, $T^1_q(\hat{I})$, to tensors defined in space-fixed coordinates, $T^1_p(\hat{I})$.

$$\begin{aligned} T^1_q(\hat{I}) &= \sum_p T^1_p(\hat{I}) \mathfrak{D}^1_{pq}(\omega) \\ &= \sum_p (-1)^{p-q} T^1_p(\hat{I}) {\mathfrak{D}^1_{-p-q}}^*(\omega) \\ &= (-1)^q T^1(\hat{I}) \cdot {\mathfrak{D}^1_{\cdot -q}}^*(\omega) \end{aligned} \tag{4.106}$$

The dot product $T^1(\hat{I}) \cdot {\mathfrak{D}^1_{\cdot -q}}^*(\omega)$ has a part that operates on the nuclear spin wavefunction ($T^1(\hat{I})$) and a part that operates on the total angular momentum wavefunction (${\mathfrak{D}^1_{\cdot -q}}^*(\omega)$). Using equation (4.63), this can be rewritten as

$$\begin{aligned} \langle J\Omega I F M_F | {\mathfrak{D}^1_{\cdot -q}}^*(\omega) \cdot T^1(\hat{I}) | J'\Omega' I F M_F \rangle = &(-1)^{J'+I+F} \begin{Bmatrix} J & J' & 1 \\ I & I & F \end{Bmatrix} \\ &\langle J\Omega || {\mathfrak{D}^1_{\cdot -q}}^*(\omega) || J'\Omega' \rangle \langle I || T^1(\hat{I}) || I \rangle \end{aligned} \tag{4.107}$$

Therefore, the matrix element of $T^1_q(\hat{I})$ in the a_β basis is

$$\langle J\Omega IFM_F|T^1_q(\hat{I})|J'\Omega' IFM_F\rangle = (-1)^{J'+I+F+J-\Omega+q}\begin{Bmatrix} J & J' & 1 \\ I & I & F\end{Bmatrix}\begin{pmatrix} J & 1 & J' \\ -\Omega & -q & \Omega'\end{pmatrix} \sqrt{I(I+1)(2I+1)(2J+1)(2J'+1)} \tag{4.108}$$

In the magnetic hyperfine Hamiltonian, $T^1_q(\hat{I})$ is the only factor dependent on the total angular momentum and the nuclear spin angular momentum: the other factors depend only on the electronic orbital angular momentum and the electron spin angular momentum. The $T^1_{q=0}(\hat{L})$ factor in the first term operates only on the electronic orbital angular momentum part of the wavefunction and has an eigenvalue of Λ. Thus, the matrix element of $T^1_{q=0}(\hat{I})T^1_{q=0}(\hat{L})$ is

$$\begin{aligned}&\langle \Lambda J\Omega S\Sigma IFM_F|T^1_{q=0}(\hat{I})T^1_{q=0}(\hat{L})|\Lambda J'\Omega S\Sigma IFM_F\rangle \\ =&\Lambda(-1)^{J'+I+F+J-\Omega}\begin{Bmatrix} J & J' & 1 \\ I & I & F\end{Bmatrix}\begin{pmatrix} J & 1 & J' \\ -\Omega & 0 & \Omega\end{pmatrix}\sqrt{I(I+1)(2I+1)(2J+1)(2J'+1)}\end{aligned} \tag{4.109}$$

The second and third terms only contain $\hat{I}$ and $\hat{S}$, and these can be divided into separate factors

$$T^1(\hat{I})\cdot T^1(\hat{S}) = \sum_q (-1)^q T^1_{-q}(\hat{I})T^1_q(\hat{S}) \tag{4.110}$$

$$\frac{\sqrt{6}}{3}T^2_{q=0}(\hat{I},\hat{S}) = \sum_q \frac{\sqrt{30}}{3}\begin{pmatrix} 1 & 1 & 2 \\ -q & q & 0\end{pmatrix}T^1_{-q}(\hat{I})T^1_q(\hat{S}) = \sum_q (-1)^q\Big(\frac{2}{3}-q^2\Big)T^1_{-q}(\hat{I})T^1_q(\hat{S}) \tag{4.111}$$

The matrix elements of the $T^1_q(\hat{S})$ factors can be evaluated using the Wigner-Eckart theorem. The matrix elements for $T^1(\hat{I})\cdot T^1(\hat{S})$ and $\frac{\sqrt{6}}{3}T^2_{q=0}(\hat{I},\hat{S})$ are then given by

$$\begin{aligned}&\langle J\Omega S\Sigma IFM_F|T^1(\hat{I})\cdot T^1(\hat{S})|J'\Omega' S\Sigma' IFM_F\rangle = \\ &\sum_q (-1)^{J'+I+F+J-\Omega+S-\Sigma}\begin{Bmatrix} J & J' & 1 \\ I & I & F\end{Bmatrix}\begin{pmatrix} J & 1 & J' \\ -\Omega & q & \Omega'\end{pmatrix}\begin{pmatrix} S & 1 & S \\ -\Sigma & q & \Sigma'\end{pmatrix} \\ &\sqrt{S(S+1)(2S+1)I(I+1)(2I+1)(2J+1)(2J'+1)}\end{aligned} \tag{4.112}$$

$$\begin{aligned}&\langle J\Omega S\Sigma IFM_F|\frac{\sqrt{6}}{3}T^2_{q=0}(\hat{I},\hat{S})|J'\Omega' S\Sigma' IFM_F\rangle = \\ &\sum_q (-1)^{J'+I+F+J-\Omega+S-\Sigma}\Big(\frac{2}{3}-q^2\Big)\begin{Bmatrix} J & J' & 1 \\ I & I & F\end{Bmatrix}\begin{pmatrix} J & 1 & J' \\ -\Omega & q & \Omega'\end{pmatrix}\begin{pmatrix} S & 1 & S \\ -\Sigma & q & \Sigma'\end{pmatrix} \\ &\sqrt{S(S+1)(2S+1)I(I+1)(2I+1)(2J+1)(2J'+1)}\end{aligned} \tag{4.113}$$

In both equations, the 3-j symbol is zero unless $q = \Omega - \Omega' = \Sigma - \Sigma'$. Therefore, each sum can be reduced to a single term.

The final term of the magnetic hyperfine Hamiltonian resembles a Λ-doubling: it only connects $\Lambda = 1$ states to $\Lambda = -1$ states. Using the fact that $T^2_{q=\pm2}(\hat{I},\hat{S}) = T^1_{q=\pm1}(\hat{I})T^1_{q=\pm1}(\hat{S})$, the matrix element is given by

$$\begin{aligned}
&\langle(\Lambda=\mp1)J(\mp\Omega)S(\mp\Sigma)IFM_F|-e^{\mp2i\phi}T^2_{q=\pm2}(\hat{I},\hat{S})|(\Lambda=\pm1)J'(\pm\Omega')S(\pm\Sigma')IFM_F\rangle\\
=&(-1)^{J'+I+F+J\pm\Omega+S\pm\Sigma}\begin{Bmatrix}J & J' & 1\\ I & I & F\end{Bmatrix}\begin{pmatrix}J & 1 & J'\\ \pm\Omega & \mp1 & \pm\Omega'\end{pmatrix}\begin{pmatrix}S & 1 & S\\ \pm\Sigma & \pm1 & \pm\Sigma'\end{pmatrix}\\
&\sqrt{S(S+1)(2S+1)I(I+1)(2I+1)(2J+1)(2J'+1)}\\
=&(-1)^{\frac{1}{2}((J-J')\mp(J-J'))}(-1)^{J'+I+F+J+\Omega+S+\Sigma}\begin{Bmatrix}J & J' & 1\\ I & I & F\end{Bmatrix}\begin{pmatrix}J & 1 & J'\\ \Omega & -1 & \Omega'\end{pmatrix}\begin{pmatrix}S & 1 & S\\ \Sigma & 1 & \Sigma'\end{pmatrix}\\
&\sqrt{S(S+1)(2S+1)I(I+1)(2I+1)(2J+1)(2J'+1)}
\end{aligned} \tag{4.114}$$

Using the definite-parity basis set, the third and fourth term of equation (4.29) are equal, and the matrix element is given by

$$\begin{aligned}
&\sum_{q=\pm1}\langle(\Lambda=1)J\Omega S\Sigma IFM_F\pm|-e^{-2iq\phi}T^2_{2q}(\hat{I},\hat{S})|(\Lambda=1)J'\Omega'S\Sigma'IFM_F\pm\rangle=\\
&\qquad\pm(-1)^{J'+I+F+\Omega-\Sigma}\begin{Bmatrix}J & J' & 1\\ I & I & F\end{Bmatrix}\begin{pmatrix}J & 1 & J'\\ \Omega & -1 & \Omega'\end{pmatrix}\begin{pmatrix}S & 1 & S\\ \Sigma & 1 & \Sigma'\end{pmatrix}\\
&\qquad\sqrt{S(S+1)(2S+1)I(I+1)(2I+1)(2J+1)(2J'+1)}
\end{aligned} \tag{4.115}$$

Combining these equations, the matrix elements of the magnetic hyperfine Hamiltonian are given by

$$\begin{aligned}
&\langle\Lambda J\Omega S\Sigma IFM_F\pm|\hat{H}_{\rm mhf}|\Lambda J'\Omega'S\Sigma'IFM_F\pm\rangle\\
=&(-1)^{J'+I+F+J-\Omega}\begin{Bmatrix}J & J' & 1\\ I & I & F\end{Bmatrix}\sqrt{I(I+1)(2I+1)(2J+1)(2J'+1)}\\
&\Bigg(a_{\eta v}\Lambda\delta_{\Omega\Omega'}\begin{pmatrix}J & 1 & J'\\ -\Omega & 0 & \Omega\end{pmatrix}\\
&+b_{F\eta v}(-1)^{S-\Sigma}\begin{pmatrix}J & 1 & J'\\ -\Omega & \Omega-\Omega' & \Omega'\end{pmatrix}\begin{pmatrix}S & 1 & S\\ -\Sigma & \Sigma-\Sigma' & \Sigma'\end{pmatrix}\sqrt{S(S+1)(2S+1)}\\
&+c_{\eta v}(-1)^{S-\Sigma}\Big(\frac{2}{3}-(\Omega-\Omega')^2\Big)\begin{pmatrix}J & 1 & J'\\ -\Omega & \Omega-\Omega' & \Omega'\end{pmatrix}\begin{pmatrix}S & 1 & S\\ -\Sigma & \Sigma-\Sigma' & \Sigma'\end{pmatrix}\sqrt{S(S+1)(2S+1)}\\
&\pm d_{\eta v}\delta_{\Lambda1}(-1)^{J-\Sigma}\begin{pmatrix}J & 1 & J'\\ \Omega & -1 & \Omega'\end{pmatrix}\begin{pmatrix}S & 1 & S\\ \Sigma & -1 & \Sigma'\end{pmatrix}\sqrt{S(S+1)(2S+1)}\Bigg)
\end{aligned} \tag{4.116}$$

4.5 $a^3\Pi$ CO States

4.5.1 Zero-Field Energy Levels

The fine structure energy levels of $a^3\Pi$ CO in the absence of a field can be calculated by writing the couplings within and between states in a matrix and diagonalizing the

matrix. If the definite parity basis vectors are used (as in equation (4.28)), a maximum three basis vectors can contribute to any given energy eigenvector in ^{12}CO: $|(\Lambda = 1)(S = 1)(\Sigma = \Omega - 1)J\Omega M\pm\rangle$, where Ω can be 0, 1, or 2. In the same state in ^{13}CO, at most six vectors from the a_β basis contribute: $|(\Lambda = 1)(S = 1)(\Sigma = \Omega - 1)J\Omega(I = \frac{1}{2})FM_F\pm\rangle$, where Ω is 0, 1, or 2, and J is $F + \frac{1}{2}$ or $F - \frac{1}{2}$. If $J < 2$, certain values of Ω would lead to a non-physical state, so for such cases, these states must be excluded.

What are still missing are the various parameters used in section 4.4. In principle, these can be found from ab initio calculations of the electronic structure. However, it is generally more accurate and somewhat more straightforward to use spectroscopic measurements. With a reasonable initial guess of the parameters, one can perform a non-linear least squares fit of the splittings between individual states. For ^{12}CO, data is available in the form of microwave measurements of the Λ-doubling splittings [79], millimeter wave spectroscopy of transitions between rotational states [93, 94, 95], and optical absorption measurements involving transitions from the electronic ground state [96]. For ^{13}CO, somewhat less data is available: only measurements of Λ-doubling splittings [97] and a few measurements of rotational transitions [98] have been performed. Using this data, it is possible to fit the various parameters of the Hamiltonian and produce a model that can reproduce all of the energy levels of the $a^3\Pi$, $v = 0$ state.

The results of fitting these parameters in ^{12}CO and ^{13}CO are shown in table (4.1). The parameters A_D, λ_D, o_D, p_D, and q_D are the centrifugal distortion parameters for A, λ, o, p, and q, respectively. An additional parameter, E_0, is an offset added to all eigenenergies and is chosen such that an energy of zero corresponds to the absolute ground state of the molecule ($X^1\Sigma^+$, $v = 0$, $N = 0$).

In ^{12}CO, E_0 can be determined using the measurements of optical transitions from the ground state [96], but this requires knowledge of the ground state rotational structure. Fortunately, there is very little structure in a $^1\Sigma$ state of a molecule with no nuclear spin: the energy only depends on the rotational quantum number N [99].

$$E_{\mathrm{gnd}}/\mathrm{cm}^{-1} = 1.9225289523\mathrm{N(N+1)} - 6.121064\cdot10^{-6}(\mathrm{N(N+1)})^2 + 5.727\cdot10^{-12}(\mathrm{N(N+1)})^3 \tag{4.117}$$

In ^{13}CO, the only information available on the $a^3\Pi$ state with respect to the ground state is the shift that we have measured in the $Q_2(1)$ transition (from $N = 1$ in the ground state to upper Λ-doublet component of $J = 1$, $\Omega = 1$ in the excited state) in ^{12}CO and ^{13}CO. In ^{13}CO, the transition is 4.929 cm^{-1} higher than in ^{12}CO. Combining this with the energy of the $N = 1$ level in the ground state (i.e. the $N = 1$ to $N = 0$ splitting) [100, 99] and the energy of the upper Λ-doublet component of the $J = 1$, $\Omega = 1$ in ^{12}CO, the energy of the upper Λ-doublet component of the $J = 1$, $\Omega = 1$ in ^{13}CO is found to be 48483.247 cm^{-1} above the absolute ground state. The value of E_0 for ^{13}CO is chosen to match this information.

4.5.2 Energy Levels in an Electric Field

Although a neutral molecule has no charge, it can have a net separation of charge that leads to a dipole moment. A molecule with a dipole moment in an electric field has a potential energy proportional to the dot product of the dipole moment and the electric

Parameter	^{12}CO	^{13}CO
$E_{0\eta v}$	48471.537 ± 0.002	48476.637 ± 0.005
$B_{\eta v}$	$1.68167658 \pm 5.6 \cdot 10^{-8}$	$1.60776012 \pm 2.6 \cdot 10^{-5}$
$D_{\eta v}$	$6.37710308 \cdot 10^{-6} \pm 6.9 \cdot 10^{-10}$	$5.18927095 \cdot 10^{-6} \pm 7.0 \cdot 10^{-8}$
$A_{\eta v}$	$41.4317699 \pm 2.1 \cdot 10^{-3}$	$41.3988657 \pm 1.5 \cdot 10^{-2}$
$A_{D\eta v}$	$1.06547611 \cdot 10^{-3} \pm 1.1 \cdot 10^{-4}$	0
$\lambda_{\eta v}$	$1.78318960 \cdot 10^{-2} \pm 6.9 \cdot 10^{-4}$	$5.13591547 \cdot 10^{-2} \pm 9.5 \cdot 10^{-4}$
$\lambda_{D\eta v}$	$-1.72911227 \cdot 10^{-6} \pm 3.0 \cdot 10^{-7}$	$3.17305905 \cdot 10^{-4} \pm 1.8 \cdot 10^{-5}$
$\gamma_{\eta v}$	$1.40252011 \cdot 10^{-2} \pm 1.3 \cdot 10^{-3}$	$2.70157650 \cdot 10^{-3} \pm 1.0 \cdot 10^{-3}$
$o_{\eta v} + p_{\eta v} + q_{\eta v}$	$0.875262252 \pm 1.4 \cdot 10^{-4}$	$0.867485922 \pm 1.5 \cdot 10^{-3}$
$o_{D\eta v} + p_{D\eta v} + q_{D\eta v}$	$-3.63060479 \cdot 10^{-6} \pm 2.0 \cdot 10^{-7}$	$-2.32050770 \cdot 10^{-6} \pm 7.5 \cdot 10^{-7}$
$p_{\eta v} + 2q_{\eta v}$	$5.59958031 \cdot 10^{-3} \pm 2.9 \cdot 10^{-5}$	$5.20960655 \cdot 10^{-3} \pm 6.1 \cdot 10^{-5}$
$p_{D\eta v} + 2q_{D\eta v}$	$1.09566676 \cdot 10^{-7} \pm 5.5 \cdot 10^{-9}$	0
$q_{\eta v}$	$6.15801494 \cdot 10^{-5} \pm 3.6 \cdot 10^{-7}$	$5.47376305 \cdot 10^{-5} \pm 1.5 \cdot 10^{-6}$
$a_{\eta v}$	0	$5.43605630 \cdot 10^{-3} \pm 4.4 \cdot 10^{-7}$
$b_{F\eta v}$	0	$2.14291502 \cdot 10^{-2} \pm 7.3 \cdot 10^{-7}$
$c_{\eta v}$	0	$2.38473581 \cdot 10^{-4} \pm 1.1 \cdot 10^{-6}$
$d_{\eta v}$	0	$3.57380271 \cdot 10^{-3} \pm 1.3 \cdot 10^{-6}$

Table 4.1: Fine and hyperfine structure parameters for the $a^3\Pi, v = 0$ state of ^{12}CO and ^{13}CO. Positions containing "0" represent parameters that were constrained to be zero during the fit. All parameters are given in cm^{-1}.

	^{12}CO	^{13}CO	
Upper Λ-doublet component (+ parity)	48478.4873553909	$F = 3/2$	48483.2475803757
		$F = 1/2$	48483.2456319736
Lower Λ-doublet component (- parity)	48478.4742107712	$F = 3/2$	48483.2353135044
		$F = 1/2$	48483.2340791135

Table 4.2: Zero-field levels for the $a^3\Pi_1, v = 0, J = 1$ state of ^{12}CO and ^{13}CO, calculated using the parameters in table 4.1 and the matrix elements given throughout the chapter. Values given in cm^{-1}.

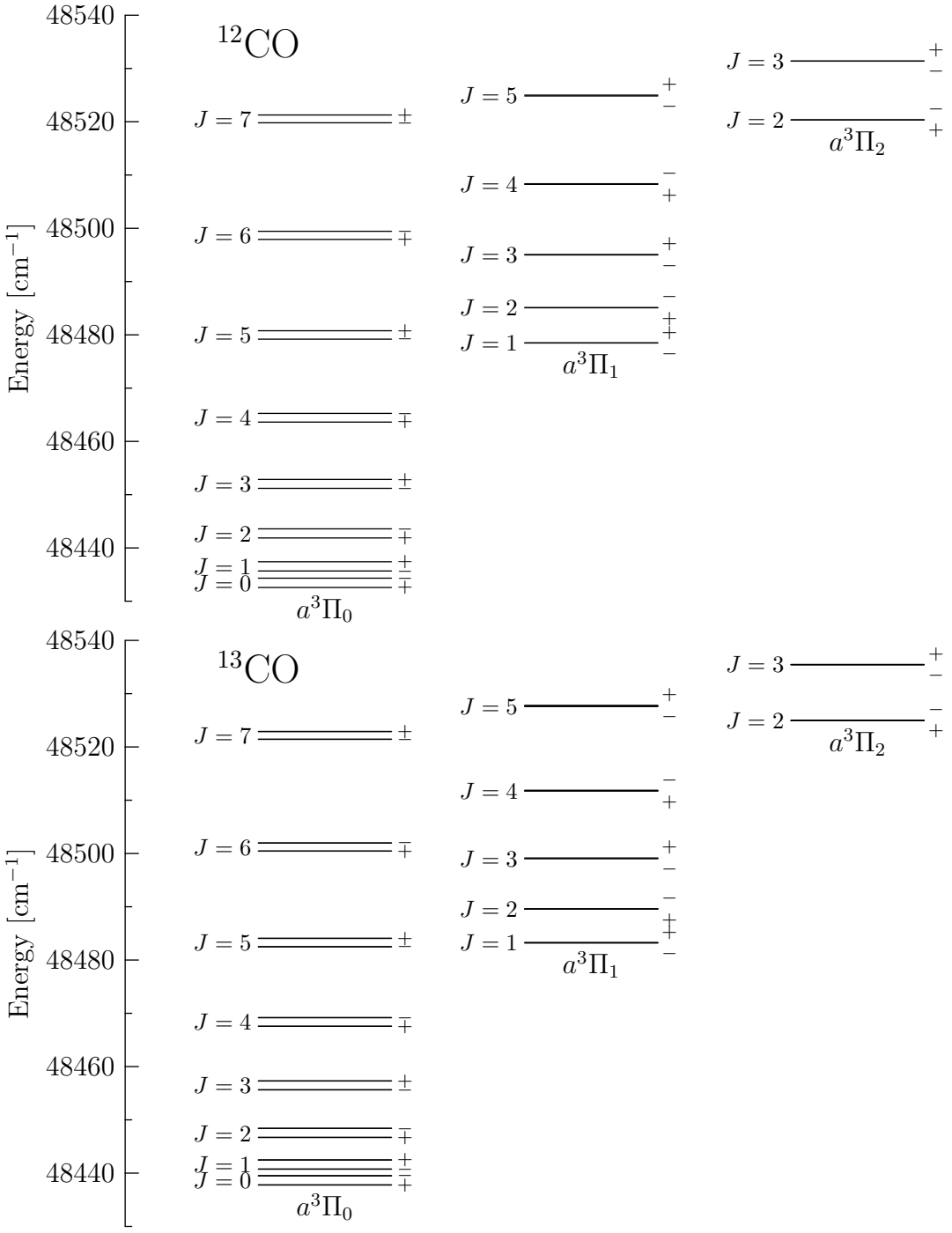

Figure 4.1: The lowest energy levels of the $a^3\Pi$ state of ^{12}CO and ^{13}CO. The spin-orbit coupling divides the state into three manifolds, where (from left to right) $\Omega = 0$, $\Omega = 1$, or $\Omega = 2$. Each manifold is divided into rotational levels, and each rotational level is divided into two Λ-doublet components with opposite parity (indicated to the right of the level). In ^{13}CO, hyperfine coupling causes each of these states to split into two more levels.

field. This potential energy is known as the Stark shift

$$\hat{H}_{\text{Stark}} = -\vec{\mu} \cdot \vec{E} \tag{4.118}$$

The vector $\vec{\mu}$, by convention, points from negative charge to positive charge, while the vector $\vec{E}$ is defined by the direction and magnitude of the force on a positive test charge. Energy is minimized when the two vectors are aligned.

To calculate the matrix elements of the Stark shift, it is useful to rewrite the dot product above in terms of spherical tensor operators.

$$\hat{H}_{\text{Stark}} = -\sum_p (-1)^p T^1_{-p}(\vec{\mu}) T^1_p(\vec{E}) = -\sum_{pq} (-1)^p \mathfrak{D}^1_{-pq}{}^* T^1_q(\vec{\mu}) T^1_p(\vec{E}) \tag{4.119}$$

For symmetry reasons, the electric dipole moment must be along the internuclear axis in a diatomic molecule. As a result, only $T^1_{q=0}(\vec{\mu})$ can be non-zero. For the $a^3\Pi$, $v = 0$ state in both ^{12}CO and ^{13}CO, the dipole moment $T^1_{q=0}(\vec{\mu})$ is 1.375 Debye [79, 97].

$$\langle \Lambda S \Sigma J \Omega M | \hat{H}_{\text{Stark}} | \Lambda S \Sigma J' \Omega M' \rangle = -\sum_p T^1_{q=0}(\vec{\mu}) T^1_p(\vec{E}) (-1)^{M-\Omega+p} \sqrt{(2J+1)(2J'+1)} \begin{pmatrix} J & 1 & J' \\ -M & -p & M' \end{pmatrix} \begin{pmatrix} J & 1 & J' \\ -\Omega & 0 & \Omega \end{pmatrix} \tag{4.120}$$

From the 3-j symbols in this equation, it is seen that the $\hat{H}_{\text{Stark}}$ operator can only connect symmetric top states of the same Ω with $\Delta J = 0, \pm 1$. If only $T^1_{p=0}(\vec{E})$ is non-zero, i.e. the electric field is along the space-fixed Z-axis, only states of the same M are connected, and M remains a rigorously good quantum number.

When applied to the definite-parity zero-field states given in equation (4.28), the $\hat{H}_{\text{Stark}}$ operator mixes only states of opposite parity. When Λ, Σ, and Ω in equation (4.120) are inverted, the matrix element only changes by a phase factor.

$$\langle -\Lambda S -\Sigma J -\Omega M | \hat{H}_{\text{Stark}} | -\Lambda S -\Sigma J' -\Omega M' \rangle = (-1)^{J'-J+1} \langle \Lambda S \Sigma J \Omega M | \hat{H}_{\text{Stark}} | \Lambda S \Sigma J' \Omega M' \rangle \tag{4.121}$$

As a result, matrix elements of $\hat{H}_{\text{Stark}}$ between two states with the same parity must vanish. Only two states of opposite parity can be connected.

$$\begin{aligned} &\langle \Lambda S \Sigma J \Omega M \pm | \hat{H}_{\text{Stark}} | \Lambda S \Sigma J' \Omega M' \pm \rangle \\ =&\frac{1}{2} \langle \Lambda S \Sigma J \Omega M | \hat{H}_{\text{Stark}} | \Lambda S \Sigma J' \Omega M' \rangle \\ +&\frac{1}{2} (-1)^{J-J'} \langle -\Lambda S -\Sigma J -\Omega M | \hat{H}_{\text{Stark}} | -\Lambda S -\Sigma J' -\Omega M' \rangle = 0 \end{aligned} \tag{4.122}$$

$$\begin{aligned} &\langle \Lambda S \Sigma J \Omega M \pm | \hat{H}_{\text{Stark}} | \Lambda S \Sigma J' \Omega M' \mp \rangle \\ =&\frac{1}{2} \langle \Lambda S \Sigma J \Omega M | \hat{H}_{\text{Stark}} | \Lambda S \Sigma J' \Omega M' \rangle \\ -&\frac{1}{2} (-1)^{J-J'} \langle -\Lambda S -\Sigma J -\Omega M | \hat{H}_{\text{Stark}} | -\Lambda S -\Sigma J' -\Omega M' \rangle \\ =&\langle \Lambda S \Sigma J \Omega M | \hat{H}_{\text{Stark}} | \Lambda S \Sigma J' \Omega M' \rangle \end{aligned} \tag{4.123}$$

In states where M is non-zero, the first states that mix to produce a Stark shift are in opposite components of the Λ-doublet. Because these pairs of states are much closer to each other than any other states that they can mix with, in the low to moderate field region, the Hamiltonian can be approximated as having just these two states, and an effective Hamiltonian can be written of the form

$$\hat{H} = \begin{pmatrix} \frac{E_\Lambda}{2} & -|\vec{\mu}||\vec{E}|\frac{M\Omega}{J(J+1)} \\ -|\vec{\mu}||\vec{E}|\frac{M\Omega}{J(J+1)} & -\frac{E_\Lambda}{2} \end{pmatrix} \tag{4.124}$$

where E_Λ is the splitting between the upper and lower Λ-doublet component. The diagonal elements represent the zero-field energy levels of these two components, and the off-diagonal elements, calculated by evaluating equation (4.120) assuming that only $T^1_{p=0}(\vec{E})$ is non-zero, describe their mixing in the field.

The eigenvalues for this Hamiltonian are

$$U = \pm\sqrt{\left(\frac{E_\Lambda}{2}\right)^2 + \left(\mu_{\text{eff}}|\vec{E}|\right)^2} \tag{4.125}$$

where

$$\mu_{\text{eff}} = -|\vec{\mu}|\frac{M\Omega}{J(J+1)} \tag{4.126}$$

This equation fits well with the actual level structure seen in figure 4.2 of ^{12}CO, $\Omega = 1$, $J = 1$. If $|\vec{E}| \gg \frac{E_\Lambda}{2\mu_{\text{eff}}}$, then U is directly proportional to $|\vec{E}|$, with a proportionality constant μ_{eff}. In this moderate field region, the sign of $M\Omega$ becomes well defined: for negative $M\Omega$, the Stark energy increases as a function of electric field, and for positive $M\Omega$, it decreases. The two states that show almost no dependence on the electric field are states where $M = 0$.

At much higher fields, usually above 100 $\frac{\text{kV}}{\text{cm}}$ for $a^3\Pi$ CO, the states with linearly increasing energies from one rotational level approach the states with linearly decreasing energies from the next rotational level. When this happens, the Stark shift is no longer linear: the two levels experience an avoided crossing, the level whose energy was decreasing as a function of electric field starts to have an increasing energy, and the level whose energy was increasing starts to have a decreasing energy.

For ^{13}CO, M is no longer a good quantum number, so the Stark shift must be evaluated in a basis where J couples to I to produce a total angular momentum F with a projection

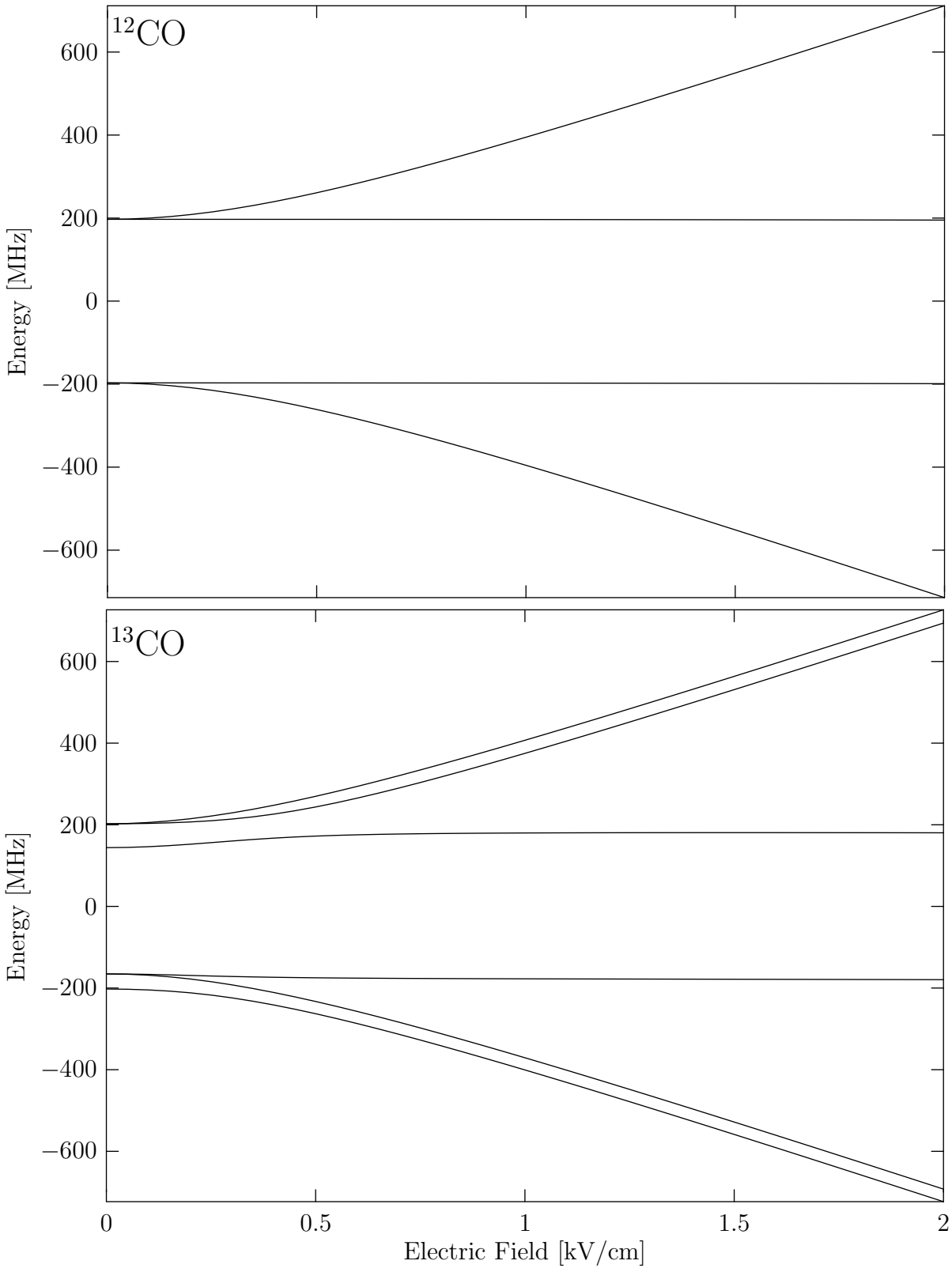

Figure 4.2: CO in the $a^3\Pi$, $J = 1$, $\Omega = 1$ state in a small electric field.

on the space-fixed Z-axis M_F.

$$\begin{aligned}
&\langle \Lambda S\Sigma J\Omega I F M_F \pm |\hat{H}_{\text{Stark}}|\Lambda S\Sigma J'\Omega I F' M_F' \mp\rangle = \\
&\sum_p T^1_{q=0}(\vec{\mu}) T^1_p(\vec{E})(-1)^p \langle \Lambda S\Sigma J\Omega I F M_F| - \mathfrak{D}^1_{-p0}{}^*|\Lambda S\Sigma J'\Omega I F' M_F'\rangle = \\
&\sum_p T^1_{q=0}(\vec{\mu}) T^1_p(\vec{E})(-1)^{F-M_F+p} \begin{pmatrix} F & 1 & F' \\ -M_F & -p & M_F' \end{pmatrix} \langle \Lambda S\Sigma J\Omega I F|| - \mathfrak{D}^1_{\cdot 0}{}^*||\Lambda S\Sigma J'\Omega I F'\rangle = \\
&\sum_p T^1_{q=0}(\vec{\mu}) T^1_p(\vec{E})(-1)^{F-M_F+p} \begin{pmatrix} F & 1 & F' \\ -M_F & -p & M_F' \end{pmatrix} (-1)^{J+I+F'} \sqrt{(2F+1)(2F'+1)} \\
&\qquad \begin{Bmatrix} F & F' & 1 \\ J' & J & I \end{Bmatrix} \langle J\Omega||\mathfrak{D}^1_{\cdot 0}{}^*||J'\Omega\rangle = \\
&\sum_p T^1_{q=0}(\vec{\mu}) T^1_p(\vec{E})(-1)^{I+F'+\Omega+F-M_F+p} \sqrt{(2F+1)(2F'+1)(2J+1)(2J'+1)} \\
&\qquad \begin{Bmatrix} F & F' & 1 \\ J' & J & I \end{Bmatrix} \begin{pmatrix} F & 1 & F' \\ -M_F & -p & M_F' \end{pmatrix} \begin{pmatrix} J & 1 & J' \\ -\Omega & 0 & \Omega \end{pmatrix}
\end{aligned} \tag{4.127}$$

Although the simple two-level model can no longer be applied to the low-field Stark shift in ^{13}CO, there are still certain similarities. At moderate fields, the Stark shift shows the same linear behavior as in ^{12}CO, since the mixing due to electric fields becomes much stronger than the mixing due to hyperfine interactions. However, as the electric field strength goes to zero, the hyperfine interaction maintains a splitting within each doublet. In the upper doublet component of the $J = 1$, $\Omega = 1$ state, the quadruply degenerate $F = \frac{3}{2}$ level has an energy about 58 MHz higher than the doubly degenerate $F = \frac{1}{2}$ component in the absence of a field. The four $F = \frac{3}{2}$ levels pass adiabatically into low field seeking states in the presence of a field, while the two $F = \frac{1}{2}$ states become states that have little interaction with an electric field. These two groups of states are never less than 50 MHz apart at any field strength.

4.5.3 Energy Levels in a Magnetic Field

In a magnetic fields, energy levels are shifted due to the Zeeman effect. While any charged particle with an angular momentum can contribute to the shift, the most significant contributions are those from the electron orbital angular momentum and from the electron spin angular momentum. The Zeeman Hamiltonian resulting from these two contributions is

$$\hat{H}_{\text{Zeeman}} = \mu_B \vec{B} \cdot (g_L \hat{L} + g_S \hat{S}) \tag{4.128}$$

where μ_B is the Bohr magneton and $\vec{B}$ is the magnetic field vector. Unless high accuracy is needed in the calculation of the Zeeman shift, it can be assumed that $g_L = 1$, $g_S = 2$, and that all other contributions, such as those from rotation of the molecule and from the nuclear spin, can be neglected.

In spherical tensor form, the Zeeman Hamiltonian has the form

$$\begin{aligned}\hat{H}_{\text{Zeeman}} &= \sum_p (-1)^p \mu_B T^1_p(\vec{B})(g_L T^1_{-p}(\hat{L}) + g_S T^1_{-p}(\hat{S})) \\ &= \sum_{p,q} (-1)^p \mu_B T^1_p(\vec{B}) \mathfrak{D}^1_{-pq}{}^*(g_L T^1_q(\hat{L}) + g_S T^1_q(\hat{S}))\end{aligned} \tag{4.129}$$

In ^{12}CO, $\mathfrak{D}^1_{-pq}{}^*$ acts on the total angular momentum wavefunction, while $T^1_q(\hat{L})$ and $T^1_q(\hat{S})$ act on the electron orbital angular momentum and electronic spin angular momentum wavefunctions, respectively. The matrix element of $\mathfrak{D}^1_{-pq}{}^*$ can be calculated using equation (4.52). The operator $T^1_q(\hat{L})$ only connects levels in the same vibronic state when $q = 0$ and then has an eigenvalue Λ. The matrix elements of $T^1_q(\hat{S})$ can be calculated using the Wigner-Eckart theorem. Since the resulting 3-j symbols are only non-zero when $q = \Omega - \Omega' = \Sigma - \Sigma'$, the matrix elements can be calculated as

$$\begin{aligned}&\langle \Lambda S \Sigma J \Omega M | \hat{H}_{\text{Zeeman}} | \Lambda S \Sigma' J' \Omega' M' \rangle = \\ &\sum_p \mu_B T^1_p(\vec{B})(-1)^{M-\Omega+p} \begin{pmatrix} J & 1 & J' \\ -M & -p & M' \end{pmatrix} \begin{pmatrix} J & 1 & J' \\ -\Omega & \Omega-\Omega' & \Omega' \end{pmatrix} \sqrt{(2J+1)(2J'+1)} \\ &\left(g_L \Lambda \delta_{\Sigma\Sigma'} + g_S (-1)^{S-\Sigma} \begin{pmatrix} S & 1 & S \\ -\Sigma & \Sigma-\Sigma' & \Sigma' \end{pmatrix} \sqrt{S(S+1)(2S+1)} \right)\end{aligned} \tag{4.130}$$

For ^{13}CO, the matrix element for $\mathfrak{D}^1_{-pq}{}^*$ must be calculated in a basis where F and M_F are good quantum numbers. Using the same technique as in equation (4.127), we find that

$$\begin{aligned}&\langle \Lambda S \Sigma J \Omega I F M_F | \hat{H}_{\text{Zeeman}} | \Lambda S \Sigma' J' \Omega' I F' M'_F \rangle = \\ &- \sum_p \mu_B T^1_p(\vec{B})(-1)^{I+F'+\Omega+F-M_F+p} \begin{pmatrix} F & 1 & F' \\ -M_F & -p & M'_F \end{pmatrix} \begin{Bmatrix} F & F' & 1 \\ J' & J & I \end{Bmatrix} \\ &\begin{pmatrix} J & 1 & J' \\ -\Omega & \Omega-\Omega' & \Omega' \end{pmatrix} \sqrt{(2F+1)(2F'+1)(2J+1)(2J'+1)} \\ &\left(g_L \Lambda \delta_{\Sigma\Sigma'} + g_S (-1)^{S-\Sigma} \begin{pmatrix} S & 1 & S \\ -\Sigma & \Sigma-\Sigma' & \Sigma' \end{pmatrix} \sqrt{S(S+1)(2S+1)} \right)\end{aligned} \tag{4.131}$$

When Λ, Σ, and Ω are inverted in the matrix elements of the Zeeman Hamiltonian, a phase factor of $(-1)^{J'-J}$ is introduced, instead of the phase factor $(-1)^{J'-J+1}$ seen in the matrix elements of the Stark Hamiltonian. The result of this is that, when calculating matrix elements using definite parity basis vectors, the Zeeman Hamiltonian only mixed states of the same parity.

$$\langle \Lambda S \Sigma J \Omega M \pm | \hat{H}_{\text{Zeeman}} | \Lambda S \Sigma J' \Omega M' \pm \rangle = \langle \Lambda S \Sigma J \Omega M | \hat{H}_{\text{Zeeman}} | \Lambda S \Sigma J' \Omega M' \rangle \tag{4.132}$$

Because magnetic fields can mix states with the same parity, they can produce diagonal contributions to the Hamiltonian, which leads to a true linear shift. By applying a small magnetic field, the components of each level split linearly according to their respective M or M_F quantum number. The case where an electric field is perpendicular

to a small electric field is shown for the $\Omega = 1$, $J = 1$ state in figure 4.3. Because the electric field is applied perpendicular to the magnetic field, the M or M_F levels can be mixed. In a strong electric field, where the electric field component of the Hamiltonian is much stronger than the magnetic field component, the effect of the magnetic field become negligible, and the energies asymptotically approach the value they would have without a field. At lower fields, however, the strengths of the electric field and magnetic field Hamiltonians become comparable, and since the M or M_F quantum are mixed, the energy levels do not cross as the electric field increases. If the two fields were parallel, states of different M or M_F would not mix.

4.6 Conclusions

The $a^3\Pi$ electronic state of CO has a rich structure. Even in a single vibrational state, there are three manifolds, labeled by the Ω quantum number, that are divided in energy by the spin-orbit coupling. Within each of these three manifolds is an extended series of rotational states, each of which is further subdivided into two levels, due to Λ-doubling. In ^{13}CO, each of these levels (with the exception of those where $J = 0$) are split once more due to hyperfine interactions. In the presence of an external electric or magnetic field, these levels can split many more times according to their M or M_F components.

Using just a few parameters, the energies and other properties for hundreds of states can be calculated. Because the fine and hyperfine structure is closely tied to angular momentum, their Hamiltonian can be written entirely in terms of spherical tensors, greatly simplifying many calculations. The matrix elements of terms of the Hamiltonian between Hund's case (a) basis vectors can be compactly represented in terms of 3-j symbols, 6-j symbols, and algebraic expressions. Once the matrix elements are calculated, diagonalizing the matrix simultaneously reveals the energy eigenvalues and the linear combination of basis states that form that state.

The energy level structure of $a^3\Pi$ CO is well suited to manipulation with electric fields, particularly in many of the closely spaced Λ-doublets which are strongly mixed by an electric field. The most strongly mixed states are the $\Omega = 1$, $J = 1$ state, which has a linear Stark shift of $\mu_{\text{eff}} = \frac{1}{2}|\vec{\mu}|$ and the $\Omega = 2$, $J = 2$ state, which has a linear Stark shift of $\mu_{\text{eff}} = \frac{2}{3}|\vec{\mu}|$.

Examining the $\Omega = 1$, $J = 1$ levels of CO shows that, for the ^{12}CO isotopologue with only an electric field (first part of figure 4.2), the energetic level structure is very simple. In the upper doublet component, one degenerate pair of states has increasing energy as a function of electric field (i.e. are low field seeking), and another state is mostly independent of field. At zero field, however, all three states are degenerate. This opens up a possibility that molecules initially in the low field seeking states can, when approaching regions of zero electric field, exit in the state that is uninfluenced by the field.

There are a few possible ways to avoid this problem. The first is to create an electric field distribution that never reaches zero field. The molecules will never see the degeneracy, and non-adiabatic losses can be prevented. This has already proven effective for preventing losses of ammonia molecules from a three-dimensional electrostatic trap [101]. Such a scheme is more difficult to implement in a two-dimensional trap: a purely

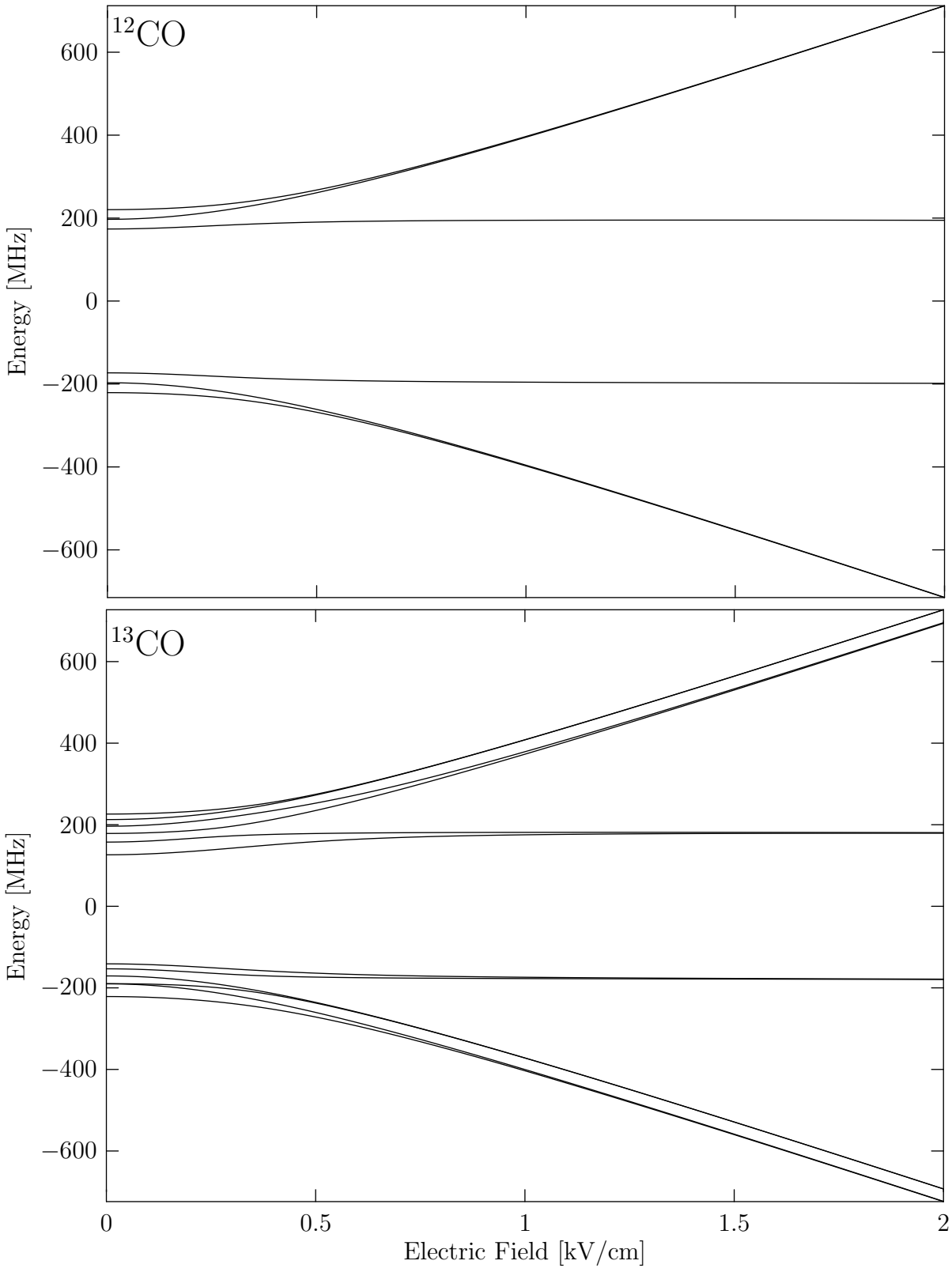

Figure 4.3: CO in the $a^3\Pi$, $J = 1$, $\Omega = 1$ state in a small electric field with a 50 Gauss magnetic field applied perpendicular to the electric field.

two-dimensional field cannot contain a field minimum that is at non-zero field [102]. A homogeneous offset field could be added in the third dimension, but the long electrodes used to produce a two-dimensional field would tend to screen this effect. Another more effective solution is to use a magnetic field instead of an electric field in the third dimension: this also breaks the degeneracy observed at zero electric field, but is not screened by non-magnetic electrodes. A third solution is to chose an isotopologue with a favorable hyperfine structure that breaks the degeneracy between low field seeking states and states unaffected by electric fields.

Simply breaking the degeneracy by an infinitesimal amount will not suffice to prevent non-adiabatic transitions, but exactly how much splitting is needed is not clear. Experimental studies must be carried out to examine such losses. In order to understand such measurements quantitatively, it becomes essential to understand the energy level structure in detail. Only then can the nature of these losses be properly understood.

Chapter 5

Experimental Setup

In this chapter, we describe the experimental apparatus that has been used to conduct the experiments presented in this thesis. At the center of the apparatus are the components of the molecular beamline seen in figure 5.1. All components shown in this figure are contained in two differentially-pumped high vacuum chambers that are separated by a skimmer with a 1 mm opening. The first chamber, which contains the pulsed valve and through which the excitation laser passes, is maintained at an average pressure of 10^{-5} mbar during operation using a 300 L/s turbomolecular pump backed by a 16 m^3/hr rotary pump; the second chamber, containing the molecule chip and the Auger detector, is pumped by a 120 L/s turbopump backed by the same rotary pump and typically has a pressure of $4 \cdot 10^{-8}$ mbar. The experiment typically runs as follows: ground state CO molecules, initially in a gas bottle and diluted in a noble gas, expand into the first vacuum chamber through the pulsed valve, creating a molecular beam. They are then excited into their metastable state using a narrow-bandwidth pulsed laser and pass through the skimmer into the next chamber. After 19 cm of free flight, the excited molecules reach the molecule chip, where they are manipulated by electric fields. Finally, after the molecules leave the chip, they continue to the Auger detector, where the arrival time of each molecule is recorded. This sequence is repeated at 10 Hz, and the data collected in each run is averaged many times (typically for 1 to 4 hours) to produce arrival time distributions.

Subsequent sections of this chapter describe these various components in detail: the pulsed valve/molecular beam, the laser system used to produce the excitation pulse, the molecule chip, along with its precision mechanical manipulator and the amplifiers used to apply potentials to its electrodes, and the Auger detector. While many of the devices described are not unique to this experiment (the laser system was developed previously and a variant of the metastable CO detector had already been constructed [103]), their importance to the experiment warrants a brief discussion of their operation. The molecule chip, along with its manipulator and electronics, is a new development of this project and will be described in more detail.

5.1 Supersonic Expansion and Molecular Beam

At the beginning of the experiment, molecules are injected into vacuum through a series 99 General Valve. In this valve, a 1 mm opening to the vacuum chamber is initially

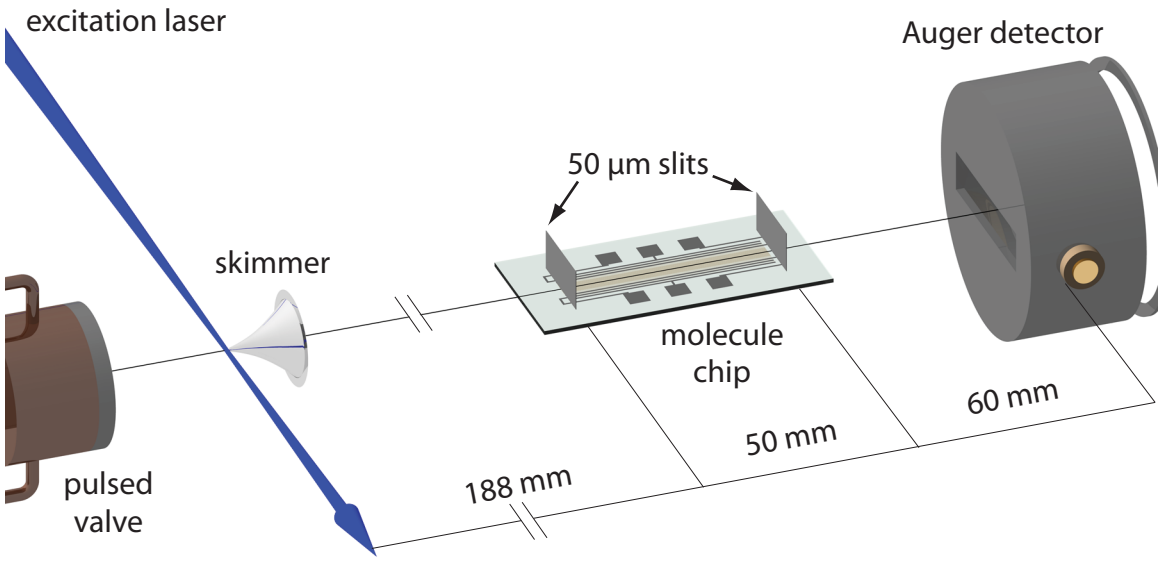

Figure 5.1: The molecular beamline used in the experiments presented here. The components are contained in two differentially pumped high vacuum chambers, separated by a skimmer. A pulsed beam of molecules is emitted from the valve, which then passes through the skimmer. The molecules are manipulated by the chip and afterward continue to the Auger detector.

sealed by a conical poppet, which is held in place by a spring. The poppet is retracted by means of a solenoid to which a 300 volt, ∼100 µs pulse is applied, and the gas expands into the vacuum. Because the opening is large and the density of gas molecules behind the opening is high, an individual molecule will undergo many collision with other gas molecules as it enters the vacuum chamber. This results in what is known as supersonic expansion.

Injecting molecules into vacuum in this manner accomplishes two goals. Firstly, simply by bringing the molecules into vacuum, they enter an environment where they behave as isolated particles. The molecules can then be manipulated without colliding or otherwise interacting with other molecules. Secondly, a supersonically expanded molecular beam cools the molecules. In fact, the supersonic expansion is the only point in the experiment where real cooling occurs: once the expansion is over and the molecules stop colliding, energetic particles can still be removed, but the resulting particle energy distribution will no longer have a thermal distribution.

The properties of an ideal supersonic expansion are based on the assumption that the gas expands adiabatically, i.e. without exchanging heat with its surroundings, and in order to conserve energy, the sum of the enthalpy of a parcel of gas and its kinetic energy must be constant [104]. Since the enthalpy per particle of a given sample of gas can be described as a function of its temperature and pressure, the differential enthalpy per particle, dH, is given by

$$dH = \left(\frac{\partial H}{\partial T}\right)_P dT + \left(\frac{\partial H}{\partial P}\right)_T dP = C_P(T,P)(dT + \mu_{\mathrm{JT}}(T,P)dP) \tag{5.1}$$

Here, $C_P = \left(\frac{\partial H}{\partial T}\right)_P$ is the heat capacity per particle at constant pressure and $\mu_{\mathrm{JT}} =$

$\left(\frac{\partial T}{\partial P}\right)_H$ is the Joule-Thomson coefficient.

For the most part, it is assumed that the gases being expanded are ideal gases. An ideal gas can be defined as fulfilling the condition $PV = kT$, where P is pressure, V is the volume per particle, k is the Boltzmann constant, and T is the absolute temperature. Based on this, it can be shown that $\left(\frac{\partial H}{\partial P}\right)_T = 0$[1], i.e. the enthalpy per particle depends only on temperature, and equation (5.1) can be simplified to $dH = C_P(T)dT$. For the expansion of an ideal gas, the maximum possible velocity at the end of the expansion (terminal velocity) is found by assuming that all enthalpy is converted to kinetic energy, i.e.

$$\frac{m}{2}{v_t}^2 = H_0 = \int_0^{T_0} C_P(T)dT \tag{5.3}$$

Here, m is the mass of an individual particle, T_0 is the initial temperature, and v_t is the terminal velocity. In most cases, C_P can be treated as being independent of temperature: though this is not quite true at very low and sometimes very high temperatures, the effect of these regions on the expansions of interest is negligible [104]. Using this approximation, v_t is given by

$$v_t = \sqrt{\frac{2C_P T_0}{m}} \tag{5.4}$$

If the expansion of an ideal gas is adiabatic ($TdS = 0$) and C_P is constant, there is a simple expression for temperature as a function of pressure or volume. First, it is noted that $dH = C_P dT = VdP$, since dH can generally be written as $dH = TdS + VdP$. Dividing $C_P dT$ by kT and VdP by PV, which are the same for ideal gases, results in the differential equation $(C_P/k)\frac{dT}{T} = \frac{dP}{P}$, which can be rewritten as $(C_P/k)d(\ln T) = d(\ln P)$. The solution to this differential equation is given by

$$\left(\frac{P}{P_0}\right) = \left(\frac{T}{T_0}\right)^{C_P/k} \tag{5.5}$$

If $\left(\frac{P}{P_0}\right)$ is replaced by $\left(\frac{TV_0}{T_0V}\right)$, an equation relating the volume per particle and the temperature can be written.

$$\left(\frac{V}{V_0}\right) = \left(\frac{T}{T_0}\right)^{1-C_P/k} \tag{5.6}$$

For CO, $C_P = 3.5\,k$ and $m = 28\,\text{amu}$, so an expansion of CO from room temperature (295 K) could have a terminal velocity as high as $v_t = 780\,\frac{\text{m}}{\text{s}}$, much higher than is desirable. From equation (5.4) it is seen that there are three parameters that can be changed to lower this speed: the temperature of the gas in the source, the heat capacity of the molecules being expanded, and their mass. Lowering the temperature of the gas in

[1]Based on the differential definition of enthalpy $dH = TdS + VdP$, $\left(\frac{\partial H}{\partial P}\right)_T$ can be written as

$$\left(\frac{\partial H}{\partial P}\right)_T = T\left(\frac{\partial S}{\partial P}\right)_T + V \tag{5.2}$$

Using the Maxwell relation derived from Gibbs free energy, $-\frac{\partial^2 S}{\partial P \partial T} = \left(\frac{\partial S}{\partial P}\right)_T = -\left(\frac{\partial V}{\partial T}\right)_P$. From the ideal gas equation, $\left(\frac{\partial V}{\partial T}\right)_P = \frac{k}{P} = \frac{V}{T}$, from which it follows that $\left(\frac{\partial H}{\partial P}\right)_T = 0$ for an ideal gas.

the source easily reduces the expansion velocity: if the same expansion is performed using a sample of CO near its boiling point (82 K), the terminal velocity is only $v_t = 410\,\frac{\mathrm{m}}{\mathrm{s}}$. Although it is impossible to change the heat capacity or mass of CO directly, it is possible to effectively improve them using a technique known as *seeding*. If a small fraction of CO is mixed with a heavy noble gas, such as krypton or xenon, and the resulting mixture is expanded, the terminal velocity will be determined by the properties of the noble gas. The properties of heavy noble gases are much better suited to producing a slow beam. Krypton and xenon, in particular, are nearly three times and five times more massive, respectively, than CO. Additionally, C_P is only $2.5\,k$ for a monoatomic molecule instead of $3.5\,k$ as for CO: C_P depends on the number of degrees of freedom of the particle, increasing by $\frac{1}{2}\,k$ for each additional degree of freedom, and since an atom lacks the two rotational degrees of freedom present in CO, its C_P is reduced by k. More than just lowering the terminal velocity, reducing the heat capacity C_P also improves the cooling[2], if the collision cross sections of the two gases are the same. Even in a mixture with a somewhat higher concentration of CO (e.g. 20% CO), the seeding principle works, though C_P and m in equation (5.4) must be taken as the average heat capacity per particle and the average mass per particle, respectively.

In the experiments presented here, three different carrier gases were used: xenon, krypton, and argon. In each case, the gas mixture that was expanded consisted of 20% CO and 80% noble gas at an initial total pressure of about 1 bar. To achieve the lowest possible velocity, the mixtures were cooled to a temperature slightly above the boiling point of the noble gas: 200 K for xenon, 140 K for krypton, and 102 K for argon. Although these initial temperatures are higher than the 0.8 bar boiling points of each noble gas (see details in table 5.1), it was empirically determined that temperatures much lower than those used led to an instability of the expansion. The inability to use initial temperatures closer to the boiling point is probably a result of the rapid cooling during the expansion. For example, after each mixture has expanded to half its initial pressure,

[2]A complete argument as to why lowering C_P improves the cooling is somewhat subtle. One simple argument would be to assume that cooling stops at a specific collision rate, which for a given collision cross section and mass, should be proportional to $\frac{\sqrt{T}}{V}$, where T is the temperature and V is the volume per particle.

$$S = \frac{T_0}{T} \approx \left(\frac{V}{V_0}\sqrt{\frac{T_0}{T}}\right)^{\left(\frac{C_p}{k}-\frac{1}{2}\right)^{-1}} \tag{5.7}$$

The initial collision rate is larger than the final collision rate, so $\left(\frac{V}{V_0}\sqrt{\frac{T_0}{T}}\right)$ is larger than 1. Since the exponent increases for decreasing C_p (as long as $C_p > \frac{1}{2}$), the degree of cooling $S = \frac{T_0}{T}$ must be larger when C_p is smaller.

A more exact solution, presented by D.R. Miller [104], is given by

$$S = A(\sqrt{2}V_0^{-1}\sigma d)^B \tag{5.8}$$

where V_0 is the volume per particle in the source, σ in the collision cross section, d is the nozzle diameter, and A and B are parameters that depend on C_P. The factor $V_0^{-1}\sigma d$ describes the ratio of the nozzle diameter to the mean free path of molecules in the source, so this is generally much larger than 1. As a result, larger exponents correspond to larger cooling. For $C_P = 3.5\,k$, $B = 0.353$, but for $C_P = 2.5k$, the exponent increases to $B = 0.545$, yielding a better cooling. Surprisingly, these values of B are not much different from the values 0.333 and 0.5 given by the simple model above.

	Xe	Kr	Ar
Carrier gas boiling point at 0.8 bar [K]	162	117	87
Minimum valve temperature [K]	200	140	102
Temperature of gas after expanding to $P = 0.5P_0$ [K]	155	108	79
Boiling point at 0.4 bar [K]	153	109	80
Expected terminal velocity [m/s]	285	294	349
Observed terminal velocity [m/s]	310	310	360

Table 5.1: Parameters of the supersonic expansion of mixtures of 20% CO in xenon, krypton, and argon, starting with an initial total pressure of 1 bar. While it would be expected that the initial temperature of the gas could be lowered to just above the 0.8 bar boiling point, the minimum temperature below which the expansion breaks down is actually somewhat higher. On the other hand, a gas expanding adiabatically from the observed minimum valve temperature to half of its initial pressure will cool to a temperature close to the 0.4 bar boiling point of the carrier gas. Using equation (5.4), it is possible to predict the terminal velocity of the expansion, but the experimentally observed velocities are consistently somewhat higher. Vapor pressure data from reference [105].

the temperature of the gas will reduce to a value close to the 0.4 bar boiling point. After further expansion, it is likely that some amount of clustering will occur as the noble gas cools below its boiling point, which will cause the molecules in the expansion to cool less due to the heat released in cluster formation. Since the boiling point of CO is 82 K and its partial pressure is only 0.2 bar, however, CO is never a limiting factor in the minimum initial temperature of the expanded gas. Using equation (5.4), it is possible to estimate the terminal velocity of the expansion (summarized in table 5.1). The observed velocity is somewhat higher, possibly due to clustering in the beam. Additionally, the observed velocity of a krypton-seeded beam at 140 K is no faster than the xenon-seeded beam at 200 K, but because the krypton-seeded beam results in more signal at the detector (possibly due to a lower transverse velocity distribution), krypton is used preferentially in later experiments.

5.2 The Laser System

The freshly-expanded CO molecules are cold, occupying only the first few rotational levels of its $X^1\Sigma^+$, $v = 0$ ground state. Unfortunately, CO in its ground state has little Stark shift: the combination of a relatively tiny 0.1 Debye dipole moment and the large splitting between states that can be mixed by the electric field results in a quadratic Stark shift that, even at 100 $\frac{\text{kV}}{\text{cm}}$, is less than 100 MHz. In the $a^3\Pi$ electronic state, however, the body fixed dipole moment of 1.37 Debye and the small splittings between field mixed states result in strong linear Stark shifts even at 1 $\frac{\text{kV}}{\text{cm}}$. In principle, optical dipole transitions should not be allowed between the ground state and the a state, due to selection rules that forbid changes of spin state. The $a^3\Pi$ state, however, is not a pure triplet state: through spin-orbit coupling, it is slightly mixed with the higher-lying $A^1\Pi$ state, and transitions between this state and the ground state are strongly allowed.

	^{12}CO	^{13}CO
$Q_2(1)$ Produces low field seekers	48474.642 = 3·16158.214 cm^{-1}	48479.571 = 3·16159.857 cm^{-1}
$R_2(0)$ Produces high field seekers	48478.474 = 3·16159.491 cm^{-1}	48483.234 = 3·16161.078 cm^{-1}

Table 5.2: Experimentally-relevant $a^3\Pi(v' = 0) \leftarrow X^1\Sigma^+(v'' = 0)$ transitions in CO. Because the light used to drive these transitions is frequency tripled, the frequencies of the fundamental (i.e. before tripling) are included for convenience.

Because the spin-orbit interaction in diatomic molecules preserves angular momentum along the internuclear axis, this mixing is only possible when $|\Omega| = 1$, so levels that have the most $|\Omega| = 1$ character are easiest to reach.

To excite CO to the a state with a pulsed laser requires that laser to have a fairly high pulse energy and narrow bandwidth. The laser system available produces 3 ns pulses of 206 nm light with a pulse intensity of 2 mJ and a bandwidth of 150 MHz, a bandwidth limited only by the width of the pulse. If these 2 mJ are focused to a 1 mm^2 spot, transitions to $|\Omega| = 1$ levels can be saturated. In principle, it is also possible to reach $|\Omega| = 0$ and $|\Omega| = 2$ levels, since they contain a slight $|\Omega| = 1$ character, but the transitions cannot be saturated so easily.

The largest Stark shift in the $|\Omega| = 1$ manifold occurs in the $J = 1$, $|M| = 1$ levels, so the transition is generally driven to this state. At zero field, the state is divided into Λ-doublet components separated by 394 MHz, and as a field is applied, low field seeking components originate from the upper doublet component and high field seeking components originate from the lower component (see figure (4.2)). The two components have opposite parity: the upper has positive parity and the lower negative parity. Because the parity of the state must change during a transition, the upper level can only be excited from states of negative parity and the lower level can only be excited from states of positive parity. In the ground state, the parity of the Nth rotational state is given by $(-1)^N$. Combined with ΔJ selection rules, the lower level can be excited from $N = 0$ or $N = 2$, but the upper level can only be excited from the $N = 1$ rotational level in the ground state. To produce low field seeking CO molecules, a $Q_2(1)$ transition is induced: Q implies that $\Delta J = 0$, the subscript 2 refers to the second spin-orbit manifold, i.e. $|\Omega| = 1$, and 1 indicates that the transition originates from $N = 1$ in the ground state. To produce high field seekers, either an $R_2(0)$ ($\Delta J = +1$, $N = 0$) or a $P_2(2)$ ($\Delta J = -1$, $N = 2$) can be driven, but because the population of molecules in the $N = 2$ state in the beam is relatively low, using the $R_2(0)$ transition is much more practical. The frequencies of these transitions are summarized in table 5.2.

The first components of the laser system used to drive these transitions operate in continuous wave (CW) mode (see figure 5.2). A frequency doubled Nd:YVO_4 laser (Coherent Verdi), producing a power of 5 W at a wavelength of 532 nm, is used to pump a ring dye laser. The 532 nm laser is focused onto a thin, fast moving jet of sulforhodamine B dye dissolved in ethylene glycol. A configuration of four mirrors is placed such that photons emitted from this laser focus can reflect once from each mirror, tracing out a path that resembles a bow tie, and return to the jet at the same position from which it

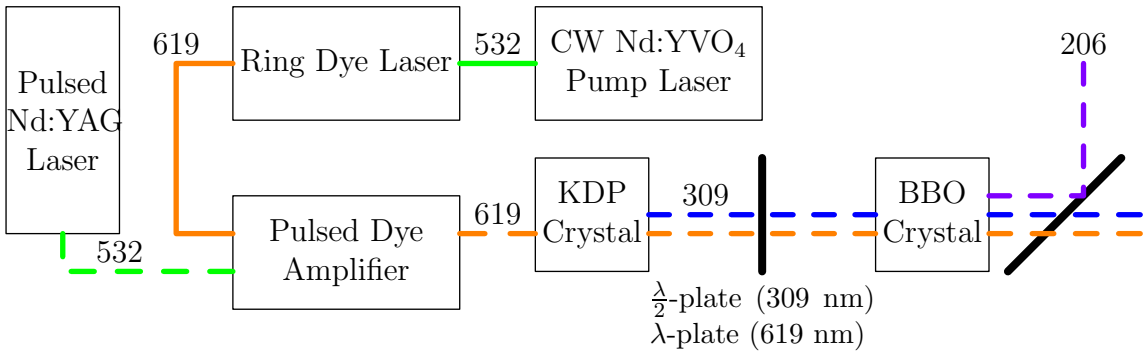

Figure 5.2: Overview of the laser system used to produce Fourier limited bandwidth pulses of 206 nm light. A continuous 619 nm laser beam from a ring dye laser is pulse amplified and subsequently tripled. These pulses are used to excite CO molecules to the $a^3\Pi_1$ metastable state.

left, traveling in the same direction [106]. It can then induce stimulated emission in the dye jet, and if the photon experiences an integral number of oscillations over this path, the light will be amplified. Since the path through the four mirrors in about 3 m long, the laser could in principle resonate on thousands of modes, separated by 100 MHz, over the entire gain curve of the dye. To prevent this, several additional elements are inserted into the cavity: a birefringent filter provides a wide mode structure (a few THz), a thin etalon provides an intermediate mode spacing (200 GHz), and a thick etalon yields a fine mode spacing (10 GHz). Only a very narrow range of modes (< 1 GHz) are transmitted by all three elements, and only one is amplified, resulting in a single mode laser.

The beam that emerges from the ring dye laser has a wavelength of 619 nm and a power of about 300 mW. This beam continues to the pulsed dye amplifier and passes through three cuvettes containing a solution of *DCM Special* dye in ethanol. These three cuvettes are then illuminated from the side by a 5ns pulsed Nd:YAG laser. This pulse-amplifies the 619 nm beam, resulting in a 100 mJ pulse with very narrow bandwidth. A KDP crystal frequency doubles the vertically-polarized 619 nm laser pulse, producing a horizontally-polarized pulse of 309 nm radiation. The polarization of the 309 nm light is made vertical with a $\frac{\lambda}{2}$-plate, and the vertically-polarized 619 nm and 309 nm beams are sum frequency mixed to produce 2 mJ of 150 MHz-bandwidth 206 nm light.

5.3 The Molecule Chip

After the CO molecules are excited to their metastable state, they pass through a skimmer and continue flying to the chip, where they are manipulated by electric fields. The chip itself is based around an array of 1254 gold electrodes deposited onto a glass substrate, each 10 μm wide and approximately 100 nm high with a 40 μm center-to-center spacing, forming a decelerator structure that is 50.16 mm long. The electrodes are arranged into six independent sets of 209 electrodes.

In a single plane, it is only possible to connect two sets of independent periodic electrodes. (This arrangement resembles two interleaved combs and can be seen in [73].), To connect all six sets of electrodes, the chip needs to have more than one layer. In the

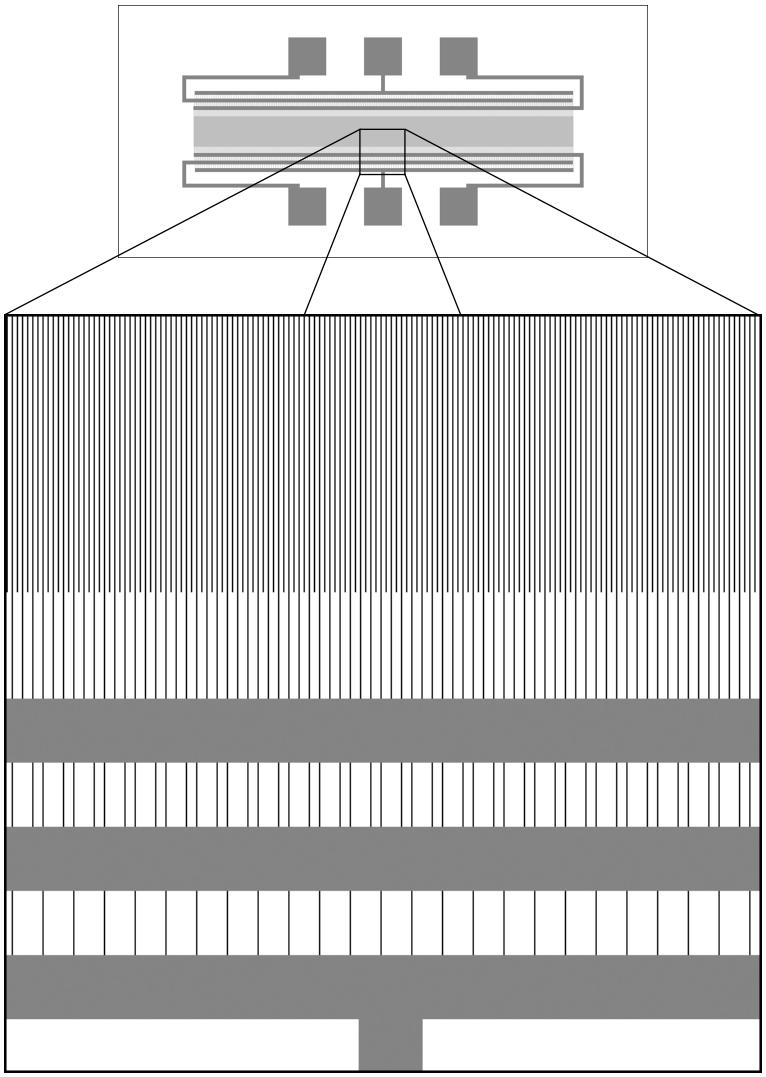

Figure 5.3: The molecule chip at actual size, with a section magnified by a factor of 17. The 10 µm wide electrodes, separated by a center-to-center spacing of 40 µm, extend alternatingly to the two sides of the chip. In the magnified image, only the lower side is shown. The electrodes terminate at three different lengths and are connected to the amplifiers through six nickel strips, three of which are shown here.

present chip, this is solved as follows: all electrodes extend over a central 4 mm region, but outside this region, the electrodes extend alternatingly to the left or to the right and terminate at three different lengths. The portions of the electrodes outside the central region are covered with a 200 nm-thick layer of dielectric, except at the tips, where the dielectric is etched away. Six 0.5 mm wide nickel strips, running perpendicular to the electrodes, are deposited on top of this dielectric layer such that they each only make contact to one of the sets of electrodes through the etched holes. The six nickel strips, three on each side, are used to connect the microscopic electrodes to the amplifiers.

Because the microelectrodes are very long (4 mm) compared to their width and spacing, the potential they produce is quasi two dimensional: the changes in the electric potential along the direction parallel to the long axis of the electrodes is very gradual (on the millimeter length scale) compared to changes in the other two directions and can be neglected when calculating electric fields. Chapter 3 extensively discusses the fields produced by two-dimensional periodic arrays of electrodes, and describes how, using six electrodes per period, two movable quadrupole minima per period are produced (see figure 3.7). For molecules in low field seeking states, these electric field minima act as traps. The form of these traps is shown in figure 5.4 for the low field seeking components of $a^3\Pi_1$, $v = 0, J = 1$ CO for various positions above the surface. The shape of the contour lines is very similar to the shape of the electric field strength contours except near the electric field minima, where the form of the mechanical potential is slightly quadratic in electric field due to the Λ-doubling, described in chapter 4. The waveforms required to produce this motion are sine waves, three positive and three negative with 120 degree phase shifts, that are applied as shown in figure 5.5.

One question that arises, however, is what happens near the edges of the active area, where the assumptions of a purely two dimensional potential and strict periodicity break down. At the ends of the array, the assumption of periodicity breaks down when the electrodes stop repeating. In practice, however, the minima have already attained their normal form one period (6 electrode spacings) from the ends of the array. At the sides, where half of the long, thin electrodes terminate, the structure of the fields is no longer two-dimensional. In fact, three-dimensional calculations show that, even 1 mm from the edge of the 4 mm active area, there is a noticeable distortion of the minima, but the depth of the trap is hardly influenced. The same calculations also show that the traps have an electric field barrier in the third dimension that is as strong as the saddle point that limits the trap depth in the other two dimensions. Qualitatively, this can be understood by recognizing that, on the side of the array where all negative electrodes end, all positive electrodes continue to their connection points: the negative ends surrounded by a most positive environment results in a strong electric field. A similar argument can be made for the other side of the chip by reversing positive and negative.

The chip is oriented such that the metastable CO molecules fly parallel to the surface and perpendicular to the electrodes. In this way, the molecular beam axis matches the translation direction of the two-dimensional potential wells, and by translating the traps over the surface at the same velocity as the molecules, the molecules can be carried in moving traps over the surface. Additionally, if the velocity of the traps is decreased while the molecules are in them, as long as the rate of deceleration is not too high, the molecules will be decelerated along with the traps. Since the minima maintain the same shape while traveling over the chip, one way to visualize the deceleration is to consider

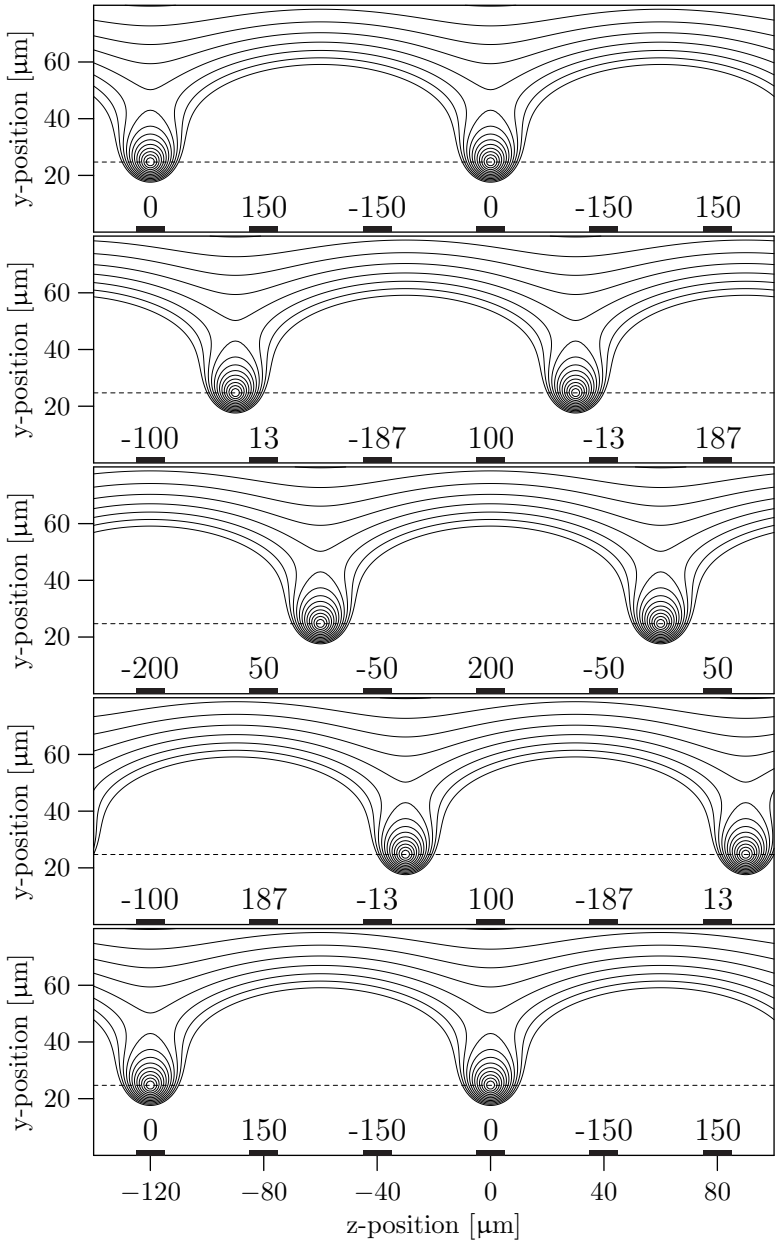

Figure 5.4: Potential energy contours seen by ^{12}CO in the low field seeking components of the $a^3\Pi_1$ ($J = 1$, $v = 0$) state when waveforms with a 200 V peak-to-peak amplitude are applied to the electrodes. Roughly 70 mK deep traps can be translated at a constant distance from the surface. The electrodes are shown schematically at the bottom of each frame along with the potential applied to each one. Contour lines are separated by 7.5 mK.

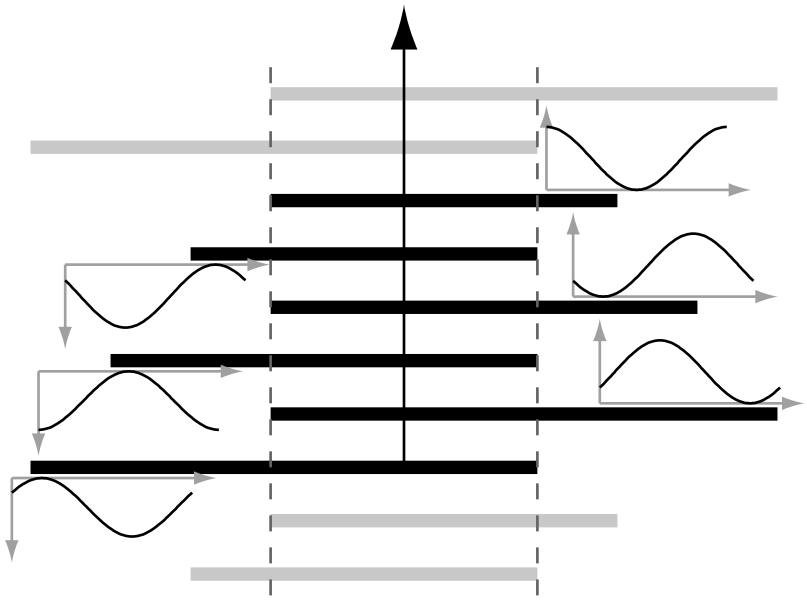

Figure 5.5: Schematic diagram of the six electrodes that make up a period on the chip. All six electrodes in each period extend over a central region, but to facilitate connections to the amplifiers, the electrodes extend alternatingly to opposite sides and terminate at three different lengths, where they connect to larger conductors that run over the tips of the electrodes. The six waveforms applied to the electrodes are three positive and three negative sine waves with 120 degree phase shifts. Using this arrangement, the positive waveforms are all applied from the right side of the chip, and the negative waveforms from the left side of the chip.

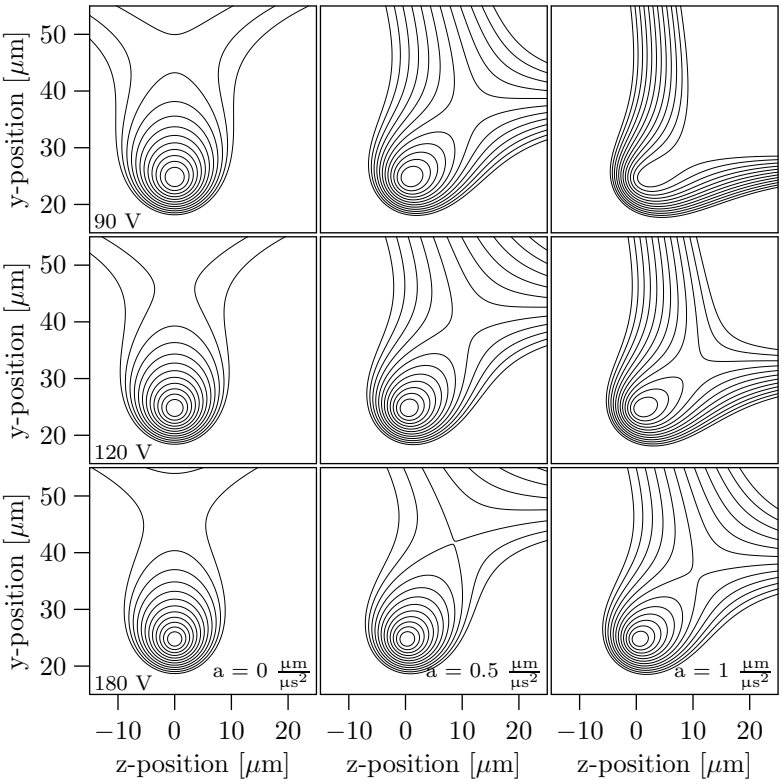

Figure 5.6: If a microtrap is decelerated at a constant rate, the potential energy surface is distorted by the addition of a pseudoforce. Here, this effect is shown for potentials created by waveforms with a peak-to-peak amplitude of 90 V, 120 V, or 180 V. Contour lines are separated by 2.6 mK, 3.5 mK, and 5.3 mK in the 90 V, 120 V, and 180 V plots, respectively. At zero acceleration, the traps are symmetric around $z = 0$, but as the deceleration increases, the traps tilt to the right and become shallower. In the extreme case, seen at the upper right, the trap completely disappears.

the equations of motion in an accelerated frame moving with the decelerating traps. In an accelerated coordinate system, an additional term must be added to the potential to account for the pseudoforce which has the form $U_{\text{pseudo}} = -maz$, where m is the mass of the molecule, a is the rate of deceleration, and z is the longitudinal position. The result of combining the standard trap potential with this pseudopotential is shown in figure 5.6 for various peak-to-peak waveform amplitudes and accelerations. As the traps are decelerated, the potential is distorted, and the volume and depth of the traps decrease, from which it becomes clear that fewer molecules will be captured at higher decelerations. In the extreme case (seen in figure 5.6 for 90 V waveforms at an acceleration of 1.0 $\frac{\mu m}{\mu s^2}$), the potential no longer contains a minimum, and no molecules can be captured at all.

Two razor edges are placed 50 µm above the first and the last electrodes of the array, parallel to the electrodes. In the region outside the potential wells there is a strong electric field gradient away from the surface, i.e. the fields are very strong near the surface and decay exponentially as a function of transverse position. The front razor edge ensures that molecules arriving above the chip are at most 50 µm from the surface. Low field seeking molecules that are this close to the surface but are not in traps are pushed away and will be filtered out by the back razor edge. Molecules that are in the traps, however, will be efficiently guided to the end of electrode array. Not all metastable CO molecules that are not in the traps are filtered out: molecules in the $M = 0$ state are weakly high field seeking, and will see a slight force toward the surface. This force, when applied during the molecule's entire flight over the chip, is of a sufficient order of magnitude that a large fraction of the molecules will be pulled to the surface and thus be lost. Some smaller fraction, however, can just barely pass over the entire chip without colliding with the razors or the surface. These molecules will generally pass just under the first razor with an initial transverse velocity away from the chip, reach a maximum distance from the surface near the center of the chip, and pass under the second razor with a transverse velocity toward the chip. The $M = 0$ molecules that reach the detector produce a broad background signal that can make the molecules that were in the traps more difficult to detect.

5.3.1 Chip Manipulator

To effectively bring the molecules onto the chip, it is necessary to have precise control of the position and orientation of the chip with respect to the incoming molecular beam. Fortunately, not all degrees of freedom are important. The exact position along the molecular beam, for example, while important for the timings of the waveforms, does not need to be adjusted on length scales shorter than a centimeter. Precise control of the tilt around the molecular beam axis is also unimportant. The tilt around the axis perpendicular to the chip surface and the position of the chip along the axis parallel to the microelectrodes should be adjusted such that the molecular beam axis is perpendicular to the electrodes and centered on the active area. Since the active area is 4 mm wide, the adjustments only need to be made within about 0.5 mm. This can be done with sufficient accuracy by replacing the valve with a HeNe laser, directing the laser beam through the skimmer, and adjusting the chip so that the beam is centered on the array over its entire length. Because the adjustment does not need to be done while the chip is under vacuum, it can be accomplished with normal fine-threaded screws.

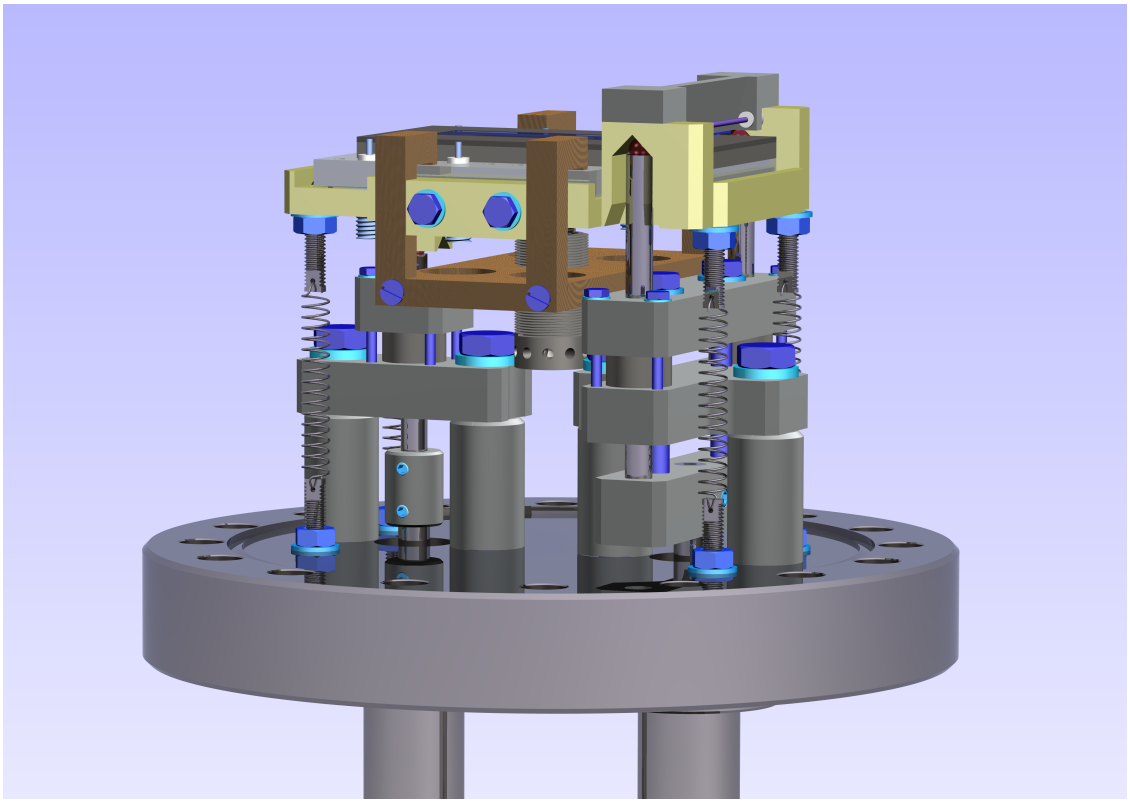

Figure 5.7: The precision manipulator for the molecule chip. Linear motion feedthroughs allow precision adjustment of the height and tilt of the chip while it is in vacuum, and other adjustments are possible while the chamber is vented. (Design and drawing by H. Haak)

There are two remaining degrees of freedom: the tilt of the chip around the axis parallel to the electrodes and the position of the chip along the direction perpendicular to its surface. Though the position only needs to be adjusted within 0.5 mm, the tilt must be adjusted very precisely. First, the depth of the traps is much less than the longitudinal kinetic energy of the beam. In early experiments, the trap was only 25 mK deep, so a molecule at the center of the trap with a relative velocity of 4 m/s would have enough energy to escape. If the chip were tilted even by a few tenths of a degree with respect to the molecular beam, the molecules would gain a significant transverse velocity component and could no longer be confined by the traps. The ability to precisely control the tilt of the chip also enables the suppression of signal from molecules in $M = 0$ states that contribute to background signal. If the chip is slightly tilted toward the incoming molecular beam, i.e. such that the molecules have a slight transverse velocity toward the surface, molecules in the $M = 0$ states will be blocked, since they must have a transverse velocity away from the surface to traverse the entire length of the chip. To accomplish these tasks effectively, the control of this tilt should be better than 0.1 degree.

The manipulator constructed to precisely position the chip is shown in figure 5.7. The chip, represented by the large, dark gray plate near the top of the figure, can be manipulated while in vacuum using two linear motion feedthroughs with micrometer screws. Their extension can be adjusted to a precision of 10 μm, allowing linear positioning of the

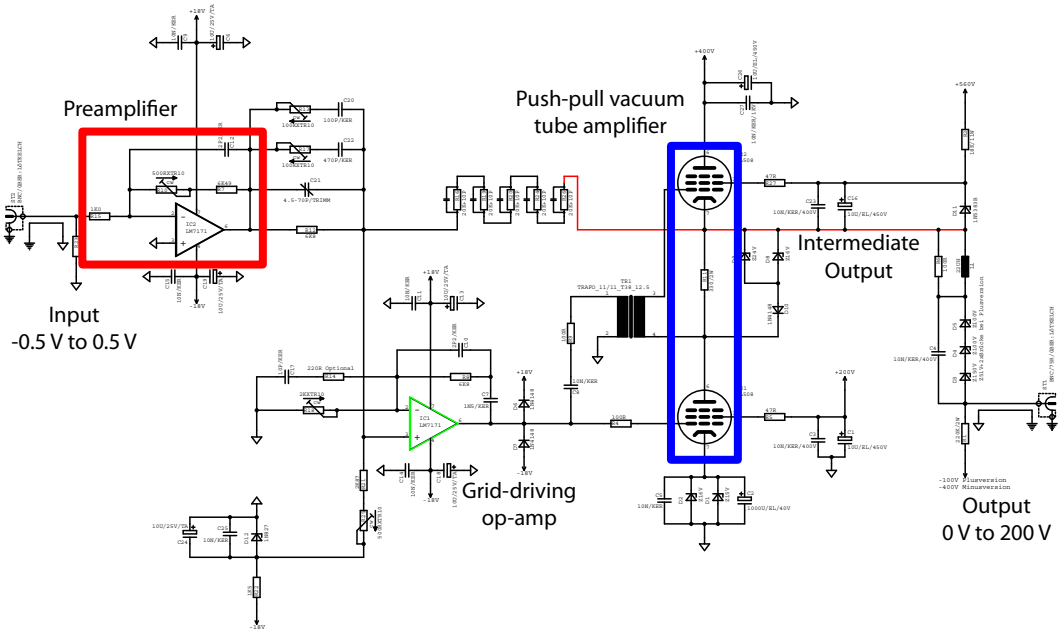

Figure 5.8: Vacuum tube amplifier used to produce the waveforms applied to the chip. (Design by H. Müller and drawing by V. Platschkowski)

chip perpendicular to its surface by the same amount. Since the two contact points are roughly 56 mm apart, a 1 mm change in the position of one of the two linear positioners tilts the chip around the long axis of the electrodes by about 1°, giving an adjustment precision of 0.01°. If the chamber is vented, the chip can also be translated in the plane of its surface and rotated perpendicular to the surface by sliding the light gray plate across the top surface of the yellow part in figure 5.7. In addition to the mechanical positioning features, the manipulator also contains sockets for the six electrical connections to the chip's electrodes and clamps for the entrance and exit slits.

5.3.2 Amplifiers

To manipulate the molecules on the chip requires waveforms with peak-to-peak amplitudes up to 200 V and frequencies between 0 and 3 MHz. Creating an amplifier that is capable of a slew rate of up to 2 $\frac{\text{kV}}{\mu\text{s}}$ and covers such a wide bandwidth (especially when the bandwidth range includes zero frequency) pushes the limits of current technology. The solution that was developed uses pentode vacuum tubes to achieve this high slew rate and a high frequency op-amp to operate the negative feedback loop. The schematic for this amplifier is shown in figure 5.8. The input signal is preamplified using an LM7171 high frequency (700 MHz unity-gain bandwidth) op-amp and passed to the positive input of a second LM7171 that drives the grid of a PL508 pentode. This pentode is the sinking component of a push-pull amplifier; a second PL508 (upper pentode in the diagram) sources current to the intermediate output when the first pentode stops conducting. The intermediate output is coupled back to the positive input of the second op-amp to provide negative feedback. Since the intermediate output can only vary from 100 V to 300 V, it is offset in a positive amplifier by 100 V using Zener diodes to produce an output potential

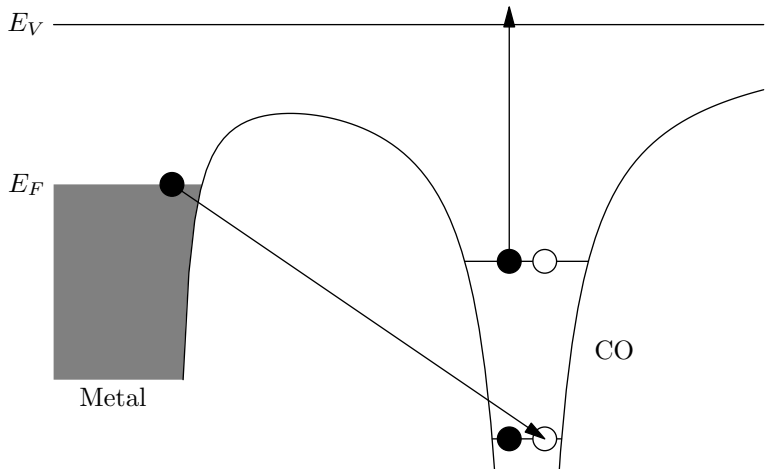

Figure 5.9: The Auger process involving a metal surface and a molecule in an excited state. As the molecule approaches the surface, an electron in the metal's conduction band (at the Fermi level in the diagram) can tunnel into the unoccupied molecular orbital, releasing enough energy to drive the electron in the excited orbital into the vacuum.

from 0 V to 200 V. In the negative version of the amplifier, the offset is 300 V, resulting in an output between −200 V and 0 V.

5.4 Auger Metastable CO Detector

After the molecules have been manipulated by the chip, they are ejected toward the detector. This detector makes use of the Auger process, shown in figure 5.9. Because the CO molecule is in an excited state, one electron is in an orbital that is normally unoccupied in the ground state, and a normally occupied orbital with lower energy is left unoccupied. As the metastable CO molecule approaches a metal surface, a conduction band electron can tunnel into the lower unoccupied orbital, and the energy released is then transferred to the electron in the higher-lying orbital. Since the energy of metastable CO is 6.0 eV, if the Fermi level is less than 6.0 eV below the vacuum energy (i.e. the work function is less than 6.0 eV) the higher-lying CO electron can receive enough energy from an electron tunneling from the Fermi level to leave the CO molecule and thus becomes a free electron.

Given this requirement, one would ideally choose a metal with a work function that is as low as possible, such as cesium, with a work function of only 1.95 eV [107]. Cesium, however, is hard to work with: it reacts violently when exposed to air, and thus a detector incorporating cesium or any other alkali metal must be designed such that it is never exposed to the atmosphere. In general, many of the metals that have low work functions, such as alkali metals, alkaline earth metals, and lanthanides have surfaces that change unpredictably when exposed to the atmosphere, reacting with oxygen and water vapor to form oxides and hydroxides that have much different work functions than the elemental metal they contain. Unless these surfaces are carefully prepared, the work function is often not reproducible. One metal that offers a reasonable, reproducible work function

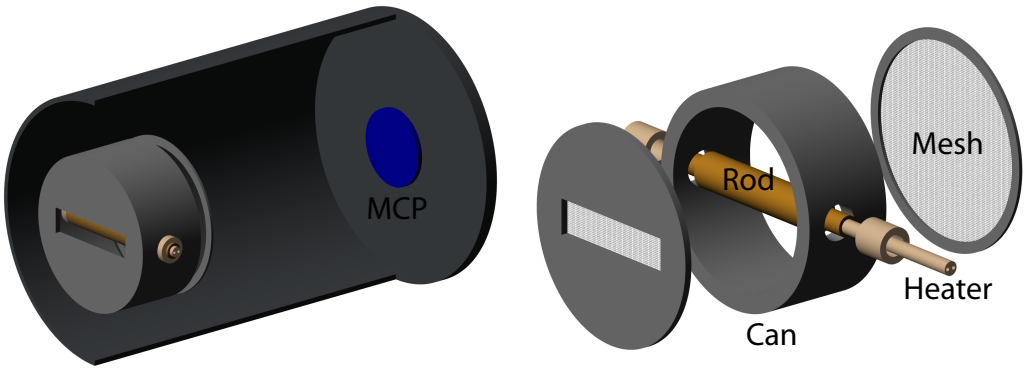

Figure 5.10: Schematic view of the Auger detector as it is placed relative to the chamber and microchannel plate (left) and an exploded view showing the individual parts (right). Metastable CO molecules enter through the rectangular, mesh-covered slot and hit the front of the gold covered rod, where they produce low energy electrons. These electrons are deflected around the rod, through the second mesh, and toward the MCP. A heater is inserted inside of the rod to heat the gold surface and keep it free of contaminants.

with little preparation is gold. While its work function is somewhat higher (5.4 eV), its surface does not form oxide layers when it is exposed to air. Heating the surface to 100°C ensures that it remains free of contamination such as oils that are present in trace amounts in the vacuum system.

The detector constructed is shown in figure 5.10. Metastable CO molecules, arriving from the left side, pass through a mesh on the front side of the can and collide with the surface of a gold-coated rod where they can emit Auger electrons. Potentials are applied to the rod and the outer metal can such that the electrons are directed around the rod, through the grounded metal mesh behind the can, and toward the microchannel plate (MCP), which multiplies the single electron into many to produce a measurable signal. Bringing the electrons to the MCP efficiently requires a careful balance of potentials: the can is charged to −3 kV, while the rod is about 20 V less negative. If this potential difference between the rod and can is too small, the electrons pass through the mesh at the front of the detector (where the metastable CO molecules entered), but if it is too large, the electrons are repelled back to the rod. It is difficult to predict the exact potential difference needed between the can and the rod a priori, since it can be affected by objects on the other side of the mesh, so the potential is best adjusted by optimizing the count rate seen at the MCP. The rod is hollow to allow space for a heater, which consists of a thin tungsten wire inserted into a ceramic tube. This enables the gold coated rod to be heated while remaining electrically insulated from the heater's power supply.

It is estimated that this device detects metastable CO molecules with an efficiency of 1%, and does so in such a way that the entire arrival time distribution can be recorded in every measurement cycle. This is a major advantage over molecular detect methods that use a pulsed laser: since the pulsed laser generally only runs once per measurement cycle, only one arrival time can be measured in any given experiment, and to measure an arrival time distribution, the measurement must be performed many times with different delay times for the pulsed laser. However, the Auger detector only works with molecules with

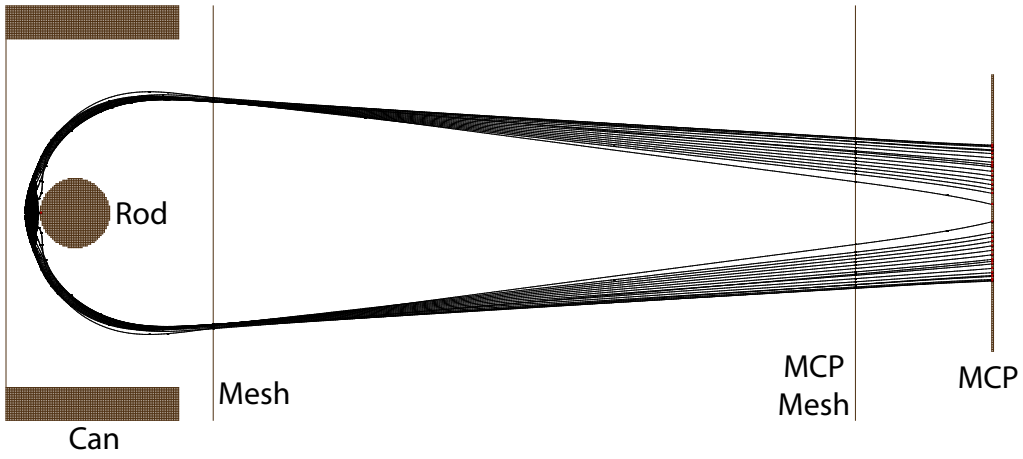

Figure 5.11: Trajectories of the electrons in the Auger detector. With the proper ratios of potentials, the low energy electrons produced at the front surface of the gold-coated rod are deflected around the rod, through the mesh, and to the microchannel plate. Although the trajectories shown assume an initial kinetic energy of 1 eV, electrons with much lower kinetic energies also reach the MCP

a large internal electronic energy, such as metastable CO. Also, because the electrons emerging from the surface take a rather complicated path while at low velocity, the efficiency with which they reach the detector is greatly influenced by external magnetic fields: in fact, magnetic fields of only a few Gauss completely eliminate all signal at the MCP. If only measurements of a single arrival time are desired, methods using a pulsed laser for detection are superior as these offer efficiencies much higher than 1%.

For situations in which the Auger metastable CO detector is not suitable, there are a few other options available to detect $a^3\Pi$ CO molecules. One possibility is to detect their phosphorescence: since the $v = 0$, $|\Omega| = 1$, $J = 1$ level has a radiative lifetime of 2.6 ms [16], the molecules must emit photons on this timescale. Over 90% of the molecules decay back to the first four vibrational levels of the ground state, resulting in four sharp emission lines between 206 nm and 238 nm [19]. This technique is, in a sense, non-destructive: while the molecules that emitted photons are no longer metastable, they indicate the presence of many more molecules that have not yet decayed. For the experiments presented in this thesis, the metastable CO beam is monitored by placing a photomultiplier tube (PMT) off the molecular beam axis between the skimmer and the chip to observe the phosphorescence. By doing so, the wavelength of the laser can be stabilized to maximize the production of metastable molecules.

Metastable CO can also be detected using transitions to the $b^3\Sigma^+$ state with a 283 nm laser. This strongly-allowed transition (The lifetime of $b^3\Sigma^+$, $v = 0$ is 54 ns [108], after which the molecules primarily decay to the $a^3\Pi$ state) can be saturated with a 0.1 cm^{-1}-bandwidth pulsed laser with a fluence of 10 $\frac{\mu\text{J}}{\text{cm}^2}$. The fluorescence of this state can be detected with a PMT, or by increasing the power of the 283 nm laser, the CO molecule can be ionized from the b state, and the ions can be detected on an MCP. This enables 1+1 REMPI detection of the a state with high efficiency. Further discussion of this and other detection methods for metastable CO can be found in reference [103].

Chapter 6

Guiding, Decelerating, and Trapping Metastable CO on a Chip

6.1 Guiding of CO* Molecules at Constant Velocity

In the first experiments, a mixture of 20% CO in Xe with an initial pressure of about 1 bar and an initial temperature of 200 K was expanded into vacuum through a pulsed valve. The resulting arrival time distribution observed at the Auger detector when no potentials are applied to the chip is shown in figure 6.1. In this and all subsequent figures, arrival time $t = 0$ is given by the laser pulse that excites the CO molecules to their metastable state. Since the distance between the laser excitation point and the detector is 298.3 mm, the peak of the distribution at 0.96 ms corresponds to a velocity of 310 $\frac{\text{m}}{\text{s}}$, and the full width at half maximum (FWHM) arrival time spread of 160 µs corresponds to a FWHM velocity spread of 50 $\frac{\text{m}}{\text{s}}$.

Figure 6.2 shows, in red, the arrival time distribution measured when 2.6 MHz, 90 V peak-to-peak amplitude waveforms like those shown in figure 5.5 are applied to the molecule chip's electrodes. These waveforms produce a series of 25 mK deep traps moving at a constant velocity of 312 $\frac{\text{m}}{\text{s}}$. Most of the molecules are either not spatially in one of these traps or have a velocity relative to the traps that is too large to be captured. Some small fraction of the molecules that have the correct initial velocity and are in the volume of the trap can be guided over the surface of the chip. Because these molecules have the same velocity and the same initial position, they arrive at the detector at the same time, resulting in the small peak seen at an arrival time of 0.96 ms.

If waveforms with other frequencies are applied to the electrodes, molecules in the molecular beam with the corresponding initial velocities can be selectively guided. Figure 6.3 shows several such arrival time distributions, along with the field-free distribution, scaled down by a factor of 9. The relative intensities of the peaks of guided molecules nicely match the field-free distribution: fewer molecules are detected in the 348 $\frac{\text{m}}{\text{s}}$ guiding peak, for example, because there are fewer molecules in the molecular beam with that velocity. The 2.6 MHz peak has a FWHM of 9 µs which, based on trajectory simulations, corresponds to a FWHM velocity spread of 5 $\frac{\text{m}}{\text{s}}$.

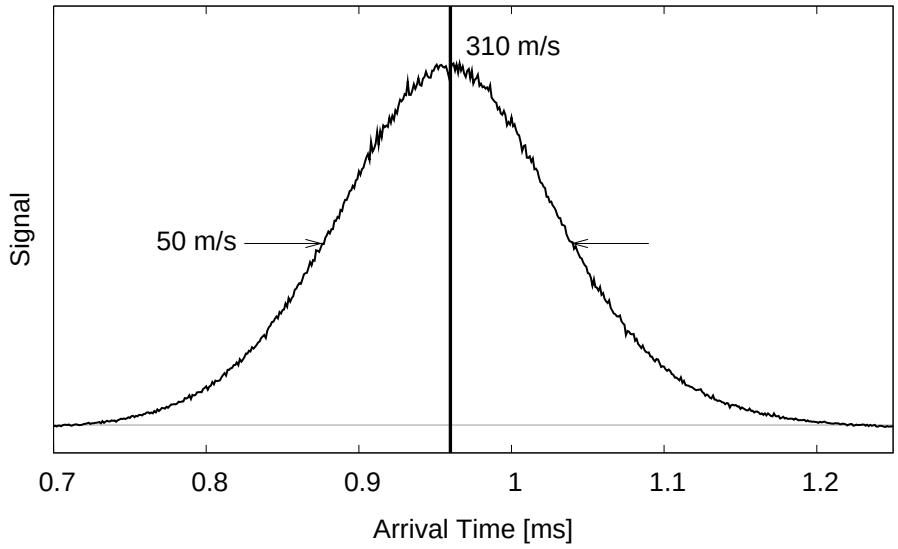

Figure 6.1: Arrival time distribution at the Auger detector when a mixture of 20% CO in xenon with an initial pressure of about 1 bar and an initial temperature of 200 K is expanded through the pulsed valve, and no fields are applied to the electrodes of the chip. Since arrival time and velocity are directly correlated, the peak arrival time corresponds to a velocity of 310 $\frac{\mathrm{m}}{\mathrm{s}}$ with a spread of about 50 $\frac{\mathrm{m}}{\mathrm{s}}$.

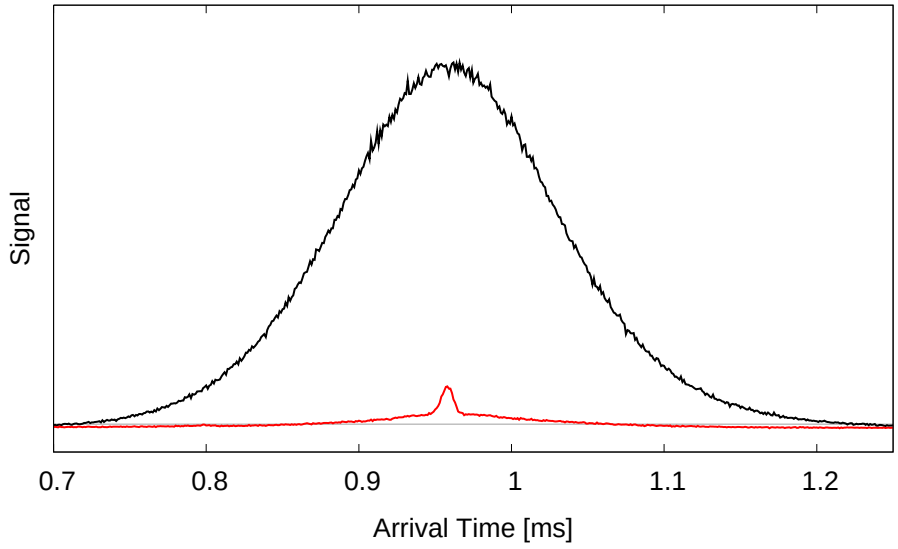

Figure 6.2: The arrival time distribution when waveforms with a constant frequency of 2.6 MHz (resulting in traps moving at a constant velocity of 312 $\frac{\mathrm{m}}{\mathrm{s}}$) are applied to the chip (red) contrasted to the case where no fields are applied to the chip (black). When fields are applied to the chip, most of the molecules are either not spatially in a trap or have a velocity relative to the traps that is too large to be captured. Some small fraction of the molecules, however, have an initial velocity close to 312 $\frac{\mathrm{m}}{\mathrm{s}}$ and are initially in the volume of the trap. These molecules arrive at the detector at 0.96 ms, forming a narrow peak.

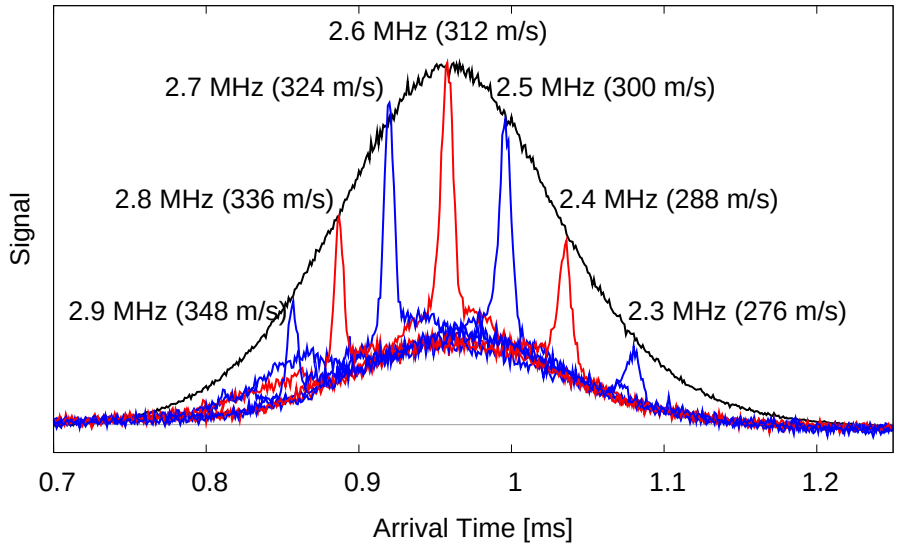

Figure 6.3: Arrival time distributions when 90 V amplitude waveforms with various frequencies are applied to the chip. The field-free arrival time distribution has been included for comparison, scaled down by a factor of 9.

6.1.1 Trajectory Simulations for Arrival Time Distributions

The basic framework for molecular trajectory simulations is given in chapter 3. To summarize the results in that chapter: based on the electric potentials applied to the chip, it is possible to calculate an electric field distribution, and using the assumption that the mechanical potential only depends on electric field strength, the force on a molecule as a function of position and time can also be calculated. Simulating the molecule's trajectory is then only a matter of solving a system of second-order ordinary differential equations: $\frac{d^2\vec{r}}{dt^2} = \frac{\vec{F}(r)}{m}$, where $\vec{r}$ is position of the molecule in space, $\vec{F}(r)$ is the force and m is the molecule's mass. Such calculations can be carried out numerically, e.g. using a Runge-Kutta algorithm, as long as the initial position $\vec{r}(t=0)$ and the initial velocity $\left.\frac{d\vec{r}}{dt}\right|_{t=0}$ of a particle are known.

The calculations in chapter 3 assume that the chip is two dimensional (i.e. the electrodes are infinitely long) and that the electrodes are strictly periodic, repeating over infinitely many periods. Since neither of these conditions is strictly true, two approximations are made. First, the finite length of the electrodes is ignored: it is assumed at the point where traps are closed by the fringe fields at the end of the electrodes is a hard wall, and the molecules simply bounce back from this edge with no motion parallel to the electrodes being coupled to the other two dimensions. Second, it is assumed that in the region near where the electrodes stop repeating, the field distribution transitions sharply from a field free region to the field distribution that would be produced by an infinite array at the first and last electrodes of the array. Since the molecules spend very little time in this transition region compared to their total time above the chip, this assumption is allowed.

Based on these approximations, the calculation of the two-dimensional path of the molecules from the laser excitation to the detector can be divided into calculations in

three separate regions. In the first region, between the laser excitation point and the beginning of the chip, the molecules fly freely, in the second region, above the chip, the motion of the molecules is affected by the electric fields, and in the third region, between the end of the chip and the detector, the molecules again fly freely. The trajectory of a molecule in the field-free regions is given by $\vec{r}(t) = \vec{v}t + \vec{r}(t = 0)$, where $\vec{v}$ is the molecule's velocity: in the field free regions, a molecule flies with a constant velocity in a straight line. If this trajectory crosses the physical barriers posed by the surface of the chip or the razor edges at the ends of the electrode array, however, it is discarded, since the molecule it represents would likely not remain in a detectable state after a collision with a surface. In the region above the chip, the trajectory is calculated using the numerical methods described before, and the trajectory is discarded if the trajectory ever passes below the surface of the chip.

To calculate the arrival time distributions, a random starting position and velocity is chosen for each molecule, its trajectory from the excitation to the detector is calculated, and if the molecule reaches the detector without colliding with any obstacles, its arrival time is recorded. The positions of the molecules at time $t = 0$ are assumed to be distributed uniformly over a cylinder at the laser excitation position. One circular face of the cylinder coincides with the aperture of the skimmer, the axis of the cylinder extends backwards along the molecular beam axis toward the valve. Since the molecules that are detected must be excited by the $\sim$1 mm wide laser pulse and pass through the skimmer's opening, the molecules must originate somewhere in this volume. The initial longitudinal velocity distribution is chosen to have a Gaussian distribution with a mean and standard deviation chosen to match those observed experimentally in the molecular beam, and the initial transverse velocity is chosen from the range of values that lead to trajectories that pass through the chip's entrance slit.

Figure 6.4 shows simulated arrival time distributions for molecules guided over the chip at a constant velocity under the same conditions as those in the experiment. The initial longitudinal velocity distribution is chosen from a Gaussian distribution with a mean of 308 $\frac{\mathrm{m}}{\mathrm{s}}$ and a standard deviation of 23 $\frac{\mathrm{m}}{\mathrm{s}}$. For each applied waveform, 10^7 trajectories are calculated for molecules in the low field seeking $J = 1$, $|\Omega| = 1$, $M\Omega = -1$ state, and a further 10^7 trajectories for molecules in the weakly high field seeking $M = 0$ state. Another 10^7 trajectories are calculated with no fields applied to the chip. The accepted molecules in the $M\Omega = -1$ state arrive in a narrow peak, while the molecules in the $M = 0$ state, which are less affected by the fields, arrive with a wider distribution that resembles the initial distribution (although the presence of the fields reduces the number of molecules in the $M = 0$ state that reach the detector to one-third of the amount that would reach the detector without electric fields). By taking a weighted average of the arrival time distributions of molecules in each of the two states, assuming that 10% of the molecules are in the $M = 0$ state and the remaining 90% are in the $M\Omega = -1$ state, the relative magnitudes of the narrow peaks and the broad background can be matched to the ratio seen in experiments. The field-free arrival time distribution, in black, is scaled down by a factor of 6. This is somewhat smaller than the scaling factor of 9 used in the experiments and may be a sign of the non-adiabatic losses that are described in section 6.3.

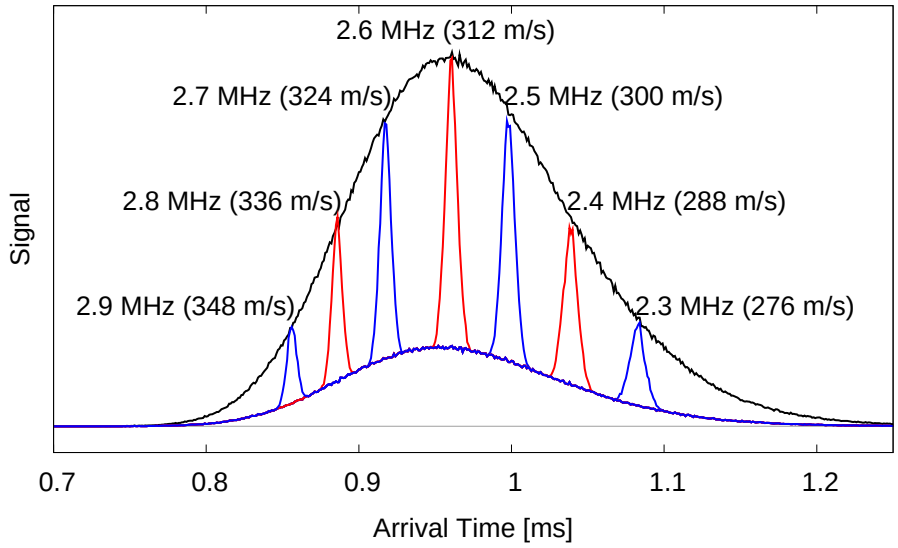

Figure 6.4: Simulated arrival time distributions for molecules guided over the chip at a constant velocity. The molecules are assumed to have an initially Gaussian velocity distribution with a mean velocity of 308 $\frac{\mathrm{m}}{\mathrm{s}}$ and a standard deviation of 23 $\frac{\mathrm{m}}{\mathrm{s}}$ (corresponding to a FWHM of slightly over 54 $\frac{\mathrm{m}}{\mathrm{s}}$). By assuming that 10% of the molecules are in the $M = 0$ (weakly high field seeking) state, the relative intensities of the narrow peaks and the broad background are well matched to those seen in the experimental data. The field-free arrival time distribution, in black, is scaled down by a factor of 6.

6.2 Deceleration of ^{12}CO

In the next set of experiments, molecules in the traps were decelerated by decreasing the frequency of the waveforms and thus the velocity of the traps. For these experiments, the gas mixture expanded into vacuum consisted of 20% CO in argon with an initial pressure of about 1 bar and an initial temperature of 102 K. The resulting molecular beam is somewhat faster than before (360 $\frac{\mathrm{m}}{\mathrm{s}}$ instead of 310 $\frac{\mathrm{m}}{\mathrm{s}}$) but also has a somewhat narrower velocity spread (45 $\frac{\mathrm{m}}{\mathrm{s}}$ versus slightly more than 50 $\frac{\mathrm{m}}{\mathrm{s}}$) and has roughly double the peak intensity. Since the largest number of molecules in the molecular beam have an initial velocity around 360 $\frac{\mathrm{m}}{\mathrm{s}}$, waveforms with an initial frequency of 3.0 MHz are used in the measurements. Figure 6.5 shows the arrival time distribution when no fields are applied to the chip (black) and when waveforms with a peak-to-peak amplitude of 120 V and constant frequency of 3.0 MHz are applied (red, scaled up by a factor of 25). As before, most of the molecules either are not in the physical volume of the trap or have a velocity relative to the traps that is too large to be captured; only the molecules initially in the trap volume with an initial velocity close to 360 $\frac{\mathrm{m}}{\mathrm{s}}$ contribute to the small peak at an arrival time of 0.83 ms. The scaling factor of 25 between the signal without potentials and the guided signal is larger than expected and may be the result of a combination the structure being tilted less than before (and thus allow more molecules through when no potentials are applied) and the non-adiabatic losses that will be described in section 6.3.

Unlike in the previous experiments, the waveforms are first switched on after the guided molecules have traversed the first 3 mm of electrodes (530 µs after the laser

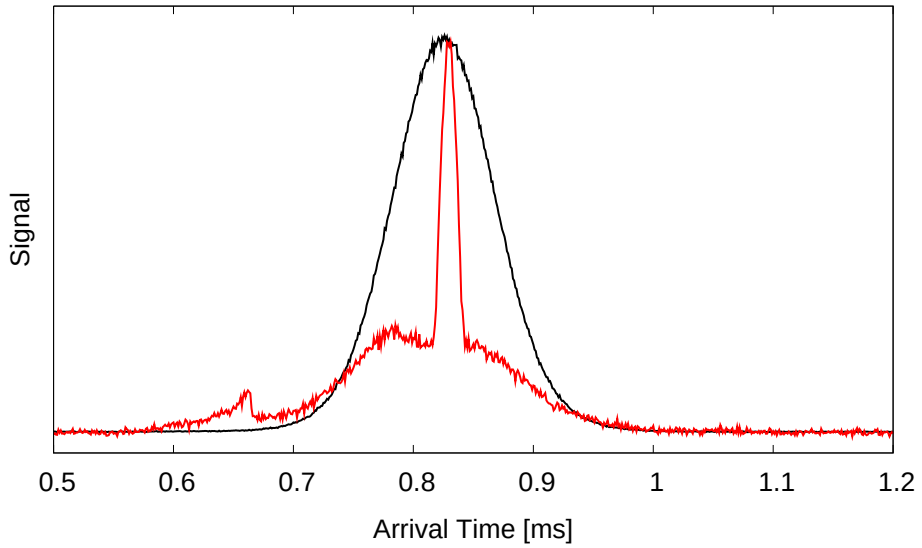

Figure 6.5: Arrival time distribution at the detector when a mixture of 20% CO in argon with an initial pressure of about 1 bar and an initial temperature of 102 K is expanded through the pulsed valve. The black curve shows the distribution when no fields are applied to the electrodes of the chip. The peak arrival time corresponds to a velocity of 360 $\frac{\mathrm{m}}{\mathrm{s}}$ with a spread of about 45 $\frac{\mathrm{m}}{\mathrm{s}}$. For the red curve, waveforms with an amplitude of 120 V and a frequency of 3.0 MHz are applied to the chip, guiding molecules over the chip at 360 $\frac{\mathrm{m}}{\mathrm{s}}$ which arrive at the detector in a narrow peak at 0.83 ms. The red curve has been scaled up by a factor of 25.

excitation) and are switched off again when they are less than 1 mm from the last electrode (130 µs later). Because of this, the fastest molecules in the molecular beam traverse the entire active area of the chip before the fields are even switched on. This effect is seen in the arrival time distribution at 0.665 ms, where there is a sudden drop in signal: molecules arriving at the detector just before the drop had just left the chip as the fields were switched on while those that do not arrive right after the drop were still on the chip. In other experiments, a similar effect can also be observed for molecules that are slow enough that they do not reach the start of the chip until the fields have already been switched off: in such cases, a sudden rise in signal will be observed at late arrival times. With the waveforms applied in figure 6.5, the rise would be expected at 1.05 ms after the laser excitation; this sudden rise is not observed because very few molecules in the beam are traveling slowly enough.

These two effects can also be used to measure the position of the chip along the molecular beam axis. If the distance from the laser excitation to the detector, d_{det}, is already known (this can be measured using the arrival time of molecules guided at a constant velocity), the distance from the laser excitation to the edge of the chip facing the detector, d_{back}, is given by

$$d_{\mathrm{back}} = d_{\mathrm{det}} \frac{t_{\mathrm{on}}}{t_{\mathrm{fall}}} \tag{6.1}$$

where t_{on} is the time, relative to the laser excitation, that the waveforms are turned on, and t_{fall} is the time of the falling edge in the early part of the arrival time distribution. Similarly, the distance from the laser excitation to the edge of the chip facing the valve d_{front} can be found with the equation

$$d_{\mathrm{front}} = d_{\mathrm{det}} \frac{t_{\mathrm{off}}}{t_{\mathrm{rise}}} \tag{6.2}$$

where t_{off} is the time that the waveforms are turned off, and t_{rise} is the time of the rising edge in the late part of the arrival time distribution. If these two values are consistent, $d_{\mathrm{back}} - d_{\mathrm{front}}$ should be close to the length of the chip, 50.1 mm.

Figure 6.6 shows the arrival time distributions that result when waveforms with an initial frequency of 3.0 MHz are reduced at a constant rate to a different final frequency while the molecules are above the chip. In each case, the waveforms are switched on 530 µs after the laser excitation, after the molecules moving at 360 $\frac{\mathrm{m}}{\mathrm{s}}$ have traversed the first 3 mm of electrodes. The leftmost trace is the same as that seen in figure 6.5: here, waveforms with a constant frequency of 3.0 MHz are applied to the chip for 130 µs, guiding the molecules at a constant velocity over the length of the chip. In the next traces, the frequency of the waveforms was reduced to (from left to right) 2.8 MHz, 2.6 MHz, 2.4 MHz, 2.2 MHz, or 2.0 MHz over a time-interval of 133 µs, 137 µs, 144 µs, 148 µs, or 154 µs, respectively, after which the waveforms were switched off. The time period of the sweeps is chosen such that the traps 3 mm from the first electrode at the beginning of the sweep are less than 1 mm from the last electrode at the end. The peaks, as a result, shift to progressively later arrival times, indicating that some of the molecules initially traveling at 360 $\frac{\mathrm{m}}{\mathrm{s}}$ have been decelerated to lower velocities. Since a molecule must stay in the same trap in order to reach the detector, the final frequency of the waveform corresponds to the final velocity of the molecules; the various peaks then correspond to molecules decelerated to 336 $\frac{\mathrm{m}}{\mathrm{s}}$, 312 $\frac{\mathrm{m}}{\mathrm{s}}$, 288 $\frac{\mathrm{m}}{\mathrm{s}}$, 264 $\frac{\mathrm{m}}{\mathrm{s}}$, or 240 $\frac{\mathrm{m}}{\mathrm{s}}$, respectively.

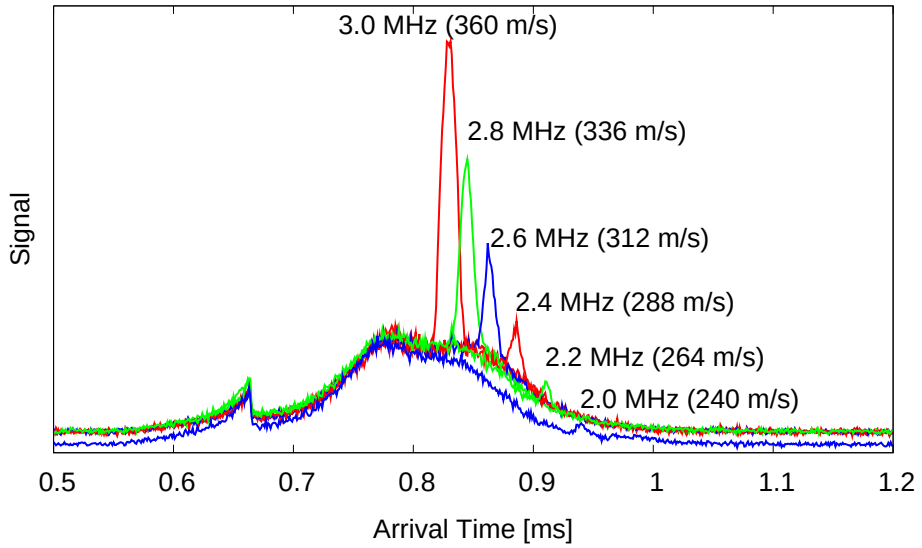

Figure 6.6: Guiding and deceleration of CO molecules in an argon-seeded expansion from 360 $\frac{\mathrm{m}}{\mathrm{s}}$ to various final velocities. Waveforms are applied to the chip that have an initial frequency of 3.0 MHz starting 530 µs after the laser excitation. In the leftmost trace, the waveforms have a constant frequency of 3.0 MHz and are applied for 130 µs, and the arrival time distribution shows a peak at 0.83 ms, corresponding to a constant velocity of 360 $\frac{\mathrm{m}}{\mathrm{s}}$. In subsequent traces, the frequency of the waveform is reduced to (from left to right) 2.8 MHz, 2.6 MHz, 2.4 MHz, 2.2 MHz, or 2.0 MHz over a time-interval of 133 µs, 137 µs, 144 µs, 148 µs, or 154 µs, respectively, after which the waveforms are switched off. The molecules are decelerated to 336 $\frac{\mathrm{m}}{\mathrm{s}}$, 312 $\frac{\mathrm{m}}{\mathrm{s}}$, 288 $\frac{\mathrm{m}}{\mathrm{s}}$, 264 $\frac{\mathrm{m}}{\mathrm{s}}$, or 240 $\frac{\mathrm{m}}{\mathrm{s}}$ and arrive successively later at the detector as the final velocity decreases.

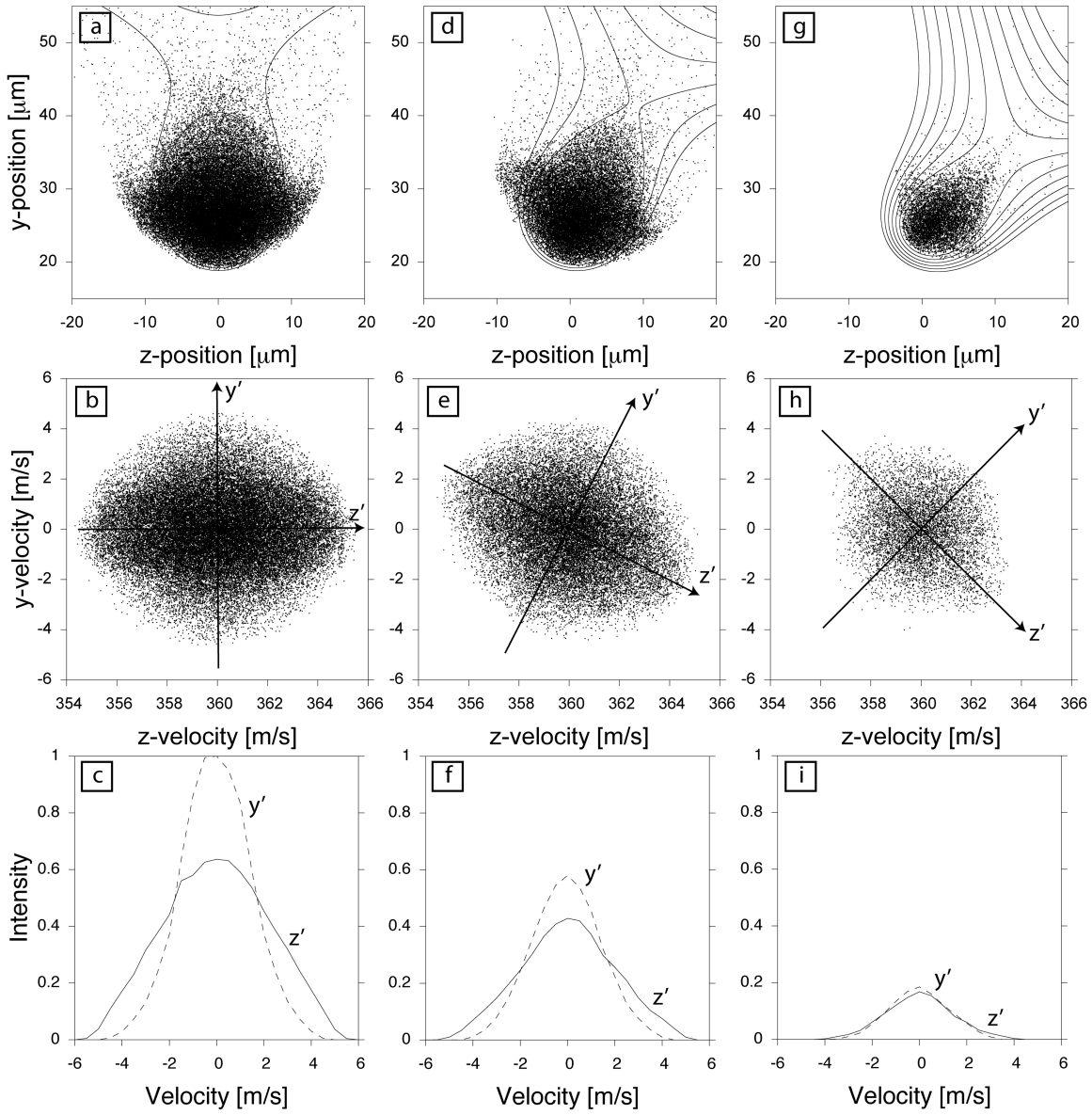

Figure 6.7: Calculated initial positions and velocities of molecules that reach the detector after being guided at a constant velocity of 360 $\frac{\mathrm{m}}{\mathrm{s}}$ ((a)–(c)), after being decelerated from 360 $\frac{\mathrm{m}}{\mathrm{s}}$ to 312 $\frac{\mathrm{m}}{\mathrm{s}}$ ((d)–(f)), and after being decelerated from 360 $\frac{\mathrm{m}}{\mathrm{s}}$ to 240 $\frac{\mathrm{m}}{\mathrm{s}}$ ((g)–(i)). The top row shows the initial position of each molecule, plotted together with the effective trap (trap combined with pseudopotential), the middle row shows the velocity distribution, and the bottom row shows the integrated velocity distribution along the principal axes indicated in the middle row.

It can be seen that, as the deceleration increases, the total number of molecules decelerated decreases. This is expected: in the previous chapter (figure 5.6) it is shown that, as the acceleration increases, the volume and depth of each trap decreases. Figure 6.7 shows the effective traps (traps combined with pseudopotentials), together with the initial positions and velocities of particles in these traps which reach the detector. Parts (a)–(c) show the case in which molecules are guided at a constant velocity of 360 $\frac{\text{m}}{\text{s}}$, (d)–(f) when molecules are decelerated from 360 $\frac{\text{m}}{\text{s}}$ to 312 $\frac{\text{m}}{\text{s}}$, and (g)–(i) when molecules are decelerated from 360 $\frac{\text{m}}{\text{s}}$ to 240 $\frac{\text{m}}{\text{s}}$. The initial positions and velocity are found by randomly choosing 10^7 initial positions and velocities in a uniform distribution from a 50 μm × 50 μm × 20 $\frac{\text{m}}{\text{s}}$ × 20 $\frac{\text{m}}{\text{s}}$ hyperrectangle centered at $y = 30$ μm, $z = 0$ μm, $v_y = 0$ $\frac{\text{m}}{\text{s}}$, and $v_z = 360$ $\frac{\text{m}}{\text{s}}$. For each of the chosen initial conditions, a particle trajectory is calculated, and if this shows that the particle would reach the detector, the initial position and velocity are recorded. The top row shows the initial positions overlayed on contour plots of the effective traps. While most of the particles reaching the detector generally fall in the region where the potential energy is lower than the potential energy of the barrier to the field free region far from the chip, there are some molecules along an axis perpendicular to the barrier that, despite having a total energy above the barrier, never find the exit. The middle row shows the velocity distribution, and the bottom row shows the integrated velocity distribution along the principle axes indicated in the middle row. It can be seen in these plots that the velocity distribution perpendicular to the barrier is somewhat higher that the velocity distribution in the direction of the barrier.

To quantitatively understand the effect of increasing acceleration on the number of molecules reaching the detector, simulations of the expected arrival time distribution have been carried out for each set of waveforms. The results of these simulations are shown in figure 6.8. The dashed black curves represent the simulated arrival time distributions for the same six sets of waveforms used for figure 6.6, and the solid red curves show the experimentally-measured distributions with the broad background signal subtracted. The experimental and simulated data have been independently scaled such that the peak intensity of the molecules guided at a constant 3.0 MHz (360 $\frac{\text{m}}{\text{s}}$) is one in each of the two. Comparing the simulated data with the experimental data, it becomes clear that as the acceleration increases, many more molecules are lost from the traps in the experiment than would be expected from the simulations. The inset shows the integrated intensity of each peak as a function final velocity for the simulated (dashed black) and experimental (solid red) data. In the last point, deceleration from 360 $\frac{\text{m}}{\text{s}}$ to 240 $\frac{\text{m}}{\text{s}}$, simulations predict that the number of molecules reaching the detector should be reduced by a factor of six compared to guiding at a constant 360 $\frac{\text{m}}{\text{s}}$, but the experiment shows that the number is in fact reduced by a factor of about 25.

6.3 Results in Decelerating and Trapping ^{13}CO

The discrepancy between theory and experiment regarding the fraction of the molecules lost at high accelerations was somewhat of a mystery for a while. At the time, there were two leading hypotheses. The first was that collisions with the carrier gas in the molecular beam cause the molecules to be ejected from the traps, and that this effect was stronger at high accelerations because the molecules then have a higher velocity relative

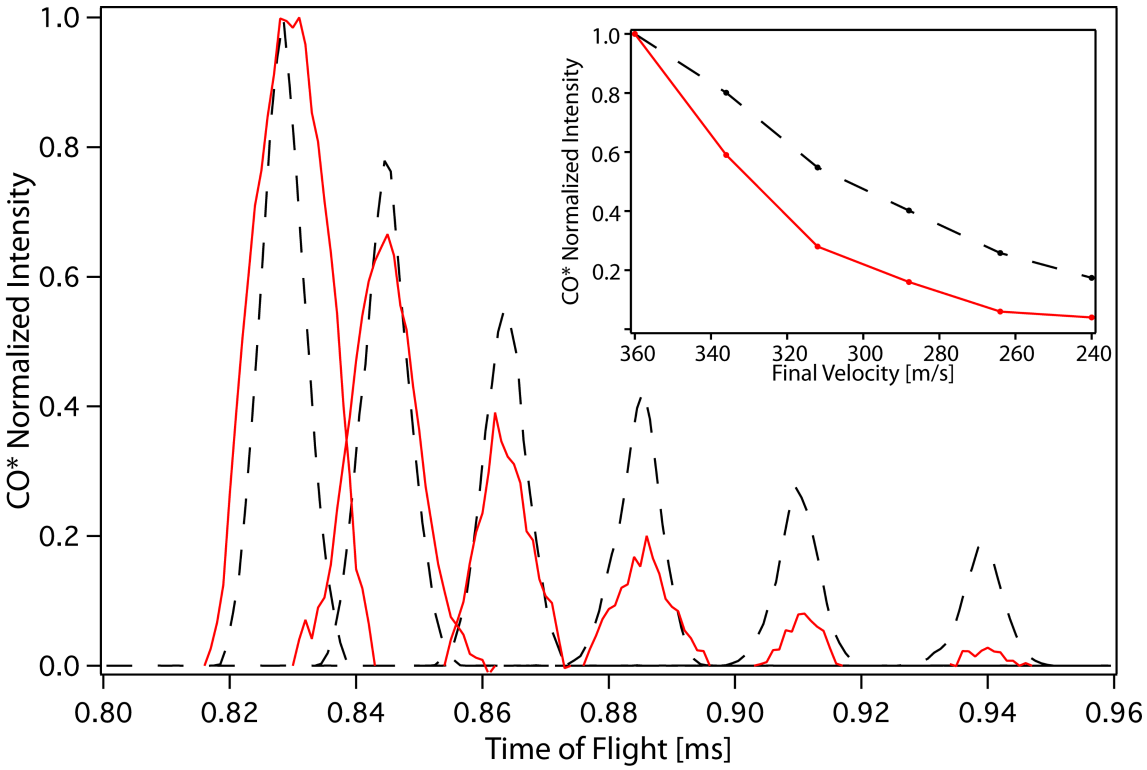

Figure 6.8: Simulated (dashed black) and experimental (solid red) arrival time distributions for molecules guided at 360 $\frac{\mathrm{m}}{\mathrm{s}}$ and molecules decelerated from 360 $\frac{\mathrm{m}}{\mathrm{s}}$ to 336 $\frac{\mathrm{m}}{\mathrm{s}}$, 312 $\frac{\mathrm{m}}{\mathrm{s}}$, 288 $\frac{\mathrm{m}}{\mathrm{s}}$, 264 $\frac{\mathrm{m}}{\mathrm{s}}$, or 240 $\frac{\mathrm{m}}{\mathrm{s}}$. While the trajectory simulations predict that the number of decelerated molecules should decrease as the acceleration increases, the loss in experiments is much higher than the simulations predict. The inset shows the integrated intensity of each peak, plotted against final velocity of the molecules in that peak. While the simulations predict that the number of molecules that can be decelerated from 360 $\frac{\mathrm{m}}{\mathrm{s}}$ to 240 $\frac{\mathrm{m}}{\mathrm{s}}$ is a factor of six lower than the number of molecules than can be guided at 360 $\frac{\mathrm{m}}{\mathrm{s}}$, the experiments show the ratio to be about 25.

to the carrier gas. To mitigate this effect, an electrostatic deflector was designed that could be inserted between the laser excitation and the chip to separate the carrier gas from the low field seeking molecules. The second hypothesis was that imperfections in the waveforms applied to the chip or imperfections in the electrodes cause the effective depth of the traps to be much lower than if the waveforms and electrodes were perfect.

In the end, the dominant loss mechanism over the relevant range of velocities turned out to be non-adiabatic transitions from the low field seeking $J = 1$, $\Omega = 1$, $M\Omega = -1$ state to the $M = 0$ state. The idea had been considered early on in the experiment and was tested at the time by applying a 30 Gauss magnetic field to the chip (accomplished practically by setting a large, permanent magnet on top of the machine) to separate the low field seeking states from the $M = 0$ levels by 14 MHz. Since the 14 MHz splitting was much larger than the frequency of the waveforms applied to the chip and the maximum oscillation frequency of the molecules in the traps, it was reasoned that this splitting should prevent any non-adiabatic transitions. An experiment was carried out in which waveforms were applied to decelerate the molecules from 300 $\frac{\text{m}}{\text{s}}$ to 288 $\frac{\text{m}}{\text{s}}$, and no change was observed in the arrival time distribution, so it was assumed that there were not significant losses due to non-adiabatic transitions to untrapped states. Likely, the strength of the magnetic field was not large enough: it is shown in chapter 7 that fields upward of 50 Gauss (that must be in the right direction) are needed to expect a significant decrease in the non-adiabatic losses. Inspired by an article showing that non-adiabatic loses are a dominant loss mechanism for ND_3 in quadrupole electric traps [101], we began to reconsider the possibility that such losses could nevertheless be a problem. Instead of using a magnetic field to break the degeneracy of the levels in ^{12}CO, the ^{13}CO isotopologue was used. Due to its hyperfine structure, the low field seeking levels of the $J = 1$, $\Omega = 1$ state are never closer than 50 MHz to the non-trappable $M = 0$ states.

Figure 6.9 shows the arrival time distributions of ^{12}CO (black) and ^{13}CO (red) molecules guided over the chip at 312 $\frac{\text{m}}{\text{s}}$ and decelerated from 312 $\frac{\text{m}}{\text{s}}$ to various final velocities. Even during guiding, many more ^{13}CO molecules reach the detector than ^{12}CO, despite the fact that the beams of ^{13}CO molecules and ^{12}CO molecules are comparable in their velocity distribution and intensity. When the ^{12}CO molecules are decelerated from 312 $\frac{\text{m}}{\text{s}}$ to 240 $\frac{\text{m}}{\text{s}}$, only half as many molecules reach the detector as when the molecules are guided at 312 $\frac{\text{m}}{\text{s}}$, and deceleration to velocities lower than 240 $\frac{\text{m}}{\text{s}}$ results in no measurable signal. In contrast, when the ^{13}CO molecules are decelerated from 312 $\frac{\text{m}}{\text{s}}$ to 240 $\frac{\text{m}}{\text{s}}$, the number of molecules reaching the detector is almost the same as when they are guided at 312 $\frac{\text{m}}{\text{s}}$, and when the molecules are decelerated from 312 $\frac{\text{m}}{\text{s}}$ to 168 $\frac{\text{m}}{\text{s}}$ or 96 $\frac{\text{m}}{\text{s}}$, 45% or 5%, respectively, of molecules still reach the detector. Trajectory simulations confirm that, compared to guiding at 312 $\frac{\text{m}}{\text{s}}$, few molecules should be lost when decelerating to 240 $\frac{\text{m}}{\text{s}}$, and 50% or 10% of the molecules should remain when decelerating to 168 $\frac{\text{m}}{\text{s}}$ or 96 $\frac{\text{m}}{\text{s}}$, respectively.

Since ^{13}CO molecules are much more resistant to non-adiabatic transitions, the remaining experiments shown in this chapter will be performed with ^{13}CO. In the next chapter, however, we will return to ^{12}CO and reexamine the prevention of non-adiabatic loss through the application of a magnetic field.

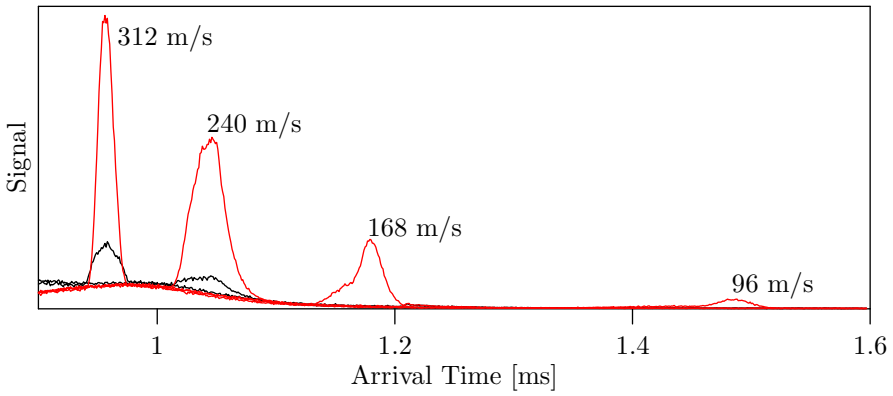

Figure 6.9: Guiding and deceleration of ^{12}CO (black) and ^{13}CO (red) from 312 $\frac{\text{m}}{\text{s}}$. For all traces, waveforms with an initial frequency of 2.6 MHz were applied to the electrodes, starting 605 µs after the laser excitation. The molecular beam is produced with a mixture of 20% CO in krypton with an initial pressure of 1 bar and initial temperature of 140 K. In the leftmost traces, waveforms with a constant frequency of 2.6 MHz were applied to the chip for 159 µs, guiding the molecules over the chip at 312 $\frac{\text{m}}{\text{s}}$. Despite the molecular beams having similar intensities, nearly five times more ^{13}CO molecules are guided to the detector than ^{12}CO molecules. In the next three sets of traces, the frequency of the waveforms is reduced to 2.0 MHz over 180 µs, to 1.4 MHz over 207 µs, or to 0.8 MHz over 244 µs, decelerating the molecules to 240 $\frac{\text{m}}{\text{s}}$, 168 $\frac{\text{m}}{\text{s}}$, or 96 $\frac{\text{m}}{\text{s}}$, respectively. When ^{12}CO is decelerated to 240 $\frac{\text{m}}{\text{s}}$, the number of molecules reaching the detector is reduced by half compared to when they are guided, and when waveforms are applied to decelerate to lower velocities, no decelerated molecules are detected. In contrast, the integrated intensity of ^{13}CO molecules decelerated to 240 $\frac{\text{m}}{\text{s}}$ is not less than that of the 312 $\frac{\text{m}}{\text{s}}$ guiding peak, and after decelerating to 168 $\frac{\text{m}}{\text{s}}$ or 96 $\frac{\text{m}}{\text{s}}$, 45% or 5%, respectively, of the molecules remain.

6.3.1 Velocity and Space Focusing

Although the molecules above the chip must have roughly the same longitudinal velocity as the moving traps in order to reach the detector, before they reach the chip and after they leave, the molecules can have a velocity different from that of the traps. Since all molecules originate from the same 1 mm long region at the same time, molecules with different velocities will reach the chip at different times. The velocity of the molecules arriving at the chip at any given time is given by

$$v(t) = \frac{d_{\text{front}}}{t} \tag{6.3}$$

where d_{front} is the distance from the laser excitation to the first electrode of the chip. If the velocity of the traps is chosen to match equation (6.3) during the time that molecules are arriving at the chip, molecules with many different initial velocities can be captured on the chip simultaneously. This technique is called velocity focusing.

There are two practical limits to the velocities and range of velocities that can be captured simultaneously. The first is that the physical length of the packet of captured molecules cannot exceed the length of the chip. If the molecules are captured starting at time t_1 and ending at time t_2, the length of the packet on the chip, d_{packet}, is given by

$$\begin{aligned} d_{\text{packet}} = \int_{t_1}^{t_2} \frac{d_{\text{front}}}{t}\, dt &= d_{\text{front}} \ln\left(\frac{t_2}{t_1}\right) \\ &= d_{\text{front}} \ln\left(\frac{v_1}{v_2}\right) \approx d_{\text{front}} \frac{v_1 - v_2}{\frac{1}{2}(v_1 + v_2)} \end{aligned} \tag{6.4}$$

Here, $v_1 = \frac{d_{\text{front}}}{t_1}$ and $v_2 = \frac{d_{\text{front}}}{t_2}$ are the fastest and slowest velocities captured. The second limitation comes from the fact that changing the velocity of the traps requires an acceleration, and if the acceleration is too high, the molecules do not remain in the traps. The acceleration that the traps experience, $a(t)$, is only a function of the velocity of the traps and d_{front},i.e.

$$a(t) = \frac{dv}{dt} = -\frac{d_{\text{front}}}{t^2} = -\frac{v(t)^2}{d_{\text{front}}} \tag{6.5}$$

The choice of d_{front} is a trade off between having a reasonably low acceleration and having a reasonably short packet. If d_{front} is large, the acceleration of the traps is low, but the packet on the chip for a given velocity spread will be long, and if d_{front} is small, the packet on the chip will be short, but the acceleration required to bring it on the chip will be much higher. A large d_{front} also leads to a lower density of molecules arriving at the chip. In the configuration used for most of the experiments in this thesis, d_{front} is 188 mm, so at 300 $\frac{\text{m}}{\text{s}}$, the required acceleration is a modest $4.8 \cdot 10^5$ $\frac{\text{m}}{\text{s}^2}$, but capturing a 20% velocity spread uses more than two-thirds of the entire electrode array, leaving little space left to decelerate the molecules to low velocities. For the experiments in the next chapter, the machine was rebuilt and the laser excitation brought much closer to the chip, resulting in a new d_{front} of 59 mm. While the same 20% velocity spread will only be 12 mm long on the chip, the acceleration at 300 $\frac{\text{m}}{\text{s}}$ increases to $1.5 \cdot 10^6$ $\frac{\text{m}}{\text{s}^2}$, pushing the limits of the ability of the traps to confine the molecules.

In the discussion of velocity focusing, the emphasis has been on capturing molecules with many different velocities at the entrance of the chip, but in fact, the entire sequence

can be carried out in reverse as the molecules exit the chip. The question that must be posed is, at what velocity do the molecules need to leave the chip to reach the detector at a specific time? If t_{det} is the detection time then the velocity they must have when leaving the chip is given by

$$v(t) = \frac{d_{\mathrm{det}} - d_{\mathrm{back}}}{t_{\mathrm{det}} - t} \tag{6.6}$$

where $d_{\mathrm{det}} - d_{\mathrm{back}}$ is the distance from the exit of the chip to the detector. The corresponding acceleration and packet length are

$$a(t) = -\frac{v(t)^2}{d_{\mathrm{det}} - d_{\mathrm{back}}} \tag{6.7}$$

$$d_{\mathrm{packet}} = (d_{\mathrm{det}} - d_{\mathrm{back}}) \ln\left(\frac{v_1}{v_2}\right) \approx (d_{\mathrm{det}} - d_{\mathrm{back}}) \frac{v_1 - v_2}{\frac{1}{2}(v_1 + v_2)} \tag{6.8}$$

If the velocity function given in equation (6.6) is followed as the trapped molecules are exiting the chip, all of these molecules will reach the detector at a single time t_{det}. Thus, this technique is called space focusing.

In the original version of the beamline, the distance from the exit of the chip to the detector is 60 mm. If the velocity of the molecules leaving the chip were still 300 $\frac{\mathrm{m}}{\mathrm{s}}$, an acceleration of $1.5 \cdot 10^6$ $\frac{\mathrm{m}}{\mathrm{s}^2}$ would be necessary, but because this step is done after the molecules have been decelerated, and the necessary acceleration is proportional to velocity squared, the acceleration actually needed to bring the molecules onto the detector at the same time is much lower. Molecules leaving the chip at 120 $\frac{\mathrm{m}}{\mathrm{s}}$, for example, would only be accelerated at $2.4 \cdot 10^5$ $\frac{\mathrm{m}}{\mathrm{s}^2}$. Because the distance from the chip exit to the detector is less than one-third the distance from the laser excitation to the chip entrance, the velocity spread of the molecules exiting the chip will be three times larger than the velocity spread of the captured packet.

Figure 6.10 shows two arrival time profiles in which waveforms were applied to capture a large distribution of velocities. For both traces, the velocity of the traps is set according to equation (6.3) over the period from time $t_1 = 582$ µs to time $t_2 = 683$ µs. This deceleration sequence captures molecules in the velocity range from 324 $\frac{\mathrm{m}}{\mathrm{s}}$ (corresponding to a frequency of 2.7 MHz) down to 276 $\frac{\mathrm{m}}{\mathrm{s}}$ (2.3 MHz). The 30 mm long packet is then decelerated from 276 $\frac{\mathrm{m}}{\mathrm{s}}$ to 180 $\frac{\mathrm{m}}{\mathrm{s}}$ in 80 µs, at which point the first molecules to enter the chip are now at the end of the electrode array. If the molecules are guided off the chip at a constant velocity of 180 $\frac{\mathrm{m}}{\mathrm{s}}$, the broad distribution seen in the black trace is observed. For the red trace, the velocity of the traps was accelerated according to equation (6.6), using $t_{\mathrm{det}} = 1.098$ ms, as the molecules are leaving the chip. Instead of arriving over a large range of times, the molecules arrive together, producing a single sharp peak in the arrival time distribution. In order to arrive simultaneously, these molecules must span a range of velocities from 180 $\frac{\mathrm{m}}{\mathrm{s}}$ for the first molecules leaving the chip to 300 $\frac{\mathrm{m}}{\mathrm{s}}$ for the last molecules to leave.

The results of trajectory simulations for this pair of waveforms are shown in figure 6.11 as a phase space plot. Here, the longitudinal position and longitudinal velocity of each particle that eventually reaches the detector are plotted at various snapshots in time. At the first snapshot (A), the molecules have just been excited into their metastable state, so while they have a large velocity distribution, their spacial distribution is only 1 mm. At a time 0.58 ms later (B), the fastest molecules of the distribution that will be captured

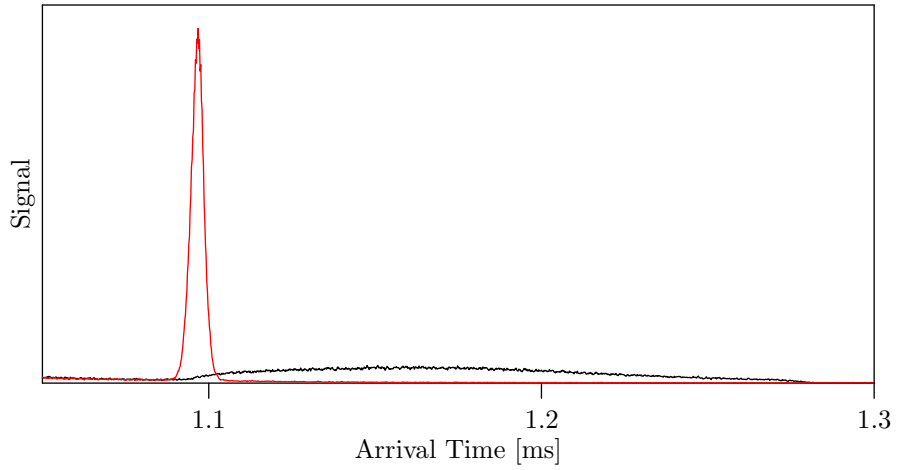

Figure 6.10: Velocity and space focusing of ^{13}CO molecules. Waveforms are applied to load molecules in the velocity range from 324 $\frac{\text{m}}{\text{s}}$ down to 276 $\frac{\text{m}}{\text{s}}$ onto the chip. The 30 mm long packet is then decelerated to 180 $\frac{\text{m}}{\text{s}}$, at which point the first molecules to arrive on the chip are near the chip's exit. In the black curve, all molecules leave the chip at 180 $\frac{\text{m}}{\text{s}}$, producing a broad arrival time distribution. In the red curve, the molecules are reaccelerated, focusing their arrival times into an intense, narrow peak.

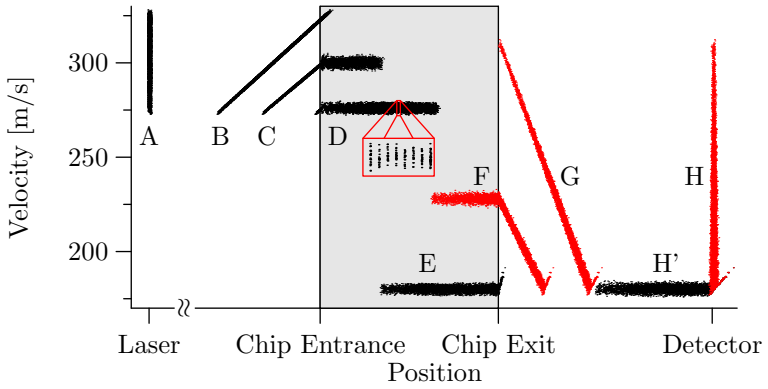

Figure 6.11: Trajectory simulations for velocity and space focusing waveforms, illustrated through the longitudinal position and velocity distributions at various snapshots in time for the molecules that eventually reach the detector. Immediately after the laser excitation, the molecules have a wide range of velocities. The fastest molecules reach the chip first (B) and are loaded at high velocity. The velocity of the traps is then reduced to load molecules with successively lower velocities (C and D). While on the chip, the packet of molecules is contained in roughly 250 individual minima. The molecules are decelerated to 180 $\frac{\text{m}}{\text{s}}$ (E) and are either extracted from the chip at constant velocity (H') or are reaccelerated (F and G). If the acceleration is chosen correctly, all molecules will arrive at the detector at the same time (H).

have just reached the chip, while the slowest molecules are still a few centimeters away. At time (B), the waveforms are switched on with a frequency of 2.7 MHz (corresponding to 324 $\frac{\mathrm{m}}{\mathrm{s}}$), and during the period from (B) to (D), are ramped down to 2.3 MHz (276 $\frac{\mathrm{m}}{\mathrm{s}}$), bringing the entire packet onto the chip at time (D). From time (D) to time (E), the traps are rapidly decelerated to 180 $\frac{\mathrm{m}}{\mathrm{s}}$ (1.5 MHz), at which point the first molecules to arrive on the chip are at the end of the electrode array. In one alternative, the molecules leave at a constant velocity and arrive to the detector over a long time period (H'). In the other alternative, the molecules are reaccelerated as they are leaving the chip (E–G) such that the slowest molecules are close to the detector and the fastest molecules are far from the detector at time (G). At time (H), all of the molecules in the packet arrive at the detector.

6.3.2 Trapping ^{13}CO

With the assistance of the velocity focusing and space focusing techniques, a waveform sequence is composed to bring molecules to a standstill on the chip. First the molecules with a longitudinal velocity from 312 $\frac{\mathrm{m}}{\mathrm{s}}$ (2.6 MHz) down to 300 $\frac{\mathrm{m}}{\mathrm{s}}$ (2.5 MHz) are velocity focused onto the chip. In the next 250 µs, the molecules are rapidly decelerated from 300 $\frac{\mathrm{m}}{\mathrm{s}}$ (2.5 MHz) to 0 $\frac{\mathrm{m}}{\mathrm{s}}$. After a variable time at standstill, the molecules are reaccelerated to 96 $\frac{\mathrm{m}}{\mathrm{s}}$ (0.8 MHz), at which point the first molecules to enter the chip are near the last electrode. The velocity of the traps is then accelerated at a rate such that the molecules all reach the detector 0.63 ms later.

The resulting arrival time distributions are shown in figure 6.12. In the uppermost trace of the main figure, the molecules, after being brought to a standstill, are immediately reaccelerated, and arrive at the detector 1.6 ms after the laser excitation. In the next trace, the molecules are held at standstill for 0.5 ms before being reaccelerated, so the molecules arrive 0.5 ms later than before, i.e. at 2.1 ms. The holding time on the chip has been increased in successive traces in 0.5 ms steps up to 2.5 ms. Although some molecules can still be detected after they have been stored in the trap for 2.5 ms, the number reaching the detector is significantly less than in the case where the molecules were immediately reaccelerated after being stopped. This loss is expected though: since the lifetime of the $a^3\Pi_1$ state of CO is only 2.6 ms [16], less than 40% of the molecules should remain in the trap after 2.5 ms of trapping time. The inset of figure 6.12 shows the integrated intensity of the peaks as a function of trapping time (points with error bars). These points agree well with the 2.6 ms exponential decay curve (solid curve).

6.3.3 Mechanical Resonances

Although molecules have been trapped above the chip successfully, the number of molecules that reach standstill and are successfully reaccelerated is very small: on average, a molecule is detected only once every ten laser pulses. This is smaller than simple density arguments would suggest: there are likely about 10^{11} metastable CO molecules per cubic centimeter in the laser excitation, and by the time these molecules reach the chip, the density will have dropped to 10^7 cm^{-3}. Each trap has a volume of about 10^{-6} cm^3, and about 60 traps were filled when the molecules were decelerated to standstill, so one could expect about 600 molecules per pulse to be trapped. With a 1% detection efficiency, this

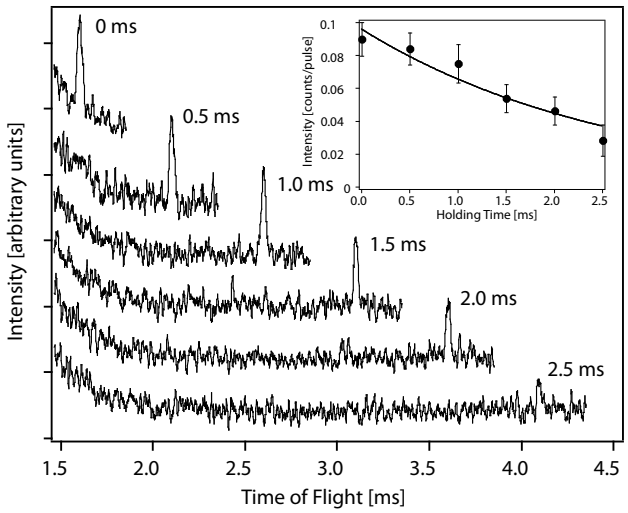

Figure 6.12: Arrival time distributions for molecules that have been trapped on the chip. Molecules in the velocity range from 312 $\frac{\mathrm{m}}{\mathrm{s}}$ (2.6 MHz) down to 300 $\frac{\mathrm{m}}{\mathrm{s}}$ (2.5 MHz) are velocity focused onto the chip, and in the next 250 µs, are decelerated to 0 $\frac{\mathrm{m}}{\mathrm{s}}$. After a variable holding time above the chip, the molecules are reaccelerated to 96 $\frac{\mathrm{m}}{\mathrm{s}}$ (0.8 MHz) and then space focused to the detector. In the uppermost trace, the molecules are immediately reaccelerated after being brought to a standstill, and in subsequent traces, the molecules are held for 0.5 ms, 1.0 ms, 1.5 ms, 2.0 ms, or 2.5 ms. The inset shows the total number of molecules reaching the detector per pulse as a function of holding time. While the integrated intensity of the peaks decreases with increasing holding time, this loss is expected as a consequence of the 2.6 ms lifetime of the $a^3\Pi_1$ state.

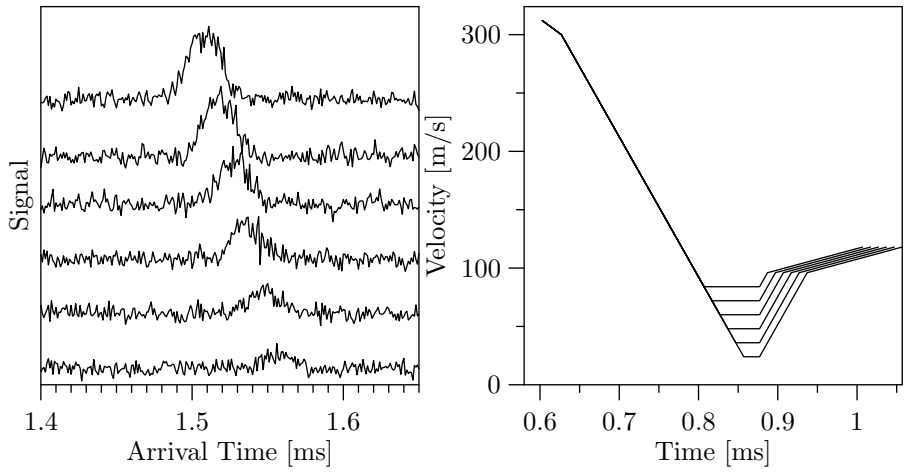

Figure 6.13: A series of waveforms were constructed to decelerate molecules to successively lower velocities without changing how the molecules enter the chip, leave the chip, or the maximum acceleration they experience. The velocities of these waveforms as a function of time after the laser excitation are shown on the right. Molecules from 312 $\frac{\mathrm{m}}{\mathrm{s}}$ to 300 $\frac{\mathrm{m}}{\mathrm{s}}$ are velocity focused and the packet is then decelerated at $1.2 \cdot 10^6$ $\frac{\mathrm{m}}{\mathrm{s}^2}$ to a minimum velocity ranging from 84 $\frac{\mathrm{m}}{\mathrm{s}}$ down to 24 $\frac{\mathrm{m}}{\mathrm{s}}$. After being guided at the low velocity for a period of time, the molecules are reaccelerated to 96 $\frac{\mathrm{m}}{\mathrm{s}}$ at an acceleration of $1.2 \cdot 10^6$ $\frac{\mathrm{m}}{\mathrm{s}^2}$ and space focused from the chip to the detector. The guiding period is chosen such that the molecules traverse the same distance over the chip, i.e. the integral of all of the velocity curves is the same. On the left are arrival time distributions for molecules manipulated by these waveforms. The molecules in the uppermost trace have been decelerated to 84 $\frac{\mathrm{m}}{\mathrm{s}}$, and the molecules in subsequent traces to 72 $\frac{\mathrm{m}}{\mathrm{s}}$, 60 $\frac{\mathrm{m}}{\mathrm{s}}$, 48 $\frac{\mathrm{m}}{\mathrm{s}}$, 36 $\frac{\mathrm{m}}{\mathrm{s}}$, and 24 $\frac{\mathrm{m}}{\mathrm{s}}$. As the minimum velocity of the traps decreases, fewer and fewer molecules reach the detector.

should result in about 6 molecules being detected per pulse, about 60 times larger than what was actually observed.

The losses seem to occur most strongly when the molecules are decelerated to very low velocities, but generally to reach these lower velocities, several features of the waveform sequence are changed simultaneously: higher acceleration is used, and the waveform sequence used to couple the molecules onto the chip or eject them from the chip might also be different. To disentangle losses associated with molecules being in the traps at low velocities from these other effects, a series of waveforms were constructed in which the lowest velocity on the chip is varied without changing the maximum acceleration, the waveform sequence to couple the molecules onto the chip, or the waveform sequence to eject molecules from the chip. The trap velocity produced by the waveform sequences as a function of time is shown in the right half of figure 6.13. Each of the waveform sequences uses the same velocity focusing at the beginning, followed by a $1.2 \cdot 10^6 \ \frac{\mathrm{m}}{\mathrm{s}^2}$ deceleration to various final velocities. At the end, the molecules are reaccelerated at $1.2 \cdot 10^6 \ \frac{\mathrm{m}}{\mathrm{s}^2}$, and the same space focusing is used in each sequence. In between, a segment of constant velocity guiding is inserted so that the molecules are at the same position on the chip when the space focusing waveforms begin. The arrival time traces in the left half of figure show the molecules that have been decelerated to the various minimum velocities, ranging from $84 \ \frac{\mathrm{m}}{\mathrm{s}}$ in the uppermost trace to $24 \ \frac{\mathrm{m}}{\mathrm{s}}$ in the lowermost. Despite nearly all details of the waveform sequences other than the minimum velocity being the same, fewer molecules reach the detector if they have been decelerated to a lower velocity.

Although most parameters other than the minimum velocity were kept the same in each waveform sequence, the total deceleration time and the total time that the molecules spend on the chip both increased as the minimum velocity decreased. To test whether either of these parameters could be responsible for the decrease in signal observed in figure 6.13, a second set of waveform sequences was constructed with much higher minimum velocities, ranging from $252 \ \frac{\mathrm{m}}{\mathrm{s}}$ to $180 \ \frac{\mathrm{m}}{\mathrm{s}}$. These waveforms sequences and the resulting arrival time distributions are shown in figure 6.14. Unlike before, the number of molecules reaching the detector seems to depend little on the minimum velocity that the molecules see on the chip. From this, it can be concluded that neither the time that the molecules spend on the chip nor the time that they are being accelerated or decelerated significantly affects the number of molecules reaching the detector.

One likely explanation for a trap loss that becomes significant at lower velocities is that, due to imperfections in the applied waveforms introduced in the amplifier, the electric field minima do not move over the chip at a constant velocity but instead jitter around the ideal, constant velocity point. This jittering motion could heat the molecules in the trap if it contains frequency components that are not too much higher than the oscillation frequency of the molecules within the trap. Since the quadrupole traps produce a potential that is a linear function of displacement from the center for a molecule with a linear Stark shift, there is no single oscillation frequency in the trap. Because the Λ-doubling makes the potential somewhat quadratic at very low electric field strengths, there is a maximum trap frequency: for waveforms with a 160 V peak-to-peak amplitude, this maximum frequency is about 220 kHz. A more typical trap frequency, assuming a linear potential and a maximum displacement from the trap center of 5 μm, would be about 110 kHz. If the waveforms are periodic, the jittering motion has frequency components that are multiples of one half of the frequency of the applied waveforms. If

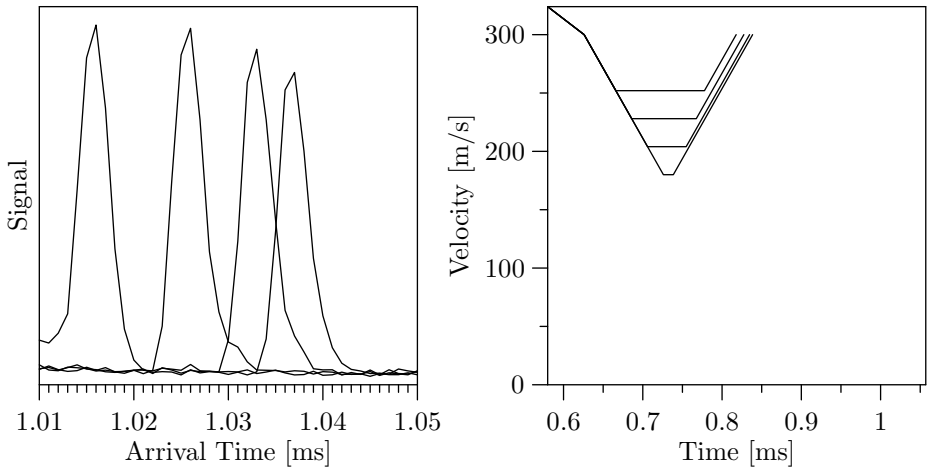

Figure 6.14: A second set of waveforms constructed to probe a higher range of minimum velocities, but still without changing how the molecules enter the chip, leave the chip, or the maximum acceleration they experience. The velocities of these waveforms as a function of time after the laser excitation are shown on the right. Molecules from 324 $\frac{\mathrm{m}}{\mathrm{s}}$ to 300 $\frac{\mathrm{m}}{\mathrm{s}}$ are velocity focused and the packet is then decelerated at $1.2 \cdot 10^6$ $\frac{\mathrm{m}}{\mathrm{s}^2}$ to a minimum velocity ranging from 252 $\frac{\mathrm{m}}{\mathrm{s}}$ down to 180 $\frac{\mathrm{m}}{\mathrm{s}}$. After being guided at the minimum velocity for a period of time, the molecules are space focused from the chip to the detector. The guiding period is chosen such that the molecules traverse the same distance over the chip, i.e. the integral of all of the velocity curves is the same. On the left are arrival time distributions for molecules manipulated by these waveforms. The molecules in the leftmost trace have been decelerated to 252 $\frac{\mathrm{m}}{\mathrm{s}}$, and the molecules in subsequent traces to 228 $\frac{\mathrm{m}}{\mathrm{s}}$, 204 $\frac{\mathrm{m}}{\mathrm{s}}$, and 180 $\frac{\mathrm{m}}{\mathrm{s}}$. In contrast to the losses seen at lower velocities in figure 6.13, little change is seen between the waveform sequences with different minimum velocities.

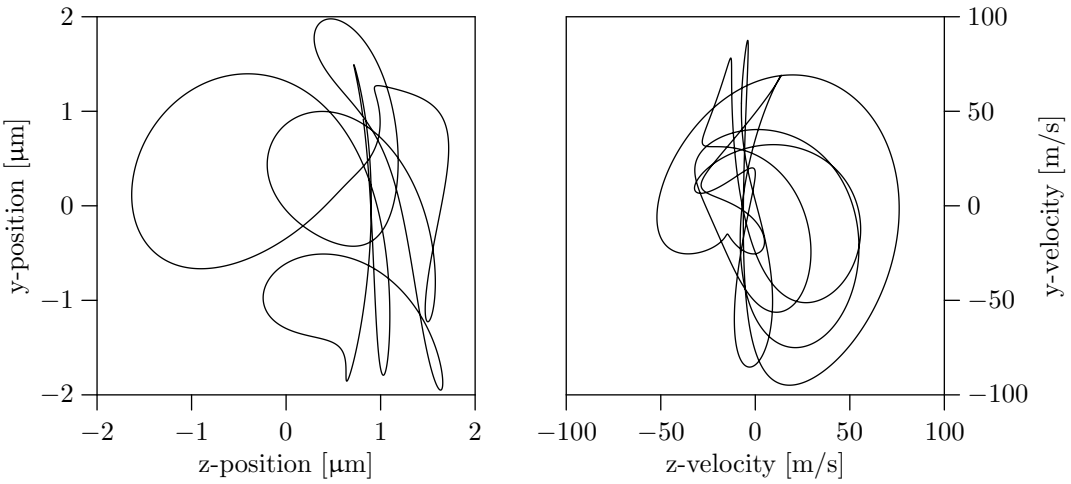

Figure 6.15: Position (left) and velocity (right) of the quadrupole minimum generated by real waveforms relative to an ideal trap that travels at constant velocity. The 2.5 MHz, 180 V peak-to-peak waveforms applied to the chip were recorded with an oscilloscope, and for each point in time, the six potentials are used to calculate the position of the minimum. By numerically taking the derivative of position with respect to time, the velocity of the trap center is also found.

the waveforms have a frequency of 1 MHz, corresponding to a trap velocity of 120 $\frac{\text{m}}{\text{s}}$, the jittering motion of the minimum can have Fourier components with a frequency as low 500 kHz.

To examine the motion of the real traps, 2.5 MHz, 180 V peak-to-peak waveforms were applied to the electrodes and simultaneously recorded on an oscilloscope. Using the six applied potentials recorded at each point in time, the position of the quadrupole minimum is calculated for every point of the waveform. The left side of figure 6.15 shows position of this minimum relative to an ideal trap moving transversely over the surface at 300 $\frac{\text{m}}{\text{s}}$ over one cycle of its oscillation or two cycles of the applied waveform. Relative to the ideal motion, the trap wanders over a ± 2 μm-wide region, a motion that corresponds to nearly 20% of the width of the entire trap. The velocity of this motion, found by numerically taking the derivative of the position, is shown on the right side of the figure. It can be seen that the real minimum frequently has a velocity in excess of 50 $\frac{\text{m}}{\text{s}}$ relative to the ideal minimum, although at lower frequencies, the velocity of the jittering would be proportionally lower.

With motions with such extreme displacement and velocity, it is somewhat surprising that the molecules can be trapped in the moving potential wells at all. The trapping in the moving potential likely only works because the jittering is much faster than the motion of the molecules in the traps and the molecules still see a trap on average. If the trap velocity is greatly reduced, however, the frequency of these motions is similarly reduced, and the assumption that the trap motion is much faster than the motion of the molecules no longer holds. Mechanical heating is not the only problem that results from this rapid motion: in the next chapter, it will be shown that the rapid jittering also leads to non-adiabatic transitions. In future experiments, it will likely be necessary to improve the quality of the waveforms to improve the guiding, deceleration, and trapping of molecules above the chip.

Chapter 7

Suppression of Non-Adiabatic Trap Losses Using a Magnetic Field

The goal of the most recent experiment is to quantify how much energetic splitting is needed between low field seeking levels and levels with little Stark shift to prevent losses from the traps due to non-adiabatic transitions. It was shown in the last chapter that the 50 MHz splitting in ^{13}CO due to hyperfine interactions suppresses these losses, but because this splitting cannot be varied, it is not clear how large the splitting needs to be to suppress all losses. In chapter 4, it was observed that if a magnetic field is applied to ^{12}CO molecules in the $a^3\Pi_1$, $v = 0$, $J = 1$ state, the low field seeking levels are split from the levels with little Stark shift by an amount given by the Zeeman splitting, and if an electric field is applied perpendicular to the magnetic field, the splitting only increases. By applying a uniform magnetic field to the chip along the axis of the electrodes (along which there is no electric field) and measuring the number of molecules that reach the detector after being guided over the chip for various magnetic field strengths, it can be determined how much splitting is necessary to prevent trap losses due to non-adiabatic transitions.

7.1 A New Machine

Preliminary experiments were conducted in the same machine used for all experiments in the last chapter and described in chapter 5. Unfortunately, the Auger detector is fairly sensitive to magnetic fields, since the electrons leave the surface with low kinetic energy and must be accelerated along a curved path to reach the detector. At magnetic fields higher than a few Gauss, no more signal is observed at the MCP, and since the magnetic field was applied to the chip using a pair of 30 cm diameter coils, the field at the Auger detector was nearly as high as at the chip. This problem could not be mitigated by turning off the magnetic field during the time that the molecules fly from the chip to the detector, because of the eddy currents induced in the metal chamber and frame. This was further exacerbated by a support frame out of magnetic steel that could remain magnetized for more than a millisecond.

These issues can be eliminated by detecting the molecules using resonance-enhanced multiphoton ionization (REMPI). For metastable CO, a molecule in the $a^3\Pi$ state is excited to the $b^3\Sigma^+$ state using a 283 nm, 4 mJ, 5 ns laser pulse, after which one more

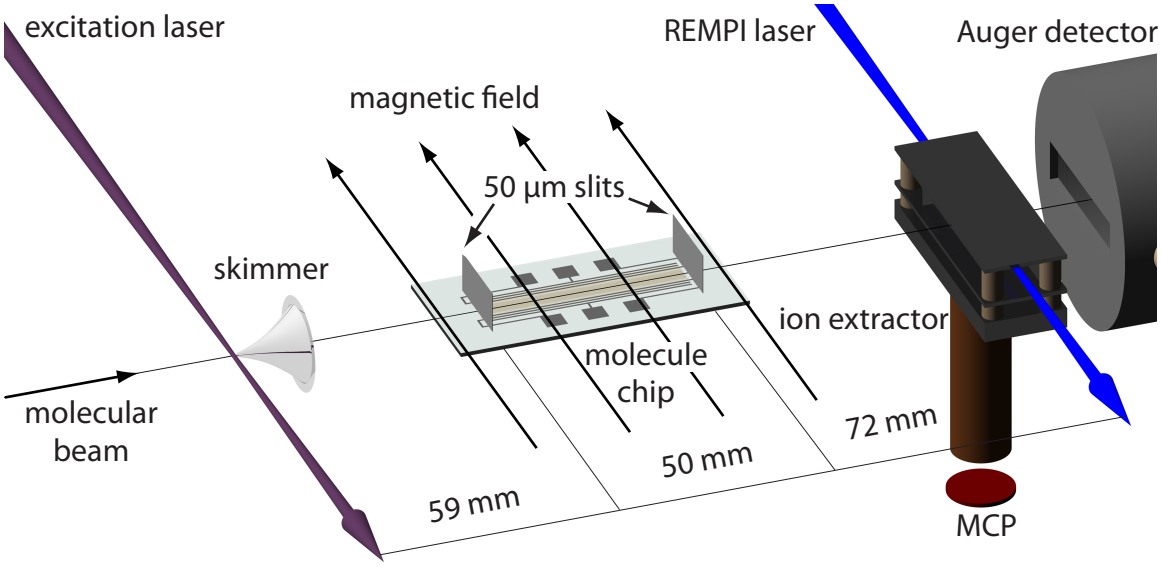

Figure 7.1: The new beamline used for the experiments in this chapter. The setup features a third differentially-pumped chamber to improve the pressure in the chamber containing the chip and a laser excitation much closer to the first electrode of the array. Additionally, the new beamline includes an ionization detector in which the metastable CO molecules are ionized in a 1+1 REMPI process and the ions extracted to a microchannel plate. The ionization detection scheme has the advantage of being insensitive to magnetic fields.

283 nm photon is sufficient to ionize the molecule. Once the CO molecule is ionized, it can be accelerated directly to a microchannel plate (MCP) detector, and because the ion is much heavier than an electron, its trajectory is less influenced by magnetic fields. Since major modifications would be needed to implement REMPI in the existing machine, plans to move the chip to a new machine were accelerated.

The beamline of the new machine is seen in figure 7.1. To improve the vacuum in the chip chamber for future experiments, the new machine is separated into three differentially-pumped chambers, separated by two skimmers. The molecular beam is produced using the same pulsed valve as before and passes through the first skimmer (not shown). Immediately before passing through the second skimmer, the CO molecules are excited to their metastable state. The region around the chip is in a uniform magnetic field produced by a pair of 30 cm diameter planar coils, separated by 23 cm, outside the chamber. The direction of this field is chosen such that it is always perpendicular to the electric fields that manipulate the metastable CO molecules on the chip. After exiting from the chip, the molecules can be detected in one of two ways: either they can be ionized between the ion extractor plates, after which the CO ions are extracted to the side and detected on the off-axis MCP, or they can fly further and be detected by the same Auger detector used previously. The REMPI detection scheme is insensitive to magnetic fields: calculations show that, even in a 100 Gauss magnetic field, the ions are deflected by less than 2 mm from their magnetic field free trajectory, which is sufficiently small to still impact the 8 mm diameter MCP. Even though the magnetic field can now in principle be applied continuously, it is switched off after the molecules have been detected and

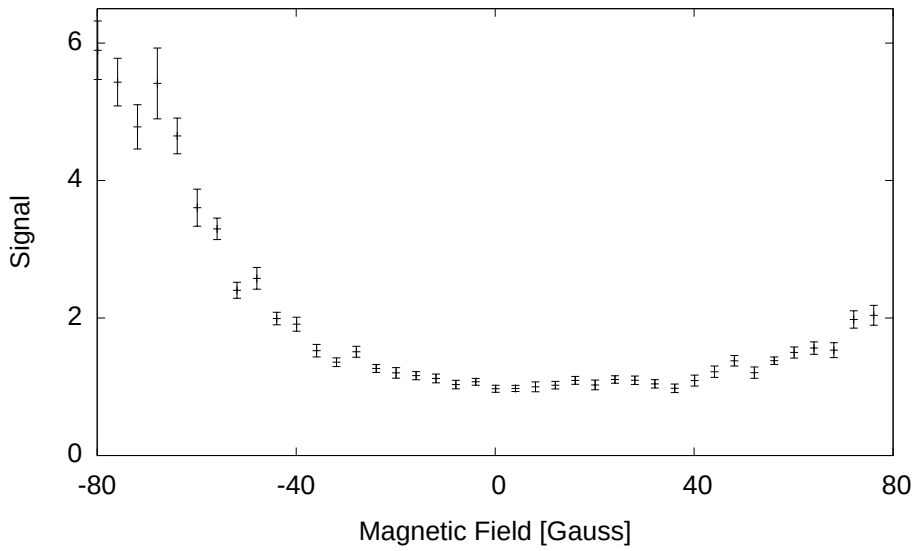

Figure 7.2: Relative number of ^{12}CO molecules in the low field seeking levels of the $a^3\Pi_1$, $v = 0$, $J = 1$ metastable state guided over the chip at 300 $\frac{\mathrm{m}}{\mathrm{s}}$ as a function of magnetic field. The signal intensity is normalized such that the guiding signal at zero magnetic field is one. The direction of positive magnetic field corresponds to the direction shown in figure 7.1, which is also the $+\hat{x}$-axis, if the $+\hat{y}$-axis is defined as a normal vector directed away from the chip surface and the $+\hat{z}$-axis is the direction of the molecular beam. At the highest magnetic field strengths, the number of guided molecules is enhanced by a factor of six.

switched on again shortly before the new pulsed beam is emitted to reduce the heating of the coils.

7.2 Experimental Results

To examine the rate of non-adiabatic losses as a function of magnetic field strength, metastable CO molecules are guided over the full length of the chip at a constant 300 $\frac{\mathrm{m}}{\mathrm{s}}$ and subsequently detected using REMPI. The relative number of guided metastable ^{12}CO molecules detected as a function of magnetic field is shown in figure 7.2. In this and all subsequent data plots in this chapter, the signal is normalized to the signal at zero magnetic field. The measurements are also carried out for positive and negative magnetic fields along a single axis: the direction of positive magnetic field is shown in figure 7.1, and it coincides with the $+\hat{x}$-axis, if the $+\hat{y}$-axis is defined as a normal vector directed away from the chip surface and the $+\hat{z}$-axis is in the direction of the molecular beam. At the highest magnetic field strengths, the number of guided molecules is enhanced by a factor of six. This supports the idea that, as the splitting between low field seeking states and untrapped states increases, the probability of non-adiabatic transitions decreases, and fewer molecules are lost from the moving traps. The enhancement depends on the direction of the magnetic field: while there is significant enhancement for negative magnetic fields, less enhancement is seen for positive magnetic fields.

Figure 7.3 shows the intensity of ^{13}CO guided at 300 $\frac{\mathrm{m}}{\mathrm{s}}$ as a function of magnetic

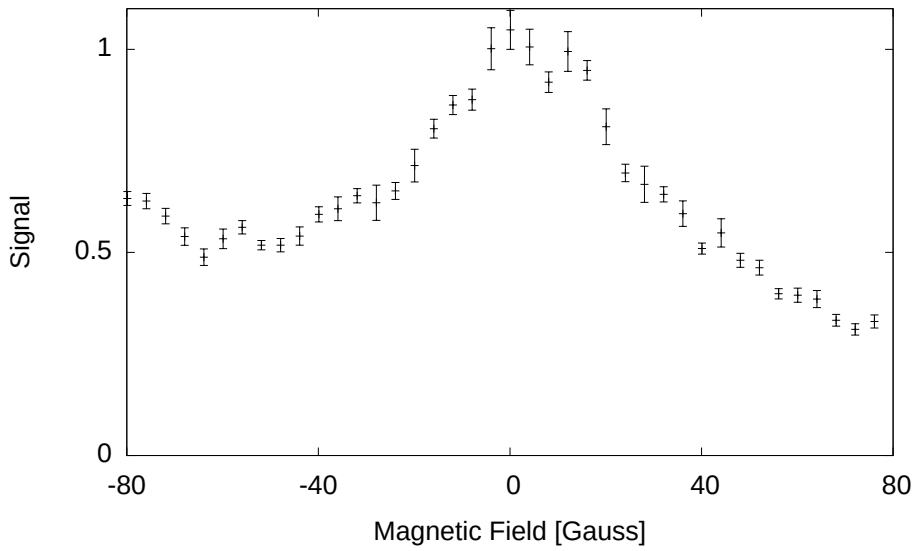

Figure 7.3: Relative number of ^{13}CO molecules in the low field seeking levels of the $a^3\Pi_1$, $v = 0$, $J = 1$ metastable state guided over the chip at 300 $\frac{\mathrm{m}}{\mathrm{s}}$ as a function of magnetic field. The normalization of the signal and the direction of positive magnetic field are the same as in figure 7.2. While ^{12}CO guiding is enhanced by a magnetic field, applying a magnetic field to the chip while guiding ^{13}CO actually decreases the number of guided molecules reaching the detector.

field. While ^{12}CO guiding is enhanced by a magnetic field, applying a magnetic field to the chip while guiding ^{13}CO actually decreases the number of guided molecules reaching the detector. This signal reduction can be explained by the level structure of ^{13}CO. With zero magnetic field, the low field seeking levels in the $a^3\Pi_1$, $v = 0$, $J = 1$ state of ^{13}CO are already well separated from the levels unaffected by electric fields (see figure 4.2). By applying a magnetic field, the splitting between some of the low field seeking levels and some of the levels unaffected by electric fields decreases, increasing the likelihood of non-adiabatic transitions between these states (see figure 4.3). As in ^{12}CO, the ^{13}CO guiding signal is asymmetric for positive and negative magnetic fields. While it appears from the guiding data of ^{12}CO that these could be symmetric around a magnetic field strength of +15 Gauss, no such symmetry exists for the ^{13}CO data.

7.3 Quasienergy Hamiltonian in a Rotating Field

The strength of non-adiabatic transitions that lead to loss of molecules from the traps is determined largely by the minimum separation between the low field seeking levels and the levels with little Stark shift. In a static trap, this splitting would be given by the Zeeman shift in ^{12}CO and a combination of the Zeeman shift and hyperfine structure in ^{13}CO. The electric fields in the trap are not static, however: as the minima move over the chip, the direction of the electric field vector at every point relative to the minimum rotates at a rate 1.5 times the frequency of the applied waveforms. If this rotation is ignored, and a wavefunction is chosen that is an eigenvector of the Hamiltonian at a

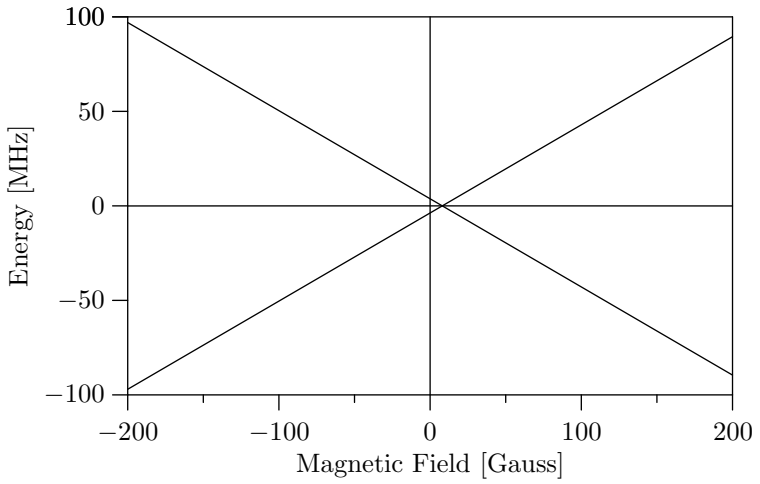

Figure 7.4: Quasienergies in the upper Λ-doublet component of the $a^3\Pi_1$, $v = 0$, $J = 1$ state of ^{12}CO that result from the combination of a static magnetic field and a 3.75 MHz rotating electric field. The three levels are degenerate at $B = +8.0$ Gauss and have a structure that is symmetric about this point.

particular time, the wavefunction will rapidly oscillate from its original eigenstate to other eigenstates.

In chapter 2, it was shown that, for the specific case of ^{12}CO in the $a^3\Pi_1$, $v = 0$, $J = 1$ state, it is possible to choose a linear combination of instantaneous eigenstates that is stationary under the rotating Hamiltonian, i.e. as the wavefunction evolves, it remains the same linear combination of the instantaneous eigenstates up to a phase. The rate at which this phase changes is given by the quasienergy, in much the same way that the rate of change of phase in a time-independent Hamiltonian is given by the energy. To extend the quasienergy description to ^{13}CO in a rotating field, we first consider a general Hamiltonian that rotates at a constant rate around the $\hat{z}$-axis (although the rotation is around the $\hat{x}$-axis in the experiment, it is more conventional to use the $\hat{z}$-axis as a symmetry axis). Such a Hamiltonian can be expressed as a sequence of three operations: a rotation of the system around the $\hat{z}$-axis through an angle $-2\pi\nu t$, the application of a time-independent Hamiltonian, and a rotation back through an angle $2\pi\nu t$. Mathematically, the Hamiltonian can be written as

$$\hat{H}(t) = e^{-i\hat{F}_z 2\pi\nu t}\hat{H}_0 e^{i\hat{F}_z 2\pi\nu t} \tag{7.1}$$

where $\hat{F}_z$ is the total angular momentum operator along the space-fixed $\hat{z}$-axis, and ν is the frequency of the rotation. If $\hat{U}$ in equation (2.42) is chosen to be $\hat{U} = e^{-i\hat{F}_z 2\pi\nu t}$ (a rotation about the $\hat{z}$-axis through an angle $2\pi\nu t$) then the resulting quasienergy Hamiltonian is given by

$$\hat{H}_Q = \hat{U}^\dagger \hat{H}(t)\hat{U} - i\hbar\hat{U}^\dagger \frac{\partial \hat{U}}{\partial t} = \hat{H}_0 - h\nu\hat{F}_z. \tag{7.2}$$

This quasienergy Hamiltonian is time independent.

In ^{12}CO, the Zeeman splitting is proportional to $\hat{F}_z$ for all levels of the $a^3\Pi_1$, $v = 0$, $J = 1$ state, so the magnetic field and the rotation have the same effect on the quasienergy Hamiltonian, but act with opposite signs. If the direction of the rotation, as defined by the

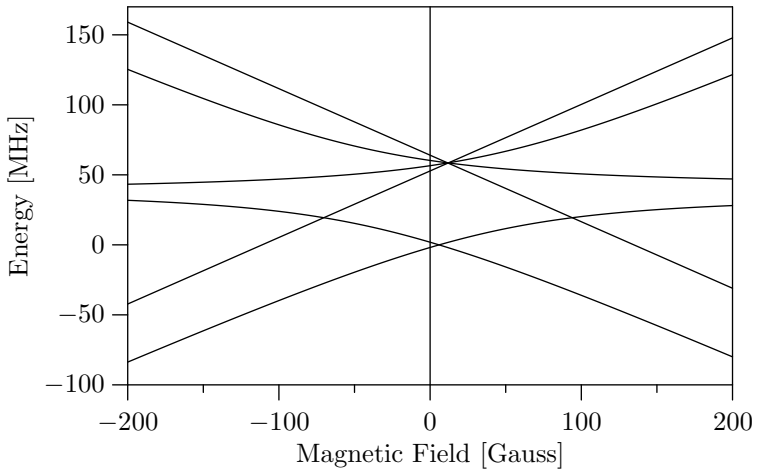

Figure 7.5: Quasienergies in the upper Λ-doublet component of the $a^3\Pi_1$, $v = 0$, $J = 1$ state of ^{13}CO that result from the combination of a static magnetic field and 3.75 MHz rotating electric field. Unlike in ^{12}CO, the application of a magnetic field to ^{13}CO brings some of the low field seeking levels (upper four levels at zero field) closer to the levels with little Stark shift (lower two levels), increasing the likelihood of non-adiabatic transitions. With the inclusion of the rotating electric field, the level structure is no longer symmetric around a particular magnetic field as in ^{12}CO: the upper four levels become nearly degenerate at 11.8 Gauss, while the lower two levels become degenerate at 5.9 Gauss.

right hand rule, and the direction of the magnetic field are the same, then at a particular field strength, the two components cancel each other out. Furthermore, the quasienergy Hamiltonian as a function of magnetic field strength is symmetric around the point at which the rotation and magnetic field cancel out. Qualitatively, the data for ^{12}CO guided at 300 $\frac{\mathrm{m}}{\mathrm{s}}$ match this prediction: the measured signal seems to be symmetric around the magnetic field $B = +15$ Gauss. Based on the Zeeman shift known for this state and the field rotation frequency of 3.75 MHz, the symmetry point is expected at $B = +8.0$ Gauss (see figure 7.4). Although this differs in magnitude from the experimental value by almost a factor of two, the correct sign is obtained.

The quasienergy of ^{13}CO in a combined magnetic field and rotating infinitesimal electric field is shown in figure 7.5. While applying a magnetic field to ^{12}CO separates the low field seeking levels from the states with little Stark shift, applying a magnetic field to ^{13}CO pushes some of the levels closer together. Additionally, the symmetry around a specific magnetic field strength seen in ^{12}CO is absent in ^{13}CO: the upper four levels become nearly degenerate at 11.8 Gauss, while the lower two levels become degenerate at 5.9 Gauss. The data qualitatively reflect the decreased splitting and asymmetry: the maximum intensity is observed at +4 Gauss, and the intensity decreases asymmetrically around this point.

7.4 Theoretical Calculations for ^{12}CO

Since it is not possible to greatly enhance the number of ^{13}CO molecules that can be guided over the chip by applying a magnetic field (in fact, for most magnetic field strengths, applying a field makes the signal worse), the remainder of this chapter will focus on better understanding the non-adiabatic losses that occur when ^{12}CO molecules pass near the center of the microtraps and how these losses can be influenced by a magnetic field. To do this, we start with the quasienergy Hamiltonian given in equation (2.43). This quasienergy Hamiltonian produces two low field seeking states. The first, with intensity primarily in the third basis vector, is only coupled to levels in the lower Λ-doublet component, and this coupling is especially weak at low electric field strengths. The second low field seeking level, with intensity primarily in the fourth basis vector, is strongly coupled to levels in the upper Λ-doublet component and can undergo non-adiabatic transitions. Based on the given quasienergy Hamiltonian, the first low field seeking level should not undergo non-adiabatic transitions. If this were the case, though, half of all low field seeking molecules would be immune to non-adiabatic transitions, yet the data show that the number of molecules reaching the detector increases by more than a factor of two between zero magnetic field and high magnetic fields. One likely explanation is that the population in the two low field seeking levels redistributes at higher electric field strengths: figure 4.3 shows that the splitting between the two low field seeking levels asymptotically approaches zero as the electric field strength increases. To obtain a pessimistic estimate of non-adiabatic loss rates, it will be assumed that only the second of these two low field seeking levels is populated.

Since the quasienergy Hamiltonian only mixes the fourth basis vector with the fifth and the sixth, the three by three submatrix in the lower right corner is used as the quasienergy Hamiltonian for calculations here.

$$\hat{H}_Q(t) = \begin{pmatrix} \frac{\Lambda}{2}(\sec(2\beta) - 1) & R\cos\beta & 0 \\ R\cos\beta & 0 & R\sin\beta \\ 0 & R\sin\beta & -\frac{\Lambda}{2}(\sec(2\beta) + 1) \end{pmatrix} \tag{7.3}$$

The parameter $\Lambda = 394$ MHz is the Λ-doublet splitting. The diagonal elements here are offset by $-\frac{\Lambda}{2}$ from the quasienergy Hamiltonian in chapter 2: this does not change the physics, but the numerical calculations become easier if the levels that contain most of the intensity are closer to zero. In chapter 2, the quasienergy Hamiltonian was written based on the assumption that the magnetic field is along the $\hat{z}$-axis and that the electric field is in the xy-plane, automatically making the two perpendicular. To match the quasienergy Hamiltonian to the coordinate system of the experiment, in which the electric field is in the yz-plane and the magnetic field is along the $\hat{x}$-axis, the coordinates are cycled: all instances of the x in the previous definition are replaced with y, all instances of y with z, and all instances of z with x. The parameters R and β are then derived from $|\vec{E}|$, the strength of the electric field, α, the angle of the electric field vector in the yz-plane with respect to the $+\hat{y}$-axis (positive values toward the $+\hat{z}$-axis), and B_x, the magnetic field, which is positive if the magnetic field is in the $+\hat{x}$-direction and negative if the magnetic

field is in the $-\hat{x}$-direction.

$$R = \hbar\frac{d\alpha}{dt} - Z \tag{7.4}$$

$$\tan(2\beta) = \frac{2S}{\Lambda} \tag{7.5}$$

$$S = 0.4967\,\mu_E|\vec{E}| = 343\,\mathrm{MHz}\left(\frac{\mathrm{kV}}{\mathrm{cm}}\right)^{-1}|\vec{E}| \tag{7.6}$$

$$Z = 0.3332\,\mu_B B_x = 0.466\,\mathrm{MHz\,Gauss}^{-1}B_x \tag{7.7}$$

The parameters S and Z are the Stark and Zeeman splittings, respectively.

Using this quasienergy Hamiltonian matrix, the time-dependent Schrödinger-like equation (equation (2.42)) is solved numerically as a system of coupled first-order ordinary differential equations. While the magnetic field strength and direction is held constant, $\vec{E}$ changes in time, due both to the motion of the molecule through the inhomogeneous field and the inherent time dependence of the electric field. To track the motion of the molecules in the electric field, the system of differential equations is augmented with four additional equations, describing the velocity components v_y and v_z and the position components y and z. The force on the molecule, which determines the rate of change of its velocity, is calculated using the mechanical potential $U(|\vec{E}|)$ of a low field seeking molecule in the manner described in chapter 3. The effect of the magnetic field and electric field rotation on the potential energy are neglected for this calculation.

The spatial distribution of the field is taken to be an infinite quadrupole field. At each position relative to the quadrupole minimum, the electric field vector rotates at a constant rate, simulating the rotation that occurs as the minima move over the electrodes in the experiment. The electric potential for this field can then be written as

$$V = -\frac{A}{2}r^2\cos(2\phi - 2\pi\nu t) = -\frac{A}{2}\left(y^2 - z^2\right)\cos(2\pi\nu t) - Ayz\sin(2\pi\nu t) \tag{7.8}$$

$$\vec{E} = A(y\cos(2\pi\nu t) + z\sin(2\pi\nu t))\hat{y} + A(y\sin(2\pi\nu t) - z\cos(2\pi\nu t))\hat{z} \tag{7.9}$$

The parameter A is non-negative. In the current set of experiments, $A = 0.054\,\frac{\mathrm{V}}{\mu\mathrm{m}^2}$, corresponding to a peak-to-peak amplitude of the applied waveforms of 180 V, and $\nu =$ 3.75 MHz, 1.5 times the frequency of the applied waveforms. Using this electric potential, the electric field strength $|\vec{E}|$ and the angle of the field vector α are given by

$$|\vec{E}| = A\sqrt{(y\cos(2\pi\nu t) + z\sin(2\pi\nu t))^2 + (y\sin(2\pi\nu t) - z\cos(2\pi\nu t))^2} \tag{7.10}$$

$$\alpha(t) = \arg((y\cos(2\pi\nu t) + z\sin(2\pi\nu t)) + i(y\sin(2\pi\nu t) - z\cos(2\pi\nu t))) \tag{7.11}$$

which simplify to

$$|\vec{E}| = A\sqrt{y^2 + z^2} \tag{7.12}$$

$$\alpha(t) = \arg(y - iz) + 2\pi\nu t \tag{7.13}$$

From this, the parameter R can be calculated.

$$R = \hbar\left(y^2 + z^2\right)^{-1}(zv_y - yv_z) + (h\nu - Z) \tag{7.14}$$

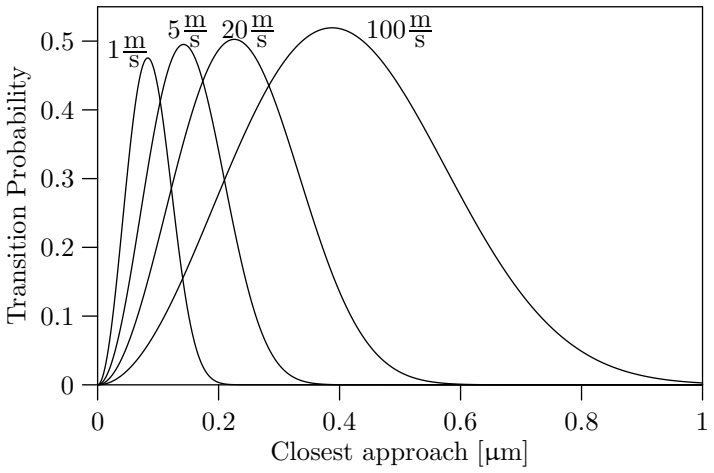

Figure 7.6: Transition probability as a function of closest approach at several different interaction velocities with $h\nu - Z = 0$. As the velocity increases, the integrated probability increases, although the peak transition probability only grows slightly.

To find the transition probability of a molecule that passes the quadrupole minimum at a velocity v_0 and a closest approach distance b, a set of initial conditions are chosen where $v_y = v_0$, $v_z = 0$, $y = 0$, and $z = b$, and for now, the equations that determine the wavefunction are ignored. The differential equation solution is propagated backwards in time until $y = -3$ μm. At this point, the components of the wavefunction are given initial values corresponding to the eigenvector of the quasienergy Hamiltonian with the highest quasienergy, which is the low field seeking state. Note that the electric field rotation due to the velocity of the molecule is also included in the quasienergy Hamiltonian used to initialize the wavefunction. From here, the differential equation solution is propagated forward in time until $y = +3$ μm, passing a point where $v_y = v_0$, $v_z = 0$, $y = 0$, and $z = b$ along the way. At the end of the propagation, the wavefunction is decomposed into eigenvectors of the quasienergy Hamiltonian (which again includes the electric field rotation from the velocity of the molecule), and from this, the probability of the molecule being in one of the two lower eigenstates is calculated. The calculations are repeated for a range of b, both positive and negative, for fixed values of v_0 and $h\nu - Z$.

Through repeated simulations, it was found that the transition probability integrated over all b increases as a function of velocity. Figure 7.6 shows the transition probability as a function of closest approach (b) at several different interaction velocities (v_0) with $h\nu - Z = 0$. While the maximum transition probability does not increase significantly as the velocity increases, the distribution becomes wider, so the overall transition probability for a sample of molecules passing within 1 μm of the minimum increases. For the case where $h\nu - Z = 0$, the integrated transition probability as a function of velocity empirically follows a power law scaling, and is given by

$$\sigma = 0.07926 {v_0}^{0.362} \tag{7.15}$$

Here, v_0 is measured in meters per second and the integrated transition probability, σ, has units of micrometers.

It was initially assumed that, since the maximum velocity of the molecules in the traps is about 5 $\frac{\text{m}}{\text{s}}$, applying a magnetic field to prevent transitions for all molecules with

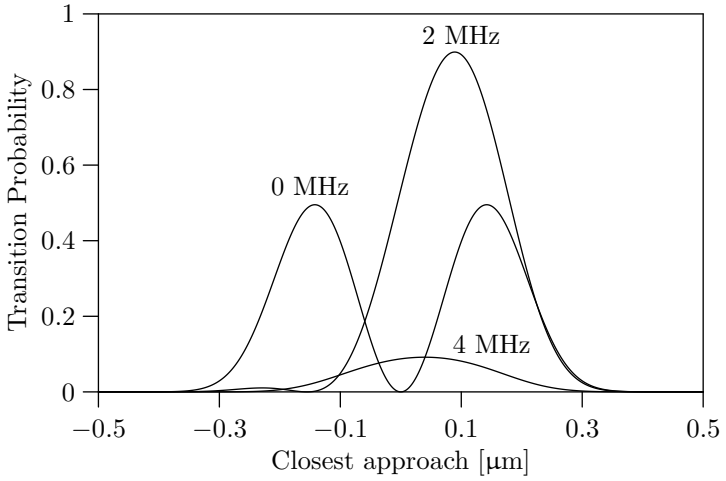

Figure 7.7: Transition probability as a function of closest approach at several values of $h\nu - Z$ with an interaction velocity of 5 $\frac{\text{m}}{\text{s}}$. While the integrated transition probability increases from $h\nu - Z = 0$ MHz to $h\nu - Z = 2$ MHz, at higher splittings, the transition probability decreases. At $h\nu - Z = 10$ MHz, the maximum transition probability is less than 10^{-6}.

this velocity should prevent trap losses. Figure 7.7 shows the transition probability as a function of closest approach for several values of $h\nu - Z$ for $v_0 = 5\ \frac{\text{m}}{\text{s}}$. While the integrated transition probability initially increases from $h\nu - Z = 0$ MHz to $h\nu - Z = 2$ MHz, between 2 MHz and 4 MHz, the transition probability rapidly decreases. It is estimated from further calculations that if $h\nu - Z = 10$ MHz, the transition probability per pass is less than 10^{-6} for all closest approach distances. This splitting can be produced by a 15 Gauss magnetic field applied opposite to the direction of the electric field rotation.

The experimental data clearly show, however, that trap losses continue to decrease at fields more negative than −15 Gauss. While the reason for this was not immediately clear, it now seems that the excess field needed to suppress non-adiabatic losses is a consequence of the trap jittering seen in chapter 6. Figure 6.15 shows that, as a result of the real waveforms applied to the chip, the field minima move with a velocity in excess of 50 $\frac{\text{m}}{\text{s}}$ with respect to the molecules moving over the chip at 300 $\frac{\text{m}}{\text{s}}$. The non-adiabatic losses are not due to the molecules passing the minima at 5 $\frac{\text{m}}{\text{s}}$ but rather the minima passing the molecules at 50 $\frac{\text{m}}{\text{s}}$. Because the frequency of this motion is much higher than the oscillation frequency of the molecules in the traps, the number of passes of the electric field minimum is increased, magnifying the loss rate.

Figure 7.8 shows the transition probability as a function of closest approach distance when the molecules and traps pass at 50 $\frac{\text{m}}{\text{s}}$. While a splitting of 10 MHz suppresses all non-adiabatic transitions in molecules passing the trap center at 5 $\frac{\text{m}}{\text{s}}$, the integrated transition probability actually increases for molecules encountering the minimum at 50 $\frac{\text{m}}{\text{s}}$. Only when the splitting is increased above 10 MHz is the transition probability reduced.

To estimate the splitting necessary to suppress all non-adiabatic transitions in the jittering trap, transition probabilities were calculated for molecules traveling at 100 $\frac{\text{m}}{\text{s}}$, a cautious estimation of the maximum relative velocity between the field minimum and the molecules. For a splitting of 60 MHz, the maximum transition probability per pass

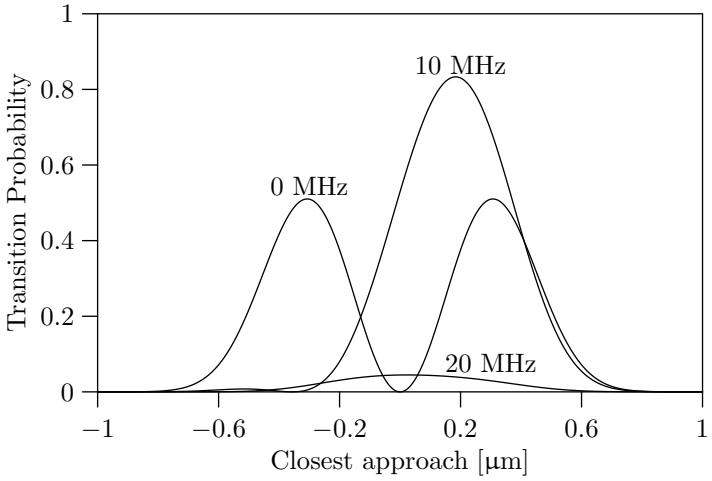

Figure 7.8: Transition probability as a function of closest approach at several values of $h\nu - Z$ with an interaction velocity of 50 $\frac{\text{m}}{\text{s}}$. Although non-adiabatic transitions are completely suppressed at $h\nu - Z = 10$ MHz when the interaction velocity is 5 $\frac{\text{m}}{\text{s}}$, the integrated transition probability actually increases from $h\nu - Z = 0$ MHz to $h\nu - Z =$ 10 MHz but decreases thereafter. At $h\nu - Z = 50$ MHz, the maximum transition probability is about 10^{-6}

is $4 \cdot 10^{-5}$. The left side of figure 6.15 shows that, in one cycle of the motion of the minimum, the minimum passes any point a maximum of about six times, corresponding to one pass per electrode. In the worst case, the molecules would remain at the most unfavorable position for their entire traversal of the chip, seeing 1254 passes of the minimum. For molecules in this position, the total transition probability would only be about 5%, so it can be assumed that with 60 MHz of splitting, nearly all non-adiabatic losses should be prevented. This degree of splitting can be produced with a magnetic field of 120 Gauss applied opposite to the direction of rotation. It can be predicted from this that measurements of the guided molecule signal as a function of magnetic field should saturate somewhere between −80 Gauss and −120 Gauss.

7.5 Additional Measurements

Based on the predictions that the jittering of the microtraps is responsible for non-adiabatic losses at magnetic fields more negative than −15 Gauss and that nearly all non-adiabatic transitions can be prevented with magnetic field around −80 to −120 Gauss, two additional measurements were carried out. One measurement was made under nearly the same conditions as in figure 7.2 but for magnetic fields from −20 to −140 Gauss. The results of these measurements are shown in red in figure 7.9, together with the measurements from figure 7.2 in black. At −80 Gauss, the guiding signal reaches a maximum value, and at more negative field strengths, the signal remains nearly constant, indicating that all non-adiabatic have been prevented. The discrepancy between the two sets of measurements in the overlap region results from a slight misalignment of the detection laser in the earlier experiments: at zero magnetic field, the packet of CO^+ ions was impacting the MCP near its edge and some ions were not being detected, but at

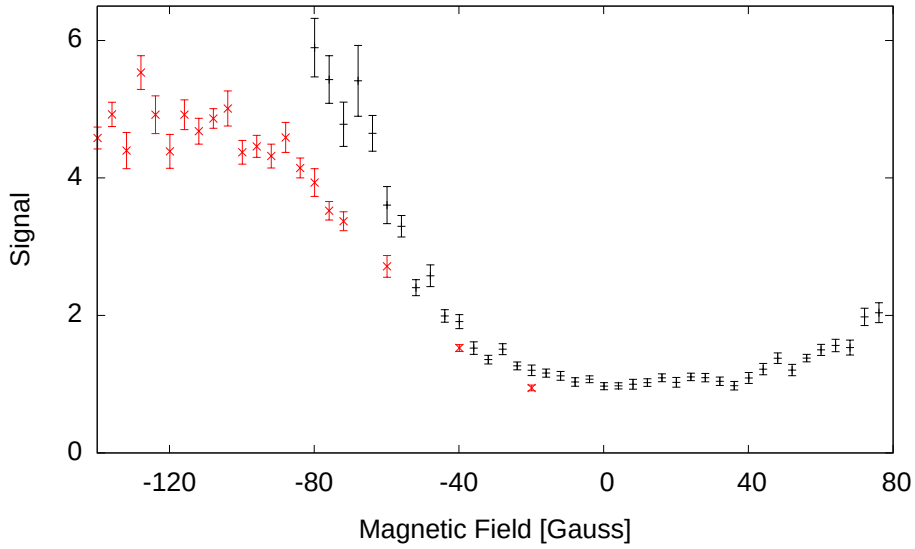

Figure 7.9: Relative number of ^{12}CO molecules in the low field seeking levels of the $a^3\Pi_1$, $v = 0$, $J = 1$ metastable state guided over the chip at 300 $\frac{\mathrm{m}}{\mathrm{s}}$ as a function of magnetic field. The new measurements (red crosses) extend the range of magnetic fields measured to -140 Gauss, and the measurements from figure 7.2 (black pluses) are included for comparison. At magnetic fields more negative than -80 Gauss, the signal saturates, indicating that all non-adiabatic transitions have been prevented.

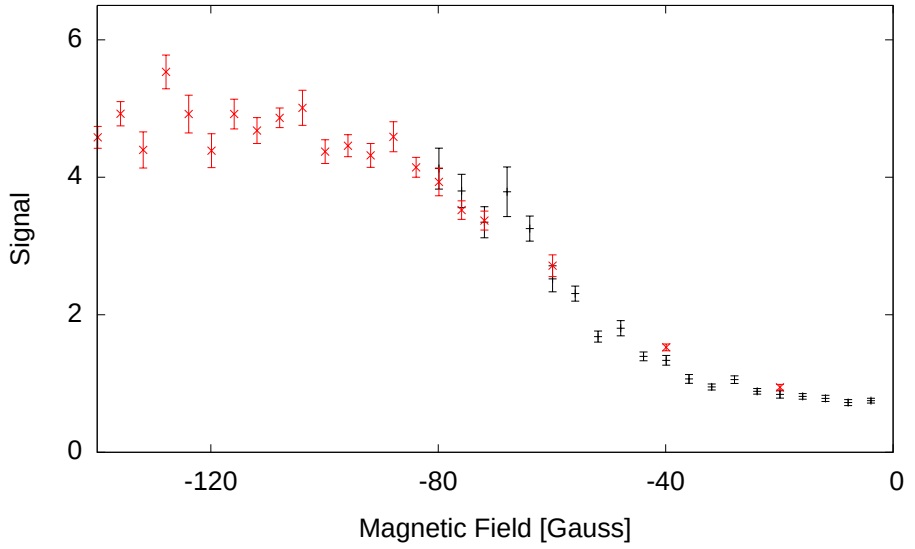

Figure 7.10: Due to a misalignment of the detection laser when measuring the black data points in figure 7.9, the signal at zero magnetic field was underestimated, and as a result, the normalized signal for large, negative magnetic field is overestimated. If these black plus points in figure 7.9 are scaled down to 70% of their original value and the red cross points, which were not affected by this error, are left unchanged, the two data sets agree well in their overlap region.

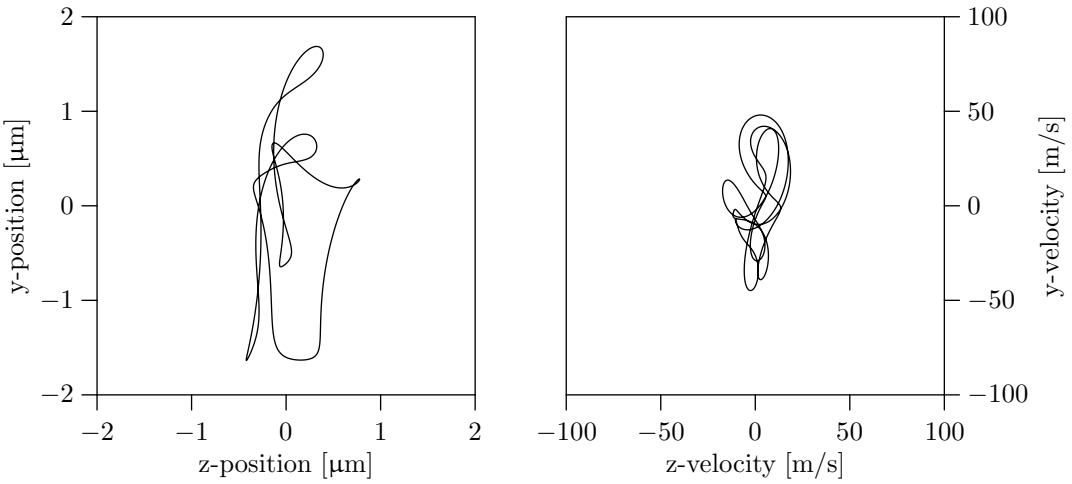

Figure 7.11: Position (left) and velocity (right) of the quadrupole minimum generated by the improved waveforms relative to an ideal trap that moves at constant velocity. The harmonic distortion was reduced by inserting an LC circuit into the output stage of the amplifier. By doing so, the maximum velocity of the field minimum relative to the ideal trap was reduced from nearly 100 $\frac{\mathrm{m}}{\mathrm{s}}$ to less than 50 $\frac{\mathrm{m}}{\mathrm{s}}$. Unfortunately, the modification introduces a strong frequency dependence to the amplification factor, so the modified amplifiers cannot be used for deceleration.

higher magnetic fields, the deflection of the ions by the magnetic fields results in the entire ion packet reaching the MCP. If the earlier data set is scaled to 70% of its original value (which is appropriate if 30% of the ions were not detected at zero magnetic field), the two data sets agree quite well in their overlap range (figure 7.10).

A second measurement was carried out in which ^{12}CO molecules were guided over the chip at 300 $\frac{\mathrm{m}}{\mathrm{s}}$ using more accurate waveforms to produce the moving minima. By inserting an LC circuit into the output stage of the amplifier, the harmonic distortion of the sine waves was reduced, and the maximum velocity of the electric field minimum around its average value is reduced from nearly 100 $\frac{\mathrm{m}}{\mathrm{s}}$ (figure 6.15) to less than 50 $\frac{\mathrm{m}}{\mathrm{s}}$ (figure 7.11). The result is shown in figure 7.12 in red, together with the measurements from figure 7.2 in black. With the improved waveforms, the guiding signal saturates at a magnetic field strength of 40 Gauss instead of 80 Gauss, and the ratio between the number guided at large magnetic fields and the number guided at zero field is smaller, likely because fewer molecules are lost when there is no magnetic field. The asymmetry between positive and negative magnetic fields is also reduced, and the data are largely unchanged by reflection around +8 Gauss (blue line), consistent with the theoretical prediction in section 7.3.

7.6 Conclusions

By applying a magnetic field to the chip perpendicular to the electric fields, non-adiabatic transitions to untrapped states can be prevented in ^{12}CO. The minimum magnetic field strength necessary to prevent all losses also depends on the accuracy of the waveforms applied to produce the moving traps: errors in the applied waveforms lead to a jitter-

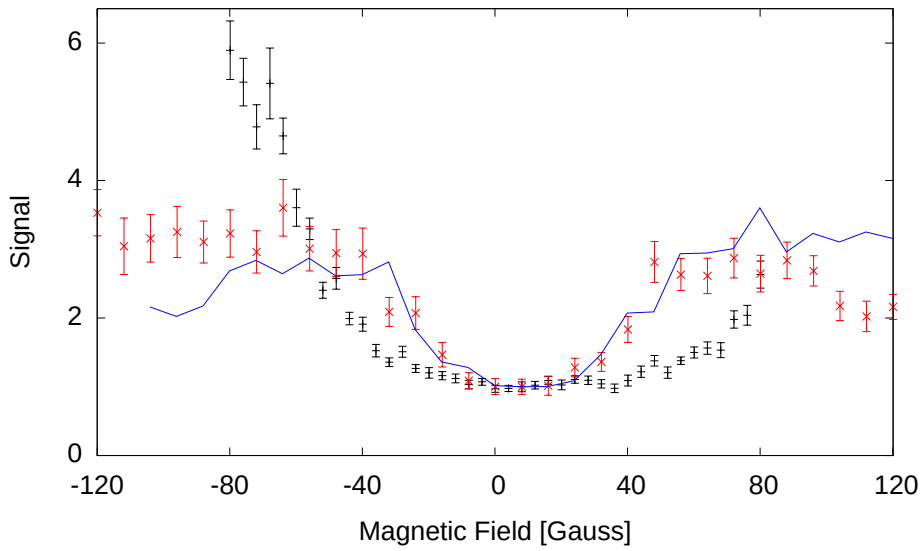

Figure 7.12: Relative number of ^{12}CO molecules in the low field seeking levels of the $a^3\Pi_1$, $v = 0$, $J = 1$ metastable state guided over the chip at 300 $\frac{\text{m}}{\text{s}}$ as a function of magnetic field with improved waveforms (red crosses) compared to the data from figure 7 (black pluses). While magnetic field strengths of more than 80 Gauss were needed to prevent all non-adiabatic losses when using the original waveforms, only 40 Gauss is needed with the improved waveforms. The asymmetry between positive and negative magnetic fields is also reduced, and the data are largely unchanged by reflection around +8 Gauss (blue line), consistent with the theoretical prediction in section 7.3.

ing of the electric field minima that amplify the non-adiabatic losses. Modeling the non-adiabatic loss rate theoretically requires including this motion, and while first calculations are based on a single pass at a particular velocity and closest approach distance, a better approach would be to include the full motion of the jittering field minimum. The discrepancy between the theory and experiment on the asymmetry of the signal enhancement as function of magnetic field (described in section 7.3) might also be better explained by including this motion. Future experiments could also benefit from improved waveforms, since this reduces the strength of the magnetic field needed to prevent the non-adiabatic losses.

Chapter 8

Summary and Outlook

It has been shown in thesis that neutral polar molecules can be guided, decelerated, and trapped 25 μm above the surface of a microstructured electrode array using electric fields. The large number of individual traps on the chip enables efficient manipulation of the phase space distribution: molecules in the beam with a wide distribution of initial velocities can be focused to a single velocity on the chip, and molecules leaving the chip can be reaccelerated such that all molecules reach the detector at the same time, resulting in an order of magnitude more signal at the detector. One critical loss mechanism that has been identified during this work results from non-adiabatic transitions to untrappable states. Such losses are exacerbated by a rapid "jittering" of the electric field minima around their average positions. It has been shown that non-adiabatic losses can nonetheless be suppressed by using the $^{13}C^{16}O$ isotopologue or by applying a magnetic field when decelerating $^{12}C^{16}O$, but at low velocities, the same jittering also causes many molecules to be lost through mechanical resonances. Since the jittering is caused by imperfections in the waveforms applied to produce the moving minima, it will be critical in future experiments to gain better control over the waveforms. Constructing better amplifiers that provide a more linear amplification of the input waveforms will probably be the best solution in the long term. Some improvement might be found in the more immediate future by implementing a feedback mechanism in which the input waveforms are iteratively modified in order to compensate for the amplifier distortions.

A new chip with a 74 mm-long electrode array (consisting of about 1850 electrodes that each have the same dimensions as in the previous chip) has been constructed and is presently being installed. The extra space on this chip will allow the molecules to be brought to a standstill with a low deceleration and will also enable longer packets to be velocity focused onto the chip. Once a larger number of molecules can be trapped on the chip, the lifetime of various isotopologues of CO (starting with $^{13}C^{16}O$) in various vibrational and rotational levels of the $a^3\Pi$ state can be measured above the chip. In principle, figure 6.12 already shows a lifetime measurement, albeit with a low signal to noise ratio.

Metastable CO molecules can in principle be detected while they are trapped above the chip by imaging the phosphorescence they emit when they decay back to the ground state, though a previous attempt to detect the molecules in this way was unsuccessful due to too much background signal. The signal to noise ratio might by improved by exciting $a^3\Pi$, $v = 0$ CO molecules to the $b^3\Sigma^+$, $v = 0$ state using a pulsed laser and imaging

the off-resonant fluorescence of molecules decaying to the $a^3\Pi$, $v = 1$ state. Off-resonant imaging enables filters to be used to suppress scattered light from the excitation laser, and background from ambient light and dark counts are also reduced, since the fluorescent light arrives in a narrow 100 ns time interval. Such a method would also be applicable to the wider range of polar molecules that can be detected using laser-induced fluorescence (LIF).

An experiment is planned to drive transitions from the low field seeking components of the $a^3\Pi_1$, $v = 0$, $J = 1$ to the low field components of the $J = 2$ level using a millimeter-wave source. Since both of these states are trappable, such an experiment could be a first step toward quantum information storage using molecules on a chip.

The relatively low electric fields present in the microtraps (less than 5 $\frac{\text{kV}}{\text{cm}}$ so far) make them suitable for deceleration of molecular states that are only low field seeking at low field strengths. For example, the $X^2\Sigma^+$, $v = 0$, $N = 1$ state of YbF has a component that is low field seeking, but only up to a field strength of 18 $\frac{\text{kV}}{\text{cm}}$. While decelerating this state would be very inefficient using a standard Stark decelerator, it should be feasible using the chip decelerator.

In the more distant future, new chips will be designed and constructed. One feature that might be useful to include in such a design is an electric field bias such that the minimum field strength is non-zero. Such a design could be useful for preventing non-adiabatic losses while decelerating polar molecules that do not have a significant Zeeman shift. This practice is well established for atom chips, where Z-shape traps are used to prevent losses due to spin flip transitions[51]. Optical cavities integrated on the chip could provide a means of on-chip detection that would be applicable to a wide range of molecules. Low-energy chemical reactions between molecules could be studied by creating a chip with two parallel decelerators. Molecules arriving from opposite directions would be decelerated to a standstill in opposite decelerators, and after reaching standstill, the microtraps would be merged to allow the two species to react. Many new experiments will certainly become possible as work is continued toward building a molecular laboratory on a chip.

Bibliography

[1] H. L. Bethlem, G. Berden, and G. Meijer. Decelerating neutral dipolar molecules. *Physical Review Letters*, 83:1558–1561, 1999.

[2] H. L. Bethlem, G. Berden, F. M. H. Crompvoets, R. T. Jongma, A. J. A. van Roij, and G. Meijer. Electrostatic trapping of ammonia molecules. *Nature*, 406:491–494, 2000.

[3] S. Y. T. van de Meerakker, N. Vanhaecke, and G. Meijer. Stark deceleration and trapping of OH radicals. *Annual Review of Physical Chemistry*, 57:159–190, 2006.

[4] R. C. Jaeger. *Introduction to Microelectronic Fabrication*, chapter 2: Lithography. Prentice Hall, 2002.

[5] D. Hanneke, S. Fogwell, and G. Gabrielse. New measurement of the electron magnetic moment and the fine structure constant. *Physical Review Letters*, 100:120801, 2008.

[6] R. Wynands and S. Weyers. Atomic fountain clocks. *Metrologia*, 42:S64–S79, 2005.

[7] J. Crassous, C. Chardonnet, T. Saue, and P. Schwerdtfeger. Recent experimental and theoretical developments towards the observation of parity violation (PV) effects in molecules by spectroscopy. *Organic and Biomolecular Chemistry*, 3:2218–2224, 2005.

[8] J. J. Hudson, B. E. Sauer, M. R. Tarbutt, and E. A. Hinds. Measurement of the electron electric dipole moment using YbF molecules. *Physical Review Letters*, 89:023003, 2002.

[9] B. C. Regan, E. D. Commins, C. J. Schmidt, and D. DeMille. New limit on the electron electric dipole moment. *Physical Review Letters*, 88:071805, 2002.

[10] V. V. Flambaum. Enhanced effect of temporal variation of the fine-structure constant in diatomic molecules. *Physical Review A*, 73:034101, 2006.

[11] H. L. Bethlem and W. Ubachs. Testing the time-invariance of fundamental constants using microwave spectroscopy on cold diatomic radicals. *Faraday Discussion*, 142:25–36, 2009.

[12] M. R. Tarbutt, J. J. Hudson, B. E. Sauer, and E. A. Hinds. Prospects for measuring the electric dipole moment of the electron using electrically trapped polar molecules. *Faraday Discussions*, 142:37–56, 2009.

[13] J. van Veldhoven, J. Küpper, H. L. Bethlem, B. Sartakov, A. J. A. van Roij, and G. Meijer. Decelerated molecular beams for high-resolution spectroscopy: The hyperfine structure of $^{15}ND_3$. *The European Physical Journal D*, 31:337–349, 2004.

[14] R. Schneider and G. Werth. Ion storage technique for very long living states: The decay rate of the 5 $D_{3/2}$ state of Ba II. *Zeitschrift für Physik A*, 293:103–106, 1979.

[15] S. Y. T. van de Meerakker, N. Vanhaecke, M. P. J. van der Loo, G. C. Groenenboom, and G. Meijer. Direct measurement of the radiative lifetime of vibrationally excited OH radicals. *Physical Review Letters*, 95:013003, 2005.

[16] J. J. Gilijamse, S. Hoekstra, S. A. Meek, M. Metsälä, S. Y. T. van de Meerakker, G. Meijer, and G. C. Groenenboom. The radiative lifetime of metastable CO ($a^3\Pi$, $v = 0$). *Journal of Chemical Physics*, 127:221102, 2007.

[17] S. Hoekstra, M. Metsälä, P. C. Zieger, L. Scharfenberg, J. J. Gilijamse, G. Meijer, and S. Y. T. van de Meerakker. Electrostatic trapping of metastable NH molecules. *Physical Review A*, 76:063408, 2007.

[18] W. C. Campbell, G. C. Groenenboom, H.-I. Lu, E. Tsikata, and J. M. Doyle. Time-domain measurement of spontaneous vibrational decay of magnetically trapped NH. *Physical Review Letters*, 100:083003, 2008.

[19] R. T. Jongma, G. Berden, and G. Meijer. State-specific lifetime determination of the $a^3\Pi$ state in CO. *Journal of Chemical Physics*, 107:7034–7040, 1997.

[20] D. DeMille. Quantum computation with trapped polar molecules. *Physical Review Letters*, 88:067901, 2002.

[21] A. André, D. DeMille, J. M. Doyle, M. D. Lukin, S. E. Maxwell, P. Rabl, R. J. Schoelkopf, and P. Zoller. A coherent all-electrical interface between polar molecules and mesoscopic superconducting resonators. *Nature Physics*, 2:636–642, 2006.

[22] N. Balakrishnan, A. Dalgarno, and R. C. Forrey. Vibrational relaxation of CO by collisions with ^{4}He at ultracold temperatures. *Journal of Chemical Physics*, 113:621–627, 2000.

[23] E. P. Wigner. On the behavior of cross sections near thresholds. *Physical Review*, 73:1002–1009, 1948.

[24] J. J. Gilijamse, S. Hoekstra, S. Y. T. van de Meerakker, G. C. Groenenboom, and G. Meijer. Near-threshold inelastic collisions using molecular beams with a tunable velocity. *Science*, 313:1617–1620, 2006.

[25] B. C. Sawyer, B. K. Stuhl, D. Wang, M. Yeo, and J. Ye. Molecular beam collisions with a magnetically trapped target. *Physical Review Letters*, 101:203203, 2008.

[26] L. Scharfenberg, J. Kłos, P. J. Dagdigian, M. H. Alexander, G. Meijer, and S. Y. T. van de Meerakker. State-to-state inelastic scattering of Stark-decelerated OH radicals with Ar atoms. *Physical Chemistry Chemical Physics*, 2010. (in press).

[27] J. D. Weinstein, R. deCarvalho, T. Guillet, B. Friedrich, and J. M. Doyle. Magnetic trapping of calcium monohydride molecules at millikelvin temperatures. *Nature*, 395:148–150, 1998.

[28] S. Y. T. van de Meerakker, H. L. Bethlem, and G. Meijer. Taming molecular beams. *Nature Physics*, 4:595–602, 2008.

[29] R. Fulton, A. I. Bishop, M. N. Shneider, and P. F. Barker. Controlling the motion of cold molecules with deep periodic optical potentials. *Nature Physics*, 2:465–468, 2006.

[30] S. D. Hogan, D. Sprecher, M. Andrist, N. Vanhaecke, and F. Merkt. Zeeman deceleration of H and D. *Physical Review A*, 76:023412, 2007.

[31] E. Narevicius, A. Libson, C. G. Parthey, I. Chavez, J. Narevicius, U. Even, and M. G. Raizen. Stopping supersonic oxygen with a series of pulsed electromagnetic coils: A molecular coilgun. *Physical Review A*, 77:051401(R), 2008.

[32] T. Middelmann. Entwicklung einer Methode zur Erzeugung translatorisch kalter neutraler Moleküle. Master's thesis, Technische Universität Berlin, 2007.

[33] M. Gupta and D. Herschbach. A mechanical means to produce intense beams of slow molecules. *Journal of Physical Chemistry A*, 103:10670–10673, 1999.

[34] M. Strebel, F. Stienkemeier, and M. Mudrich. Improved setup for producing slow beams of cold molecules using a rotating nozzle. *Physical Review A*, 81:033409, 2010.

[35] E. Narevicius, A. Libson, M. F. Riedel, C. G. Parthey, I. Chavez, U. Even, and M. G. Raizen. Coherent slowing of a supersonic beam with an atomic paddle. *Physical Review Letters*, 98:103201, 2007.

[36] M. S. Elioff, J. J. Valenti, and D. W. Chandler. Subkelvin cooling NO molecules via "billiard-like" collisions with argon. *Science*, 302:1940–1943, 2003.

[37] B. S. Zhao, S. E. Shin, S. T. Park, X. Sun, and D. S. Chung. Slow molecules produced by photodissociation. *Journal of the Physical Society of Japan*, 78:094302, 2009.

[38] A. Trottier, D. Carty, and E. Wrede. Photostop: Production of zero-velocity molecules by photodissociation in a molecular beam, 2010. arXiv:1002.3698.

[39] N.-N. Liu and H. Loesch. Kinematic slowing of molecules formed by reactive collisions. *Physical Review Letters*, 98:103002, 2007.

[40] S. A. Rangwala, T. Junglen, T. Rieger, P. W. H. Pinkse, and G. Rempe. Continuous source of translationally cold dipolar molecules. *Physical Review A*, 67:043406, 2003.

[41] E. Nikitin, E. Dashevskaya, J. Alnis, M. Auzinsh, E. R. I. Abraham, B. R. Furneaux, M. Keil, C. McRaven, N. Shafer-Ray, and R. Waskowski. Measurement and prediction of the speed-dependent throughput of a magnetic octupole velocity filter including nonadiabatic effects. *Physical Review A*, 68:023403, 2003.

[42] B. Bertsche and A. Osterwalder. State selective detection of velocity filtered ND_3 molecules, 2010. arXiv:1004.3812.

[43] K.-K. Ni, O. Ospelkaus, M. H. G. de Miranda, A. Pe'er, B. Neyenhuis, J. J. Zirbel, S. Kotochigova, P. S. Julienne, D. S. Jin, and J. Ye. A high phase-space-density gas of polar molecules. *Science*, 322:231–235, 2008.

[44] J. G. Danzl, E. Haller, M. Gustavsson, M. J. Mark, R. Hart, N. Bouloufa, O. Dulieu, H. Ritsch, and H.-C. Nägerl. Quantum gas of deeply bound ground state molecules. *Science*, 321:1062–1066, 2008.

[45] F. Lang, K. Winkler, C. Strauss, R. Grimm, and J. H. Denschlag. Ultracold triplet molecules in the rovibrational ground state. *Physical Review Letters*, 101:133005, 2008.

[46] J. Deiglmayr, A. Grochola, M. Repp, K. Mötlbauer, C. Glück, J. Lange, O. Dulieu, R. Wester, and M. Weidemüller. Formation of ultracold polar molecules in the rovibrational ground state. *Physical Review Letters*, 101:133004, 2008.

[47] A. L. Migdall, J. V. Prodan, W. D. Phillips, T. H. Bergeman, and H. J. Metcalf. First observation of magnetically trapped neutral atoms. *Physical Review Letters*, 54:2596–2599, 1985.

[48] M. A. Kasevich, E. Riis, S. Chu, and R. G. DeVoe. rf spectroscopy in an atomic fountain. *Physical Review Letters*, 63:612–615, 1989.

[49] N. R. Newbury, C. J. Myatt, and C. E. Wieman. *s*-wave elastic collisions between cold ground-state ^{87}Rb atoms. *Physical Review A*, 51:R2680–R2683, 1995.

[50] M. H. Anderson, J. R. Ensher, M. R. Matthews, C. E. Wieman, and E. A. Cornell. Observation of Bose-Einstein condensation in a dilute atomic vapor. *Science*, 269:198–201, 1995.

[51] J. Fortágh and C. Zimmermann. Magnetic microtraps for ultracold atoms. *Reviews of Modern Physics*, 79:235–289, 2007.

[52] M. Trupke, J. Goldwin, B. Darquié, G. Dutier, S. Eriksson, J. Ashmore, and E. A. Hinds. Atom detection and photon production in a scalable, open, optical microcavity. *Physical Review Letters*, 99:063601, 2007.

[53] Y. Colombe, T. Steinmetz, G. Dubois, F. Linke, D. Hunger, and J. Reichel. Strong atom-field coupling for Bose-Einstein condensates in an optical cavity on a chip. *Nature*, 450:272–277, 2007.

[54] Y. Shin, C. Sanner, G.-B. Jo, T. A. Pasquini, M. Saba, W. Ketterle, D. E. Pritchard, M. Vengalattore, and M. Prentiss. Interference of Bose-Einstein condensates split with an atom chip. *Physical Review A*, 72:021604, 2005.

[55] L. Santos, G. V. Shlyapnikov, P. Zoller, and M. Lewenstein. Bose-Einstein condensation in trapped dipolar gases. *Physical Review Letters*, 85:1791–1794, 2000.

[56] T. Lahaye, T. Koch, B. Frölich, M. Fattori, J. Metz, A. Griesmaier, S. Giovanazzi, and T. Pfau. Strong dipolar effects in a quantum ferrofluid. *Nature*, 448:672–675, 2007.

[57] V. Vuletić and S. Chu. Laser cooling of atoms, ions, or molecules by coherent scattering. *Physical Review Letters*, 84:3787–3790, 2000.

[58] B. L. Lev, A. Vukics, E. R. Hudson, B. C. Sawyer, P. Domokos, H. Ritsch, and J. Ye. Prospects for the cavity-assisted laser cooling of molecules. *Physical Review A*, 77:023402, 2008.

[59] F. Robicheaux. A proposal for laser cooling of OH molecules. *Journal of Physics B*, 42:195301, 2009.

[60] E. S. Shuman, J. F. Barry, D. R. Glenn, and D. DeMille. Radiative force from optical cycling on a diatomic molecule. *Physical Review Letters*, 103:223001, 2009.

[61] H. J. Metcalf and P. van der Straten. *Laser Cooling and Trapping*, page 274. Springer-Verlag, 1999.

[62] J. Stark. Beobachtungen über den Effekt des elektrischen Feldes auf Spektrallinien. *Sitzungsberichte der Königlich Preussischen Akademie der Wissenschaften*, pages 932–946, 1913.

[63] E. Schrödinger. An undulatory theory of the mechanics of atoms and molecules. *The Physical Review*, 28:1049–1070, 1926.

[64] N. Bohr. On the constitution of atoms and molecules. *Philosophical Magazine Series 6*, 26:1–25, 1913.

[65] N. E. Shafer-Ray, K. A. Milton, B. R. Furneaux, E. R. I. Abraham, and G. R. Kalbfleisch. Design of a biased Stark trap of molecules that move adiabatically in an electric field. *Physical Review A*, 67:045401, 2003.

[66] J. P. Gordon, H. J. Zeiger, and C. H. Townes. The maser — new type of microwave amplifier, frequency standard, and spectrometer. *Physical Review*, 99:1264–1274, 1955.

[67] J. Reuss. State selection by nonoptical methods. In G. Scoles, editor, *Atomic and Molecular Beam Methods Volume I*. Oxford University Press, 1988.

[68] W. Paul. Electromagnetic traps for charged and neutral particles. In G. Ekspong, editor, *Nobel Lectures in Physics 1981–1990*. World Scientific Publishing Company, 1993.

[69] D. Kakati and D. C. Lainé. Alternate-gradient focusing of a molecular beam of ammonia. *Physics Letters*, 24A:676, 1967.

[70] M. Born and V. Fock. Beweis des Adiabatensatzes. *Zeitschrift für Physik*, 51:165–180, 1928.

[71] Y. B. Zeldovich. The quasienergy of a quantum-mechanical system subjected to a periodic action. *Soviet Physics JETP*, 24:1006–1008, 1967.

[72] V. I. Ritus. Shift and splitting of atomic energy levels by the field of an electromagnetic wave. *Soviet Physics JETP*, 24:1041–1044, 1967.

[73] S. A. Schulz, H. L. Bethlem, J. van Veldhoven, J. Küpper, H. Conrad, and G. Meijer. Microstructured switchable mirror for polar molecules. *Physical Review Letters*, 93:020406, 2004.

[74] C. E. Shannon. Communication in the presence of noise. *Proceedings of the IRE*, 37:10–21, 1949.

[75] C. W. Gear. *Numerical Initial Value Problems in Ordinary Differential Equations*, pages 10–24. Prentice Hall, Inc., 1971.

[76] M. Galassi, J. Davies, J. Theiler, B. Gough, G. Jungman, P. Alken, M. Booth, and F. Rossi. *GNU Scientific Library Reference Manual*. Network Theory Limited, third edition, 2009.

[77] C. A. Burrus. Stark effect from 1.1 to 2.6 millimeters wavelength: PH_3, PD_3, DI, and CO. *Journal of Chemical Physics*, 28:427–429, 1958.

[78] W. L. Jorgensen and L. Salem. *The Organic Chemist's Book of Orbitals*. Academic Press, 1973.

[79] B. G. Wicke, R. W. Field, and W. Klemperer. Fine structure, dipole moment, and perturbation analysis of $a^3\Pi$ CO. *Journal of Chemical Physics*, 56:5758–5770, 1972.

[80] F. Hund. Zur Deutung einiger Erscheinungen in den Molekelspektren. *Zeitschrift für Physik*, 36:657–674, April 1926.

[81] J. M. Brown and A. Carrington. *Rotational Spectroscopy of Diatomic Molecules*, page 233. Cambridge University Press, 2003.

[82] J. M. Brown and A. Carrington. *Rotational Spectroscopy of Diatomic Molecules*, page 146. Cambridge University Press, 2003.

[83] R. N. Zare. *Angular Momentum*, page 85. John Wiley & Sons, Inc., 1988.

[84] J. M. Brown and A. Carrington. *Rotational Spectroscopy of Diatomic Molecules*, pages 244–251. Cambridge University Press, 2003.

[85] J. M. Brown and A. Carrington. *Rotational Spectroscopy of Diatomic Molecules*, page 169. Cambridge University Press, 2003.

[86] J. M. Brown and A. Carrington. *Rotational Spectroscopy of Diatomic Molecules*, page 167. Cambridge University Press, 2003.

[87] D. A. Varshalovich, A. N. Moskalev, and V. K. Khersonskii. *Quantum Theory of Angular Momentum*, page 456. World Scientific Publishing, 1988.

[88] J. M. Brown and A. Carrington. *Rotational Spectroscopy of Diatomic Molecules*, chapter 7. Cambridge University Press, 2003.

[89] J. M. Brown and A. Carrington. *Rotational Spectroscopy of Diatomic Molecules*, page 342. Cambridge University Press, 2003.

[90] J. M. Brown, I. Kopp, C. Malmberg, and B. Rydh. An analysis of hyperfine interactions in the electronic spectrum of AlF. *Physica Scripta*, 17:55–67, 1978.

[91] E. Hirota, J. M. Brown, J. T. Hougen, T. Shida, and N. Hirota. Symbols for fine and hyperfine structure parameters. *Pure and Applied Chemistry*, 66:571–576, 1994.

[92] J. M. Brown and A. Carrington. *Rotational Spectroscopy of Diatomic Molecules*, page 136. Cambridge University Press, 2003.

[93] N. Carballo, H. E. Warner, C. S. Gudeman, and R. C. Woods. The microwave spectrum of CO in the $a^3\Pi$ state. ii. the submillimeter wave transitions in the normal isotope. *Journal of Chemical Physics*, 88:7273–7286, 1988.

[94] S. Yamamoto and S. Saito. The microwave spectra of CO in the electronically excited states ($a^3\Pi_r$ and $a'\,^3\Sigma^+$). *Journal of Chemical Physics*, 89:1936–1944, 1988.

[95] A. Wada and H. Kanamori. Submillimeter-wave spectroscopy of CO in the $a^3\Pi$ state. *Journal of Molecular Spectroscopy*, 200:196–202, 2000.

[96] R. W. Field, S. G. Tilford, R. A. Howard, and J. D. Simmons. Fine structure and perturbation analysis of the $a^3\Pi$ state of CO. *Journal of Molecular Spectroscopy*, 44:347–382, 1972.

[97] R. H. Gammon, R. C. Stern, M. E. Lesk, B. G. Wicke, and W. Klemperer. Metastable $a^3\Pi$ ^{13}CO: Molecular-beam electric-resonance measurements of the fine structure, hyperfine structure, and dipole moment. *Journal of Chemical Physics*, 54:2136–2150, 1971.

[98] H. E. Warner. *The microwave spectroscopy of ions and other transient species in DC glow and extended negative glow discharges*. PhD thesis, University of Wisconsin — Madison, 1988.

[99] G. Winnewisser, S. P. Belov, T. Klaus, and R. Schneider. Sub-doppler measurements on the rotational transitions of carbon monoxide. *Journal of Molecular Spectroscopy*, 184:468–472, 1997.

[100] G. Klapper, F. Lewen, R. Gendriesch, S. P. Belov, and G. Winnewisser. Sub-doppler measurements of the rotational spectrum of $^{13}C^{16}O$. *Journal of Molecular Spectroscopy*, 201:124–127, 2000.

[101] M. Kirste, B. G. Sartakov, M. Schnell, and G. Meijer. Nonadiabatic transitions in electrostatically trapped ammonia molecules. *Physical Review A*, 79:051401, 2009.

[102] S. A. Meek, E. R. I. Abraham, and N. E. Shafer-Ray. Impossibility of a biased Stark trap in two dimensions. *Physical Review A*, 71:065402, 2005.

[103] R. T. Jongma. *Molecular Beam Experiments and Scattering Studies with State-selected Metastable CO*. PhD thesis, Katholieke Universiteit Nijmegen, 1997.

[104] D. R. Miller. Free jet sources. In G. Scoles, editor, *Atomic and Molecular Beam Methods Volume I*. Oxford University Press, 1988.

[105] Air Liquide. Gas encyclopaedia. Available: http://encyclopedia.airliquide.com/.

[106] Radiant Dyes Laser Accessories GmbH. *Operation and Maintenance Manual Radiant Dyes cw-Ring Dye Laser*.

[107] D. R. Lide, editor. *CRC Handbook of Chemistry and Physics*, pages 12–114. CRC Press, 90th edition, 2009.

[108] A. J. Smith, R. E. Imhof, and F. H. Read. Measured lifetimes of the two vibrational levels of the $b^3\Sigma^+$ state of CO. *Journal of Physics B*, 6:1333–1338, 1973.

Acknowledgments

To conclude this thesis, I would like to thank and acknowledge the many people who helped in its creation. First, I would like to thank Gerard Meijer for giving me the opportunity to do this research in his group, for always being actively involved in the project, and for providing the insights that were decisive in the success of the project. I would also like to thank the other members of the chip group. Horst Conrad, in particular, has directed me throughout the course of this research, he has taught me much in the details of setting up and operating an experimental apparatus and has done his best to convey some of the wisdom he has acquired in an over forty year career in physics. Rick Bethlem has contributed greatly to the early design of the chip, and without him, the chip may have never been developed. Gabriele Santambrogio has done an excellent job of taking over the project and keeping it running while I've written my thesis, already rebuilding the machine to obtain the experimental results presented in chapter 7. I know that I leave the chip project in capable hands. Thanks to Boris Sartakov for providing theoretical insight and helping us to understand the non-adiabatic losses. I would also like to welcome the newest members of the group, Mark Abel and Isabel Gonzalez, and I wish them much success in their future research.

Ich möchte mich auch bei den technischen Mitarbeiter bedanken, ohne die diese Forschung nicht möglich wäre. Ein besonders entscheidender Beitrag kam aus unserem Elektroniklabor, mit dem die große Herausforderung für Hochfrequenzverstärker und Wellenformgeneratoren erfüllt wurde. Dafür und für die viele Zeit, die sie investiert haben, möchte ich mich besonders bei Georg Heyne, Viktor Platschkowski und Torsten Vetter bedanken. Ich danke auch Henrik Haak, der einen stabilen Chip-Manipulator für eine sehr enge Kammer konstruiert hat. Bei Sandy Gewinner möchte ich mich bedanken, dass er immer dafür gesorgt hat, dass die Laser Photonen geliefert haben. Dank auch an Jochen Küpper für die Einführung des KouDA Messsystems und an Uwe Hoppe dafür, dass er KouDA immer am Laufen gehalten hat. Bei Petrik Bischoff, Manfred Erdmann, Georg Hammer und Rolf Meilicke bedanke ich mich dafür, dass sie immer "auf die Schnelle" die Teile gebaut haben, dass sie die notwendigen Bauteile auf Lager gehalten haben, und dass sie die notwendige Infrastruktur (Gas, Elektrik, Wasser, usw.) bereitgestellt haben.

I am also grateful to have had the opportunity during my time here to work with other groups on projects unrelated to the chip. I was fortunate to spend many evenings at dinner and a couple weeks in Korea with Wieland Schöllkopf and Bum Suk Zhao. Inevitably some of our discussions turned to their work on the quantum reflection of atoms from surfaces, and the result was a nice collaboration. I also enjoyed the collaboration with Joop Gilijamse, Steven Hoekstra, Markus Metsälä, and Bas van de Meerakker at the big machine and the projects we did together in which I brought the laser and they brought the velocity-controlled molecules. The measurement of the lifetime of metastable CO was

a very nice result, and although our repeated attempts at measuring the density of guided OH using cavity ring down never quite worked out, I still think the experience gained was useful nonetheless. I would also like to thank Andreas Osterwalder: while we worked together for a short time in our first year doing a bit of REMPI on metastable CO, by far our more successful project has been the ring decelerator, a.k.a. macrostructure. I'm glad I can take over that project and hopefully we'll have some more nice results again in the near future.

Thanks also to the many people I never directly worked with but who were always there for moral support. Cyndi: thanks for being My Fellow American at the institute from the beginning of my time here and always being there to cheer me up. Adela: thanks for being a good neighbor...I always enjoyed the dinners and going to the movies with you and Mike on the weekends. Danke, Peter, für die interessanten Diskussionen über Physik und andere Themen während unserer sonntäglichen Kaffeepausen. Thanks also to the many members of the department who have at one time or another served as late evening (or early afternoon) drinking buddies: you know who you are (or might hazily remember bits of events that transpired), so I will avoid actively shaming you here. Danke Inga, dass Du immer die mühevolle Organisation auf Dich genommen hast, damit alles (u.a. das Sommerfest, die Wandertage, der Empfang bei meiner Doktorverteidigung) glatt läuft.

Thanks to my parents and my grandparents for supporting me for the last 28 years. Thanks also for being patient over the last few years and not taking my statements that I should be finished with my PhD in "about a year" too literally.

마지막으로 삼년 전부터 사랑하고 격려해준 우리 수영에게 고맙다는 말을 전하고 싶습니다.

Curriculum Vitae

For reasons of data protection,
the curriculum vitae is not included in the online version

List of Publications

[1] S. A. Meek, E. R. I. Abraham, and N. E. Shafer-Ray. Impossibility of a biased Stark trap in two dimensions. *Physical Review A*, 71:065402, 2005.

[2] J. J. Gilijamse, S. Hoekstra, S. A. Meek, M. Metsälä, S. Y. T. van de Meerakker, G. Meijer, and G. C. Groenenboom. The radiative lifetime of metastable CO ($a^3\Pi$, $v = 0$). *Journal of Chemical Physics*, 127:221102, 2007.

[3] S. A. Meek, H. L. Bethlem, H. Conrad, and G. Meijer. Trapping molecules on a chip in traveling potential wells. *Physical Review Letters*, 100:153003, 2008.

[4] B. S. Zhao, S. A. Schulz, S. A. Meek, G. Meijer, and W. Schöllkopf. Quantum reflection of helium atom beams from a microstructured grating. *Physical Review A*, 78:010902, 2008.

[5] S. A. Meek, H. Conrad, and G. Meijer. A Stark decelerator on a chip. *New Journal of Physics*, 11:055024, 2009.

[6] S. A. Meek, H. Conrad, and G. Meijer. Trapping molecules on a chip. *Science*, 324:1699–1702, 2009.

[7] S. A. Meek, G. Santambrogio, H. Conrad, and G. Meijer. Taming molecular beams; toward a gas-phase molecular laboratory on a chip. *Journal of Physics: Conference Series*, 194:012063, 2009.

[8] A. Osterwalder, S. A. Meek, G. Hammer, H. Haak, and G. Meijer. Deceleration of neutral polar molecules in macroscopic traveling traps. *Physical Review A*, 81:051401, 2010.